Three dimensional sensing by digital video fringe projection

Matthew J. Baker
University of Wollongong

Three Dimensional Sensing by Digital Video Fringe Projection

Matthew J. Baker

B.E. Telecommunications (Hons),
University of Wollongong

A Thesis presented for the degree of
Doctor of Philosophy

School of Electrical, Computer and Telecommunications Engineering,
University of Wollongong,
Australia,

April 2008

Thesis supervisors: A/Prof. Jiangtao Xi and Prof. Joe F. Chicharo

This thesis is dedicated to my family and friends.

Abstract

Fast, high precision and automated optical noncontact surface profile and shape measurement has been an extensively studied research area due to the diversity of potential application which extends to a variety of fields including but not limited to industrial monitoring, computer vision, virtual reality and medicine. Among others, structured light Fringe Projection approaches have proven to be one of the most promising techniques. Traditionally, the typical approach to Fringe Projection 3D sensing involves generating fringe images via interferometric procedures, however, more recent developments in the area of digital display have seen researchers adopting Digital Video Projection (DVP) technology for the task of fringe manufacture. The ongoing and extensive exploitation of DVP for Fringe Projection 3D sensing is derived from a number of key incentives the projection technology presents relative to the more traditional forms of projection. More specifically, DVP allows for the ability to accurately control various attributes of the projected fringe image at high speed in software, along with the capabilities to develop multi-channel techniques via colour projection. Furthermore, considering the typical DVP source is capable of projecting a standard 24 bit bitmap computer generated image, when interfaced to a personal computer, DVP makes for a very affordable projection source. However, despite the aforementioned incentives, in contrast to the more traditional methods of generating fringe images, the digitally projected fringe signal presents a number of shortcomings which ultimately hinder the effective application of the technology for Fringe Projection 3D sensing.

This thesis aims to improve the effectiveness of the deployment of DVP technology for Fringe Projection 3D sensing approaches. The proposed initiative is facilitated through extensive analysis of the application of DVP technology for fringe processing, and furthermore by the proposal of new digital fringe calibration procedures.

Firstly, this work demonstrates a comprehensive survey of current Fringe Projection 3D sensing approaches including an introductory review of the rudimentary notion of projecting fringes for 3D data acquisition. The survey also provides a thorough description of the evolution of the three major forms of fringe processing i.e. Fringe Phase Stepping,

Fourier Fringe analysis and Direct Detection.

The limitations of DVP for Fringe Projection are demonstrated through the development of a novel fringe phase emulation approach. The phase emulation approach is subsequently employed to establish empirical insight into the application of DVP technology for Fringe Projection. More specifically, the preliminary empirical analysis is used to test the veracity of the application of the two chief DVP technologies (Liquid Crystal Display, LCD and Digital Light Processing, DLP, Texas Instruments) for Fringe Projection. Through this study the camera / projector non-linear intensity response is shown to be the single most significant shortcoming inherent to DVP based Fringe Projection implementations.

Following the findings of the preliminary empirical analysis the influence of the Display Gamma attributes of the projection system is extensively investigated. The harmonic structure of a typical digitally projected fringe signal is examined and an approximate analysis framework proposed. The framework is subsequently utilised to form a set of equations defining the true γ sensitivity of a range of highly exploited fringe processing techniques. The approximate analysis is later verified and the practical significance of the findings demonstrated. Through this study the true nature of the Display Gamma related phase measuring residual error is revealed.

With the aid of a verified framework, investigations into additional Display Gamma related Fringe Projection phenomena is undertaken. More specifically, the optimisation of digitally projected fringes by fringe parameter manipulation is demonstrated. The temporal nature of digitally projected fringe images is studied for the well exploited single shot Fourier Transform Profilometry technique and the digital fringe harmonic dependence on the projector optical modulation transfer function is revealed. Subsequently, the elimination of Display Gamma related Fringe Projection phase measuring residual error for phase stepping techniques by projector defocus optimisation is shown.

Finally, a novel digital fringe calibration approach ideal for minimum shot fringe processing techniques is proposed. The calibration procedure is centered on the application of Artificial Neural Networks (ANNs) to correct the non-linear intensity distortion associated with the camera / projector system. Unlike previously proposed gamma correction techniques, the neural fringe calibration technique requires no additional data acquisi-

tion with effective calibration requiring no more than a single cross-section of a reference fringe. The neural network fringe calibration approach is also shown to significantly outperform simple filter based techniques of similar computational complexity. Given the reduced data requirements for the neural approach its application for multi-channel fringe calibration is also considered.

Certification

I, Matthew John Baker, declare that this thesis, submitted in fulfilment of the requirements for the award of Doctor of Philosophy, in the School of Electrical, Computer and Telecommunications Engineering, University of Wollongong, is wholly my own work unless otherwise referenced or acknowledged. The document has not been submitted for qualifications at any other academic institution.

_____

Matthew John Baker

17th February 2008

Acknowledgements

I would firstly like to convey my thanks to both my supervisors, Associate Professor Jiangtao Xi and Professor Joe Chicharo. Without their continual support, guidance and patience this research would not have been possible. I thank them both for providing me with freedom in my research and the opportunity to travel and present my research at international conferences.

I would like to thank former fellow PhD student Dr. Yingsong Hu for the many stimulating conversations and assistance in regard to many of the aspects of this research. I would also like to thank Dr. Enbang Li for his helpful discussions in the early stages of this work.

Special thanks goes to Dr. Mark O'dywer and Ying Que for sharing their PhD experience with me. Thanks to Mark for more recently reviewing sections of this dissertation and, moreover, for his continual reassurance that "things would be alright", not to mention the interesting discussions over msn messenger. Thanks to Ying for his empathetic encouragement throughout the duration of the PhD program and particularly during the later write up stages.

Not to be missed is the acknowledgement of Dr. Philip Conder. Thanks Phil! (you got your acknowledgement).

Thank you to all my friends for facilitating the essential diversions necessary to maintain my sanity and renew focus over the duration of my studies. In particular, i would like to thank Melissa Kent. Special thanks to Mel for her continual and ongoing support as i rode the often emotionally grueling rollorcoaster otherwise known as the PhD experience.

A very special thank you goes to my parents who have nurtured my desire to pursue "what makes you happy". Thanks also to Mum and Dad for being a constant source of support both financially and generally through the ups and downs of life. I will un-

doubtedly never be able to repay the latter debts, however, i should be ok for the financial debts.... eventually.

Finally, a very special thank you to my son Khye. Khye's very being is certainly without a doubt my greatest accomplishment and although he cannot read many of the words contained within this document watching him grow and learn how to has truly been an inspiration for the completion of this work.

List of Publications

Journal publications:

1. Matthew J. Baker, Jiangtao Xi, Joe Chicharo, “A Neural Network Digital Fringe Calibration Technique for Structured Light Profilometers”, *Applied Optics* 46, March 2007, pp 1233-1243.

2. Matthew J. Baker, Joe Chicharo and Jiangtao Xi, “Accuracy Limitations in Profilometric Metrology Schemes using Digital Structured Light”, *Accepted subject to revisions, IEEE Transactions on Instrumentation and Measurement*

3. Matthew J. Baker, Jiangtao Xi and Joe Chicharo “The Implications of Display Gamma for Fringe Projection 3D sensing using Digital Video Projection”, *To be submitted to Applied Optics*

Conference publications:

4. Matthew. J. Baker, J. F. Chicharo J. Xi, and E. Li, “Accuracy limitations introduced by digital projection sources in profilometric optical metrology systems”, *IEEE Conference on Optoelectronic and Microelectronic Materials and Devices, COMMAD 2004*, Brisbane, Australia, 8-10 December 2004, pp.261-264 2005IEEE

5. Matthew. J. Baker, J. Xi, E. Li and J. F. Chicharo, “A contrast between DLP and LCD digital projection technology for triangulation based optical profilometry”, *Optics East: Sensors and Photonics for Applications in Industry, Life Sciences and Communica-*

tions, Boston, Massachusetts, USA, October 25-26, 2005, (EI: 06109749730).

6. Matthew J. Baker, Jiangtao Xi, Joe Chicharo, "Fringe Calibration using Neural Network Signal Mapping for Structured Light Profilometers", *International Symposium on Intelligent Signal Processing and Communication Systems, ISPACS 2006*, Tottori, Japan, December 12-15, 2006.

7. Matthew J. Baker, Jiangtao Xi, Joe Chicharo, "Multi-channel Digital Fringe Calibration for Structured Light Profilometers using Neural Networks", *IEEE Instrumentation and Measurement Technology Conference, IMTC 2007*, Warsaw, Poland, May 1-3, 2007.

8. Matthew J. Baker, Joe Chicharo, Jiangtao Xi, "An Investigation into Temporal Gamma Luminance for Digital Fringe Fourier Transform Profilometers", *IEEE International Symposium on Intelligent Signal Processing, WISP 2007*, Madrid, Spain, October 3-5, 2007.

9. Matthew J. Baker, Jiangtao Xi, Joe Chicharo, "Elimination of γ Non-linear Luminance Effects for Digital Video Projection Phase Measuring Profilometers" *4th International Symposium on Electronic Design, Test and Applications, DELTA 2008*, Hong Kong, January 23-25 2008.

Table of Contents

List of Abbreviations

3D	Three-Dimensional
2DFTP	Two-Dimensional Fourier Transform Profilometry
Am-Si	Amorphous Silicon
ANN	Artificial Neural Network
AOM	Acousto-Optic Modulator
CCD	Charged Couple Device
DC	Direct Component
DFP	Digital Fringe Projection
DFT	Discrete Fourier Transform
DLP	Digital Light Processing
DMD	Digital Micromirror Device
DPD	Direct Phase Detection
DVP	Digital Video Projection
FIR	Finite Impulse Response
FTP	Fourier Transform Profilometry
I3PSP	Improved Three Step Phase Stepping Profilometry
IFTP	Improved Fourier Transform Profilometry
IIR	Infinite Impulse Response
LCD	Liquid Crystal Display
LCOS	Liquid Crystal on Silicon
MEMS	MircroElectroMechanical System
MFTP	Modified Fourier Transform Profilometry
MMP	Modulation Measurement Profilometry
OPD	Optical Path Difference

PC	Personal Computer
PLL	Phase Locked Loop
PMP	Phase Measuring Profilometry
Poly-Si	Polycrystalline Silicon
PSD	Position Sensitive Detector
PSI	Phase Shifting Interferometry
PSP	Phase Stepping Profilometry
SLM	Spatial Light Modulator
SNR	Signal to Noise Ratio
SPD	Spatial Phase Detection
TFT	Thin Film Transistor
TI	Texas Instruments
TN	Twisted Nematic

List of Figures

List of Tables

Chapter 1

Preliminaries

1.1 Introduction

Fast, high precision and automated optical noncontact surface profile and shape measurement has been an extensively studied research area due to its many potential applications, including, industrial monitoring, machine vision, animation, virtual reality, dressmaking, prosthetics and ergonomics, etc. Among others, structured light approaches including fringe profilometry have proven to be one of the most promising techniques, particularly, since recent advancements in Digital Video Projection (DVP) Technology have provided the required attributes for the development of dynamic and more robust structured light approaches. However, since DVP technology is designed and optimised for viewing applications such as video presentations and home theater, the technology presents a number of shortcomings when applied in the structured light environment. The application of DVP for structured light 3D sensing including analysis and alleviation of these shortcomings form the basis of this thesis.

In this chapter a brief introduction into 3D sensing is provided, highlighting some of the more significant existing approaches. Subsequently, the motivation for this research is addressed, including the approach and contribution of the author's works. Finally, the structure of this dissertation is outlined.

1.2 Three-Dimensional Sensing

Throughout time the science of measurement or metrology has often attracted the interest of mankind. In fact, primitive measurements of weight, length and time serve as evidence of the considerable role metrology has played right throughout the ages and furthermore in the development of the modern world. More recently through technological advancements, namely, in the areas of computer processing power, and digital imaging and display, the application and feasibility of optical metrology methods has grown considerably. Of particular interest are those optical approaches dedicated to obtaining 3D data.

Over the past few decades a range of optical methods for 3D sensing have been proposed and their practical implementations demonstrated [1]. In general 3D sensing techniques can be broadly categorised as either passive or active. Passive approaches typically utilise multiple views or image scene characteristics to determine 3D information. While it is arguable that passive approaches are more widely applicable for 3D sensing, often the resolution for the measurement of complex scenes is somewhat limited [2] and hence the evolution to active approaches was realised. Active approaches determine scene depth information by way of projection of a controlled light source(s) and the adequate capture of a reflected energy distribution. In contrast to passive techniques, the measurement accuracy of active methods can often be significantly increased, however, with this comes the burden of the reliance on additional phenomenon such reflectance and dispersion of light not to mention the control and generation of adequate signals which is often performed by additional equipment.

Contrary to the classification of passive and active, the majority of techniques can also be further generalised as triangulation or coaxial in terms of the physical arrangement of sensing devices. The well exploited triangulation principle behind many techniques can often provide for high precision, however, yield the problem of “missing parts” not included in one or more views. Coaxial systems where sensing devices are aligned along a common axis do not suffer from such view obscurities, however, they may often be limited in terms of range of field and dynamic application.

Since no one particular 3D sensing classification “active” / “passive”, “triangulation” / “coaxial”, clearly offers significant proficiency in terms of speed, accuracy, implemen-

tation, cost etc, it is important to evaluate a number of proposed methods. The purpose of this section is to briefly outline some of the more significant approaches to 3D sensing, highlighting the advantages and shortcomings of each. They include: Photogrammetry methods such as Stereovision, Shape from Texture, Shape from Shading and Shape from Focusing; Time-of-Flight methods; Interferometric methods including Classical Interferometry and Moiré methods; and Structured Light methods such as Laser Scanning, Coded Structured Light and Fringe Projection approaches.

1.2.1 Photogrammetry Methods

Photogrammetry can be defined as the science or art of obtaining reliable measurements by means of photographic images [3]. Therefore in terms of 3D measurement, Photogrammetry methods can generally be considered as passive approaches whereby 3D information can be obtained via detailed analysis of photographic images. Photogrammetric methods often exploit image scene characteristics and / or multiple views in order to determine 3D information. Some of the more well known techniques include: Stereovision, Shape from Texture, Shape from Shading and Shape from Focusing.

1.2.1.1 Stereovision

As the name infers, “Stereovision” techniques make use of two or more views of a scene to sense 3D information. In general, the passive triangulation process of stereopsis can be broken down into three distinct stages; Image preprocessing, Matching and Height Determination [4]. In the preprocessing component, areas or features of stereo images are identified so correspondence between the multiple views can be established. The process of establishing correspondence is referred to as the matching stage and is often regarded as the most defining step in the stereopsis process. Once correspondence has been obtained the height distribution of the observed scene can then be determined. Over the past 30 years much research has been undertaken into the performance of preprocessing and matching stages, in terms of computational costs and disparity estimation accuracy [4, 5].

Stereo matching algorithms are often categorised as either Local or Global based methods. Local methods determine correspondence by considering small segments of stereo images, whilst Global methods consider entire or relatively larger portions of

stereo images. Early stereo methods focused predominantly on Local methods including Block Matching [6, 7, 8, 9, 10], Gradient Methods [11, 12, 13] and Feature based Matching [4, 14, 15, 16] due to their efficiency, however, Local methods are sensitive to occlusive and other ambiguous regions. Directly as a result of the sensitivity to occlusive views more recent research has been undertaken into the investigation and implementation of Global matching methods [17, 18, 19]. Global methods are less sensitive to such local ambiguous regions since a larger range of intensity values are taken into consideration for matching.

Despite the development of Stereopsis into a mature research field, a robust, computationally efficient and accurate 3D sensing implementation has yet to be developed, largely due to the significant problem of correspondence.

1.2.1.2 Shape from Texture

Shape from Texture is a coaxial image based technique concerned with the exploitation of scene texture to determine scene depth. More specifically Shape from Texture attempts to measure the amount of change in texture density within a 2D image of a 3D scene. Kanatani *et al.* provide a generic viewpoint on the approach in [20]. The application of Shape from Texture is a somewhat limited 3D sensing approach since the method can only be applied to highly and uniformly distributed textured images of 3D scenery [2].

1.2.1.3 Shape from Shading

For many centuries artists have been utilising cues such as shading for depth portrayal and perception, however, it was not until the early 1970's that the method of Shape from Shading was first formally investigated by Horn as a method of 3D sensing [21]. The general approach to Shape from Shading is to reverse engineer the formation of a captured image in terms of a reflection model, light source direction and surface normal. Given a grey level image, the aim of a Shape from Shading algorithm is to recover the light source and surface shape at each pixel in the image. Typically Shape from Shading techniques achieve this though Minimisation approaches, Propagation approaches, Local approaches, and Linear approaches [21].

Since Horn's initial investigations a number of methods and variations of such ap-

proaches have been proposed, including the integration of Shape from Shading with Stereo [22, 23]. More recently the integrity of core frameworks and modeling of Shape from Shading approaches have been questioned, and hence have been further investigated and seen the development of newer more robust algorithms and mathematical modeling [24, 25, 26]. Although Shape from Shading can provide image depth, the accuracy of reflection models, constraints on ambient lighting conditions and resolution of reconstruction somewhat limits it's application to 3D sensing.

1.2.1.4 Shape from Focusing

Again based on visual stimuli, Shape from Focusing is a sensing technique which relies on the depth of focus of a lens imaging arrangement. Traditional Shape from Focus methods use a sequence of images of a 3D scene, whereby, for each image the distance between the 3D scene and the imaging optics is shifted such that different regions of the 3D scene come into focus with the progression of the image sequence. Therefore by quantitatively measuring optimum focusing of local regions of the 3D scene the actual 3D depth can be establish through correlation of the displacement of imaging system and 3D scene [27, 28]. A range of methods to quantify focus/defocus exist [2, 29], all methods exploit the underlying principle that defocusing can be modeled in terms of filter theory as a low-pass filter, where higher frequency content is attenuated. Since Shape from Focusing requires a finite sequence of images, interpolation is often utilised to improve the accuracy of the estimated depth map.

Recently, Pradeep *et al.* [30] proposed a strategy to improve depth estimate using a relative defocus blur among the image sequence combined with an image restoration technique, the approach was shown to improve on traditional methods for both synthetic and empirical data. Furthermore, bearing in mind the considerable amount of data and processing required for focused based measurement, other recent advances have been concerned with the optimisation of Shape from Focus methods using dynamic programming [31]. Probably one of the most significant drawbacks of Shape from Focusing is the amount of data required for 3D reconstruction, limiting the method to the static or quasi-static metrology applications. The reliance on significant data acquisition could be somewhat reduced by qualitatively measuring defocus, however, this would inevitably

result in reduced accuracy due to lens depth of focus sensitivity.

1.2.2 Time-of-Flight Techniques

Time-of-Flight techniques can be categorised as an active technology in which a light source is pulsed at a point on an object within a 3D scene. The time taken for the pulse to travel from the source to the target and back to a receiver with reference to a calibration pulse is measured, and thus the distance traveled by the pulse is calculated [1]. The method does not require any form of image processing and therefore has minimal computational requirements. Further since Time-of-Flight methods can be applied in the coaxial sense, the problem of missing parts familiar with triangulation based 3D sensors can be avoided. Time-of-Flight systems are commonly implemented utilising ultrasonic or laser sources for measurement of 3D scenes with a range depth in the order of meters [2]. The relatively large depth range of Time-of-Flight methods is attributed to the fact that range is limited only by the ability to receive a reliable reflected signal. Typical accuracy of Time-of-Flight approaches is in the order of mm's [32] however, more recently the development of a system based on single photon counting has been shown to obtain accuracy's within 10's of μm's [33]. Probably the most significant constraint of Time-of-Flight methods is a limited spatial field, with scanning technology required to obtain a full frame of depth information.

1.2.3 Interferometric Techniques

Interferometric methods are based on the fundamental principles of wave theory, and in particular the superposition or interference of multiple coherent electromagnetic wavefronts. The interference of coherent electromagnetic wavefronts results in an interferogram otherwise referred to as a fringe pattern. A fringe pattern conveys an intensity distribution that varies as a function of the geometrical properties of the viewing surface and therefore can be a very useful means to undertake surface measurements. The history of fringe processing can be traced back to the late 1800's, when Righi recognised that the relative displacement of two gratings could be determined by measuring the resultant Moiré fringe [34]. Although Righi's method could provide for reasonable insight into the

displacement of the gratings, much like any early fringe processing method prior to the conception of computers, the measurement application was limited as it only analysed the fringe based on fringe maxima and minima, with all other useful information ignored. Given the usefulness and great deal of detailed information a single fringe could undoubtedly yield for a multitude of applications, by the 1960's more complex fringe processing algorithms to autonomously provide more accurate information at each point of the sampled fringe began to evolve (typically for optical interferometry applications). The field then became very popular in the early 1980's in accordance with the availability of quality Charged Couple Devices (CCD's) and improved processing power. Thus, relatively speaking, the processing of fringes to yield measurement is most certainly not a new concept, and since its initial instantiation has found various useful applications. Given the maturity of the interferometric research field, a huge range of literature in regard to this particular form of measurement is abundantly available and no single review can embrace each and every development and variation of the methodology. Hence, only the major evolutions of Interferometric 3D sensing methods are briefly discussed. Included in the survey is what we have termed Traditional Interferometry techniques, which encompasses a wide range of interferogram types, and Moiré techniques, based on fringes generated by the Moiré phenomenon.

1.2.3.1 Traditional Interferometry

The principle of traditional interferometry is quite a well understood concept. Coherent light is directed onto a surface of interest with the reflected wavefront superposed with a reference beam, to form an interference fringe image observable to a CCD. Analysis of the fringe image can reveal phase information which can then yield the Optical Path Difference (OPD) or relative height distribution of the surface.

Interferometric surface profiling methods can often be generalised by the method in which fringe images are fabricated. Fringe patterns for surface profiling are typically created through manipulation of either

- Wavelength [35, 36, 37, 38],
- Refractive Index [39, 40] and/or;

- Illumination Direction/Number of sources [41, 42, 43].

With the primary focus of pioneer interferometric 3D sensing research focused on the adequate generation of reliable fringe patterns, subsequent research was aimed at improving the measurement accuracy of fringe processing techniques. Phase measuring interferometry methods were developed and provided for depth measurement at each pixel of the fringe image [44]. In contrast to previous single wavelength methods where accuracy was limited to half a wavelength, measuring only fringe maxima and minima, phase measuring methods provided the means for measurements of 1/100th of a fringe [45]. A further development of fringe phase analysis has seen the combination of phase measuring methods with multiple wavelength approaches to produce reliable measurements with accuracies of 1/1000th of a fringe [46].

Despite the very high accuracy associated with phase measuring interferometric methods the most significant shortcoming is the measurable range between adjacent pixels. This limitation can be expressed in terms of a phase ambiguity equal to the optical or synthetic wavelength for single wavelength or multiple wavelength variations, respectively. The phase ambiguity problem often limits the effective application of such phase measuring approaches to smooth continuous surfaces, since the change of height between adjacent pixels for rough and complex surfaces with discontinuities may be large relative to the equivalent wavelength of the source. More recently wavelength scanning using a tunable dye laser has been proposed to solve the phase ambiguity problem, yielding accuracies as high as 1μm [47], while other methods utilising white light [48] and the combination of speckle interferometry with heterodyne approaches [49] have also been proposed for the measurement of rough surfaces.

1.2.3.2 Moiré

Moiré fringes are produced when two gratings of approximately the same spatial frequency are superposed upon one another. The phenomenon can be observed as a visual beat pattern in everyday scenarios such as the overlapping of semi-transparent fabric, or when a highly textured image appears on a digital display or television screen. Relative to the interferograms discussed in 1.2.3.1, where the pitch of the fringe image is directly proportional to the wavelength of the source, Moiré fringes can be produced where the pitch

is source independent. In fact, the mathematical formulation of Moiré patterns resulting from the superposition of sinusoidal gratings is identical for interferograms produced by the superposition of electromagnetic wavefronts [50]. Conversely, the pitch of the resolved fringe image can be controlled by the physical grating medium used to produce the signal, thereby making the Moiré technique an effective tool in contouring relatively larger more coarse surfaces.

The application of Moiré fringes for surface topology was first investigated in the late 1960's early 70's, chiefly by Meadows *et al.* [51] and Takasaki [52]. Moiré methods for 3D sensing can be regarded as an active triangulation technique implemented in one of two variations; Shadow Moiré or Projection Moiré. Shadow Moiré approaches use a single grating to cast a shadow onto the surface to be profiled which is imaged through the grating from an offset angle. Projection Moiré methods utilise two gratings, one to project a grating onto the surface and a second to resolve the Moiré fringe.

Computer analysis of Moiré fringe images to distinguish between concavity and convexity posed as one of the most challenging problems with early Moiré methods, which also suffered from poor resolution, with depth information obtained only at fringe maxima and minima [53]. Hence, similar to the evolution of other classical interferometric methods, traditional Moiré approaches adopted the phase measuring ideology which significantly improved not only the accuracy but also practical implementation of Moiré methods [54, 55]. The typical measurement range of phase shifting Moiré methods is from 1mm to 0.5m with the resolution at 1/10th to 1/100th of a fringe. A further significant development in Moiré topography was the application of video projection technology to accurately and more rapidly generate Moiré contours to complement phase shifting approaches [56]. Moreover, video projection technology makes high speed 3D Moiré sensing more conceivable, an interesting discussion on high speed Moiré contouring methods is provided in Reference [57].

1.2.4 Structured Light Techniques

Structured Light approaches for 3D sensing can be considered as an active advancement in stereovision ideology, where one camera is replaced with an illumination source. The projection of a known pattern illuminating a surface to be profiled effectively resolves

correspondence between the multiple views of the stereo system without the need for geometrical constraints such as those briefed in Section 1.2.1.1 [58]. The height distribution of the surface is directly modulated into the projected intensity distribution which is generally imaged by a single camera. Through analysis of the deformed intensity distribution(s) the 3D information can be obtained and the height distribution reconstructed in 3D space in accordance with the well known triangulation configuration.

Structured light approaches for 3D sensing are typically differentiated on the basis of the nature of the projection. The most significant approaches can be classified as Laser Scanning approaches, Coded Structured Light approaches and Fringe Projection approaches.

1.2.4.1 Laser Scanning

Laser Scanning is probably one of the most simple yet effective methods of obtaining 3D data. Such characteristics can be attributed to the very rudimentary optical method of triangulation, which forms the basis of Laser Scanning approaches [59]. Typically a single dot or slit-like line of laser light is focused onto the surface of interest, a portion of the light is scattered from the surface and is imaged onto a detector such as a CCD or Position Sensitive Detector (PSD). The position of the captured laser light in conjunction with an appropriate calibration process can then yield the corresponding 3D displacement [60].

The typical range associated with Laser Scanning methods is from 200mm to 1mm with an accuracy of 1 part in 1000, at 40kHz or higher, although applications with a range of as small as 0.1mm and accuracies of less than a micrometer have also been reported [61]. Since depth data is obtained in a point by point or line by line fashion, scanning of an entire surface is required for a full frame of 3D data. Typically this is conducted by scanning the laser source through the scene, although pending on the application the scene may be shifted relative to the source / camera configuration [62, 63].

Despite the reputable accuracy and simplicity of Laser Scanning approaches, given that the approach is not a full field technology its application is limited to the measurement of static scenes.

1.2.4.2 Coded Structured Light

Coded Structured Light can be principally conceptualised as a full field variation of the Laser Scanning methodology. Coded Structure Light methods obtain full field analysis by illuminating the 3D scene with a coded pattern which can be used to identify correspondence within the scene. A significant number of coded light approaches have been matured over the past two decades most of which can be classified as one of three methods; Time multiplexed methods, Spatial Neighbourhood methods and Direct Codification methods [64].

Time Multiplex methods temporally code correspondence through the projection of a sequence of patterns that successively illuminate the target surface. The temporal intensity values of each pixel of the captured image sequence forms a codeword uniquely identifying scene correspondence. An early example of temporal codification was put forth by Posdamer and Altschuler [65]. The binary method projected a black and white sequence of patterns where the spatial frequency of successive patterns was increased by a factor of two. The method was later improved by Inokuchi *et al.* [66, 67] using the now well known Gray Code method. This development made the binary approach more robust in the presence of noise, however, due to the strong correlation between data quantity and resolution, efforts to reduce the number of projected patterns while retaining accuracy were made. As a result, techniques based on N-ary codes utilising intermediate intensity values were devised [68, 69].

Ideally, to facilitate optimal spatial resolution for Binary / N-ary techniques, the resolutions of the projected and captured images should be matched. However, due to limitations in intensity detection, the spatial resolution of such methods are limited accordingly. Therefore, the combination of Binary / N-ary methods with phase shifting methods were proposed, where pixel resolution could be obtained with the ability to measure complex surfaces with discontinuities [70, 71, 72].

The most significant shortcoming of all time multiplex methods results from the requirement that the scene must be static for the duration of the projected sequence. Spatial Neighbourhood methods can overcome the static scene drawbacks associated with time multiplex methods by coding a unique or quasi-unique illumination pattern, where correspondence codewords can be formed based on pixels surrounding the point of interest.

Clearly, with reference to Time Multiplexed methods, in order to obtain similar spatial accuracy, the requirement is for the projection of a significantly more complex pattern, and accordingly, a significantly more complex decoding stage. A range of methods with intuitively designed patterns have been proposed [73, 74, 75], however, many lack in spatial resolution and scalability in terms of computational complexity. Some of the more interesting approaches use mathematical techniques for pattern design such as those based on De Brujin sequences [76, 77, 78]. Reference [79], describes an interesting method to facilitate the projection of a unique pattern coding based on De Brujin sequences using a novel multi-pass dynamic programming approach. The proposed method enabled for the measurement of complex scenes based on a single shot and was also extended into a temporal application for more reliable space-time surface profiling. Some other interesting examples of Spatial Neighbourhood methods include approaches that utilise the mathematical properties of specialised matrices termed M-arrays, to manufacture completely unique projections [78, 80].

The final classification of Coded Light approaches refers to methods where correspondence is directly coded into each pixel of the resolved image. Probably the most well known of all Direct Coding approaches is Carrhill and Hummel's "Intensity Ratio Depth Sensor" [81]. The intensity ratio method forms a ratio of the intensity value of each pixel within the scene when illuminated by a wedged greyscale projection and a constant reference illumination. The ratio essentially defines a code for each individual pixel. Although theoretically, Direct Coding methods including the Intensity Ratio method, can reveal significantly higher spatial resolutions relative to the two previously discussed Coded Light classifications, the approach is least favoured of all coding schemes since noise bears a significant burden in practical applications. Some other interesting Direct Coding examples code using colour projections most of which are limited to the space of profiling neutral coloured surfaces [82].

1.2.4.3 Fringe Projection

Fringe Projection approaches can be liken to the Moiré technique described in Section 1.2.3.2, however, rather than resolving a fringe image to yield contours, the 3D surface distribution is directly modulated into the projected fringe image. The typical Fringe

projection approach projects a reference sinusoidal fringe image onto the diffuse surface of interest which is recorded using a CCD camera. The captured fringe image can be regarded as a phase modulated version of the initial reference signal, with the modulation directly related to the depth distribution of the diffuse surface. The recorded modulated fringe image is then processed by a fringe processing algorithm to extract the spatial phase modulation, which is thereby used to recreate the surface of interest in three-dimensional space using geometrical relations prominent with the conventional triangulation optical arrangement.

Fringe Projection approaches can facilitate for variable sensitivity to yield high accuracy over a large field depth with a range of well known single and multiple shot fringe processing algorithms. Some of the more well known Fringe Projection processing algorithms include Phase Measuring Profilometry (PMP) [83], Fourier Transform Profilometry (FTP) [84], Modulation Measurement Profilometry (MMP) [85], Spatial Phase Detection (SPD) [86] and Phase Locked Loop (PLL) [87] methods. Similar to the evolution of Coded Structured Light methods, Fringe projection methods have enjoyed the more recent technological advancements in the field of digital projection, making the development of robust, accurate, high speed and cost effective 3D sensing solutions more viable. An example of such is the more recent work of Huang *et al.* [88] who proposed a colour-encoded digital fringe projection technique for high speed 3D surface profiling. The proposed system utilised the RGB colour channels of a Digital Light Processing (DLP) video projector to project three phase shifted images onto the measurement scene. The three individual phase maps were captured in one image, decomposed using a linear separation technique and a PMP fringe processing approach was used to reconstruct the object. The method was restricted to profiling neutral coloured surface and hence the technique was further refined to utilise the inherent nature of DLP projection to overcome the problem [89]. The improved system temporally projected phase shifted images onto the measurement scene at high speed, which were recorded by synchronising the projection system with a video camera. The system was shown to ascertain potential measurement speeds of up to 100 Hz however, the data processing was conducted offline as a result of the computational costs associated with the arctangent calculation required in PMP fringe processing. Consequently, Zhang and Huang incorporated a novel intensity ratio measure to process the

captured data in realtime [90, 91]. As a result the system was shown to be capable of capturing and processing a 532 x 500 frame of relative 3D data at 40 frames per second, with a second colour camera included to capture and map object texture information. More recent developments of this work has seen the transition back to sinusoidal fringe projection techniques for absolute realtime space measurement to improve the field depth and practical application of the method [92]. Furthermore, to aid the computational demands associated with arctangent processing, the application of a Graphics Processing Unit for the absolute measurement has also been demonstrated [93].

Another interesting example involving the DLP technology is Chen and Huang's [94] work on the practical miniaturised 3D surface profilometer. Here Chen and Huang designed a probe unit small enough to fit inside a subjects mouth for dental profiling. In fact, the non-coherent nature of DVP light sources has made the deployment of DVP for the measurement of human tissues ideal. This has been illustrated through the work of Skydan *et al.* [95] where a multichannel multi-projector technique was utilised to profile human body shape. The system made use of two or possibly three projectors each projecting an individual primary colour phase map, imaged with a single CCD camera. The captured phase maps were processed individually using a FTP method and the individual reconstructions were accurately mapped together into the final reconstruction.

In contrast to the sibling Coded Light technology, Fringe Projection methods can typically provide higher spatial accuracy often with much less data, while, relative to the parent Moiré technology projected fringes provide a much more flexible and practical approach for 3D sensing. The only major drawbacks with Fringe Projection methods as with all triangulation methods is the problem of missing parts and the additional requirement for robust phase unwrapping algorithms.

1.2.5 Applications

The increasing demand for high speed, accurate and automated non-contact 3D sensing is exemplified through the diversity of possible application which extends to a wide variety of different fields including the following key areas;

- Medicine: Accurate and robust dimensioning of the human body has received considerable attention in an effort to monitor the progression of medical conditions to

allow medical practitioners to more effectively treat patients. Some example applications of this would include the measurement of the human body to observe the progressive human spine displacement disease otherwise referred to as scoliosis or for the more effective treatment of cancer through conformal radiation therapy. Furthermore, considering the hugely growing popularity of cosmetic surgery, the accurate high speed measurement of human tissue could greatly assist cosmetic surgeons and customers to more effectively undertake various procedures.

- Industrial Automation: Realtime 3D sensing approaches could most definitely make the concept of fully autonomous robotic production lines more realisable. Moreover, in addition to the deployment of 3D realtime measurement to improve efficiency, noncontact accurate measurement will also aid in the quality of high precision industrial manufacturing. An interesting example of this would be the application of 3D sensing for gauging body size for industrial dressmaking. This particular type of application would also serve as an interesting tool for population demographics.

- Computer Vision, Virtual Reality and Recognition: Among all other intriguing applications one of the key research initiatives for 3D sensing technology lies with Computer Vision, and more specifically Computer Vision to aid Virtual Reality and Recognition systems. Bearing in mind that very recently entire virtual existences have been developed based on real world attributes (albeit primitive in terms of actual real life 3D vision), there is a clear requirement for the accurate creation of such virtual environments via the accurate dimensioning of the real world environment. Further, another interesting Virtual Reality example would be the 3D feature extraction of the human face which could be utilised to replace avatars in network games with actual player features. Whilst this example sees the mapping of accurate facial features for incorporation into entertainment applications, given the precision of the measurement, 3D facial feature extraction provides the ability to spawn recognition techniques for security or identification applications.

Therefore, considering the multitude of possible applications it is essential to facilitate continued research efforts to produce more advanced high speed non-contact, high

precision, 3D measurement.

1.3 Motivation for this Research

Reflecting on the literature survey provided in Section 1.2, the Structured Light Fringe Projection approach appears to present itself as one of the most promising methods for dynamic, accurate and cost effective optical 3D sensing. Also as pointed out in Section 1.2.4.3, the approach has become increasingly popular with the recent advances in digital projection display technology. More specifically, DVP is a technology which has been actively pursued by the Fringe Projection research community because it provides a number of key advantages over more traditional methods of generating fringe patterns. For instance, DVP provides the ability to manipulate fringe patterns quickly and easily with high precision in software, along with the capability to develop multi-channel algorithms via colour pattern projection. In general, a conventional Liquid Crystal Display (LCD) or Digital Light Processing (DLP) digital video projector serves as the typical DVP source, which is capable of projecting a standard 24 bit bitmap computer generated image. Hence, when interfaced to a personal computer, DVP makes for a very affordable, flexible and robust projection source. However, while the aforementioned incentives in conjunction with advancements in the performance of such digital technology have fueled continued interest from the research community over recent years, a number of key attributes of the DVP image significantly hinder the veracity of the projection source as a fringe projector.

Following the initial work's of Huang *et al.* as described in Section 1.2.4.3, subsequent work was aimed at creating and implementing algorithms to compensate for the inherent Fringe Projection limitations associated with DVP. Closely related to this particular line of work was the identifying and understanding of the nature of the DVP associated Fringe Projection limitations. The investigation was chiefly initiated by Huang *et al.* in [96] where they proposed the non-linear intensity resilient Double Three Step technique and further identified the projection phenomena as the single most significant error source for the application of DVP for Fringe Projection 3D sensing. Huang *et al.* speculated that the camera / projector non-linear intensity response was responsible for significant fringe harmonic distortion and consequently for a systematic residual phase measuring error.

While the Double Three Step technique was shown to be reasonably effective at reducing the non-linear intensity systematic limitations, Huang's empirical evaluation and following analytical investigation on the issue somewhat misconstrued the problem for phase stepping approaches. More specifically, Huang's evaluation has introduced significant confusion in regard to the sensitivity of a range of popular fringe processing techniques in the presence of non-linear intensity related fringe distortion.

Sometime later the non-linear camera / projector response was more formally identified by Guo *et al.* in [97] to be resultant of the Display Gamma attributes of the projection system. Guo *et al.* verified their findings by proposing a gamma correction procedure for gamma distorted fringe images and accordingly were able to successfully improve the accuracy of their DVP fringe profilometer. Although the technique was shown to be effective in mitigating the associated non-linear intensity phase measuring residual error, the gamma correction process was quite computationally demanding and required a significant amount of data.

More recently, Zhang and Yau [98] showed the residual phase measurement error associated with the gamma distorted fringe was independent of the camera response (assuming the camera response is linear), the reflectivity of the surface and ambient light intensity and thereby, proposed a generic phase lookup table based solution. The technique was shown to be quite effective at minimising gamma related phase measuring errors, however, questionable generalisations about the true nature of the resulting phase residual were made. More specifically, the authors claimed that the residual phase error was independent of the spatial carrier frequency based on empirical observation, and further they generalised the residual function for all fringe processing algorithms.

Therefore, despite the research attention the DVP shortcomings and in particular the Fringe Projection Display Gamma phenomena has received, a number of issues still remain misunderstood or uninvestigated. Of principle concern is the lack of a formal and thorough investigation into the Display Gamma Fringe Projection issue, including the true practical nature of a gamma distorted fringe and the resulting phase measuring residual. This entails the study of the fringe image formation process from and optical perspective and further analysis of the temporal nature of the DVP fringe image. Supplementary to this is the clarification of the previously misconstrued Display Gamma sensitivity issue

for a range of well exploited fringe processing algorithms.

In addition to the important investigative issues described above, as previously mentioned many of the proposed gamma correction procedures make assumptions about the nature of the gamma distorted fringe and often demonstrate the requirement for significant additional computation and / or the requirement for additional data. Therefore, the further development of effective yet efficient gamma correction or elimination of Display Gamma related residual measuring errors is paramount in facilitating effective 3D sensing via Fringe Projection.

Hence, the basis of the research presented in this dissertation is primarily concerned with addressing the aforementioned outstanding issues by studying the associated DVP limitations in order to provide clear insight into the development of robust DVP based Fringe Projection 3D sensing solutions.

1.4 Approach and Contributions of this Thesis

The aim of the work presented within this thesis is two-fold; Firstly this research attempts to facilitate the requirement to effectively identify and describe the limitations associated with DVP for Fringe Projection 3D sensing techniques. Secondly, this thesis attempts to improve the effectiveness of the deployment of DVP for Fringe Projection 3D sensors through the development of novel calibration procedures.

1.4.1 Overview of Structured Light 3D Sensing by Fringe Projection

In order to understand and interpret the key concepts and contributions demonstrated in this research, it is vital to have a strong grasp on the notion of 3D sensing by projecting fringes. Chapter 2 facilitates this necessity by providing a thorough yet concise framework of the concept of Fringe Projection including a review of the three major forms of fringe processing.

1.4.2 Creating Structured Light

To realise the shortcomings of the application of DVP technology for Fringe Projection one must clearly understand the principles and functionality of the projection technology and moreover have an appreciation for the more traditional methods of producing fringe images.

Chapter 3 serves as an investigation into the various methods and technologies involved in the creation of structured light fringe images, and secondly it provides an introductory analysis into the shortcomings of the more recently adopted DVP based methods of Fringe Projection. The investigation outlines both analog and digital methods of projection, with a succinct focus on DVP methods of producing fringe images. The functionality of the two chief DVP technologies, LCD, and DLP, Texas Instruments (TI) is reviewed, and the integrity of the application of each for both single and multiple channel Fringe Projection scenarios is studied by establishing preliminary empirical results. Moreover, the preliminary empirical analysis provides for clear insight into the major shortcomings of the application of DVP for Fringe Projection.

1.4.3 Fringe Projection and Display Gamma

Chapter 4 expands on the concept of Display Gamma facilitating the requirement for a formal investigation into the resulting errors for a range of well exploited fringe processing techniques. Firstly the spectral harmonic structure and magnitude of the harmonic distortion typical of a digitally projected fringe is analytically studied and an approximate analysis framework proposed. Given the findings of this study the influence of harmonics for a range of fringe processing algorithms is analytically investigated. The analytical study yields a set of functions defining both the residual phase error and associated sensitivity of the phase measuring process in the presence of Display Gamma for each of the studied fringe processing algorithms. The analytical findings are verified through simulation analysis and insight into the sensitivity of each of the studied fringe processing algorithms in the presence of Display Gamma is established. Furthermore, the practical significance of the analysis is verified.

1.4.4 Additional Display Gamma Phenomena

Chapter 5 extends on the analytical framework presented in Chapter 4 to consider some of the additional practical phenomena prominent with Display Gamma. More specifically, Chapter 5 deals with the manipulation of fringe offset and contrast parameters, the temporal instabilities associated with Display Gamma and the effects of the projection optics on the formation of digitally projected fringe images.

The harmonic dependence on the fringe offset and contrast parameters is demonstrated and, moreover, the effective manipulation of fringe offset and contrast to minimise gamma associated reconstruction errors is experimentally undertaken. Further the important practical correlation between fringe contrast and Signal to Noise Ratio (SNR) is also demonstrated.

The temporal instabilities of the projector / camera luminance response is analytically evaluated and subsequently verified via simulation for the temporally sensitive FTP approach. The important identification of temporal fringe artifacts is discussed and further analysed through the derivation of the reference plane ripple function. A further practical example of the associated temporal aspects of Display Gamma is also demonstrated to highlight the prominence of the projection phenomena.

The important practical issue of fringe image formation is investigated, with the derivation of the optical modulation transfer function for the projection optics. Subsequently, the elimination of Display Gamma related Fringe Projection phase measuring residual error for phase stepping techniques by projector defocus optimisation is shown. These findings are demonstrated through both simulation and empirical analysis.

1.4.5 Digital Fringe Calibration using Neural Networks

While the early chapters of this dissertation demonstrate the vital requirement to necessitate the gamma correction process and particularly for minimum step approaches, the final contribution chapter of this dissertation deals with the implementation of a robust and novel gamma correction procedure. The gamma correction process is centered on the application of Artificial Neural Networks (ANNs) for fringe calibration. The generalisation properties of ANNs are exploited to interpolate modulated structured light patterns and

consequentially are successfully capable of improving the estimation of the true fringe modulation and therefore system accuracy in the presence of Display Gamma. The proposed approach does not rely on prior calibration information and requires only a single cross-section from a single fringe image for calibration, thus, the technique is suitable for dynamic minimum shot techniques including robotic vision where rapid calibration is required. Finally, since the approach is aimed at calibrating a fringe image, its application and functionality is not limited to operation with specific reconstruction algorithms.

The validity of the proposed approach is verified via both simulation and empirical analysis and also the comparative analysis of the proposed technique relative to existing approaches is undertaken. Finally, the application of the neural fringe calibration approach in the multi-channel environment is also considered.

1.5 Summary of Contributions in Order of Presentation

- A methodology to effectively empirically benchmark the application of DVP technology for Fringe Projection 3D sensing is proposed (Chapter 3). The methodology enables the identification of the key limitations of the application of DVP for Fringe Projection and, moreover, provides a means to gauge the performance of a number of fringe processing techniques under experimental DVP conditions (Chapter 4).

- The spectral harmonic structure and magnitude of the harmonic distortion typical of a digitally projected fringe is examined and an approximate analysis framework is proposed (Chapter 4).

- The influence of harmonics for a range of well exploited fringe processing algorithms is investigated yielding a set of functions defining both the residual phase error and associated Display Gamma sensitivity for a range of well exploited fringe processing algorithms (Chapter 4).

- The validity of the analytical functions defining the Display Gamma sensitivity of each of the presented fringe processing algorithms is verified through simulation and practical evaluation clarifying the previously misconstrued concept is demonstrated (Chapter 4).

- The significance of fringe offset and contrast parameter manipulation is evaluated and the optimisation of digital fringe images via fringe parameter manipulation is investigated practically (Chapter 5).

- For the first time the temporal instabilities of the projector / camera luminance response is analytically evaluated for the temporally sensitive FTP approach. The validity of the study is verified by simulation analysis and the prominence of the projection phenomena demonstrated by practical example (Chapter 5).

- An analytical model for the typical projector optical modulation transfer function is proposed to gain insight into the digital fringe image formation process from an optical perspective. This analysis extends on the model for a gamma distorted fringe proposed in Chapter 4 and demonstrates the frequency dependence of the Display Gamma phase measuring residual error (Chapter 5).

- The validity of the fringe formation investigation is verified by defining the minimum stepping requirements to eliminate Display Gamma related phase estimation errors for stepping fringe processing techniques via a fringe defocusing optimisation (Chapter 5). This study is verified via both simulation and empirical analysis. This study implies that by marginally increasing data requirements, the need for Display Gamma compensation techniques can be omitted with no additional computational overhead.

- A novel gamma correction procedure based on ANN's is proposed (Chapter 6). The performance of the approach is evaluated by simulation and empirical analysis and further a comparative theoretical analysis with existing approaches is demonstrated. The approach is characterised by significantly reducing the data requirements for effective Display Gamma correction. The application of the neural network gamma correction process is also extended to multi-channel fringe calibration.

Chapter 2

Overview of Structured Light 3D Sensing by Fringe Projection

2.1 Introduction

The primary objective of this chapter is to familiarise the reader with the fundamental concepts employed by Fringe Projection 3D sensing methods, and furthermore with some of the more well exploited fringe processing algorithms. Rudimentary concepts reviewed in this chapter include the derivation of the elementary principle of optical triangulation, the projection of fringes for full field measurement, and phase to height conversion. The reviewed fringe processing algorithms encompass all three major fringe processing approaches these being, Phase Measuring or Shifting approaches, Fourier Transform approaches and Direct Phase Detection approaches. Finally, discussions on the important concepts of phase unwrapping and the translation of phase to real world coordinates are undertaken.

2.2 Optical Triangulation

As described in Chapter 1 perhaps one of the most simple yet highly exploited concepts employed by an array of 3D sensing approaches including Fringe Projection techniques, is the elementary method of optical triangulation. The optical triangulation principle is best initially conceptualised by the single dot or slit like method similar to that employed

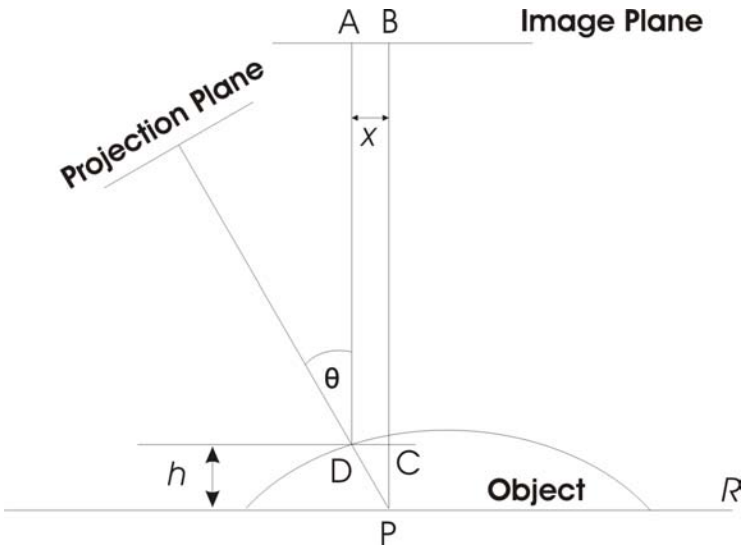

Figure 2.1: Simple Telecentric Optical Triangulation

by Laser Scanning approaches, as briefly discussed in Section 1.2.4.1. Figure 2.1 depicts a simple telecentric optical triangulation situation, similar to this analogy where a single point or slit like image is projected onto an object positioned on a reference plane R from an angle of θ relative to the imaging optical axis. Point D expresses a tested point on the object's surface, P represents the projection of the same image (dot or slit of light) onto the reference plane R, whilst points A and B represent the imaged projections of points D and C respectively. Given the geometrical arrangement it is clear that

$$\tan(\theta) = \frac{DC}{PC} \tag{2.1}$$

and moreover,

$$h = \frac{x}{\tan(\theta)}. \tag{2.2}$$

Hence, it can be concluded that for a finite deviation in h i.e. dh, a proportional deviation in x i.e. dx will be incurred, and we can obtain an expression for the theoretical accuracy of the triangulation measurement given by

$$\frac{dh}{dx} = \frac{1}{\tan(\theta)}. \tag{2.3}$$

Considering Equation (2.3) and it becomes clear that the sensitivity of the measurement system is inversely proportional to the angle between the image and projection planes. Therefore intuitively, in order to yield a more sensitive measurement, one would simply

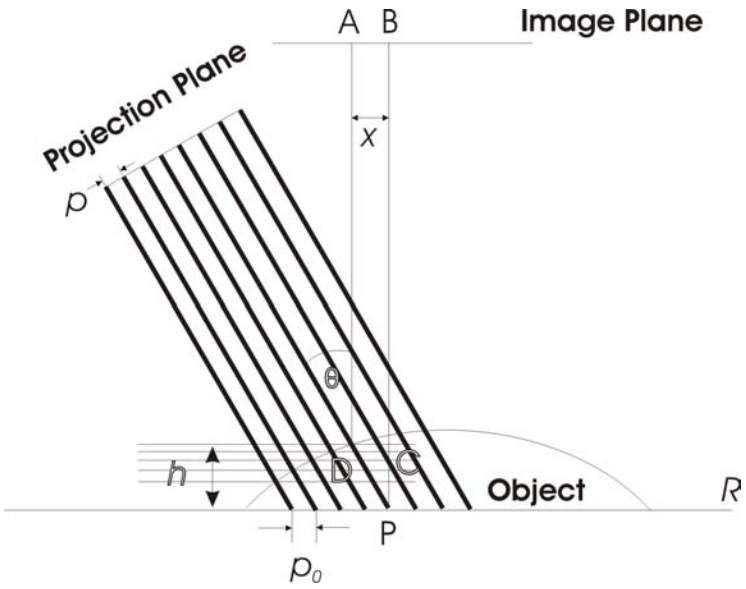

Figure 2.2: Simple Full Field Optical Triangulation via the projection of a Structured Light Pattern

increase the angle between the image and projection devices till a maximum sensitivity is obtained when $\theta = 90°$. However, as $\theta \rightarrow 90°$ the measurable range is decreased, and furthermore, pending on the complexity of the surface being profiled, will result in occlusions where parts of the scenery are unable to be imaged onto the image plane. This problem is more commonly known as "the problem of missing parts" and poses as the single most significant shortcoming of all triangulation based measurement approaches. Often for optical triangulation measurement approaches it is desirable to adjust θ for maximum sensitivity with some prior knowledge of the dimensions of the surface being profiled.

The depiction of the very simple theoretical optical triangulation system in Figure 2.1 is quite clearly limited in terms of field of measurement, with scanning required to obtain measurements over the entire surface. Therefore, to extend the concept to full field analysis, a structured light pattern such as a coded Ronchi grating or a sinusoidal fringe can be projected onto the surface such as depicted in Figure 2.2. The telecentric structured light extension depicts the projection of a pattern with spatial pitch p onto R, which when imaged yields a pitch of

$$p_0 = \frac{p}{\cos(\theta)}. \tag{2.4}$$

Thus, assuming the same principle as with the previous single dot or slit like example, the

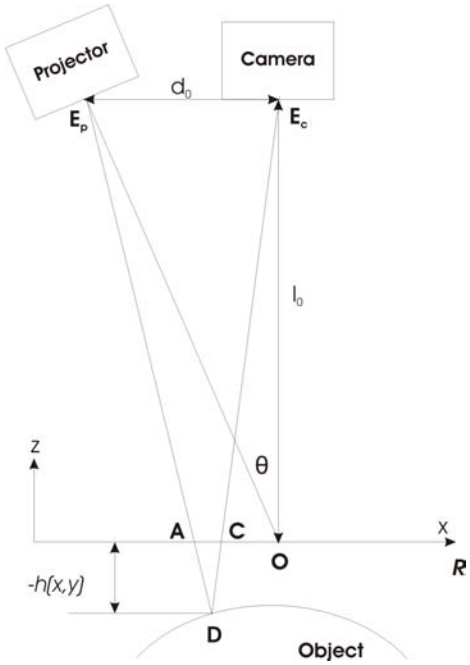

Figure 2.3: Typical Crossed Optical Axes arrangement

imaged displacements of each of the projections can be measured to give a corresponding set of height displacements for a full field measurement.

2.2.1 Optical Arrangement

The two previously discussed arrangements depict telecentric conditions whereby the projection and image planes can be considered to be positioned at infinity. A more appropriate and practical model for this scenario would be a non-telecentric pinhole model. Although still a theoretical model, as a practical lens cannot be modeled as a pinhole, the pinhole model is more applicable to practical situations given the finite aspects of the practical triangulation arrangement. The Crossed Optical Axes pin hole geometry as seen in Figure 2.3 is probably the most exploited optical arrangement for Fringe Projection approaches. Projector and camera optical axes intersect at point O on reference plane R which is a fictitious plane normal to the camera optical axis and serves as a reference from which height *h(x,y)* is measured. Point D expresses a tested point on the diffuse object. Points A and C represent points on R, d_0 is the distance between E_p and E_c and l_0 is the distance between E_c and O. The *y*-axis is normal to the plane of the Figure (i.e. into the page) with the *x* and *z*-axes as indicated. One of the defining traits of this arrangement is

its simplicity in terms of practical construction and implementation.

2.2.2 Extracting Height

Using geometrical relationships apparent in the pin hole arrangement the physical height distribution of the object can be extracted. Noting that $\triangle E_p E_c D$ and $\triangle ACD$ are similar it can be shown that

$$\begin{aligned} \frac{\overline{AC}}{-h(x,y)} &= \frac{d_0}{l_0 - h(x,y)} \\ h(x,y) &= \frac{l_0 \overline{AC}}{\overline{AC} - d_0} \end{aligned} \tag{2.5}$$

Thus, assuming that system parameters d_0 and l_0 are known or can be established via calibration, the aim of any structured light profiling algorithm is to accurately determine spatial distance $\overline{AC}$.

2.3 Projecting Fringes

As implied by the name, Fringe Projection approaches establish the measurement of $\overline{AC}$ via the projection of a fringe or sequence of fringe images. The typical reference fringe image is commonly a sinusoidal or sinusoidal-like grating, such as a Ronchi, and can be given by or in the case of a Ronchi, be fundamentally resolved as

$$g_r(x') = a + b\cos\left(\frac{2\pi x'}{p}\right), \tag{2.6}$$

where a and b represent fringe offset and contrast parameters, respectively, and p denotes the fringe pitch for the x' projection plane coordinate space. When the reference fringe is projected onto a surface the imaged resultant yields a phase modulated version of the initial reference waveform, where the phase modulation component essentially carries the information about the measurement of spatial displacement $\overline{AC}$. When $g_r(x')$ is projected onto R the recorded fringe image can be mathematically formed as

$$g_0(x,y) = a(x,y) + b(x,y)\cos\left(2\pi f_0 x + \phi_0(x,y)\right), \tag{2.7}$$

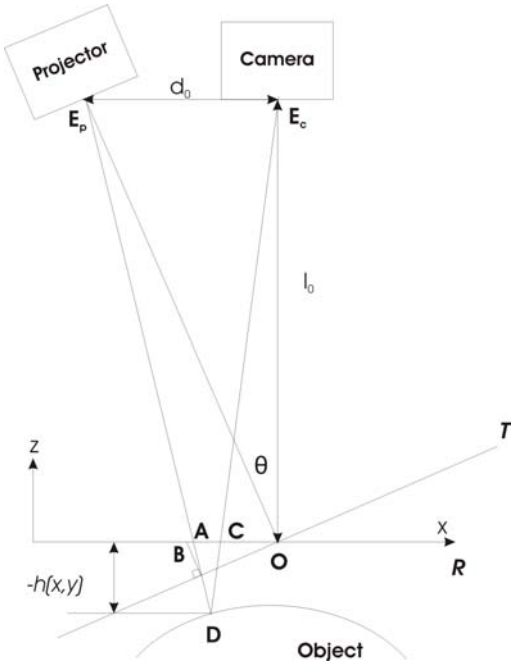

Figure 2.4: Diverging Illuminance:- Typical Crossed Optical Axes arrangement

where $a(x, y)$ and $b(x, y)$ represent spatially variant functions to describe the direct and contrast components of the fringe, respectively, f_0 can be given as

$$\begin{aligned} f_0 &= \frac{1}{p_0} \\ &= \frac{\cos(\theta)}{p}, \end{aligned} \tag{2.8}$$

and $\phi_0(x, y)$ is the phase modulation function associated with the diverging illuminance of the crossed optical arrangement. The divergent nature of the projection and the resultant phase modulation $\phi_0(x, y)$, is best conceived via the depiction in Figure 2.4. The Figure shows the addition of a second fictitious reference plane T, normal to the projector optical axis, where a regular fringe with period p will be formed under telecentric conditions. The projection of a normal from the point where projection E_pD intersects T to R then demonstrates the relative spatial displacement associated with the modulation which can be given as

$$\phi_0(x, y) = 2\pi f_0.\overline{AB}. \tag{2.9}$$

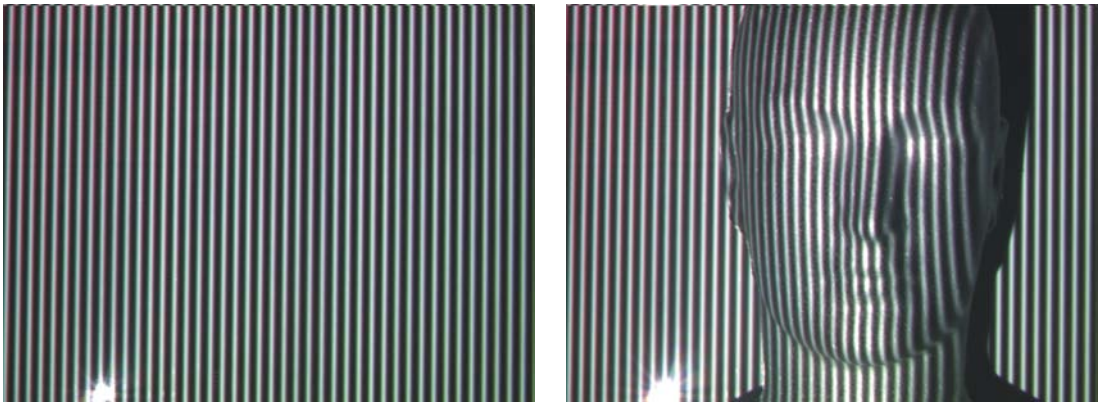

(a) Reference Fringe (b) Object Fringe

Figure 2.5: Example Projecting Fringes

And as shown by Toyooka and Iwaasa [86], through further derivation can be given as

$$\begin{aligned} \phi_0(x,y) &= 2\pi f_0(\overline{OA} - \overline{OB}), \\ &= -\frac{2\pi f_0 x^2 \sin\theta\cos\theta}{l_0 + x\sin\theta\cos\theta}. \end{aligned} \tag{2.10}$$

It should be noted that although $\phi_0(x,y)$ can be estimated by the geometric parameters, it is often measured from the fringe image to reduce the influence of measurement errors.

Similar to the reference plane scenario, when the reference grating is projected onto the object's surface, the phase modulated fringe can be given as

$$g(x,y) = a(x,y) + b(x,y)\cos\left(2\pi f_0 x + \phi(x,y)\right), \tag{2.11}$$

where

$$\phi(x,y) = 2\pi f_0.\overline{CB}. \tag{2.12}$$

Figures 2.5 (a) and (b) visually demonstrate the concept of projecting fringes, clearly demonstrating how the depth of the scene is phase modulated into the projected fringe image for both a reference plane and diffuse surface.

Hence, if the phase modulations $\phi_0(x,y)$ and $\phi(x,y)$ can be extracted from the redundant direct components and amplitude modulations, the spatial displacement $\overline{AC}$ can be

obtained by calculating

$$\begin{aligned} \Delta\phi(x,y) &= \phi(x,y) - \phi_0(x,y) \\ &= 2\pi f_0(\overline{CB} - \overline{AB}) \\ &= 2\pi f_0.\overline{AC} \end{aligned} \tag{2.13}$$

And therefore, rearranging Equation (2.13) and substituting into Equation (2.5), the height distribution of the object $h(x,y)$ can be given as

$$h(x,y) = \frac{l_0\Delta\phi(x,y)}{\Delta\phi(x,y) - 2\pi f_0 d_0} \tag{2.14}$$

Hence, it becomes clear that the most defining element of any Fringe Projection 3D sensing approach is the fringe processing algorithm to estimate $\Delta\phi(x,y)$.

2.4 Fringe Processing Techniques

The purpose of this section is to outline the more significant fringe processing algorithms applicable for Fringe Projection profilometry. Fringe processing techniques for Fringe Projection methods can usually be categorised by one of three approaches; Phase Measuring or Shifting approaches, Fourier Transform approaches and Direct Phase Detection approaches. Examples of each of these approaches will now be discussed with specific reference to methods employed within the work embodied within this dissertation.

2.4.1 Phase Measuring or Shifting

Phase Measuring or Shifting approaches are fundamentally derived from the work undertaken in the field of Phase-Shifting Interferometry (PSI), although the concept was initially borrowed from electrical engineering concepts [99]. In general, a sequence of N interferograms (fringes) are obtained, with each fringe image of the sequence offset by a known phase shift ζ_n. The nth fringe of a sequence of N fringes can therefore be given

as

$$g_n(x,y) = a(x,y) + b(x,y)\cos(\omega(x,y) + \zeta_n)$$
$$\text{for n=0,1,2,...,N-1,} \tag{2.15}$$

where the phase modulation term, $\omega(x,y)$, is given by

$$\omega(x,y) = 2\pi f_0 x + \varphi(x,y) \tag{2.16}$$

where $\varphi(x,y)$ denotes the spatial phase modulation corresponding to the projection surface i.e. $\phi(x,y)$ or $\phi_0(x,y)$ for the object and reference fringe set, respectively. The underlying aim of the phase measuring principle is to then form two orthogonal vectors using weighted summations of the fringe images to eliminate unwanted direct and contrast components and extract the associated phase component using an arctangent operator.

Since its conception many different phase shifting algorithms have been developed to serve a range of specific purposes. For instance, some algorithms have been proposed to alleviate errors resulting from erroneous phase shifting, detector / projector non-linearity, scene vibration and noise. Some methods, namely 3 Step variations are also employed in dynamic applications since this is the minimum number of frames required to resolve the fringe parameters. Included in this survey is the Traditional Phase Measuring or Shifting algorithms [100, 83], General 3 Step and variations [100, 101, 102], 2+1 [103], 3+3 [104] and the Double 3 Step algorithm [96] with a succinct focus on 3 step methods since these form the basis of many techniques currently being utilised for dynamic Fringe Projection profiling methods.

2.4.1.1 Traditional Phase Measuring Algorithm

The traditional Phase Measuring approach, otherwise known as Synchronous Detection [100] in communication theory, is centered around the projection and acquisition of N fringe images. The phase offset ζ_n between each consecutive fringe image is equally spaced over the spatial period of the fringe with

$$\zeta_n = 2\pi n/N;$$
$$\text{for n=0,1,2,...,N-1,} \tag{2.17}$$

Each of the captured fringe images are appropriately weighted and summed to remove the unwanted direct components to give a pair of orthogonal vectors. The two vectors still contain the unwanted amplitude modulation component $b(x, y)$, and thus by calculating the arctangent of the division of the pair, the required phase information can be obtained as shown in Equation (2.18).

$$\omega(x,y) = -\arctan\left[\frac{\sum_{n=0}^{N-1} g_n(x,y)\sin(2\pi n/N)}{\sum_{n=0}^{N-1} g_n(x,y)\cos(2\pi n/N)}\right] \tag{2.18}$$

This method is employed in PMP methods [83] and can be considered the most generic phase shifting algorithm. Given its general form the approach can be extended to large values of N and used in situations where speed of acquisition is not critical to reduce most forms of error including noise.

2.4.1.2 General 3 Step

Given that for any arbitrarily projected fringe there are 3 unknowns, $a(x, y)$, $b(x, y)$ and $\omega(x, y)$, the minimum requirement to completely solve for any fringe image is 3 fringe measurements i.e $N = 3$. For this very reason 3 step variations have been extensively employed in high speed Fringe Projection 3D sensing applications. For the general 3 step case the phase shift ζ, between consecutive fringe images can be defined as

$$\begin{aligned} \zeta_0 &= -\alpha, \\ \zeta_1 &= 0, \\ \zeta_2 &= \alpha; \end{aligned} \tag{2.19}$$

and the general form for extracting the phase modulation is then given by [100]

$$\omega(x,y) = \arctan\left[\left(\frac{1-\cos(\alpha)}{\sin(\alpha)}\right).\frac{g_0(x,y) - g_2(x,y)}{2.g_1(x,y) - g_0(x,y) - g_2(x,y)}\right] \tag{2.20}$$

Although, any arbitrary phase shift α can be used to solve for the fringe parameters, conventionally two phase steps are most popular; $\alpha = 90°$ and $\alpha = 120°$. The $\alpha = 90° = \frac{\pi}{2}$ is often favored purely for computational convenience with Equation (2.20) becoming

$$\omega(x,y) = \arctan\left[\frac{g_0(x,y) - g_2(x,y)}{2.g_1(x,y) - g_0(x,y) - g_2(x,y)}\right] \tag{2.21}$$

The $\alpha = 120^\circ = \frac{2\pi}{3}$ is a popular choice as the phase shift ζ equally divides the spatial period of the fringe and essentially reduces to the traditional Phase Measuring method with $N = 3$, which can be otherwise described as

$$\omega(x,y) = \arctan\left[\sqrt{3}\frac{g_0(x,y) - g_2(x,y)}{2.g_1(x,y) - g_0(x,y) - g_2(x,y)}\right] \tag{2.22}$$

Also adding to the popularity of this method as will be shown in Chapter 4, the $\alpha = \frac{2\pi}{3}$ variation presents as the least error sensitive 3 step phase shifting algorithm in the presence of a non-linear intensity response.

2.4.1.3 90° 3 Step with Phase Offset

As with the general 90° variation discussed above, the 90° 3 step with phase offset method was developed with the idea of simplifying computational complexity in mind [101, 102]. Similar to the general 90° approach each of the 3 fringe images are phase shifted by $\frac{\pi}{2}$, however, with an initial phase offset of $\frac{\pi}{4}$, thus, ζ can be given by

$$\begin{aligned} \zeta_0 &= \frac{\pi}{4}, \\ \zeta_1 &= \frac{3\pi}{4}, \\ \zeta_2 &= \frac{5\pi}{4}; \end{aligned} \tag{2.23}$$

Therefore, quite intuitively, the phase component can be extracted by calculating the arctangent of a simple subtraction of fringe patterns, given by

$$\omega(x,y) = \arctan\left[\frac{g_2(x,y) - g_1(x,y)}{g_0(x,y) - g_1(x,y)}\right] \tag{2.24}$$

where no additional multiplication terms are required.

2.4.1.4 2+1

Considering that all phase stepping approaches require the acquisition of a sequence of fringe images over a finite duration, fringe parameters often exhibit some form of temporal variation, leading to measurement error. The 2+1 fringe processing algorithm was developed to facilitate more accurate measurement under the conditions of vibration [103].

The technique requires in total, 3 fringe images, a pair of orthogonal fringes and a single fringe offset by π radians relative to either one of the orthogonal pair.

$$\begin{aligned} \zeta_0 &= 0, \\ \zeta_1 &= -\frac{\pi}{2}, \\ \zeta_2 &= \pi; \end{aligned} \tag{2.25}$$

Unlike the previously presented approaches, the third grating of the 2+1 approach is projected purely with the intention to estimate and remove the direct component from the pair of orthogonally projected fringes. The defining concept behind this approach is centered around the idea that the direct component is more resilient to significant variability and thus can be considered somewhat insensitive to the temporal variations in the fringe or scene. Therefore, the 2+1 method becomes a robust algorithm in the presence of temporal variation given that the two orthogonal fringe images are acquired in quick succession with the third fringe obtain sometime later. The direct component is estimated as

$$\begin{aligned} g_{dc}(x,y) &= \frac{g_0(x,y) + g_2(x,y)}{2} \\ &= \frac{1}{2}\left[a(x,y) + b(x,y)\cos(\omega(x,y))\right] + \\ &\quad \frac{1}{2}\left[a(x,y) + b(x,y)\cos(\omega(x,y) + \pi)\right] \\ &= \frac{1}{2}[2a(x,y) + b(x,y)\cos(\omega(x,y)) - \\ &\quad b(x,y)\cos(\omega(x,y))] \\ &= \frac{2a(x,y)}{2} \\ &= a(x,y) \end{aligned} \tag{2.26}$$

and accordingly, the phase distribution can be obtain by

$$\omega(x,y) = \arctan\left[\frac{g_1(x,y) - g_{dc}(x,y)}{g_0(x,y) - g_{dc}(x,y)}\right] \tag{2.27}$$

The 2+1 algorithm has received more recent attention in Reference [93], where it is employed to compensate for measurement errors caused by motion in dynamic 3D profiling.

2.4.1.5 3+3

One of the major error sources for early Phase Shifting Interferometers was measurement errors resulting from phase shifting errors. The resulting error residual was shown to present a frequency twice that of the fundamental fringe frequency [34]. It was also found that if two estimates of the fringe phase were made, each conducted with a $\frac{\pi}{2}$ phase offset between them, the corresponding residual's would effectively cancel one another when averaged [104]. Although any three sets of fringes can be utilised in the 3+3 method (provided the required offset is adhered to), perhaps the most convenient implementation of this approach is when

$$\begin{aligned} \zeta_0 &= \frac{\pi}{4}, \\ \zeta_1 &= \frac{3\pi}{4}, \\ \zeta_2 &= \frac{5\pi}{4}, \\ \zeta_3 &= \frac{7\pi}{4}; \end{aligned} \tag{2.28}$$

and $g_0(x,y), g_1(x,y)$ and $g_2(x,y)$ are used in the 3 Step variation to estimate $\omega(x,y)$ given as $\hat{\omega_1}(x,y)$. Similarly, $g_1(x,y), g_2(x,y)$ and $g_3(x,y)$ estimate $\omega(x,y)$ as $\hat{\omega_2}(x,y)$ and the two are averaged.

$$\hat{\omega}(x,y) = \frac{\hat{\omega_1}(x,y) + \hat{\omega_2}(x,y)}{2} \tag{2.29}$$

2.4.1.6 Double Three Step

Similar to the analogy of the 3+3 method, the Double Three Step method has adopted the idea of averaging phase residuals. However, rather than compensating for phase shifting errors, the aim of the Double Three Step method is to suppress measurement errors associated with a 2nd order non-linear projector / camera response, more specifically for Fringe Projection methods [96]. The algorithm is based on the traditional 3 Step phase shifting method with $\zeta = 0, \frac{2\pi}{3}$ and $\frac{4\pi}{3}$, and also three additional phase steps with a $60°$ offset

$$\zeta_n = 2\pi n/N + \pi; \quad \text{for n=0,1,2;} \tag{2.30}$$

The fringe images can also be written as

$$g_{n+\pi}(x,y) = a(x,y) + b(x,y)\cos(2\pi f_0 x + \varphi(x,y) + 2\pi n/3 + \pi) \quad \text{for n=0,1,2} \tag{2.31}$$

The three initial phase steps are used to predict the actual phase component $\omega(x,y)$, denoted $\hat{\omega}_1(x,y)$, and similarly an estimate, $\hat{\omega}_2(x,y)$ based on the second offset set of fringes is undertaken

$$\hat{\omega}_2(x,y) = -\arctan\left[\frac{\sum_{n=0}^{2} g_{n+\pi}(x,y)\sin(2\pi n/3+\pi)}{\sum_{n=0}^{2} g_{n+\pi}(x,y)\cos(2\pi n/3+\pi)}\right] \tag{2.32}$$

Since, the residuals of each prediction, $\hat{\omega}_1(x,y)$ and $\hat{\omega}_2(x,y)$ are approximately out of phase by π radians the residuals effectively cancel when averaged to give a closer approximation of $\omega(x,y)$

$$\hat{\omega}(x,y) = \frac{\hat{\omega_1}(x,y) + \hat{\omega_2}(x,y)}{2} \tag{2.33}$$

Considering the amount of data required, the Double Three Step method is rather ill posed, nevertheless, is often quoted in literature as a feasible solution for the problem. The significant shortcomings of this approach will be more thoroughly demonstrated in subsequent work outlined in this dissertation.

2.4.2 Fourier Transform Fringe Processing

The use of the Fourier Transform to aid fringe processing was first proposed by Takeda, Ina and Kobayashi [105] in the early 1980's. The approach estimate's the phase modulation component of a fringe image by first calculating it's Fourier Transformation, then by isolating one of the fundamental sidebands through filtering in the spatial frequency domain, and then finally calculating the inverse Fourier Transformation of the filtered baseband signal. Similar to Phase Shifting approaches the Fourier Transform method has the merit of fully automatic distinction between depression and elevation of a fringe, without the requirement for fringe order assignments, fringe center determination nor

interpolation of fringes, with phase data provided at each pixel of the fringe image. Conversely, unlike phase stepping techniques, the Fourier Transform approach requires just a single image to determine the phase component of the fringe, therefore making the technique more applicable for dynamic fringe measurement under various dynamic conditions, such as scene motion or vibration. Nevertheless, in contrast to Phase Shifting methods where $\omega(x, y)$ is solved for directly, the single shot advantage inevitably leads to a relative reduction in accuracy given that the additional operation of filtering is needed to effectively reduce the problem space into a solvable form.

The method of analysing fringe images via Fourier Transformation has received considerable attention since its initial proposal due to the relatively high accuracy of the approach and more importantly its single shot nature, with a number of significant variations and improvements proposed and demonstrated over the following two or so decades [106, 107, 108, 109]. The purpose of this section is to demonstrate the core principles of Fourier Transform based fringe processing and to review some of the more significant variations and implementations of the Fourier Transform Profilometry technique.

2.4.2.1 Fourier Transform Fringe Processing Principle [105]

The principle of Fourier Transform fringe processing is best understood by rewriting the typical phase modulated sinusoidal fringe previously given by Equation (2.11), in complex exponential form, to reveal the double sided nature of the Fourier fringe spectra. That is

$$g(x, y) = a(x, y) + q(x, y)e^{2\pi i f_0 x} + q^*(x, y)e^{-2\pi i f_0 x} \tag{2.34}$$

where

$$q(x, y) = \frac{1}{2} b(x, y)e^{i\phi(x,y)} \tag{2.35}$$

The first step of the process is to take the Fourier Transform of the fringe with respect to x which can be given as

$$G(f, y) = A(f, y) + Q(f - f_0, y) + Q^*(f + f_0, y) \tag{2.36}$$

where the $A(f, y)$ denotes the Fourier Transform of the direct component and $Q(f - f_0, y)$ and $Q^*(f + f_0, y)$ denote the Fourier Transforms of each of the respective sideband com-

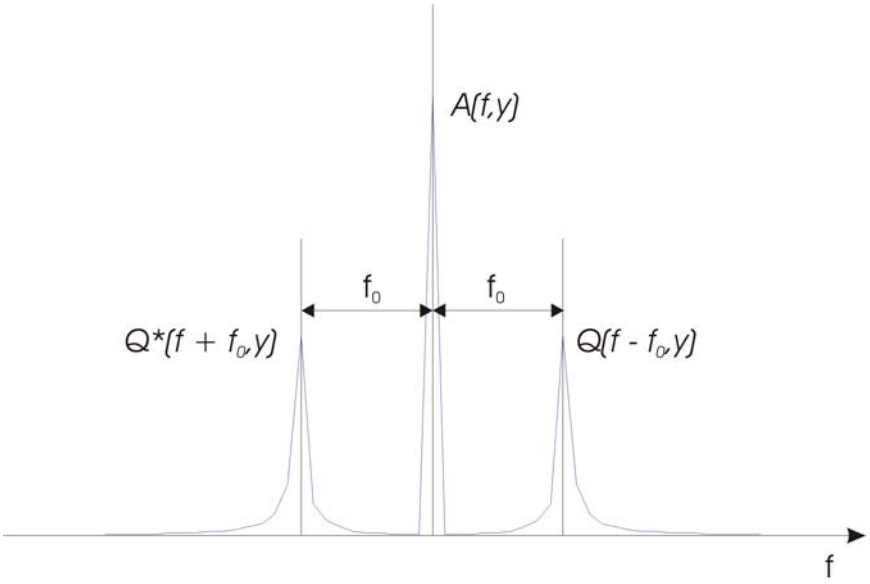

Figure 2.6: Example phase modulated sinusoidal Fourier Spectra

ponents. A sketch of the typical Fourier magnitude spectra for a phase modulated sinusoidal fringe is show in Figure 2.6. As depicted in the Figure the direct component $a(x, y)$, amplitude modulation $b(x, y)$ and phase modulation $\phi(x, y)$ vary slowly relative to the carrier frequency which separates the Fourier spectra of Equation (2.36) by f_0. Given that the spectra is divided by the fringe carrier frequency f_0, and the desired phase modulation term is contained in either one of the sidebands, the unwanted direct component and redundant sideband can be removed through filtering, leaving just the desired sideband. Assuming the fringe spectrum has been filtered to leave just the $Q(f - f_0, y)$ component, the next step in the process is to translate the spectra by f_0 to a baseband signal, $Q(f, y)$ centered around zero as shown in Figure 2.7. The inverse Fourier Transform of the baseband $Q(f, y)$ spectra is calculated giving

$$q(x, y) = \frac{1}{2} b(x, y) e^{i\phi(x,y)} \tag{2.37}$$

Finally, the phase component can be extracted from the unwanted amplitude modulation component by taking the imaginary component after calculating the logarithm of Equation (2.37)

$$\phi(x, y) = Im \left[\log \left(\frac{1}{2} b(x, y) \right) + i\phi(x, y) \right] \tag{2.38}$$

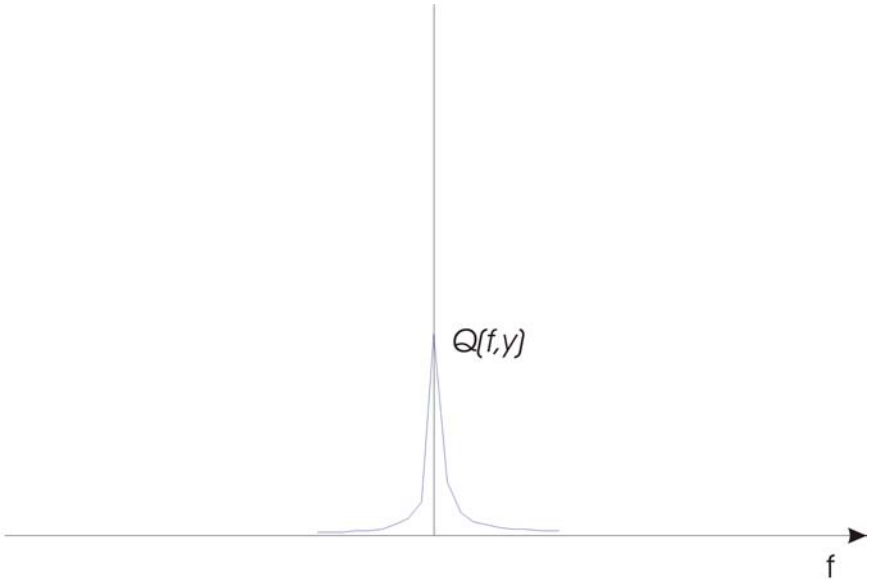

Figure 2.7: Example Baseband Fourier Spectra $Q(f, y)$

2.4.2.2 Fourier Transform Profilometry (FTP) [84]

The concept of Fourier fringe processing for 3D profilometry applications was first proposed by Takeda and Mutoh [84] soon after Takeda *et al.* [105] proposed Fourier fringe processing in the early 1980's. Although the concept of Fourier fringe processing was primarily directed at the analysis of sinusoid fringes, given that filtering is required to isolate the fundamental component of the fringe, the concept can and was extended by Takeda to consider not only sinusoid fringes but also Ronchi gratings. This is of particular significance for Fringe projection profilometry methods where the task of generating and projecting a pure sinusoid signal is often difficult. With this in mind a more generalised form to describe the projected reference and object phase modulated gratings is required. Hence, rewriting Equations (2.7) and (2.11) the projected reference and object fringe images can be given by the Fourier series

$$g_0(x, y) = \sum_{n=-\infty}^{\infty} q_{0n}(x, y) e^{2\pi i n f_0 x} \tag{2.39}$$

where

$$q_{0n}(x, y) = A_n r_0(x, y) e^{in\phi_0(x,y)} \tag{2.40}$$

and

$$g(x,y) = \sum_{n=-\infty}^{\infty} q_n(x,y)e^{2\pi i n f_0 x} \tag{2.41}$$

where

$$q_n(x,y) = A_n r(x,y)e^{in\phi(x,y)} \tag{2.42}$$

respectively, where A_n denotes the nth Fourier coefficient of the series and $r_0(x,y)$ and $r(x,y)$ represent a nonuniform function of reflectivity for both the reference plane and object's surface respectively.

Considering the latest representation of the projected fringe it becomes clear that the Fourier spectra of the signal will contain an infinite amount of harmonic terms. Considering just one of the fringe images now say, $g(x,y)$, and taking the Fourier Transform with respect to x

$$\begin{aligned} G(f,y) &= \int_{-\infty}^{\infty} g(x,y)e^{-2\pi i f x}dx \\ &= \sum_{n=-\infty}^{\infty} Q_n(f - nf_0, y) \end{aligned} \tag{2.43}$$

the infinite nature of the transformation is revealed. A simple example magnitude spectra of such a signal is depicted in Figure 2.8, much like the previous spectra for the pure sinusoid with each component separated by carrier frequency f_0, however, with harmonic components.

After transforming both the reference and object fringe to the Fourier frequency domain either one of the fundamental sidebands containing the required phase modulation is selected via bandpass filtering and the inverse Fourier Transform operation of the filtered signals is calculated. In this instance the $Q_{0\,1}(f - f_0, y)$ and $Q_1(f - f_0, y)$ sidebands have been selected and therefore the resulting reference and object fringe signals, $\mathbf{g}_0(x,y)$ and $\mathbf{g}(x,y)$ in the spatial domain are given by

$$\begin{aligned} \mathbf{g}_0(x,y) &= q_{0\,1}(x,y)e^{2\pi i f_0 x} \\ &= A_1 r_0(x,y)e^{i(2\pi f_0 x + \phi_0(x,y))} \end{aligned} \tag{2.44}$$

and

$$\begin{aligned} \mathbf{g}(x,y) &= q_1(x,y)e^{2\pi i f_0 x} \\ &= A_1 r(x,y)e^{i(2\pi f_0 x + \phi(x,y))} \end{aligned} \tag{2.45}$$

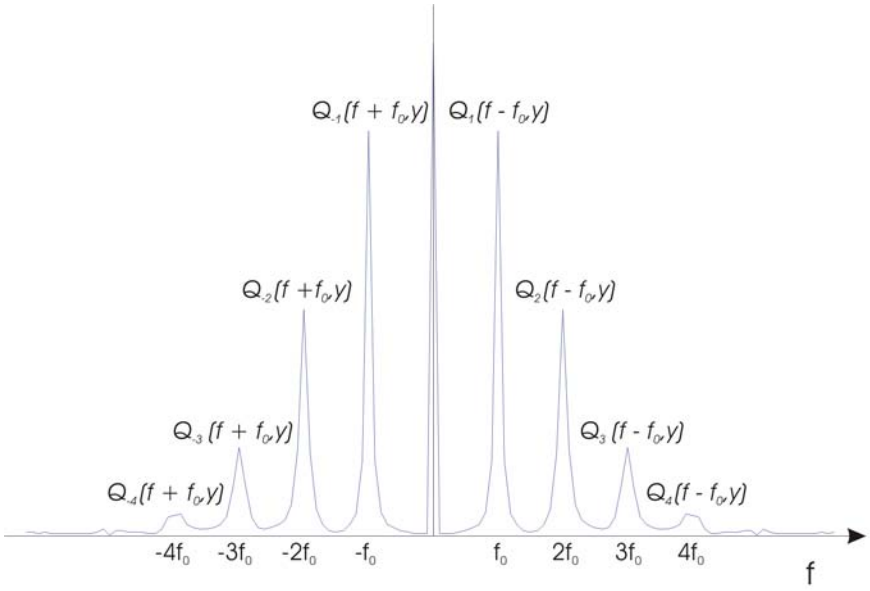

Figure 2.8: Example: General Fourier Spectra $G(f, y)$ for a Projected Fringe

Referring to the principle method of Fourier Transform fringe processing, in order to calculate the desired phase component it is necessary to translate the signal containing the desired phase component to a baseband signal. In other words, remove the tilting effects of the carrier frequency. Supplementary to this the additional phase modulation component $\phi_0(x, y)$ prominent in all Fringe Projection approaches must also be removed to reveal $\Delta\phi(x, y)$ (as discussed in Section 2.3). Therefore the equivalent translation and elimination of $\phi_0(x, y)$ can be accomplished using Equations (2.44) and (2.45) as follows

$$\mathbf{g}(x, y).\mathbf{g}_0^*(x, y) = |A_1|^2 r(x, y).r_0(x, y)e^{i\Delta\phi(x,y)} \tag{2.46}$$

and finally the phase component associated with the height distribution of the object can be removed from the unwanted amplitude modulation by

$$\Delta\phi(x, y) = Im\left(\log\left[\mathbf{g}(x, y).\mathbf{g}_0^*(x, y)\right]\right) \tag{2.47}$$

2.4.2.3 Maximum Range of Measurement

In order to solve for the unknown phase component of a fringe image using the Fourier Transform method, the requirement is for the adequate isolation of one of the fundamental sideband components from all other harmonic spectra including the direct component. If there is any overlapping of spectral components it becomes impossible to pickup only the

required fundamental sideband and hence an error is introduced into the measurement. Undoubtedly, measurement error from spectra overlapping is imminent, since theoretically a phase modulated sinusoidal presents an infinitely wide spectrum, however, for practical applications the overlapping only becomes of particular concern in situations of high fringe modulation, which has a direct correlation to $\frac{dh}{dx}$. Consequently, this imposes a limit to the maximum range of the FTP measurement. This limitation was addressed by Takeda and Mutoh [84] in their initial presentation of FTP, where the maximum range of measurement was shown to be

$$\left|\frac{\partial h(x,y)}{\partial x}\right|_{MAX} < \frac{1}{3}.\frac{l_0}{d} \tag{2.48}$$

2.4.2.4 Improved Fourier Transform Profilometry (IFTP)

In the late 1980's Su. *et al.* addressed the limited maximum range of measurement associated with FTP, by proposing an Improved FTP (IFTP) method [110] to extend the maximum measurable range of the FTP method. The method was later more formally presented in [106]. Essentially this improvement of FTP allows the fundamental component $Q_1(f - f_0, y)$ to extend theoretically upward to $2f_0$ and downward to 0 in the spatial frequency domain, keeping in mind that the height measurement limitation stems from the inability to isolate the fundamental component from other higher order components and the direct component. This bandwidth extension is made possible by firstly defocusing the projection system to yield a quasi-sinusoidal projection to reduce the effects of higher order harmonics. The defocused Ronchi reference and object gratings can effectively be modeled by the standard sinusoidal fringes presented in Equations (2.7) and (2.11), respectively, with only a fundamental and direct component. With the higher order spectra attenuated by the defocused projection the fundamental component can now extend upward theoretically towards $2f_0$, however, the direct component still hinders the measurement range. Thus, Su. *et al.* proposed the projection of an additional object fringe image with a π radian offset purely with the intention to remove the direct component as

follows

$$\begin{aligned} g(x,y) &= [a(x,y) + b(x,y)\cos(2\pi f_0 x + \phi(x,y))] - \\ &\quad [a(x,y) + b(x,y)\cos(2\pi f_0 x + \phi(x,y) + \pi)] \\ &= b(x,y)\cos(2\pi f_0 x + \phi(x,y)) + \\ &\quad b(x,y)\cos(2\pi f_0 x + \phi(x,y)) \\ &= 2b(x,y)\cos(2\pi f_0 x + \phi(x,y)) \end{aligned} \tag{2.49}$$

where like Phase Shifting techniques, the direct component is assumed to present no temporal variation. If the Fourier Transform method is applied to Equation (2.49) since the fundamental can extend downward to approximately 0 and upward to approximately $2f_0$ the new measurable range can be given as

$$\left|\frac{\partial h(x,y)}{\partial x}\right|_{MAX} < \frac{l_0}{d} \tag{2.50}$$

increasing the measurable range of the originally proposed FTP method by a factor three.

More recently another hybrid method combining the Phase Shifting and Fourier Transform approaches similar to the IFTP method has been suggested as an improvement for Three Step Phase Shifting Profilometry (I3PSP) [111]. This technique is aimed at reducing the nonlinear distortions associated with DVP sources for the highly 2nd order sensitive three step PSP method. Since the method still requires filtering in the spatial frequency domain despite the additional image, it is rather ill-posed in light of the fact that the IFTP method requires less data and is quite insensitive to 2nd order nonlinearities.

2.4.2.5 Modified Fourier Transform Profilometry (MFTP)

Like any phase shifting approach, the hybrid IFTP method, which requires the projection of a second π phase shifted fringe to remove the direct component, is vulnerable to measurement errors resulting from fringe phase shifting errors. The phase error introduced into the IFTP measurement was first investigated by Yi and Huang [107] where they proposed a FTP approach resilient to phase shifting errors while still maintaining the range of measurement associated with the IFTP method. Yi and Huang showed that for a phase

shift error of τ, the object grating previously given by Equation (2.49) can be given by

$$\begin{aligned} \acute{g}(x,y) &= [a(x,y) + b(x,y)\cos(2\pi f_0 x + \phi(x,y))] - \\ &\quad [a(x,y) + b(x,y)\cos(2\pi f_0 x + \phi(x,y) + \pi + \tau)] \\ &= 2b(x,y).\cos\left(\frac{\tau}{2}\right).\cos\left(2\pi f_0 x + \phi(x,y) + \frac{\tau}{2}\right) \end{aligned} \tag{2.51}$$

Unlike phase shifting errors in phase shifting approaches where the amplitude modulation term, $\cos\left(\frac{\tau}{2}\right)$, generated from the phase shifting error propagates through the algorithm to yield a complex phase measuring residual, the phase shifting error for the IFTP case results in a simple constant phase offset error of $\frac{\tau}{2}$. To eliminate the arbitrary phase shift error, Yi and Huang suggest the acquisition of an additional fringe image of the supposed π offset for the reference plane. Hence a new reference fringe, $\acute{g_0}(x,y)$ can be formed as

$$\begin{aligned} \acute{g_0}(x,y) &= [a(x,y) + b(x,y)\cos(2\pi f_0 x + \phi_0(x,y))] - \\ &\quad [a(x,y) + b(x,y)\cos(2\pi f_0 x + \phi_0(x,y) + \pi + \tau)] \\ &= 2b(x,y).\cos\left(\frac{\tau}{2}\right).\cos\left(2\pi f_0 x + \phi_0(x,y) + \frac{\tau}{2}\right). \end{aligned} \tag{2.52}$$

If the two newly formed gratings represented by Equations (2.51) and (2.52) are now used to estimate $\Delta\phi(x,y)$, the constant phase shift error, $\frac{\tau}{2}$, will be removed.

This variation of the FTP method has seen little use, particularly, more recently for predominantly for two reasons; Firstly, since the phase measuring error is a simple constant it can therefore be easily removed via simple calibration and, secondly, since the phase shifting error can typically be eliminated by the introduction of digital means to project fringe images.

2.4.2.6 Two-Dimensional Fourier Transform Profilometry (2DFTP)

By the mid 1990's the FTP method had been exhaustively studied and employed in various applications including the profiling of coarse objects such as sand bodies. The recorded fringe images of such rough or coarse surfaces often present discontinuities and speckle-like structures which can typically be modeled as additive noise.

$$g(x,y) = \sum_{n=-\infty}^{\infty} q_n(x,y)e^{2\pi i n f_0 x} + n(x,y) \tag{2.53}$$

The additive noise distribution, $n(x, y)$, observed in the fringe image ultimately limits the achievable resolution of the measurement and also inhibits the process of phase unwrapping (Note:- phase unwrapping will discussed in detail in Section 2.5). The measurement of coarse structures such as sand bodies using FTP was investigated by Lin and Su in [108] whereby they proposed a Two-dimensional FTP method (2DFTP). In the ideal case without noise, the 1D FTP will suffice, however, in applications such as that mentioned above the frequency spread presents 2D characteristics resulting from the speckle-like structures and discontinuities. Therefore, a two dimensional Fourier Transformation of the fringe along with an appropriate filter assists in the appropriate attenuation of the unwanted high frequency content and consequently improves the measurement accuracy of coarse surfaces and assists in the phase unwrapping process.

2.4.2.7 Frequency Multiplexed Fourier Transform Profilometry

Perhaps the most interesting application of the Fourier Transform Profilometry method is the Frequency Multiplexed FTP technique proposed by Takeda *et al.* [109]. The frequency multiplexed application is centered around the simultaneous projection of K sinusoidal fringes recorded in just one single image. For simplicity telecentric optical conditions are considered and hence the spatially multiplexed grating can be given by

$$g(x, y) = r(x, y) \sum_{k=1}^{K} [1 + \cos(2\pi f_{X,k} x + 2\pi f_{Y,k} y + \phi_k(x, y))] \tag{2.54}$$

where $f_{X,k}$ and $f_{Y,k}$ are the kth spatial carrier frequencies in the x and y directions respectively. Given the nature of the Fourier Transform operation, by the FTP method the individual carrier frequencies can be uniquely identified [112], essentially leading to K evaluations of $\phi(x, y)$ and hence height distribution $h(x, y)$.

Considering that the additional fringe dimension leads to an additional $K - 1$ phase maps for the FTP method, the surplus of information can be utilised to assist in performing more accurate measurements under certain previously difficult scenarios. In particular, the accurate profiling of scenery with large height discontinuities and/or spatially isolated areas. In fact, the motif behind Takeda *et al.*'s initial presentation of frequency multiplexed FTP with K set to 2, was the measurement of complex surfaces with discontinuities. The method specified that the projection of the two fringes were spatially

arranged such that the pitch of the individual gratings along the x axis formed relative primes. The latter constraint enabled the implementation of a specialised number theory based phase unwrapping method borrowed from Gushov and Solodkin [113], to measure discontinuous surfaces with just one image.

The spatial frequency multiplexing of FTP methods was a major realisation for the FTP techniques and has proven FTP to be a very promising 3D surface profile and shape measurement technique.

2.4.3 Direct Phase Detection

The Direct Phase Detection (DPD) fringe processing concept is fundamentally identical to that of the Fourier Transform fringe processing concept, however, as opposed to operating in the spatial frequency domain, all processing is conducted in the spatial domain. The technique was first demonstrated for the analysis of fringe images through the work of Ichioka and Inuiya [114]. The principle of DPD is centered on the idea of creating two orthogonal signals by multiplying a single fringe image by two orthogonal reference signals. Identical to the process of coherent demodulation for frequency modulated signals in communication theory, the two orthogonal reference signals separate the phase component from the other higher order terms by approximately the carrier frequency. Therefore, via low-pass filtering in the spatial domain the desired phase component can be isolated and extracted by employing an arctangent operation.

Similar to the two previously presented fringe processing methods, DPD is more precise than more primitive fringe processing methods, requiring no fringe order assignments, center determination nor interpolations of fringes, with phase data available at each pixel of the fringe image. Furthermore, like the Fourier Transform method, DPD only requires a single fringe image and also suffers from the same limitations due to inadequate isolation of spectral components.

The remainder of this section is concerned with more formally outlining the principle of DPD and moreover, providing an insight into some of the more significant DPD application for 3D sensing.

2.4.3.1 Direct Phase Detection Principle

The basic concept of DPD is depicted in Figure 2.9. The phase modulated fringe image, $g(x, y)$ is multiplied by two reference signals $\cos(2\pi f_0 x)$ and $\sin(2\pi f_0 x)$ to form two signals

$$\begin{aligned} g_1(x,y) &= g(x,y)\cos(2\pi f_0 x) \\ &= a(x,y)\cos(2\pi f_0 x) + \frac{1}{2}b(x,y)\cos[4\pi f_0 x + \varphi(x,y)] \\ &\quad + \frac{1}{2}b(x,y)\cos[\varphi(x,y)] \end{aligned} \tag{2.55}$$

and

$$\begin{aligned} g_2(x,y) &= g(x,y)\sin(2\pi f_0 x) \\ &= a(x,y)\sin(2\pi f_0 x) + \frac{1}{2}b(x,y)\sin[4\pi f_0 x + \varphi(x,y)] \\ &\quad - \frac{1}{2}b(x,y)\sin[\varphi(x,y)] \end{aligned} \tag{2.56}$$

where $\varphi(x, y)$ denotes the spatial phase modulation corresponding to the projection surface i.e. $\phi(x, y)$ or $\phi_0(x, y)$. As can be seen in Equations (2.55) and (2.56) the desired phase term is completely isolated from the higher order terms and hence by low-pass filtering each signal, the two low frequency orthogonal terms can be utilised to estimate $\varphi(x, y)$ by

$$\varphi(x,y) = -\arctan\left[\frac{g_2(x,y) * f(x,y)}{g_1(x,y) * f(x,y)}\right] \tag{2.57}$$

where $*$ denotes convolution and $f(x, y)$ represents the low-pass filter function. Ultimately, the low-pass filtering function plays a major role in the accuracy of the recovery of the phase map $\varphi(x, y)$.

With further reference to communication based concepts, considering the DPD process, the technique can also be further likened to the synchronous phase detection technique previously presented in Section 2.4.1.1, which like DPD, is also well understood in communication theory.

2.4.3.2 Direct Phase Detection for 3D Sensing

The DPD principle has been employed in a number of 3D sensing applications [86, 115, 116], most of which are differentiated purely by the filter stage variation $f(x, y)$. The first

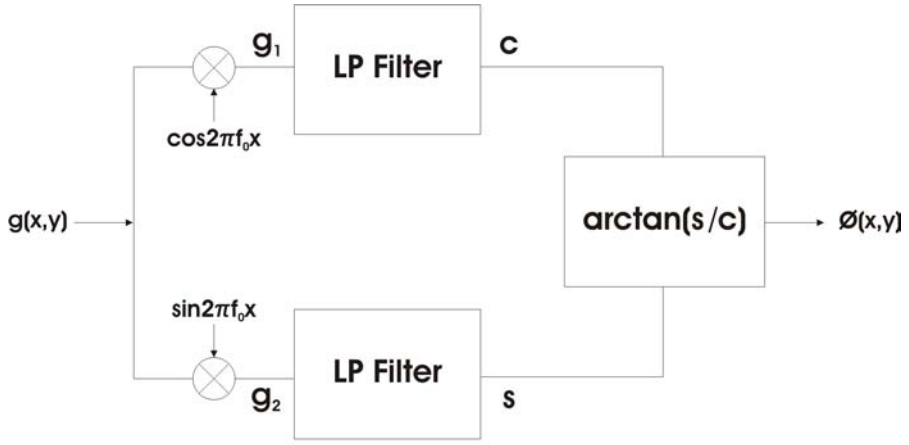

Figure 2.9: Typical Direct Phase Detection process

implementation of DPD for 3D sensing was demonstrated by Toyooka and Iwaasa [86] by the so called Spatial Phase Detection (SPD) method. The SPD method was vastly superior in terms of computational complexity relative to other fringe processing algorithms of it's time, with the filtering undertaken through simple integration of the signals $g_1(x, y)$ and $g_2(x, y)$ over an integer number of spatial periods. A later DPD variation proposed by Tang and Hung [115] overlooked the previous work of Toyooka and Iwaasa, employing Finite Impulse Response (FIR) filters to obtain the required orthogonal signals. Tang and Hung also provided an in depth analysis of the superior computational advantages of the method relative to the Fourier Transform method. Their derivation also included analysis of the finite bandwidth limitations resulting in a limited maximum range of measurement identical to that of the FTP method displayed in Equation (2.48). A more recent DPD implementation seen Villa *et al.* [116] implement the filtering stage using regularised filters. This is an interesting approach aimed at addressing the phase unwrapping and noise problems associated with previously proposed convolution based filtering methods. The use of regularised filters was shown to vastly assist phase unwrapping and improve the fringe signal to noise ratio, however, the distinct DPD computational advantages were somewhat lost given the additional processing requirements.

2.4.3.3 Phase Locked Loop Direct Phase Detection Variation

Considering the strong link between DPD and communication theory, the implementation of other coherent frequency demodulation methods such as Phase Locked Loops (PLL)

have also been shown to be quite effective tools in the processing of fringe images [87]. The distinct advantage of PLL methods is the omission of the phase unwrapping process, with relative phase values determined in a continuous operation, therefore making the approach very computationally efficient.

2.5 Phase Unwrapping

Each of the fringe processing techniques presented in Section 2.4 estimates the phase distribution, $\Delta\phi(x, y)$, by employing an arctangent calculation undertaken over the four quadrants of phasor space. The retrieved phase distribution corresponding to the object height is therefore restricted to principle values ranging between $-\pi$ and π, and consequently, the estimated phase is a modulo 2π distribution, otherwise referred to as a wrapped phase map. While the process of phase unwrapping is not explicitly a major focus of interest in the work presented within this dissertation, it is important to realise the various methods and algorithms involved in unwrapping a modulo 2π phase map. The following sections briefly describe some of the concepts and methods used in order to undertake the adequate unwrapping of a wrapped phase distribution.

2.5.1 Phase Unwrapping Principle

The wrapping nature of the arctangent operation is demonstrated in Figure 2.10, for an arbitrary dome like phase distribution. As can be seen from the arbitrary cross-section of the wrapped phase distribution shown in Figure 2.11 (a), the values of the wrapped phase are all contained within the interval $-\pi \longrightarrow \pi$. Considering phase wrapping in the single dimensional sense with reference to Figures 2.11 (a) and (b), the rudimentary phase unwrapping procedure is revealed as a process concerned with traversing through the wrapped phase vector sequentially in the x direction adding or subtracting integer multiples of 2π. A more formal description of the single dimensional process of phase unwrapping was first demonstrated by Itoh in Reference [117]. Itoh's formulation of the phase unwrapping algorithm demonstrated that the true phase can be obtained from the

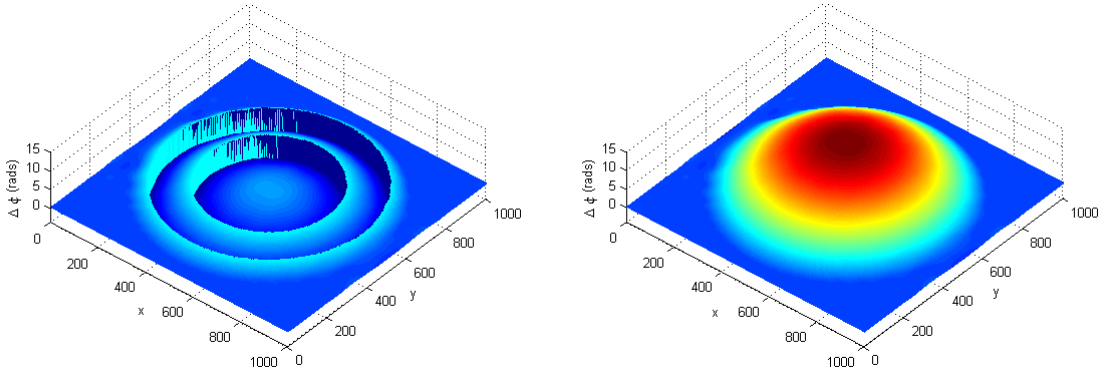

(a) Wrapped Phase Map (b) Unwrapped Phase Map

Figure 2.10: Wrapped and Unwrapped Phase Map

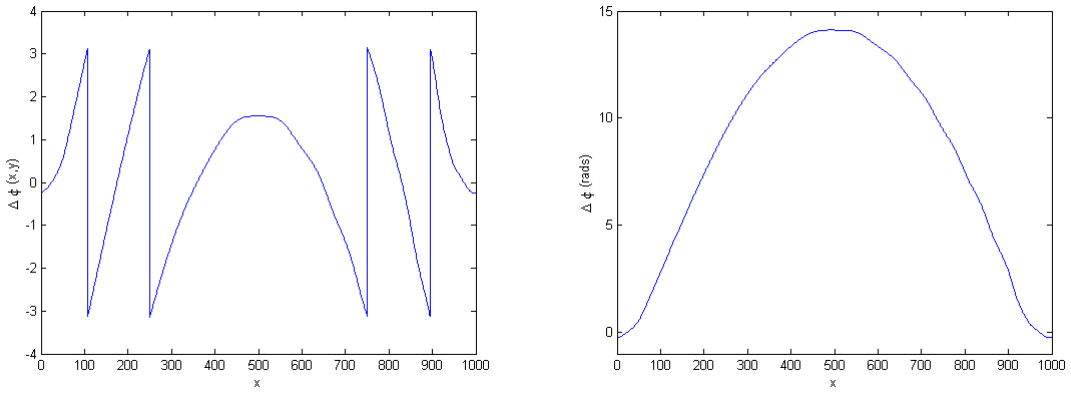

(a) Cross-section of Wrapped Phase Map (b) Cross-section of Unwrapped Phase Map

Figure 2.11: Cross-sections of Wrapped and Unwrapped Phase Maps of Figures (2.10) (a) and (b)

wrapped phase by integrating the wrapped differences of the wrapped phase values.

$$\Phi(m) = \Phi(0) + \sum_{n=0}^{m-1} W\left[W[\Delta\Phi(n)]\right] \tag{2.58}$$

where W denotes the wrapping operator given by

$$\begin{aligned} W[\Phi(n)] &= \arctan\left[\frac{\sin(\Phi(n))}{\cos(\Phi(n))}\right] \\ &= \Phi(n) + 2\pi k(n) \end{aligned} \tag{2.59}$$

where $k(n)$ is an array of integers chosen so the phase values are all contained within the interval of $-\pi \longrightarrow \pi$, and the wrapped phases are differentiated as

$$\Delta\Phi(n) = \Phi(n+1) - \Phi(n) \tag{2.60}$$

An imperative step in Itoh's derivation demonstrated that provided the signal is appropriately sampled according to sampling theorem the true phase map could only be obtained from the wrapped values using Equation (2.58) if and only if the true phase satisfies

$$-\pi \leq \Delta\Phi(n) < \pi \tag{2.61}$$

While in the theoretical sense Itoh's method will suffice, practical fringes contain additive noise phenomena and other fringe discontinuities which may void Equation (2.61) impeding the phase unwrapping process. Moreover, for Fringe Projection applications the process of phase unwrapping becomes significantly more difficult when attempting to profile geometrically complex surfaces where fringe continuity cannot be guaranteed in either x nor y directions. The fringe discontinuities typically referred to in phase unwrapping literature as "residues" are sourced from fringe occlusions resulting from shadowing and / or significant variations in the depth of the shape causing the phase to be deeply modulated. For primitive single dimensional phase unwrapping methods such as Itoh's [117], the errors resulting from fringe singularities can be propagated throughout the reconstruction, severely effecting the accuracy of the fringe projection approach.

Considering the phase unwrapping dilemma in only the single dimension presents a limited set of solutions, however, phase unwrapping as a two-dimensional problem can allow for the required flexibility to develop more robust solutions. With the additional

dimension comes additional paths in which to integrate along and therefore unwrapping in the presence of fringe anomalies or discontinuities can be accommodated. Although the task of 2D phase unwrapping is non-trivial the underlying principle of the unwrapping process is still centered on the integration of phase gradients in some form [118].

2D phase unwrapping approaches are generally categorised as Path-Dependent or Path-Independent approaches. The remainder of this section will differentiate between the two, identifying key concepts and briefly mentioning some of the more well known approaches.

2.5.2 Path-Dependent Unwrapping

The previously discussed phase unwrapping technique known as Itoh's method [117] involves integrating phase differentials along a path in the x direction. With further reference to 1D phase unwrapping algorithms it has also been previously pointed out that if a noise artifact or fringe discontinuity is encountered that inhibits the correct unwrapping of a particular pixel, the unwrapped phase value of each pixel thereafter lying along that particular path is also incorrectly unwrapped by an integer multiple of $\pm 2\pi$ radians. Therefore, the notion of path dependence for rudimentary unwrapping in the single dimensional sense has been clearly defined. In the 2D sense the foundation of 2D path dependent unwrapping is centered on the fact that the phase difference between any two points measured by integrating phase along a path between the two points is independent of the route chosen, as long as the route does not pass through a phase discontinuity. This idea is demonstrated in Figure 2.12 where two points on a continuous fringe, x and x_0, are unwrapped along two independent paths as graphically depicted. The independence of fringe paths depicted in Figure 2.12 can be mathematically written as

$$\phi(x) = \int_C \nabla\phi \, dx + \phi(x_0) \tag{2.62}$$

where C represents any arbitrary path between the two points x and x_0 and $\nabla\phi$ represents the wrapped gradients of the wrapped phases. Moreover, the independent nature of 2D unwrapping leads to one of the key concepts forming the basis of many path dependent unwrapping procedures; the evaluation of residues (otherwise known as fringe discontinuities). In theory, any closed loop integration of the wrapped gradients of wrapped phases

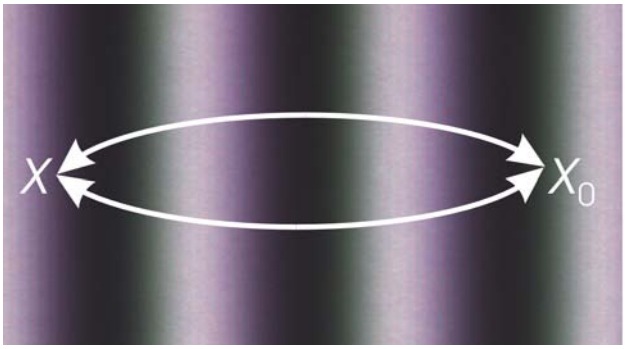

Figure 2.12: Independent Fringe Paths

on a continuous fringe should evaluate to zero, i.e. mathematically,

$$\oint \phi(x)\, dx = 0 \tag{2.63}$$

Now, if Equation (2.63) cannot be satisfied, clearly a discontinuity has been encountered along the closed loop path. Therefore, the evaluation process is

$$\oint \phi(x)\, dx = \pm 2\pi . \sum N_R \tag{2.64}$$

where N_R denotes the number of enclosed residues. The basis of path dependence and phase unwrapping including the concept of residues is derived at length in [118].

Using the concept of identifying residues or discontinuities, cut-based algorithms can be designed to robustly unwrap around the locations of fringe discontinuities typical of noise artifacts. Probably the most well known cut-based algorithms employing residue evaluation were proposed by Goldstein *et al.* [119] and Huntley [120]. Cut-based methods correlate positive and negative residues together, and by introducing a cut between the two correlated residues, force the unwrapping path algorithm to unwrap around these points.

Contrary to the evaluation of residues, other metrics for guided unwrapping have also been successfully employed to unwrap a 2D wrapped phase map, these approaches are known as reliability or quality guided unwrapping methods. One of the typical quality measures employed by these algorithms is fringe modulation, $\Gamma(x, y)$, given by

$$\Gamma(x, y) = \frac{b(x, y)}{a(x, y)} \tag{2.65}$$

for a PSP fringe set, or alternatively

$$\Gamma(x, y) = \sqrt{[Im(q(x, y))]^2 + [Re(q(x, y))]^2} \tag{2.66}$$

for a bandpass filtered fringe signal. The modulation parameter can be used as a guide in unwrapping process to prioritise unwrapping of pixels with higher modulation as opposed to pixels with lower contrast. Further to modulation guided unwrapping another commonly used fringe metric for path dependent unwrapping is phase gradient, $\Delta\Phi(x, y)$ as defined in Equation (2.60), however, with the included second dimension over an n by n space. A large value for $\Delta\Phi(x, y)$ is typically associated with a region of noise and hence can be used to navigate around "bad" pixels.

Reliability guided phase unwrapping techniques can combine two or more of these metrics and thereby improve the unwrapping procedure. A more comprehensive overview of reliability unwrapping methods and the various metrics and the combination of these measures can be found in Reference [121].

2.5.3 Path-Independent Unwrapping

While the concept of path dependence and phase unwrapping has been strongly emphasised, another variation of unwrapping algorithms known as path-independent phase unwrapping techniques have also been exhaustively practiced. Primarily, path-independent unwrapping techniques operate on the fringe data set as an entity or subset of entities, in either the spatial or temporal domains. Spatial domain path-independent phase unwrapping techniques are commonly posed as minimisation problems with the objective function leading to the minimisation of the differences between gradients of the wrapped phase and the unwrapped solution [118]. One particularly interesting minimisation implementation based on cellular automated was proposed by Ghiglia *et al.* [122]. Cellular automata unwrapping is typically concerned with iteratively minimising the discontinuities in the phase map by adding or subtracting integer multiples of 2π based on simple neighbourhood rules. Given the iteration nature of the approach, cellular automata unwrapping is often quite computationally demanding. Another interesting spatial path-independent strategy, is centered on partitioning the wrapped phase image [123]. Partitioning methods segregate the 2D phase map into regions where the boundaries are generally determined by surrounding discontinuities. Each region is thereby individually unwrapped and the phase offsets between each of the unwrapped neighbouring regions subsequently determined.

While minimum norm and partitioning methods have been shown to successfully unwrap a wrapped fringe when the overall continuity of the fringe can be guaranteed, much like the majority of the previously discussed unwrapping techniques, these methods fail for large discontinuities where the phase gradient term is significantly large. An interesting approach to combat the unwrapping of complex surfaces with large discontinuities by temporally unwrapping the fringe was first proposed by Huntley and Saldner [124]. The temporal phase unwrapping concept is successful where the other previously discussed spatial approaches fail, as each pixel is unwrapped independently of every other pixel, with the unwrapping taking place along the time axes. Another temporal based approach to assist in the unwrapping of fringes that present large discontinuities resulting from complex surface geometries is the multiple wavelength techniques. The analogy is identical to two or multiple wavelength interferometry as discussed in Section 1.2.3.1, whereby two fringe patterns are created and projected sequentially in time. One of the fringe images is created with a low sensitivity to large profile height variance and another with a higher sensitivity for a more precise measurement. While temporal approaches are generally more robust in terms of their ability to successfully unwrap complex fringe maps, since data needs to be acquired over a finite duration of time their application in the dynamic sense can be somewhat limited. A very interesting phase unwrapping procedure somewhat liken to multiple-wavelength methods, however, does not suffer the same temporal limitations, is the frequency multiplexing approach briefly discussed in Section 2.4.2.7. As opposed to temporally acquiring the multiple fringes, the FMFTP method spatially separates the fringes in the spatial frequency domain by the nature of the 2D Fourier Transform allowing the acquisition of multiple fringes in a single shot.

Although a significant amount of research has been aimed at fully automating the fringe analysis process of phase unwrapping, the unwrapping solution often tends to be an application specific solution. While programming a computer to correctly unwrap a wrapped fringe image with any kind of accuracy is a difficult task, for the human observer the unwrapping procedure is generally a very simple task to perform visually. As a result software to allow a human observer interactively unwrap a wrapped fringe have been implemented [125].

2.6 Calibration

The final step in the measurement process is the conversion of the acquired phase map to an actual physical quantity. Theoretically, this can be achieved using Equation (2.14), however, since practically it is very difficult to measure system parameters d_0, l_0 and f_0 with any kind of accuracy, a calibration procedure is required for the accurate translation from phase values to real world co-ordinates. Furthermore, since the pin-hole model is still just a theoretical model for the practical triangulation system, finite aperture size lens distortions and other model assumption inhibit true phase to height conversions. For the body of work presented in this thesis, the primary concern is for the profiling of relative height distributions, therefore, a very simplistic co-ordinate translation calibration process has been employed.

Rewriting Equation (2.14), the phase distribution corresponding to the geometry of the surface of interest can be calculated as

$$\Delta\phi(x,y) = \frac{2\pi f_0 d_0 h(x,y)}{h(x,y) - l_0} \tag{2.67}$$

Given that the projector is generally located far enough from the object i.e. $l_0 \gg h(x,y)$, the phase distribution can be approximated as

$$\Delta\phi(x,y) \approx \frac{2\pi f_0 d_0 h(x,y)}{-l_0} \tag{2.68}$$

Accordingly, the height distribution $h(x,y)$ can be approximated by

$$h(x,y) \approx -\frac{l_0}{2\pi f_0 d_0}\Delta\phi(x,y) \tag{2.69}$$

The measurement can then be calibrated by measuring $\Delta\phi(x,y)$ for a known height distribution, $h(x,y)$, and by calculating a calibration factor i.e.

$$\begin{aligned} K &\approx \frac{h(x,y)}{\Delta\phi(x,y)} \\ &\approx -\frac{l_0}{2\pi f_0 d_0} \end{aligned} \tag{2.70}$$

and hence, the measured phase distribution can be crudely converted into a real world co-ordinate space.

2.7 Summary

This Chapter has provided the reader with an overview of the fundamental concepts involved in 3D sensing by way of Fringe Projection. The overview has included rudimentary concepts such as the principle of triangulation and the typical Fringe Projection geometrical arrangement. The three most exploited forms of automated Fringe Processing algorithms were discussed and a review of the concept of Phase Unwrapping was also provided. Finally, the notion of a simple calibration approach was outlined.

Chapter 3

Creating Structured Light Fringe Images

3.1 Introduction

The two opening Chapters of this dissertation have clearly outlined the notion of Fringe Projection for 3D sensing, however, up until this point very little reference has been made in regard to the creation of structured light fringe images. The aim of this chapter is two-fold; firstly it serves as an investigation into the various methods and technologies involved in the creation of structured light fringe images, and secondly it provides an introductory analysis into the shortcomings of the more recently adopted DVP methods of Fringe Projection. The investigation outlines both analog and digital methods of projection, with a succinct focus on DVP methods of producing fringe images. The functionality of the two chief DVP technologies, LCD, and DLP is reviewed, and the integrity of the application of each for both single and multiple channel Fringe Projection is studied.

3.2 Projection Technologies

Effective 3D sensing as theoretically detailed in Chapter 2 can only be made possible through the adequate generation and projection of the appropriate fringe signals relevant to the corresponding fringe processing approach. Besides the obvious quality measures of a projected signal, such as contrast or Signal to Noise Ratio (SNR), a range of additional

projection anomaly can significantly degrade the veracity of a projection technology or technique for structured light 3D sensing. For instance, if a phase shifting error between sequential fringe images of a Phase Shifting implementation exists, a significant error will be propagated through the Phase Shifting algorithm and consequently influence the final evaluation of $\Delta\phi(x, y)$ and hence $h(x, y)$. Furthermore, the inadequate generation and projection of pure sinusoid signals can result in significant reconstruction error for the various algorithms mentioned in Section 2.4. Hence, the importance of the projection stage in any structured light 3D sensing implementation is unquestionable.

The purpose of this section is to highlight some of the technologies and methods employed to produce fringe images for 3D profiling.

3.2.1 Analog Vs. Digital

Similar to the manufacture of many signals, the projection of structured light can be undertaken in both the continuous and discrete domains. Continuous or analog techniques of producing structured light are typical of early Fringe Projection methods while discrete or digital techniques have only more recently been adopted. In general, analog projection techniques can often be attributed with the ability to produce more geometrically precise signals, however, the manipulation of analog signals is typically a laborious and tedious task. Conversely, discrete methods of projection can be generalised as producing geometrically less precise signals, however, with the advantage of simple and high speed manipulation of projected images. The following sections will now highlight some of the analog and digital projection approaches employed by Fringe Projection 3D sensing implementations.

3.2.2 Analog Fringe Projection

The traditional method of Fringe Projection, now better know as Shadow Moiré topography as discussed in Section 1.2.3.2, relies on the projection of a white light source onto a physical grating material with the fringe image resolved by viewing the scene through the same grating from an offset angle. By this analog method of projection a set of Moiré fringes detailing contour information about the surface can be readily obtained. Although

in this instance specialised fringe contours can be produced, a similar principle of grating projection is adopted for Fringe Projection techniques in the sense in which they are referred to in this work. Generally, the grating material involved in grating based analog projection is often manufactured to produce a Ronchi-like fringe, with sinusoidal fringe images produced through simple defocusing of the projection optics [126] and / or through post processing methods. One of the primary limitations of analog grating projection is that mechanical actuators are required to manipulate fringe attributes such as pitch and phase and consequently the dynamic manipulation of fringe images is quite limited. Furthermore, analog grating projection methods are prone to phase-shifting errors in phase shifting implementations.

While grating based approaches are the most common and original analog method of producing fringe images a more recently proposed analog method based on Acousto-optic modulators (AOMs) is also worth mentioning [127]. Relative to the grating approach the AOM approach has the significant advantage of being able to control the pitch and phase of the projected fringe image electronically without the need for mechanical actuators, allowing for high speed manipulation of the projected fringe signal.

3.2.3 Digital Fringe Projection (DFP)

The first reported 3D sensing work performed with digital projection sources appears to have been conducted by Stahs and Wahl [72] who developed a time space encoding measurement system whereby they mounted a computer controlled transparent LCD to a conventional white light projector to project binary structured light patterns. Since then Spatial Light Modulator's (SLM's) such as LCD line projectors [128], specialised electron beam lithography systems [129] and also LCD pocket television units [130] have been used in digital projection systems, however, conventional video projectors generally either of LCD or DLP technology have formed the basis of many fringe profilometers. Some of the more interesting video projector based 3D sensing applications have been previously outlined in Section 1.2.4.3.

Typical DVP sources are capable of projecting standard 24 bit bitmap computer generated images and hence when interfaced to a personal computer make a very robust projection source. Moreover, the ability to project coloured images brings the capability

to develop multi-channel algorithms.

Further re-enforcing the application of DVP technology for 3D sensing, is the growing demand for high speed 3D profiling for applications such as animation, face recognition and machine vision. High projection speeds along with the merits of high resolutions, contrast ratios and affordability, has seen more and more researchers adopting the technology for dynamic 3D sensing applications.

Relative to traditional analog projection procedures DVP provides the ability to easily manipulate fringes at high speed via software control, thereby making dynamic real-time 3D profiling more realisable. Further, the software controlled nature of the technology makes it immune to phase-shifting errors prominent with traditional analog projection procedures. In contrast to Li *et al.*'s [127] AOM based approach, the much more well proven DVP technology can produce significantly higher contrast fringes to embrace a much larger geometrical surface area, and furthermore, DVP presents as a more suitable projection technology for the measurement of human tissues.

The advantages as highlighted above have fueled continued DVP 3D sensing interest from the research community over recent years, however, much like any projection technique, DVP for Fringe Projection presents a number of shortcomings. The predominant projection shortcoming associated with DFP techniques is the poor geometric structure of the digitally projected fringe images. The poor geometric precision of DVP signals and thus the source of DFP associated shortcomings are typically derived from the inherent nature of the projection technology. Therefore, it is imperative to have a very clear understanding of the functionality of the popular variations of DVP technology. The following section details the functionality of the two most exploited DVP technologies, LCD and DLP.

3.3 Digital Video Projection Technology

Today's DVP market is dominated by two chief and very different projection technologies, LCD and DLP. The more recently developed projection technology DLP, is a proprietary technology founded by Texas Instruments (TI) while LCD is a more mature and generic technology open to development by a number of different digital projection organisations.

A third projection technology spawned from both LCD and DLP projection technologies known as Liquid Crystal on Silicon (LCOS) moves away from traditional transmissive LCD projection technology and combines liquid crystals with DLP reflective technology. LCOS is a relatively recent development, however, due to expense and particularly contrast ratio and physical size issues these projection sources have yet to take a foothold in the competitive DVP market. In terms of triangulation based profilometers, systems have been developed using both primary projection technologies LCD and DLP. We will now examine the functionality of these two DVP technologies.

3.3.1 Liquid Crystal Display (LCD)

Liquid crystal technology is perhaps the most common form of flat panel electronic display today. A variety of consumer industrial products such as watches, calculators, mobile phones, laptop computers, pocket-size televisions and more recently larger television applications have been developed. The popularity of this technology is derived from it's portability. Slim shape, low weight, low voltage operation and low power consumption make LCD technology ideal for portable electronic display. In general, a LCD, they can be considered either reflective or transmissive in nature. Reflective LCD's generally modulate external ambient light, examples of such technology include more simple display devices such as watches and calculators. For colour and high brightness applications such as DVP and television, transmissive LCD technology is employed, whereby the liquid crystal structures modulate an internal light source such as a fluorescent light tube.

Many different types of liquid crystal's exist, however, probably the most exploited liquid crystal used in LCD devices is the unique Twisted Nematic (TN) phase liquid crystal. The structure and manufacture of TN liquid crystal's is detailed in [131]. Each of these individual liquid crystal Spatial Light Modulator (SLM) elements or pixels that make up an LCD device can be considered as an electronically controllable light shutter. When a carefully controlled voltage is applied to the twisted liquid crystal structure, it is capable of "untwisting" and hence modulating the amount of transmitted polarized light as to produce a greyscale. Figure 3.1 displays a schematic of a typical LCD, highlighting the major optical and electrical components. The liquid crystal arrangement is contained between two transparent glass substrates. A front and rear polarizer each polarize light

emitted from the source and are situated in an orthogonal arrangement. Optical retarders or compensation films are incorporated to increase the viewing angle in terms of luminosity, greyscale, and colour.

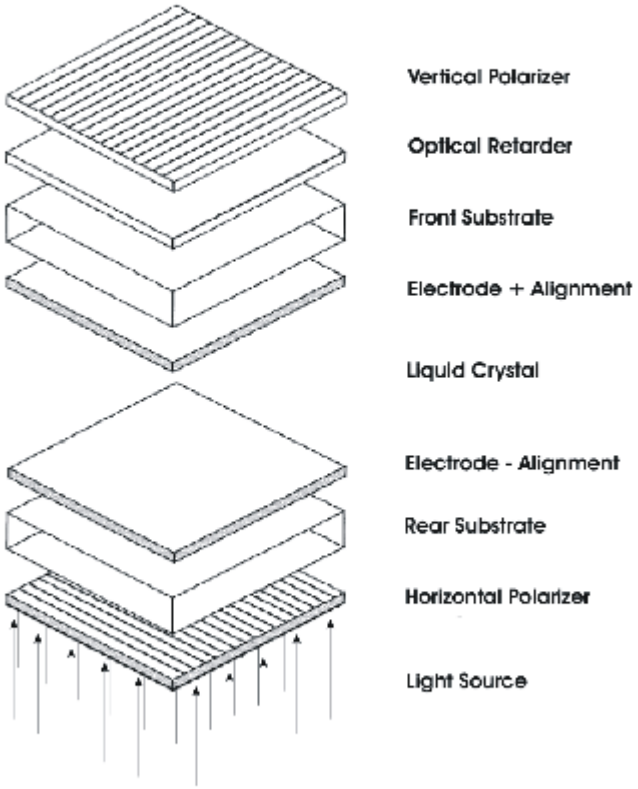

Figure 3.1: Generalised schematic of the major optical and electrical components of a LCD [131]

There exists three different methods for creating and controlling the applied voltage to manipulate liquid crystal structures. These are direct addressing, multiplex addressing and active matrix addressing. High information display applications use multiplex or active matrix addressing while simpler displays use direct addressing. Today's LCD DVP's use active matrix addressing with Thin Film Transistors (TFT). As the name suggests at each

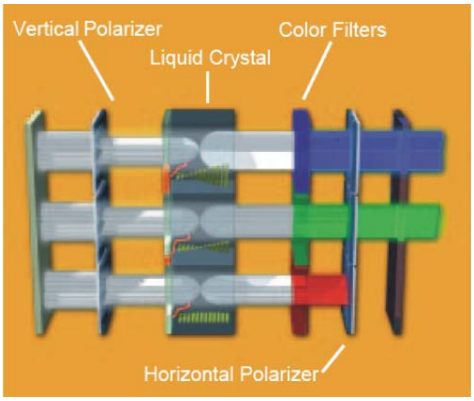

(a) Single Panel

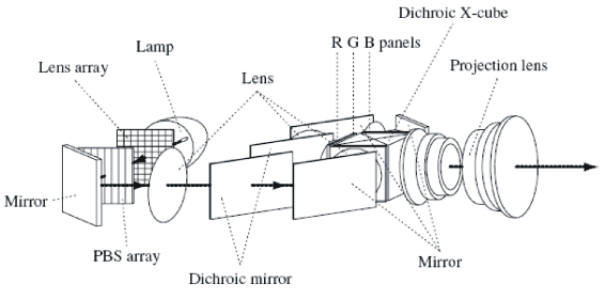

(b) Three Panel LCD

Figure 3.2: (a) Single Panel LCD. Note the side by side sub pixels structure and colour filters and the 'off' state of the lower red sub pixel [133]. (b) Three panel Poly-Si LCD [132].

pixel a transistor is used to control the voltage applied to the liquid crystal mixture. The advantages of TFT technology in contrast to other addressing schemes include high contrast ratio, negligible crosstalk (in the sense of the applied voltage effecting surrounding pixels), adequate greyscale and fast response time. One of the major problems with this technology is high production cost due to defective pixels and subsequent repair [131]. In LCD DVP applications the transistors are generally arranged onto either an amorphous silicon (Am-Si) or polycrystalline silicon (poly-Si) substrate. Generally Am-Si substrates are used to create single panel LCD's where each pixel is made up of side by side sub pixels (one sub pixel for each of the primary colours, as seen in Figure 3.2 (a)). The side by side pixel structure results in poor image quality in terms of the "pixelisation" which will be discussed further in a subsequent section. Poly-Si LCD's allow the creation of physically smaller LCD panels and provide improved "Screen Door Effect" (SDE). Due to slow liquid crystal response time and the monochromatic nature of Poly-Si LCD panels, Poly-Si LCD's are operated in a three panel mode as seen in Figure 3.2 (b) [132]. Dichroic mirrors are used to separate a white light source into it's primary components. The primary colours are then passed through three individual LCD panels and the modulated primary light components are then carefully recombined using a specialised prism as to produce a colour image.

3.3.2 Digital Light Processing (DLP)

Digital Light Processing is a reflective projection technology that combines a microeletromechanical system (MEMS) and projection display through the Digital Micromirror Device (DMD) microchip. The specialised microchip is composed of a MEMS array of semiconductor-based digital light switches that precisely control a light source. The digital light switches in a DMD chip are in fact tiny 16 x 16 μm mirrors (see Figure 3.3 (a)) hinged such that each can tilt between two states; +10 degrees as to reflect light towards the projection aperture and -10 degrees as to reflect light away from the aperture, as seen in Figure 3.3 (b). To produce the effect of a greyscale image a temporal binary pulsewidth modulation technique is utilised whereby the mirrors / pixels are switched on and off at high speed. The mirrors / pixels are capable of switching on and off more than 1000 times a second and hence the DMD chip is capable of producing numerous different shades of grey, pending of how long the mirror / pixel is in the "*on*" state relative to the "*off*" [133].

DLP projectors can be categorised as either single, two or three chip systems. The differentiation is derived from how the projector produces colour images. The single chip uses a colour filter composed of the three primary colours, Red, Green and Blue (RGB) and an additional clear segment is incorporated to boost the overall brightness of the projected image. Figure 3.3 (c) shows a schematic of a typical single chip system. A condenser lens collects light from the metal halide light source and focuses the light onto the colour wheel. The filtered light then passes through further projection optics directing the light onto the surface of the DMD chip. Single chip DLP projected images can suffer from colour breakup, a visible colour artifact more commonly known as the "rainbow effect". To somewhat alleviate this problem TI have developed the "DDR" chip. Single chip DDR DLP projectors utilise a six-segment colour wheel hence doubling the colour refresh rate and thus reducing colour breakup. The two chip arrangement makes use of a similar rotating colour wheel process however, uses dichroic mirrors to separate the spectral content of the light source. A single DMD chip is solely used to process one colour component and another chip along with a rotating colour filter is dedicated to the two remaining colours. The decision on which colour goes exclusively to one chip is based on the spectral content of the illumination source [133]. The three chip variation

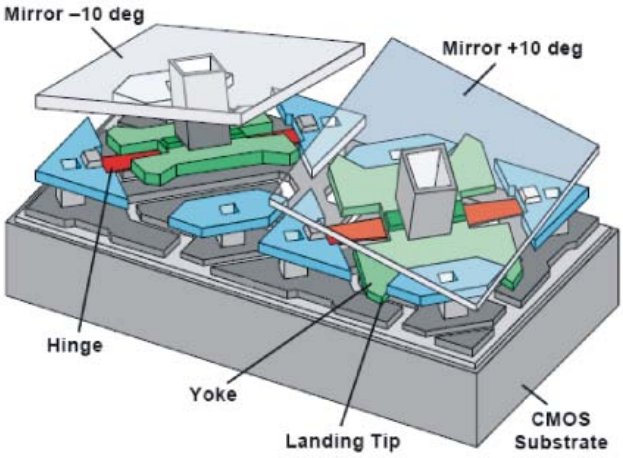

(a)

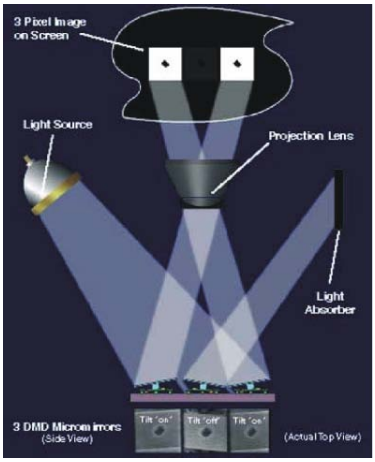

(b)

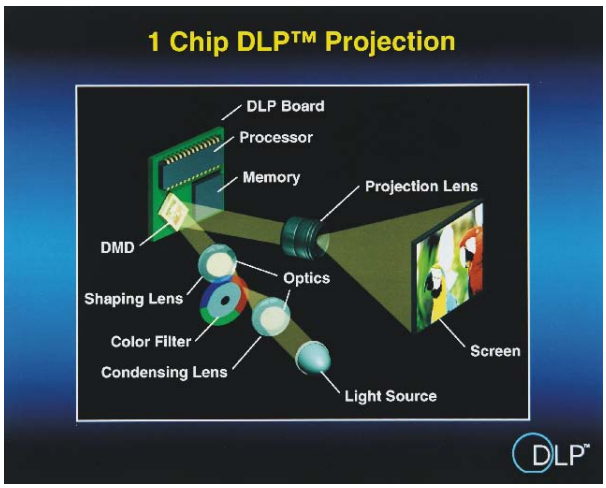

(c)

Figure 3.3: (a) Two Digital Micromirror Device (DMD) Pixels (note mirrors are shown as transparent) [134]. (b) Digital Micromirror Device (DMD) functionality [133]. (c) Example of a single chip DLP projection system [135]. Colour is incorporated into the image using a rotating colour wheel composed of the three primary colour components and an additional clear segment to boost the overall brightness of the projected image.

of the DLP projector is by far the most costly and is generally reserved for industrial applications such as Digital Cinema. Much like a three-panel LCD configuration, the three chip system utilises dichroic mirrors to separate the primary colour components and each component is dedicated its own DMD chip. Such DLP arrangements are capable of producing over 35 trillion different possible colours.

The choice of the number of DLP chips in a DLP projector is a tradeoff between cost, light efficiency, power dissipation, weight and volume [134]. In terms of triangulation based Fringe Projection profilometers, only systems based on single chip DLP projectors have been reported.

3.4 Digital Video Projection Signal Characteristics

Despite the variation of DVP technology, digitally projected signals can be characterised by a number of common observable attributes. Perhaps the most obvious characteristic of a digitally projected signal is the finite or discrete-like intensity distribution of the projected image, otherwise referred to as pixelisation. Closely related to the finite nature of the projected signal is the SDE referring to the amount of light the digital SLM elements of the projection source can actively modulate. Supplementary to the physical limitations of the digitally generated image, a number of signal preprocessing stages, inadvertently compromise the geometrical precision of the projected signal. These characteristics of the DVP signal ultimately influence the quality of the captured fringe image and accordingly the estimation of the $\Delta\phi(x, y)$ and therefore $h(x, y)$. The primary objective of this section is to outline and identify the key aspects of the digitally projected signal.

3.4.1 Finite Projection

As with any digital signal the digitally projected pattern is sampled and quantised. The intensity distribution can be defined by pixels and each pixel is confined to a finite set of intensity values. When the signal is projected onto any diffuse surface the intensity distribution can be characterised primarily by the projection source, projection surface and the surface's distance from the projector. Aspects such as projector resolution, focus, projection angle, distance from the projector and object gradient can be used to mathematically

describe the pixel deformation and hence intensity distribution. For Fringe Projection systems utilising DVP, the lack of spatial density in the projected intensity distribution results in limiting the spatial resolution over the spatial range of one projected pixel in both the x and y directions.

The important issue of limited spatial accuracy in DVP applications was first recognised by Huntley and Saldner [136] in their analysis of temporal phase unwrapping, a technique well suited to digital projection due to the associated flexibility in fringe map production. The finite spatial resolution issue was later revisited again by Coggrave and Huntley in [137], where they proposed a defocusing optimisation scheme to improve the spatial accuracy of their Fringe Projection arrangement.

Since the spatial resolution of a DVP based profilometer is limited to the spatial size of a projected pixel, the ability to describe the projected intensity distribution mathematically provides the capability to describe the system's spatial accuracy. Hence we develop a mathematical derivation to assist in the prediction and understanding of the spatial accuracy of DVP based structured light profilometers, however, prior to detailing the finite projection derivation it is important to outline the physical projection constraint commonly referred to as the "Screen Door Effect" (SDE).

3.4.1.1 Screen Door Effect (SDE)

Closely related to the finite projection characteristics of the digital projection is the tiny discontinuities that exist between pixels. This phenomenon is referred to as the "Screen Door Effect" (SDE) and is clearly seen in Figures 3.4 (a) and (b). The severity of this effect is measured by the fill factor, this measure defines the amount of area a Liquid Crystal or mirror on a DMD chip can actively modulate light to create a projected image. DLP projectors offer a fill factor up to 90% whilst an equivalent LCD projector can only yield at best a 70% fill factor [133]. Much emphasis has been placed on reducing SDE in LCD devices, Robinson *et al.* outline these developments in [132]. The discontinuities result from the small physical displacement between individual SLM elements. In the case of a DLP projector, the spatial separation between mirrors on the DMD chip, for single panel LCD, the displacement of Liquid Crystal sub-pixel structures, while for three panel LCD's, the black matrix TFT element shielding structures.

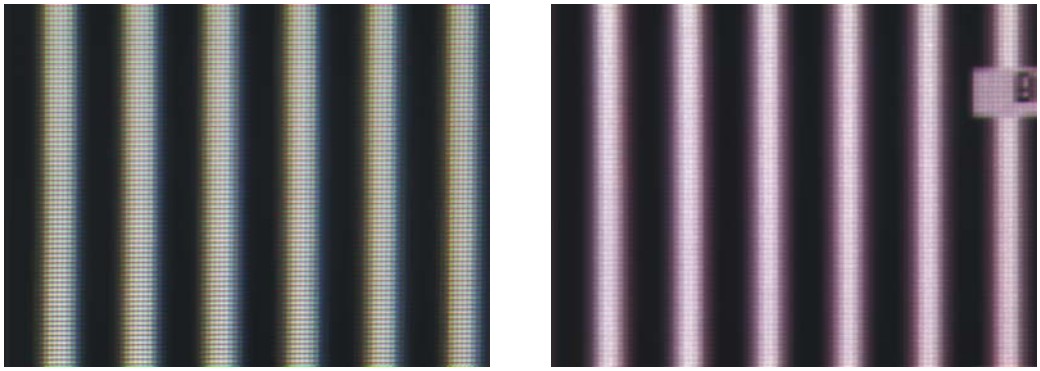

(a) LCD Screen Door Effect (b) DLP Screen Door Effect

Figure 3.4: The "Screen Door Effect" (SDE), tiny discontinuities in the digitally projected intensity distribution. Both (a) LCD and (b) DLP photos were taken under the same conditions with each projector being of identical resolution and optimised for focus and contrast.

Since these discontinuities cannot offer information about the projection surface, the accuracy of the system is inadvertently affected, hence, to alleviate this problem a high resolution projection source should be utilised for applications requiring high accuracy.

3.4.1.2 Spatial Resolution Analysis

In order to analyse the digital projection characteristics of the DVP system some assumptions about the projection source and system features are made. In this analysis we assume that the projector is adequately focused over the range of interest, the angle subtended by any one pixel is the same, the gradient of the object is constant over the range of one pixel and we also assume a fill factor of 100% henceforth neglecting the SDE. Referring to Figure 3.5 and noting that l_0 is as defined in the geometric arrangement and the projection angle as defined by β is known, it is possible to find l_1, the ray formed by the first pixel in the projection field.

$$l_1 = \frac{l_0}{\sin(\pi - \beta)} \tag{3.1}$$

Since it is assumed that each pixel subtends at angle α it is possible to determine $\angle E_p QO$ as

$$\angle E_p QO = \pi - (\alpha + \beta) \tag{3.2}$$

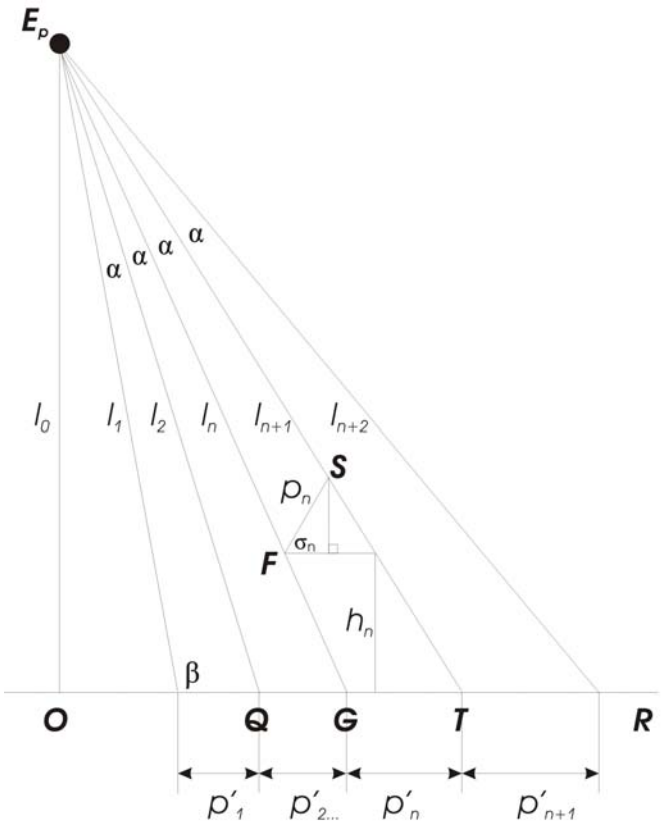

Figure 3.5: Finite Projection Characteristic

and hence using the sine rule l_2 can be found to be

$$\frac{l_2}{\sin\beta} = \frac{l_1}{\sin\angle E_pQO}$$

$$l_2 = \frac{l_1\sin\beta}{\sin(\pi-\alpha-\beta)} \tag{3.3}$$

noting that $\angle E_pQG$ and $\angle E_PGQ$ can be given as

$$\angle E_pQG = \alpha+\beta \tag{3.4}$$

and

$$\angle E_pGQ = \pi-(2\alpha+\beta) \tag{3.5}$$

respectively. Following this the n^{th} equivalent is realised to be

$$l_n = \frac{l_{n-1}\sin[\beta+(n-2)\alpha]}{\sin[\pi-\beta-(n-1)\alpha]}$$

$$\text{for } n=2 \rightarrow \text{resolution} \tag{3.6}$$

where the n^{th} equivalent angles $\angle E_pGT$ and $\angle E_pTG$ are

$$\angle E_pGT = (n-1)\alpha+\beta \tag{3.7}$$

and

$$\angle E_pTG = \pi-(n\alpha+\beta) \tag{3.8}$$

respectively and where *resolution* refers to the resolution of the digital projector in the x direction. Next the distance $\overline{FG}$ is calculated as follows

$$\overline{FG} = \frac{h_n}{\cos[\beta+(n-1)\alpha-\pi/2]} \tag{3.9}$$

and hence $\overline{E_pF}$ can be found to be

$$\overline{E_pF} = l_n - \frac{h_n}{\cos[\beta+(n-1)\alpha-\pi/2]} \tag{3.10}$$

Since $\angle E_pGT$ and ϕ_n are known $\angle E_pSF$ can be found to be

$$\angle E_pSF = \pi-\beta-(\alpha n-\phi_n) \tag{3.11}$$

and consequently utilising the sine rule p_n can be determined as

$$p_n = \left[\frac{\overline{E_pF}\sin(\alpha)}{\sin(\angle E_pSF)} \right] \tag{3.12}$$

As spatial distance AC is only measured in the x direction we can give the size of the n^{th} pixel in the x plane, p_{n_x}, as follows:

$$p_{n_x} = \left[\frac{\overline{E_pF}\sin(\alpha)}{\sin(\angle E_pSF)} \right] \cos(\phi_n) \tag{3.13}$$

Now substituting Equations (3.10) and (3.11) into Equation (3.13) we can obtain

$$p_{n_x} = \left[\frac{\left(l_n - \dfrac{h_n}{\cos(\beta + (n-1)\alpha - \pi/2)} \right) \sin(\alpha)}{\sin(\pi - \beta - (\alpha n - \phi_n))} \right] \cos(\phi_n) \tag{3.14}$$

where

$$l_n = \frac{l_{n-1}\sin(\beta + (n-2)\alpha)}{\sin(\pi - \beta - (n-1)\alpha)} \quad \text{for } n = 2 \rightarrow \text{resolution}$$

$$l_1 = \frac{l_0}{\sin(\pi - \beta)}$$

To demonstrate the pixel size and hence spatial accuracy variation, the model is used to predict the pixel size variation for an example situation where a pattern is projected onto a reference plane object with model parameters $l_0 = 2000$mm, $\beta = \frac{\pi}{2}$ and $\alpha = 4.06\text{x}10^{-4}$ (measured empirically). The model estimation of pixel size variation is depicted in Figure 3.6.

The practical applicability of this analytical model is assessed in Appendix A.

3.4.2 Projected Signal Geometric Structure

Regardless of the physical constraints imposed on the digitally projected structured light image, the geometrical structure of the projected signal is further compromised by systematic limitation. The most prominent systematic limitation associated with DVP is the non-linear camera / projection luminance response. Commonly, the nonlinear luminance associated with DVP is referred to as Gamma distortion. Gamma distortion is typical in visual display systems to enhance human perception of the sensation of *lightness*, which

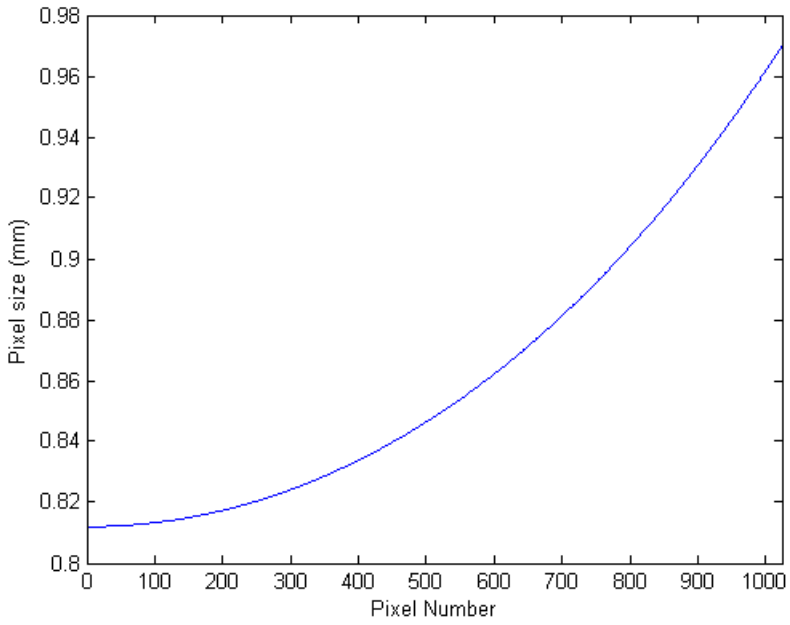

Figure 3.6: Projected Pixel Size Variation in the x direction

can be regarded as a power function of intensity [138]. In general, the gamma distortion of a digital display can be modeled using the simple power function seen in Equation (3.15)

$$w(x,y) = u(x,y)^{\gamma}, \quad \text{for } u \in [0,1] \tag{3.15}$$

where $u(x,y)$ is the normalised image delivered to the display device, $w(x,y)$ is the actual normalised image output intensity distribution and γ is typically a fractional value $1 < \gamma < 3$ specific to the display system.

The typical camera / projector intensity response curve is shown in Figure 3.7 for three distinct values of γ i.e. $\gamma = 1, 2$ and 3. Ideally, to generate a signal in software and reproduce the same signal at the detector, entails the camera / projector intensity response γ value is 1 (or very close to it) and hence a linear relationship as shown in the Figure. In practice achieving a linear camera / projector response is a non-trivial task considering the overall γ of the projection system is typically not only a function inherent to the projector itself but also of the video card driving the projector and furthermore can present dynamic attributes. To visually demonstrate the effect the non-linear camera / projector response

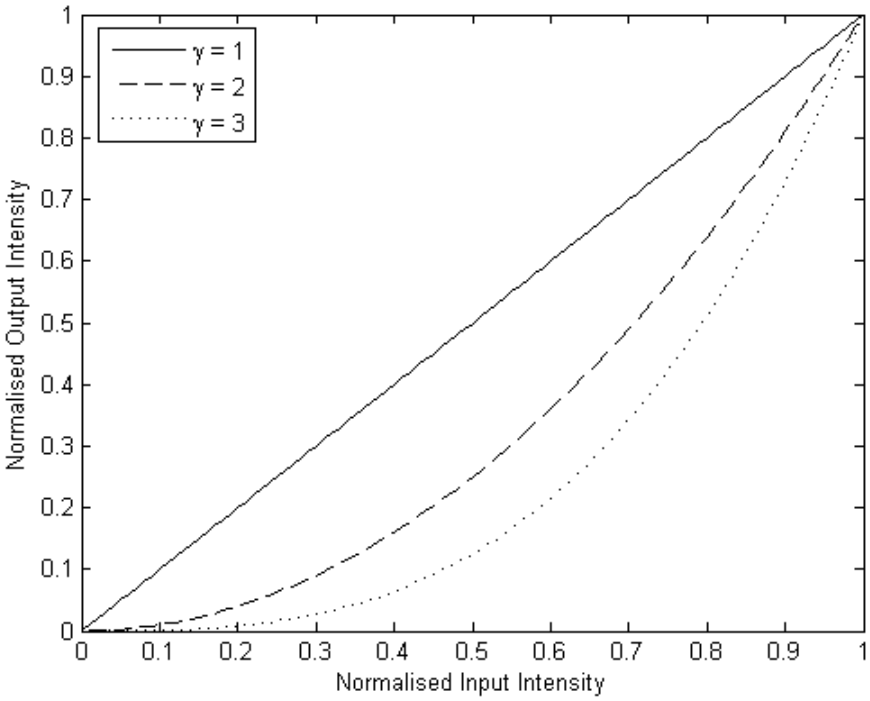

Figure 3.7: Camera / Projector Intensity Response for various γ

poses for Fringe Projection we simulate three sinusoidal cross-sections for the previously depicted camera / projector intensity responses shown in Figure 3.7, and plot them in Figure 3.8. As can be observed the larger the non-linearity of the intensity response the larger the deviation from a true sinusoidal fringe.

3.5 Colour Projection

An interesting and very desirable attribute of DVP supplementary to high speed projection and software control is the ability to project colour images. The projection of coloured images provides a useful way of encoding additional information into a projected fringe, and thereby increasing data acquisition speed. For a typical DVP application, by utilising the Red, Green and Blue (RGB) channels of the projection source, data acquisition can be increased by a factor of three relative to an equivalent single channel system, henceforth, making such multi-channel implementations suitable for dynamic applications. The multi-channel approach is primarily exploited in conjunction with 3 Step Phase Measuring approaches (as detailed in Section 2.4.1) given that all 3 required images can be ob-

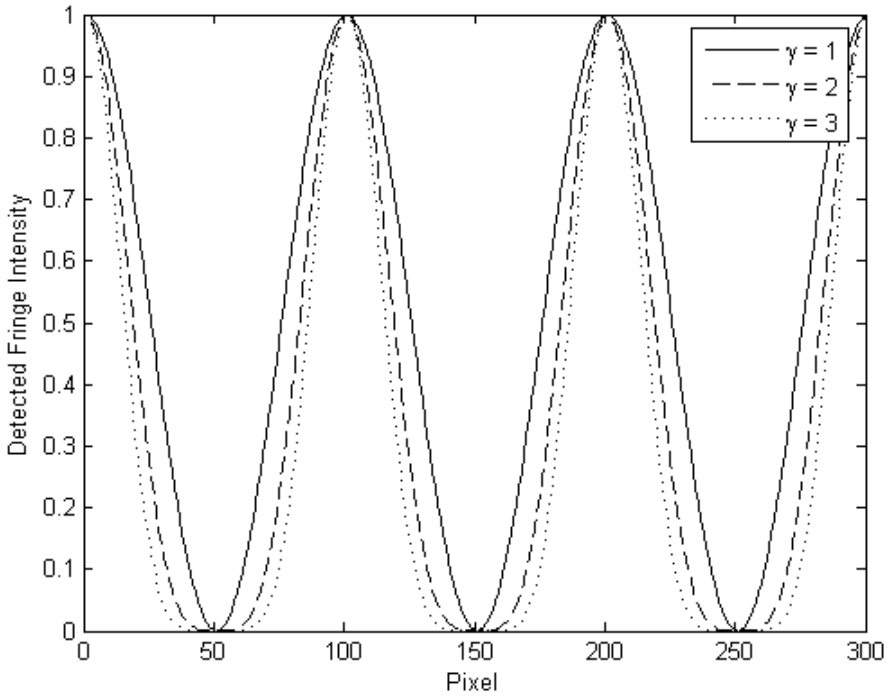

Figure 3.8: Distorted Fringe Cross-section

tained in a single exposure. An example of such is the work of Huang *et al.* [88] who proposed a colour-encoded digital fringe projection technique for high speed 3D surface profiling. The proposed system utilised the RGB colour channels of a DLP video projector to project three phase shifted images onto the measurement scene. The three individual phase maps were captured in one image, decomposed using a linear separation technique and a PMP fringe processing approach was used to reconstruct the object.

Contrary to the traditional 3 Step colour fringe projection technique some other interesting colour projection examples have also been investigated. One example includes the work of Skydan *et al.* [95] where a multi-channel multi-projector technique was utilised to profile human body shape. The system made use of two or possibly three projectors each projecting an individual primary colour phase map, imaged with a single CCD camera. The captured phase maps were processed individually using a FTP method and the individual reconstructions were accurately mapped together into the final reconstruction. A further example is the work of Kinell [139] who developed a multi-channel temporal phase unwrapping technique. This system utilised the three colour channels of a video projector to project a short sequence of phase stepped images which were acquired

sequentially in time and processed using a variation of the temporal phase unwrapping scheme.

The primary requisite for all multi-channel Fringe Projection implementations is that the fringe data contained within each colour channel can be effectively distinguished from one another. In practice this is not often the case due to a phenomenon referred to as colour cross-talk or colour channel leakage. The colour channel leakage is consequential of the spectral characteristics of the dichroic process utilised to produce colour in video projectors. This leakage or cross-talk often significantly inhibits the performance of multi-channel approaches. The aim of this section is to briefly outline colour theory and moreover the issue of colour-crosstalk.

3.5.1 Colour Theory

Colour refers to the human perception of the various wavelengths of electromagnetic radiation present over the range of visible wavelengths otherwise referred to as the visible spectrum of light. The visible spectrum of light ranges from approximately 370nm to 730nm. The electromagnetic spectrum including the visible spectrum is depicted in Figure 3.9. The sensation of colour is derived from the physiological attributes of the human visual system which has ultimately shaped the way in which colour is measured, represented and generated. Cone-like structures referred to as “retinal cones” located at the rear of the human eye are primarily responsible for the generation of the appropriate chemical stimuli and therefore conveyance of neural signalling to represent the appropriate wavelength of visible electromagnetic radiation to the brain. The three cone types of the retina detect electromagnetic radiation within overlapping wavelength bands associated with the sensation of primary colours Red, Green and Blue as depicted in Figure 3.10. Since coloured light can be represented as a spectral distribution, where power is plotted as a function of wavelength, the cones convert the spectral stimuli to three cone response values. These values are defined by integrating the product of each of the spectral sensitivity curves and the incoming colour spectrum [140]. Following this the two rudimentary principles of colorimetry; Trichromacy and Metamerism can be defined. Trichromacy refers to transformation of any spectra to just three values without loss of information with respect to the visual system, while Metamerism infers that any spectra that creates

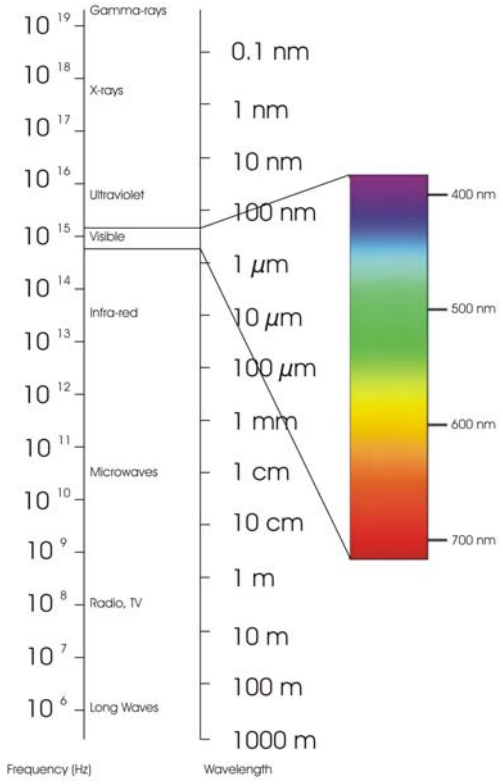

Figure 3.9: Electromagnetic Spectrum

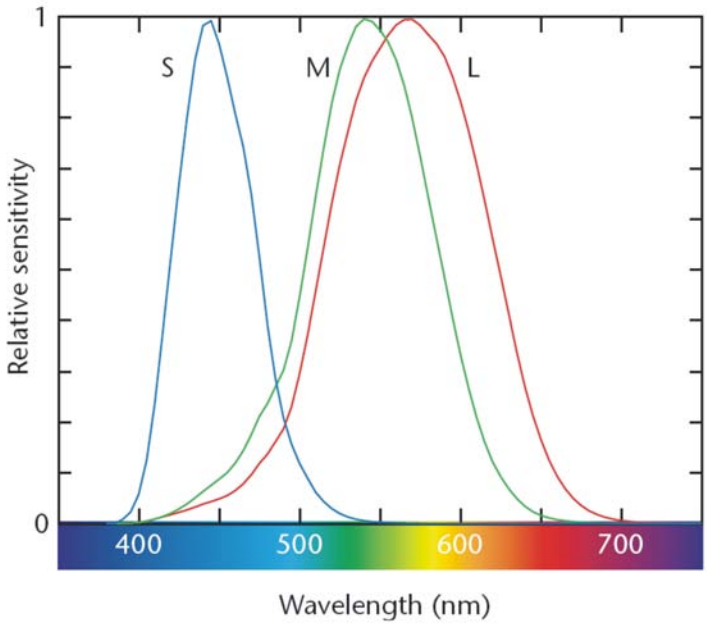

Figure 3.10: Spectral sensitivity curves for the short, medium and long cones [140]

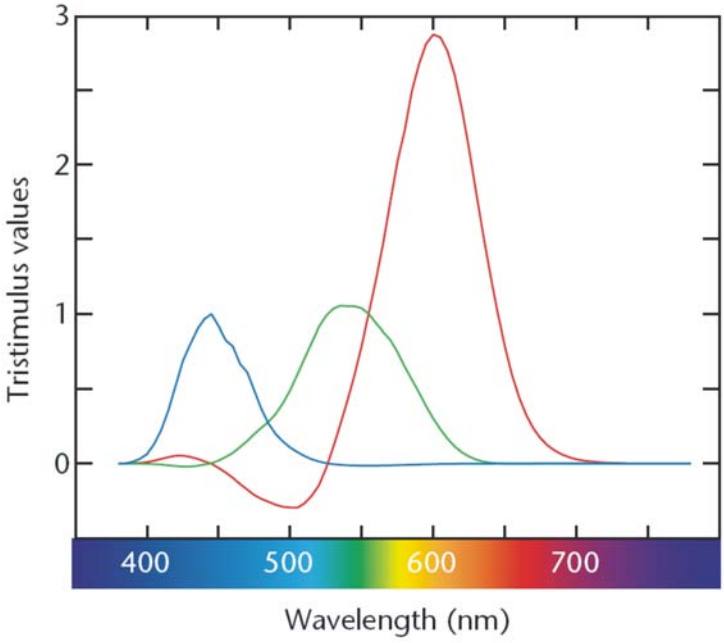

Figure 3.11: Colour Matching Functions [140]

the same trichromatic response are indistinguishable [140].

Directly as a result of the physiological attributes of the human perception of colour, colour matching experimentation can be developed whereby, a human observer can match a designated reference colour by mixing adjustable amounts of three narrow bandwidth primaries. The objective of the colour matching experimentation is to determine 3 colour matching functions such as depicted in Figure 3.11. The values of the colour matching functions are referred to as tristimulus values which identify the relative amounts of each primary as a function of the wavelength of electromagnetic radiation. An important observation to note in regard to Figure 3.11 is the negative contribution of the red primary. Negative contributions are derived from the inability to match a given reference colour without having to shine a further amount of primary (in this case red) onto the reference colour to make an appropriate match.

The body responsible for standardising colour measurement and generation known as Commission Internationale de l'Eclairage (CIE) specify a standard set of primaries referred to as *X*, *Y* and *Z*. The standardised colour matching functions, $\bar{x}(\lambda)$, $\bar{y}(\lambda)$ and $\bar{z}(\lambda)$ are shown in Figure 3.12. The CIE colour matching functions are mathematical functions derived from extensive colour matching empirical data [140]. One important

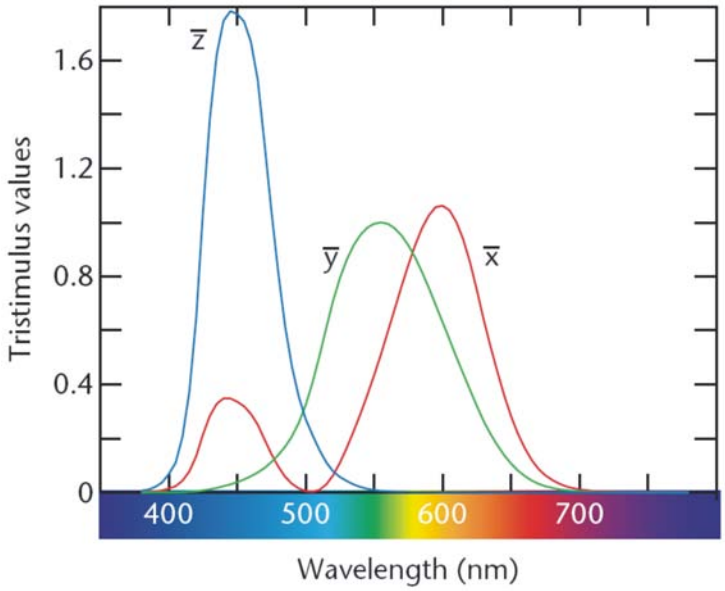

Figure 3.12: CIE Colour Matching Functions [140]

feature to note about the standard CIE colour matching functions is that the tristimulus values are all positive and therefore can be practically implemented in actual dichroic filters. Therefore mathematically to represent a spectrum $S(\lambda)$ using the standard CIE primaries we have

$$X = k \int_{-\infty}^{\infty} S(\lambda).\bar{x}d\lambda$$

$$Y = k \int_{-\infty}^{\infty} S(\lambda).\bar{y}d\lambda$$

$$Z = k \int_{-\infty}^{\infty} S(\lambda).\bar{z}d\lambda \tag{3.16}$$

where constant k is given by

$$k = \frac{100}{\int_{-\infty}^{\infty} S_W(\lambda).\bar{y}d\lambda} \tag{3.17}$$

and is used to normalise the primaries to a standard white light spectral distribution $S_W(\lambda)$.

Referring now to colour reproduction in devices such as computer controlled peripherals (Monitors, Projectors etc), colour models facilitate convenient mathematical representation of colour. The model most exploited in computing applications is the RGB model

which represents a 3D cartesian co-ordinate unit cube. Each of the three axes of the co-ordinate system represent one of the three primaries with the main diagonal of the cube representing the greyscale. The RGB colour model enables computer control of colour capable devices designed in compliance with the CIE specification and can therefore accurately reproduce an appropriate system gamut. The transformation from RGB to the CIE XYZ standardisation requires only a simple linear transform as shown in Equation 3.18 [140].

$$[R,G,B]M = [X,Y,Z]$$

where

$$M = \begin{bmatrix} X_R & Y_R & Z_R \\ X_G & Y_G & Z_G \\ X_B & Y_B & Z_B \end{bmatrix} \tag{3.18}$$

3.5.2 Coupling of Colour Channels

The generation of colour in any digital projection display device involves the use of dichroism. Typically, dichroic filters or prisms are used to separate a white light source into it's primary components, by transmitting or reflecting the appropriate wavelengths of light, and therefore, producing the sensation referred to as colour. As previously specified in Section 3.5.1 since coloured light can be regarded as a spectral distribution where power is a function of wavelength, through the trichromacy and metamerism principles, a projection device can produce controlled colour by adding weighted spectral distributions obtained from the dichroic separation of the white light source within the projector. Therefore, from a software perspective the appropriate colour model, namely RGB, is required to link the tristimulus values and the desired colour response.

As can be seen in Figure 3.12 the spectral distribution of each of the CIE specified defined primaries are typically non-zero over common intervals. In other words, overlaps in the spectra exists for each of the primary sources for common values of λ. As a result colour leaks to and from each of the primaries, the phenomenon is often referred to as coupling of colour channels. Furthermore, the dichroic optics responsible for the representation of colour within the capture device also incurs additional overlapping and

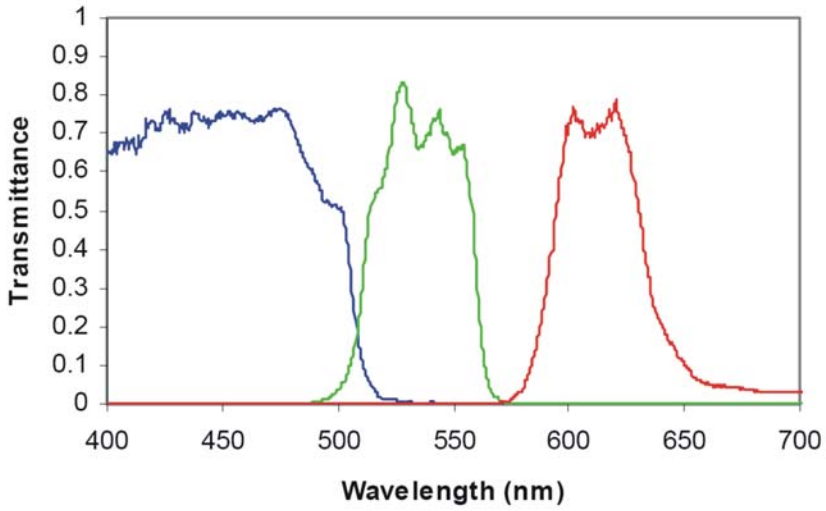

Figure 3.13: CCD Filter response [141]

further heightens the colour channel coupling. The typical filter response for a 3-CCD camera is shown in Figure 3.13 [141].

For the projection / acquisition of multi-channel fringe images for phase measuring approaches where accurate isolation of phase shifted sequential fringes is critical, the coupling of colour channels significantly impacts performance. The coupling of colour channels becomes of further concern given each channel has its own individual Display Gamma response introducing further fringe distortion. These non-linearities were somewhat confused in Hu *et al.*'s [142] initial analysis of the coupling problem. Nevertheless, assuming the spectra overlap is constant for both the acquisition and projection stages, the leakage is predictable and can be modeled as

$$\begin{pmatrix} r(\hat{x},y) \\ g(\hat{x},y) \\ b(\hat{x},y) \end{pmatrix} = \begin{pmatrix} 1 & k_{GR} & k_{BR} \\ k_{RG} & 1 & k_{BG} \\ k_{RB} & k_{GB} & 1 \end{pmatrix} \cdot \begin{pmatrix} r(x,y) \\ g(x,y) \\ b(x,y) \end{pmatrix} \tag{3.19}$$

where $r(\hat{x},y)$, $g(\hat{x},y)$ and $b(\hat{x},y)$ represent the signals obtained at the respective colour CCD sensors of the acquisition device, k_{XY} represents the normalised proportion of colour coupling between the appropriate channels and $r(x,y)$, $g(x,y)$ and $b(x,y)$ correspond to the actual intended spectral distributions prior to projection. This linear approximation was later confirmed by Hu *et al.*'s [142] work.

3.6 DLP Vs. LCD

So far the emphasis of the work presented in this chapter has been centered on the presentation of the key attributes of DVP, the functionality of the two most exploited DVP technologies and more specifically the nature of the projected fringe signal for both single and multi-channel implementations. With the aid of this insight the integrity of the application of the two most exploited DVP technologies for Fringe Projection 3D sensing can now be assessed. Prior to this research the generic advantages and disadvantages of the two DVP technologies had been extensively reviewed amongst DVP developing communities [132, 133, 134] and in particular within the home theater community for which represent the majority market share for the development of the projection technology. However, the impact these advantages and disadvantages have on the performance of a Fringe Projection 3D sensor system for each technology had yet to be analysed. In this section we outline the empirical process undertaken to contrast the two chief DVP technologies from the specific viewpoint of their application for Fringe Projection 3D sensing.

3.6.1 Empirical Procedure

In order to evaluate the effectiveness of either DVP technology as a suitable source for Fringe Projection 3D sensing the two technologies are compared in terms of the previously outlined digital projection attributes, namely, signal geometric structure and coupling of colour channels. The method by which the various projection deficiencies are compared is centered on the traditional 3 Step PMP fringe processing method (as described in Section 2.4.1.1) and a novel artificial phase emulation approach. The 3 Step variation was selected for two key reasons; firstly, the 3 Step variation is the most sensitive stepping variation of the PMP algorithm to most forms of error, including harmonic distortion and phase shifting errors [143] and therefore has the ability to provide an accurate indication of projected signal geometric structure deficiencies. And secondly, the most exploited multi-channel approaches employ the 3 Step variation since all three fringe images can be obtained in a single exposure, thereby making the 3 Step variation a good benchmark for testing the colour cross-talk deficiencies of each projection technology.

Furthermore, the 3 Step variation has been employed by many recently developed dynamic 3D profiling systems since a 3D phasemap can be determined with minimum data requirements.

The novel phase emulation technique aims to eliminate the effects of additional phenomena such as object reflectivity and also reduce data requirements by artificially introducing an arbitrary phase modulation into actual fringe data in software. Three software defined reference fringe images

$$g_{0n} = 0.5 + 0.5\cos(2\pi f_0 x + \zeta_n)$$

where

$$\zeta_n = 2\pi n/3;$$

for n=0,1,2, (3.20)

are projected and acquired by utilising the physical arrangement described in Appendix B. Following the acquisition of the three reference fringes now denoted as $\hat{g}_{0n}(x,y)$ to signify the distortion introduced by the projection / capture system, the magnitude and phase components, $|\hat{G}_{0n}(k)|$ and $\angle\hat{G}_{0n}(k)$, of each of the captured signals is obtained. Both $|\hat{G}_{0n}(k)|$ and $\angle\hat{G}_{0n}(k)$ are calculated by performing a one dimensional Fourier Transform operation on signals, $\hat{g}_{0n}(x,y)$, with respect to x. The arbitrary phase distribution $\phi(x,y)$ along with the corresponding magnitude and phase components were then utilised in an Inverse Fourier Transform operation to reconstruct three phase modulated images to emulate the reference fringe images projected onto an arbitrary surface as follows

$$\hat{g}_n(x,y) = \frac{1}{N}\sum_{x=0}^{N-1} |\hat{G}_{0n}(k)| e^{[j(2\pi kx)/N + j(\angle\hat{G}_{0n}(k) + \frac{k}{f_0}\phi(x,y))]}$$

for k=0,1,2,...,N-1, (3.21)

where N in this case refers to the number of points the Discrete Fourier Transform (DFT) operation is taken over. A cross-section, $\phi(x)$, of the phase distribution $\phi(x,y)$ utilise throughout the LCD DLP experimental analysis is shown for reference in Figure 3.14.

In total six projectors were tested, three LCD projectors and three DLP projectors. For each of the six projectors the fringe sequences as described by Equations (3.20) and (3.21) were obtained and the 3 Step PMP technique was utilised to recover, $\hat{\phi}(x,y)$, an estimation of arbitrary phase distribution $\phi(x,y)$. By way of the arbitrary phase emulation

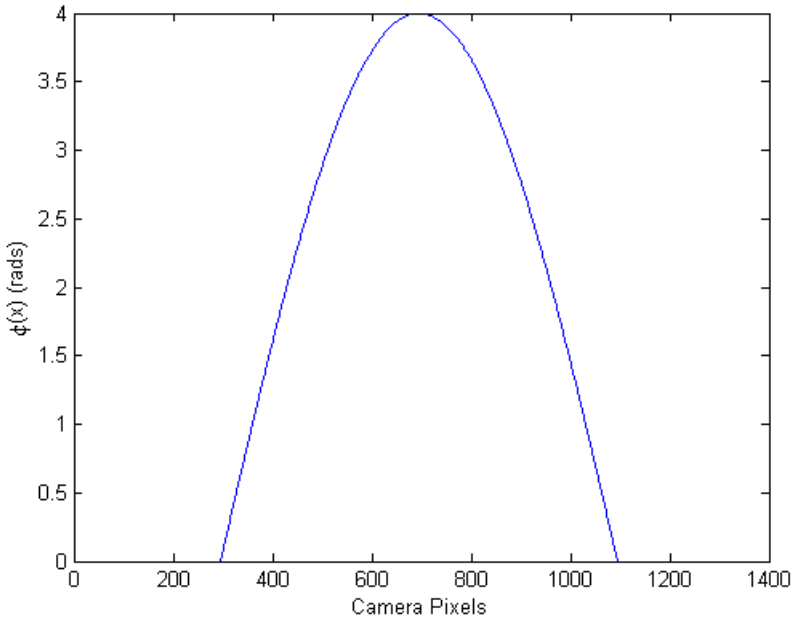

Figure 3.14: Arbitrary Phase Distribution $\phi(x)$

approach an error phase residual, $\varepsilon(x, y)$, where

$$\varepsilon(x, y) = |\phi(x, y) - \hat{\phi}(x, y)|, \tag{3.22}$$

could be established and therefore aid in the evaluation of both projection technologies.

Since the mathematics involved in obtaining estimation $\hat{\phi}(x, y)$ assume that a sinusoidal intensity distribution is captured, the performance of the phase measurement is not only dependent on the projection device but also the capture device. Therefore, to adequately assess the integrity of either DVP technology a quality capture device is essential. The capture device used for this work is the DuncanTech MS3100 digital multispectral camera. The camera is based on a color separating prism with three imaging channels that allow simultaneous image acquisition through a common aperture. Image sensors are CCD array sensors, each with a resolution of 1392 x 1040 pixels. These attributes result in high quality capture of projected fringe pattern intensity distributions and high colour fidelity makes the camera ideal for both greyscale and colour applications. Further reference to the specification of the physical Fringe Projection arrangement is outlined in Appendix B.

		Low Frequency		High Frequency	
Projector Type	Technology	Average Error (rads)	Std (rads)	Average Error (rads)	Std (rads)
Epson EMP730	LCD Poly-Si TFT 0.9”	0.3626	0.2772	0.2531	0.1960
SONY VPL-CX10	LCD Poly-Si 0.9”	0.3219	0.2120	0.2126	0.1604
SONY VPL-CS5	LCD Poly-Si TFT 0.7”	0.3668	0.2850	0.2568	0.1991
InFocus LP530	DLP 0.7” +/-12 DDR	0.4052	0.3200	0.3231	0.2495
NEC LT220	DLP 0.7” +/- 10 SDR	0.4039	0.3317	0.3175	0.2427
BENQ PB6210	DLP 0.7” +/-12 DDR	0.4714	0.3686	0.3612	0.2732

Table 3.1: Greyscale reconstruction average phase errors and standard deviations

3.6.2 Results and Discussion

3.6.2.1 Single Channel

For the six given projectors both a low and high frequency greyscale fringe pattern corresponding to 12 and 29 spatial periods spanning across the entire measurement scene, respectively, were projected onto a reference plane. The captured images were processed using the PMP algorithm and phase emulation technique detailed in the previous section and the projectors contrast in terms of average phase residual, $\varepsilon(x, y)$, and standard deviation. Table 3.1 displays the results of the empirical findings while Figure 3.15 displays cross-sections of the reconstructed phase maps for both a single DLP and LCD projector for both low and high frequency cases, respectively, with the actual phase depicted in red.

The single channel scenario allows the assessment of two key limitations as discussed in Section 3.4; i.e. finite projection and the geometric structure of the projected signal. By simply observing the results visually depicted in Figure 3.15, the nature and source of the residual error cannot be directly established. More importantly the significance of each source / limitation cannot be evaluated. However, considering the predictions of $\phi(x, y)$ for the SVGA (800x600) resolution DLP NEC LT220 and LCD SONY VPL-CS5 projectors, relative to the other tested projectors of XGA (1024x768) resolution, further insight into these issues can be established. Given that the mean measurement error for both these projectors present no significant if any increase relative to the higher resolution

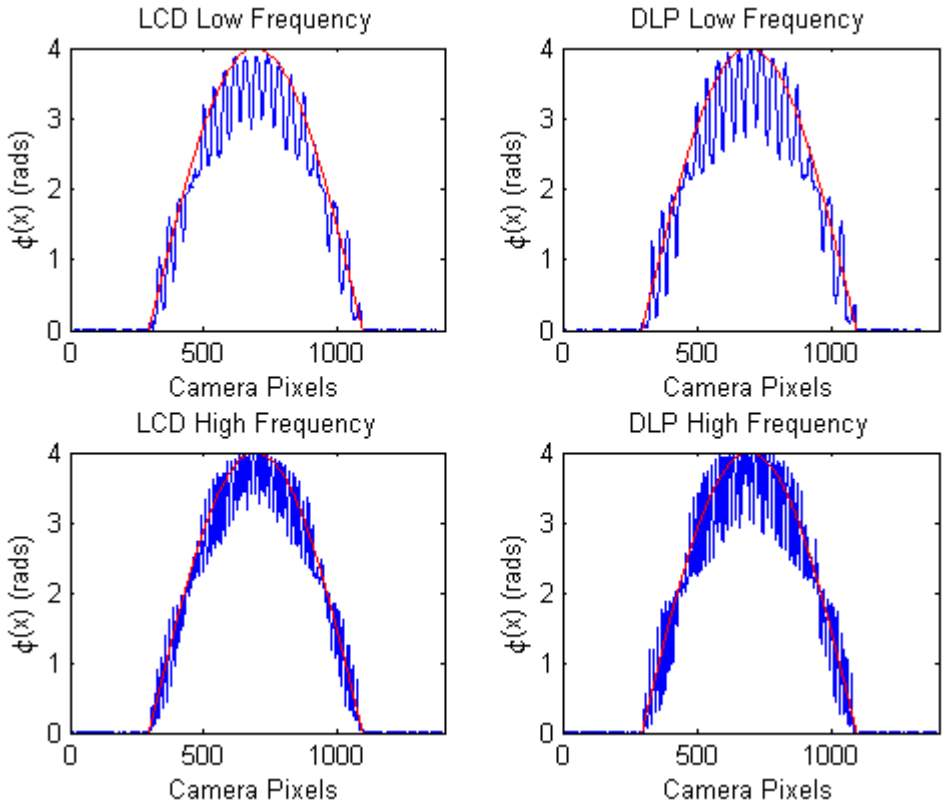

Figure 3.15: Greyscale LCD DLP sample cross-sections for both low and high frequency cases

projectors of similar technology, it can be concluded the measured phase residual error is independent of projector resolution. By this result it is revealed that the camera / projector luminance response is primarily responsible for the measurable phase residual error.

Perhaps one of the most important observations to highlight is the frequency dependence of the phase measuring residual. The phase error was significantly reduced for the high frequency case relative to the low frequency phase estimation. This phenomena was consistently observed for all projector models for both DLP and LCD projection technologies.

In general, the LCD projector's seemed to be more capable of producing more pure sinusoidal fringe signals, however, the mean phase error margin separating the poorest performing LCD projector and the best performing DLP projector was less than 0.04 radians for the low frequency scenario. If we assume system parameters l_0, d_0 and f_0 to be 2000mm, 800mm and 0.06 fringe/mm [1], respectively, and substitute the mean phase difference into Equation (2.14), the mean measurement error would equate to 0.246mm. Such a small relative mean phase error (approximately 0.01% of the measurement volume) can be considered a somewhat anticipated result considering that both projection technologies are designed and optimised for human perception of intensity and therefore would likely demonstrate similar Display Gamma characteristics as described in Section 3.4.2.

The larger mean phase measuring error for the DLP projectors may be attributed to temporal intensity characteristics as a result of the inherent nature of the DLP projection technology. In order to minimise the influence of such temporal intensity variations the integration time of each of the three CCD chips was maximised to ensure prolonged exposure. In fact, following the empirical findings and moreover the temporal nature of the single chip DLP projection technology, some interesting speculation in regard to the application of DLP projectors for high speed acquisition of dynamic fringe images can be made. Since the single chip DLP technology temporally projects each colour channel for a finite period of time, undesired temporal aspects may be captured in high speed applications where acquisition integration time is minimised. This is of particular importance

[1] f_0 estimation is based on the low frequency fringe with a field of view approximately 200mm in the x direction

		Low Frequency		High Frequency	
Projector Type	Technology	Average Crosstalk Error (rads)	Std (rads)	Average Crosstalk Error (rads)	Std (rads)
Epson EMP730	LCD Poly-Si TFT 0.9”	0.2070	0.1336	0.2153	0.1365
SONY VPL-CX10	LCD Poly-Si TFT 0.9”	0.1286	0.0884	0.1338	0.0958
SONY VPL-CS5	LCD Poly-Si TFT 0.7”	0.0506	0.0366	0.0523	0.0398
InFocus LP530	DLP 0.7” +/-12 DDR	0.4004	0.3068	0.3962	0.2966
NEC LT220	DLP 0.7” +/- 10 SDR	0.4951	0.3707	0.5292	0.3801
BENQ PB6210	DLP 0.7” +/-12 DDR	0.3217	0.2433	0.3222	0.2454

Table 3.2: Colour reconstruction average phase errors and standard deviations

considering the Display Gamma response of each colour channel is typically an individual characteristic specific to each channel. Therefore, for high speed dynamic single chip DLP fringe projection and capture it is desirable to have both projector and camera appropriately synchronised (in hardware) to avoid any temporal intensity artifacts.

3.6.2.2 Multi-Channel

To evaluate the effectiveness of the multi-channel application of DLP and LCD projection technology for Fringe Projection, a similar empirical procedure as described in Section 3.6.2.1 was employed, however, in place of the three phase shifted greyscale images all three fringes were obtained in a single exposure utilising the colour channels of each video projector. For each exposure each fringe pattern was optimised for contrast through manipulation of the corresponding CCD gain parameter via the DTControl software (the DTControl software is further detailed in Appendix B).

The amount of cross-talk in terms of phase residual was established by calculating the difference between the single and multi-channel estimations of $\phi(x, y)$. Therefore, $\varepsilon_C(x, y)$, the cross-talk residual phase measuring error is given by

$$\varepsilon_C(x, y) = |\hat{\phi}(x, y) - \hat{\phi}_C(x, y)|, \tag{3.23}$$

where $\hat{\phi}_C(x, y)$ denotes the multi-channel estimation of arbitrary phase distribution $\phi(x, y)$. The average value and standard deviation of phase residual $\varepsilon_C(x, y)$ for the six different

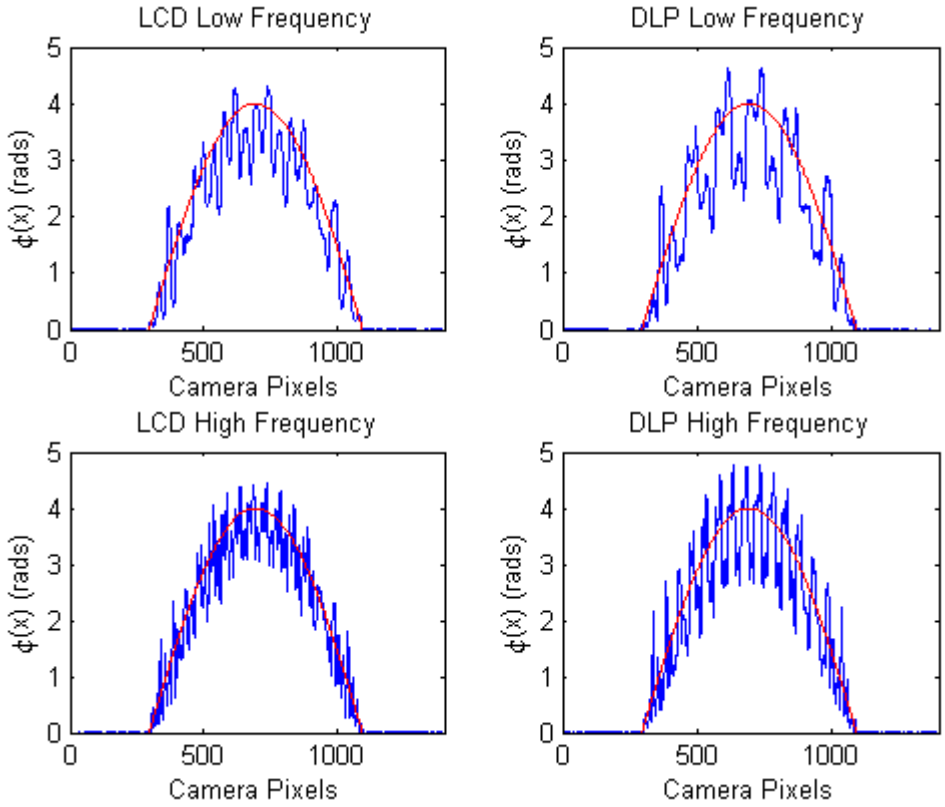

Figure 3.16: Multi-channel LCD DLP sample cross-sections for both low and high frequency cases

projectors is displayed in Table 3.2. Figure 3.16 displays cross-sections of the reconstructed phase distribution for both a LCD and DLP projector for both low and high frequency cases. The plots clearly demonstrates the additional phase measuring error associated with the colour crosstalk phenomena.

The measured crosstalk proved to be consistently lower for the LCD projectors with reference to the DLP reconstructions for both the low and high frequency scenarios with the SONY VPL-CS5 projector presenting little if any crosstalk effects in contrast to the entire array of projectors. An important observation to note is unlike the residual associated with the non-linear intensity response, the colour channel coupling phase error residual appears to be a function independent of fringe frequency, with little if any identifiable difference between low and high frequency cases.

The heighten cross-talk influence for the DLP projectors relative to the LCD projectors is likely derived from the method by which colour is manufactured in either technology. LCD projectors are typically capable of producing much more saturated colours namely due to the spinning colour-wheel technique single chip DLP projectors use to produce colour. A DLP projector using a spinning colour wheel contains a clear segment to boost the overall brightness of the projected image and hence struggle to produce highly saturated or pure colours [132] relative to an equivalent LCD projection system. A very poorly saturated colour can be deemed a shade of grey and hence in terms of the RGB colour space contain higher portions of other spectral components or primary colours. This conclusion is further confirmed by the multi-channel phase estimation for the NEC SDR projector. The DLP SDR projector utilises a first generation colour wheel resulting in a lower colour spectral sampling rate relative to the DDR projectors and as expected produces a larger measurable crosstalk phase residual error. Thus it can be concluded that DLP colour crosstalk contains both temporal and spatial artifacts where LCD projectors only suffer from spatial crosstalk as a result of dichroic colour filter design.

The DLP temporal colour generation can however render the DLP technology ideal for dynamic multichannel applications, such as demonstrated by Huang *et al.* [89]. Huang *et al.*'s work utilised the inherent temporal characteristics of the single chip DLP colour projection, to temporally project monochrome phase shifted images onto the measurement scene at high speed. The projected fringe images were captured by a video camera syn-

chronised with the projection system and were then processed by a 3 Step PMP method. An obvious shortcoming of such temporal projection methods is the acquisition speed is therefore limited by the projection speed, where an equivalent multi-channel LCD system may only be limited by the capture device, nevertheless an LCD system would have to appropriately deal with spatial crosstalk issues.

3.7 Summary

This chapter has outlined the various methods and technologies employed to create structured light for Fringe Projection 3D sensing. The major shortcomings of DVP for Fringe Projection have been identified and preliminary empirical analysis of the limitations of the projection approach have been established. Further, the empirical findings were utilised to establish insight into the effectiveness of the application of the two most exploited DVP technologies for 3D sensing by Fringe Projection. The empirical findings for the single channel case revealed the non-linear luminance effects associated with the camera / projector Display Gamma response as a dominant error source relative to the finite projection shortcomings. This result was found to be commonplace for both LCD and DLP DVP technologies. For the multi-channel case, the coupling of colour channels proved to be a significant limitation for both LCD and DLP projectors. However, it was concluded that the temporal aspects associated with the colour generation process for single chip DLP technology heightened the coupling effect. The multi-channel method was also found to suffer further as a result of Display Gamma related error, given that each individual colour channel presents an individual Display Gamma characteristic.

The significance of the Display Gamma phenomena is undoubtedly a major source of systematic limitation for the application of DVP for Fringe Projection for both single and multi-channel cases. Given the significance of the Display Gamma shortcoming, a more formal investigation into the phenomena and the influence γ has on Fringe Projection fringe processing is required. The following chapter will address these issues.

Chapter 4

Fringe Projection and Display Gamma

4.1 Introduction

Non-linear luminance is a common attribute amongst all digital and analogue display technologies. The non-linear intensity response is often referred to as Display Gamma. Display Gamma is typical in visual display systems to enhance human perception of the sensation of *lightness*, which can be regarded as a power function of intensity [138]. For Fringe Projection 3D sensors based on DVP, the nonlinear luminance effects commonplace with video projectors often significantly hinders the performance of fringe processing techniques and accordingly system accuracy. The non-linear camera / projector intensity response characterised by the display γ value and the significance of the associated limitations were somewhat demonstrated in the previous chapter.

In order for DVP based Fringe Projection to be effective, some form of gamma correction is typically required. Gamma correction for DVP based structured light profilometers was first formally identified by Guo *et al.* in [97] whereby the iterative statistical analysis of digital fringe patterns was undertaken to correct the gamma distortion in digitally projected images. Through successful identification of the projector γ value, Guo *et al.* were able to considerably reduce reconstruction errors. More common legacy solutions to counter γ non-linearities typically involve photometric fringe calibration, whereby multiple intensity distributions varying over the full range of luminance values are recorded and a camera / projector luminance curve is fitted [88, 139].

Another alternate approach proposed by Huang *et al.* [96] attempts to systematically

eliminate the gamma related phase residual using a phase shifting technique known as the Double Three Step method as outlined in Section 2.4.1.6. While the Double Three Step technique is reasonably effective at reducing the systematic display gamma limitations, Huang's empirical evaluation and following analytical investigation has somewhat misconstrued the Display Gamma problem for phase stepping approaches. More specifically Huang's evaluation of the Fringe Projection Display Gamma issue has introduced significant confusion in regard to the sensitivity of a range of popular fringe processing techniques to γ related fringe distortion.

More recently, Zhang and Yau [98] showed that the residual phase measurement error associated with the gamma distorted fringe was independent of the camera response (assuming the camera response is linear), the reflectivity of the surface and ambient light intensity and thereby, proposed a generic phase lookup table based solution. The technique was shown to be quite effective at minimising gamma related phase measuring errors, however, questionable generalisations about the true nature of the resulting phase residual were made and have fueled further need to necessitate a formal investigation into the true nature of Display Gamma related errors. More specifically, the authors claimed that the residual phase error was independent of the spatial carrier frequency based on empirical observation, and further they generalised the residual function for all fringe processing algorithms.

Such ambiguities coupled with the vital requirement for gamma fringe calibration techniques signifies the considerable influence gamma distortion has in DVP structured light profiling. However, until this point no formal analytical study investigating the magnitude of gamma related errors typical of standard projector γ has been undertaken. The performance evaluation of a number of fringe processing algorithms in the presence γ was very recently published in [143], however, this simulated analysis only surveyed a limited range of techniques more specifically applicable to Phase Shifting Interferometry applications. Further no analytical results were presented to supplement this investigation. Therefore, the requirement for a thorough analytical analysis of the influence of γ for a range of fringe processing algorithms more applicable to Fringe Projection 3D sensing is further exemplified. Some of the more notable outstanding issues to be analytically investigated include

- The spectral harmonic structure typical of a digitally projected fringe signal
- The magnitude of the harmonic distortion typical of a digitally projected fringe signal
- The nature of the resulting phase measuring residual error for a range of well exploited fringe processing algorithms and;
- The sensitivity of a range of well exploited fringe processing techniques in the presence of γ fringe distortion

Furthermore, many more practical Display Gamma Fringe Projection issues (which will be addressed in detail in Chapter 5) still remain either uninvestigated or misunderstood due to the lack of an adequate analytical framework to describe the influence of γ for projected fringes.

This chapter is primarily concerned with addressing the need for an adequate analytical framework to describe the Display Gamma phenomena for digitally projected fringes. This is undertaken by firstly providing a detailed analytical investigation into the nature of gamma distorted fringe images and, secondly, by providing an analytical survey and verification of the magnitude and nature of the resulting Display Gamma residual error for a range of fringe processing algorithms.

4.2 Modeling a γ Distorted Fringe

In general, the gamma distortion of a digital display can be modeled using the simple power function seen in Equation (3.15). Considering the Fringe Projection scenario where the projection of a sinusoidal intensity distribution is required, Equation (3.15) becomes,

$$w(x,y) = [a + b\cos(2\pi f_0 x)]^{\gamma}, \tag{4.1}$$

where f_0 is the spatial carrier frequency of the projected fringe, and a and b are constants referring to the fringe offset and contrast respectively. Clearly, if γ is a fractional value and since $\cos(x)$ is an even function, we can represent Equation (4.1) as the following Fourier Series with infinite mth order harmonic components with corresponding amplitudes c_m.

$$w(x,y) = c_0 + c_1\cos(2\pi f_0 x) + \sum_{m=2}^{\infty} c_m \cos(m[2\pi f_0 x]) \tag{4.2}$$

where

$$c_m = \frac{2}{T}\int_0^T w(x,y)\cos(m[2\pi f_0 x])dx, \tag{4.3}$$

and where T corresponds to the spatial period of the fringe image.

4.2.1 Harmonic Structure of γ Distorted Fringe

The obvious question when examining of Equations (4.1) and (4.2) is how can we relate various c_m and γ to gain further understanding of the magnitude of harmonic distortion γ introduces. To further investigate the γ harmonic phenomenon we define

$$\sum_{m=2}^{\infty}\frac{c_m}{c_1} = \frac{\sum_{m=2}^{\infty}\int_0^T w(x,y)\cos(m[2\pi f_0 x])dx}{\int_0^T w(x,y)\cos(2\pi f_0 x)dx} \tag{4.4}$$

Equation (4.4) defines a measure of the total influence of the γ distortion. If we now rewrite Equation (4.1) as

$$w(x,y) = a^{\gamma}\left[1+\frac{b}{a}\cos(2\pi f_0 x)\right]^{\gamma}, \tag{4.5}$$

Equation (4.4) becomes

$$\sum_{m=2}^{\infty}\frac{c_m}{c_1} = \frac{a^{\gamma}\sum_{m=2}^{\infty}\int_0^T\left[1+\frac{b}{a}\cos(2\pi f_0 x)\right]^{\gamma}\cos(m[2\pi f_0 x])dx}{a^{\gamma}\int_0^T\left[1+\frac{b}{a}\cos(2\pi f_0 x)\right]^{\gamma}\cos(2\pi f_0 x)dx}, \tag{4.6}$$

and it is clear that the magnitude of the harmonic distortion is dependent not only on γ, but also the ratio of fringe contrast to offset[1]. If we now assume $\sum_{m=2}^{\infty}\frac{c_m}{c_1}$ increases monotonically for all γ, considering Equation (4.6) for integer cases of typical γ only, we can reveal the impact $\frac{b}{a}$ has on harmonic distortion. For $\gamma = 2$ we have

$$\sum_{m=2}^{\infty}\frac{c_m}{c_1} = \frac{b}{a}.\frac{1}{4}, \tag{4.7}$$

[1]It should be noted that Equation (4.6) and therefore the harmonic structure of the fringe is independent of the fringe spatial carrier frequency, f_0 by the nature of the Fourier Series

and for $\gamma = 3$

$$\sum_{m=2}^{\infty} \frac{c_m}{c_1} = \frac{6\left(\frac{b}{a}\right) + \left(\frac{b}{a}\right)^2}{12 + 3\left(\frac{b}{a}\right)^2}, \tag{4.8}$$

As can be seen when $\gamma = 2$ harmonic distortion is maximised when the ratio $\frac{b}{a}$ is maximised. Considering now $\gamma = 3$ and differentiating Equation (4.8) with respect to $\frac{b}{a}$ and setting to zero we can obtain

$$-3.\left(\frac{b}{a}\right)^2 + 4.\frac{b}{a} + 12 = 0, \tag{4.9}$$

which has two roots, -1.44 and 2.77. Now noting that the function represented by Equation (4.8) is unimodal for all real $\frac{b}{a} > 0$ and referring to Equation (4.1) it is clear that a and b are constrained directly as a result of image normalisation as follows:

$$a + b \leq 1, \tag{4.10}$$

and

$$\begin{aligned} a - b &\geq 0 \\ a &\geq b \\ \frac{b}{a} &\leq 1, \end{aligned} \tag{4.11}$$

and hence for $\gamma = 3$ harmonic distortion is also maximised when $\frac{b}{a}$ is maximum i.e. $\frac{b}{a} = 1$ when $a = b$. Thus, we conclude that harmonic distortion is maximum when fringe offset and contrast parameters are equivalent.

Considering $1 < \gamma < 3$ for a standard digital video projector, the projected fringe can be commonly seen to present observable 2nd, 3rd and 4th order harmonic distortion. To better understand the order of harmonic distortion we define

$$w_n(x, y) = c_0 + c_1 \cos(2\pi f_0 x) + \sum_{m=2}^{n} c_m \cos(m[2\pi f_0 x]) \tag{4.12}$$

an approximation of $w(x, y)$ containing only up to the nth order harmonic where c_0 and c_1 represent the approximated fringe offset and contrast respectively. And accordingly we can define e_n a relative error to represent the approximation $w_n(x, y)$

$$e_n = \frac{\sum_{y=0}^{Y}\sum_{x=0}^{X} \frac{|w(x,y) - w_n(x,y)|}{w(x,y)}.100\%}{XY}, \tag{4.13}$$

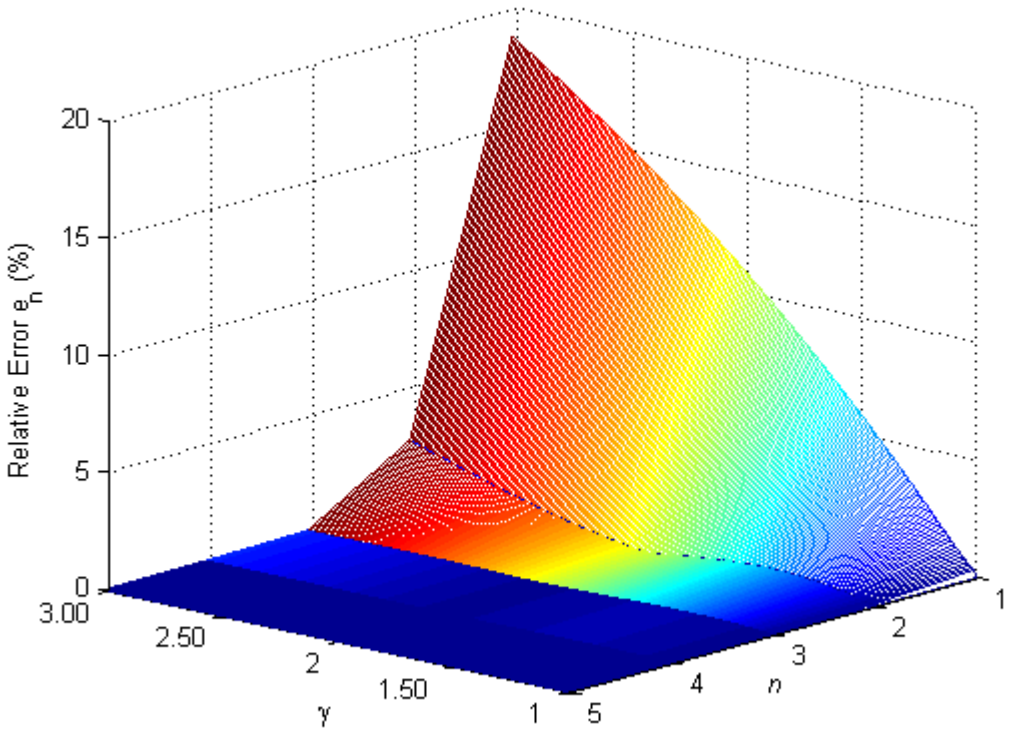

Figure 4.1: e_n, $1 < \gamma < 3$, for normalised fringe parameters $a = b$

γ	1.0	1.5	2.0	2.5	3.0
e_2 (%)	0	0.6260	0.1856	1.1931	2.7013

Table 4.1: Absolute Relative Mean Error e_2 for various γ

where X and Y represent the horizontal and vertical resolutions respectively [2].

For a range of γ values we obtain c_m via DFT of $w(x, y)$ over x, plotting e_n for the worst case scenario where fringe parameters $a = b$ for n up to 5, and reveal Figure (4.1). As can be seen for values typical of projector gamma the 2nd order harmonic serves as a decent approximation with an absolute average relative error of less than 3% right up to $\gamma = 3$. Table (4.1) displays e_2 for $1 < \gamma < 3$ where $a = b$.

[2] It should also be further noted that for simplicity the fringe image is assumed to be aligned such that the origin is located on the bottom left corner of the image

Now, that we can adequately model a gamma distorted fringe as

$$w_2(x,y) = c_0 + c_1\cos(2\pi f_0 x) + c_2\cos(4\pi f_0 x), \tag{4.14}$$

an expression linking γ and c_2 is still required to provide insight into the magnitude of gamma harmonic fringe distortion. Since analytical expansion of Equation (4.1), for the fractional γ case, poses a non-trivial task we define

$$p = \left(\frac{c_2}{c_1}\right)^2 = \frac{\left[\int_0^T w(x,y)\cos(4\pi f_0 x)\,dx\right]^2}{\left[\int_0^T w(x,y)\cos(2\pi f_0 x)\,dx\right]^2}, \tag{4.15}$$

the power ratio of the 2nd order harmonic to the fundamental, which is a function of a, b and γ. If we now just consider the case when fringe parameters $a = b$ we can give p as

$$p = \left(\frac{c_2}{c_1}\right)^2 = \frac{\left[\int_0^T [1+\cos(2\pi f_0 x)]^\gamma \cos(4\pi f_0 x)\,dx\right]^2}{\left[\int_0^T [1+\cos(2\pi f_0 x)]^\gamma \cos(2\pi f_0 x)\,dx\right]^2}, \tag{4.16}$$

which is clearly independent of a and b and dependent only on γ. Thus, resorting to numerical evaluation we utilise a 3rd order polynomial curve fitting and relate γ and p, as

$$p = -0.0139\gamma^3 + 0.1001\gamma^2 - 0.1398\gamma + 0.0520 \tag{4.17}$$

for the normalised fringe parameters $a = b$. Figure (4.2) displays a monotonically increasing function, which confirms our previous assumption that $\sum_{m=2}^{\infty} \frac{c_m}{c_1}$ is monotonically increasing for all γ.

A key practical issue in modeling a γ distorted fringe is the assumption that the acquisition device demonstrates a linear intensity response characteristic. This assumption is commonplace for all current literature published on the issue [97, 98]. For the common integrating CCD-type detectors this assumption is valid provided the detector can be operated just below saturation [143]. In the practical scenario these conditions can be easily emulated through software manipulation of the fringe contrast and offset parameters, the adjustment of sensor integration time and furthermore, by imaging optics aperture adjustments.

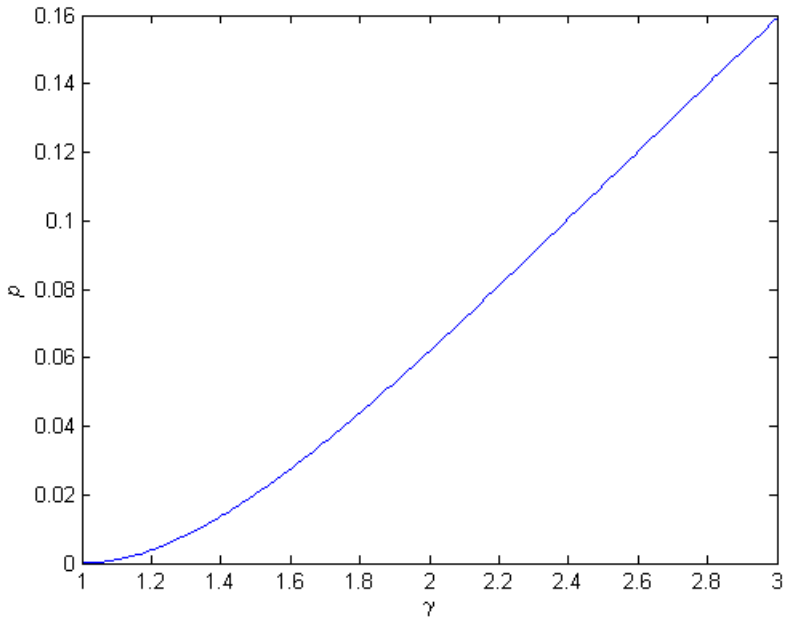

Figure 4.2: Power ratio p, 2nd order harmonic to fundamental Vs. γ, for normalised fringe parameters $a = b$

4.3 Impact of Harmonics for Fringe Processing Phase Estimation

Referring to Equation (2.14) it is clear that the predicted height distribution denoted as $h(x, y)$ is dependent on four variables, l_0, d_0, f_0 and $\Delta\phi(x, y)$. Given that l_0, d_0 and f_0 are physical constants (or can be derived as physical constants via calibration procedures as outlined in Section 2.6) it becomes evident that the Display Gamma related errors are associated with the $\Delta\phi(x, y)$ term. Since $\Delta\phi(x, y)$ is calculated based on predictions of fringe phase modulations $\phi(x, y)$ and $\phi_0(x, y)$, the impact of γ for Fringe Projection 3D sensing is solely dependent on the integrity of fringe phase estimation procedures in the presence of gamma distortion. Therefore, given the nature of a gamma distorted fringe as demonstrated in Section 4.2, in order to reveal the true impact of γ for Fringe Projection applications, the impact of harmonics for fringe phase estimation must be evaluated.

The impact of harmonics (along with a range of additional fringe phenomena) for phase shifting fringe processing techniques have been extensively studied over the past two or so decades [99, 100, 144, 145]. However much like the recent γ non-linearity sur-

vey [143], most reviews have only considered the harmonic sensitivity of phase shifting interferometry applications via simulation based analysis. Not until more recent times had the more specific influence of harmonics for Fringe Projection 3D sensing applications been analytically considered [96, 146]. These investigations were primarily concerned with the 3 Step PMP approach with Hu *et al.*'s [146] derivation also including the FTP technique. Despite providing analytical expressions to represent the phase residual measuring error for the investigated techniques, no reference to the magnitude of the harmonic distortion was provided. Furthermore, neither of these derivations considered other well exploited fringe processing techniques nor were the analytical findings verified.

Consequently, given the 2nd order approximation for a gamma distorted fringe demonstrated in Section 4.2, we analytically investigate the resulting influence the 2nd order harmonic has on the estimation of phase component $\omega(x, y)$, for a range of fringe processing techniques.

4.3.1 Analytical Procedure

The analytical investigations for each of the listed fringe processing techniques assumes the gamma distorted fringe images are given by

$$\begin{aligned}\hat{g}(x, y) = a(x, y) + b(x, y)\cos(\omega(x, y) + \zeta_n) + \\ c(x, y)\cos(2[\omega(x, y) + \zeta_n])\end{aligned} \tag{4.18}$$

where

$$\omega(x, y) = 2\pi f_0 x + \varphi(x, y) \tag{4.19}$$

where $\varphi(x, y)$ denotes the spatial phase modulation corresponding to the projection surface i.e. $\phi(x, y)$ or $\phi_0(x, y)$, and ζ_n denotes the appropriate fringe phase offset. Accordingly, the fringe harmonic power ratio, p, is given by [3]

$$p = \left(\frac{c}{b}\right)^2 \tag{4.20}$$

[3] Fringe contrast terms, b and c, are still a function of both x and y, however, just for simplicity they have been omitted

The resulting estimation of the true fringe phase modulation denoted $\hat{\omega}(x,y)$ as obtained by utilising the 2nd order harmonically distorted fringe images and the corresponding fringe processing algorithm, is then given by

$$\hat{\omega}(x,y) = \omega(x,y) + \delta(x,y) \tag{4.21}$$

where $\delta(x,y)$ represents the phase measuring residual error, resulting from the 2nd order component of the fringe signal. Therefore, rearranging Equation (4.21) the phase measuring error, $\delta(x,y)$, can be determined by calculating

$$\delta(x,y) \;=\; \hat{\omega}(x,y) - \omega(x,y) \tag{4.22}$$

which can be more conveniently written as

$$\begin{aligned} \delta(x,y) &= \arctan\Big(\tan(\hat{\omega}(x,y) - \omega(x,y))\Big) \\ &= \arctan\left(\frac{\tan(\hat{\omega}(x,y)) - \tan(\omega(x,y))}{1 + \tan(\hat{\omega}(x,y))\tan(\omega(x,y))}\right) \end{aligned} \tag{4.23}$$

where the actual phase modulation term is given by

$$\omega(x,y) = \arctan\left(\frac{b\sin(\omega(x,y))}{b\cos(\omega(x,y))}\right) \tag{4.24}$$

To gauge the magnitude of the phase measuring residual error, following [146], δ_{max} and δ_{min}, the corresponding maximum and minimum values of $\delta(x,y)$ are calculated and thereby utilised to determine the maximum measurement error, ε_{max}. In other words, ε_{max} is calculated by substituting δ_{max} and δ_{min} into Equation (2.13) as follows

$$\varepsilon_{max} = \delta_{max} - \delta_{min} \tag{4.25}$$

Therefore, by derivation of $\delta(x,y)$ and hence ε_{max} the various fringe processing algorithms can be evaluated in terms of performance in the presence of γ fringe non-linearities.

4.3.2 Traditional Phase Measuring Algorithm

The traditional Phase Measuring algorithm as outlined in Section 2.4.1.1 requires the projection of N fringe images each equally space over the spatial period of the fringe by $\zeta_n = 2\pi n/N$ radians for $n = 0, 1, 2...N-1$.

Substituting Equation (4.18) into Equation (2.18), an estimation of the actual phase modulation term, $\hat{\omega}(x,y)$ for the Nth variation of the PMP algorithm in the presence of 2nd order harmonic distortion can be obtained as

$$\begin{aligned}\hat{\omega}(x,y) &= -\arctan\left[\frac{\sum_{n=0}^{N-1}\hat{g}_n(x,y)\sin(2\pi n/N)}{\sum_{n=0}^{N-1}\hat{g}_n(x,y)\cos(2\pi n/N)}\right] \\ &= -\Big(\sum_{n=0}^{N-1} b\cos(\omega(x,y)+2\pi n/N)\sin(2\pi n/N) \\ &\quad +c\cos(2[\omega(x,y)+2\pi n/N])\sin(2\pi n/N)\Big) \\ &\quad \Big/\Big(\sum_{n=0}^{N-1} b\cos(\omega(x,y)+2\pi n/N)\cos(2\pi n/N) \\ &\quad +c\cos(2[\omega(x,y)+2\pi n/N])\cos(2\pi n/N)\Big)\end{aligned} \tag{4.26}$$

Clearly, the phase estimation is dependent on N and therefore, the resulting phase residual for each step variation of the PMP approach unique to the number of steps. Here we only evaluate the $N=3$ and $N=4$ cases since higher step numbers are typically associated with being less sensitive to low order harmonic distortion [143]. Moreover, the $N=3$ and $N=4$ variations either form the basis of, or are more suited to many techniques currently being utilised for dynamic Fringe Projection profiling methods [88, 89, 92, 139].

4.3.2.1 3 Step [146]

Substituting $N=3$ into Equation (4.26) and simplifying reveals the estimation of the fringe phase modulation to be

$$\hat{\omega}(x,y) = \arctan\left(\frac{b\sin(\omega(x,y)) - c\sin(2\omega(x,y))}{b\cos(\omega(x,y)) + c\cos(2\omega(x,y))}\right) \tag{4.27}$$

By taking the tangent of both sides of both Equations (4.27) and (4.24) and substituting into Equation (4.23) and simplifying the phase measuring residual can be given by

$$\begin{aligned}\delta(x,y) &= -\arctan\left(\frac{c\sin(3\omega(x,y))}{b+c\cos(3\omega(x,y))}\right) \\ &= -\arctan\left(\frac{\sqrt{p}\sin(3\omega(x,y))}{1+\sqrt{p}\cos(3\omega(x,y))}\right)\end{aligned} \tag{4.28}$$

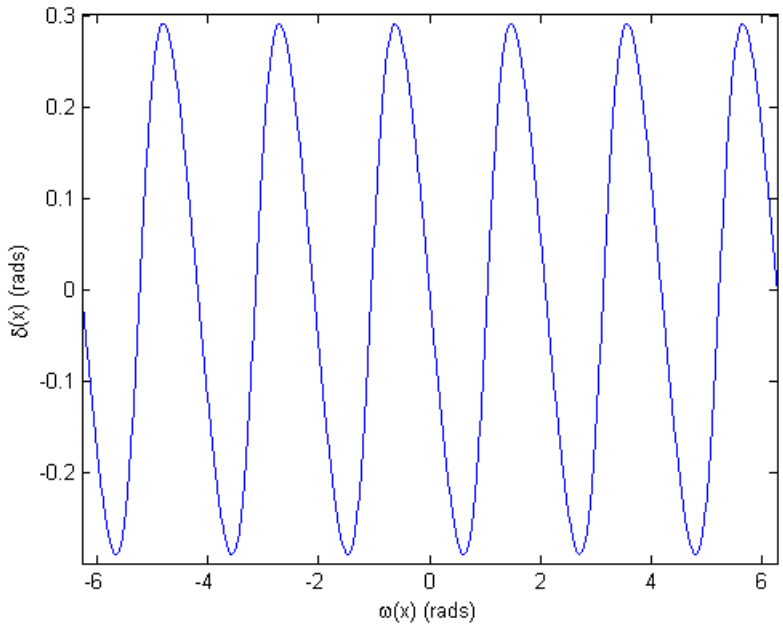

Figure 4.3: Traditional 3 Step PMP 2nd order harmonic phase measuring residual for constant phase modulation with $p = 0.082$ corresponding to $\gamma = 2.2$ for fringe offset and contrast parameters $a = b$

Clearly, the phase residual is dependent on the phase modulation corresponding to the 3D distribution of the object's surface and also the ratio of the 2nd order harmonic component to the fundamental. As $\delta(x, y)$ is dependent on $\omega(x, y)$, which is typically non-constant in both x and y directions, the phase residual presents an aperiodic nature as previously observed in Section 3.6.2.1. Figure 4.3 displays a plot of the phase measuring error associated with the 2nd order harmonic for a constant phase modulation with $p = 0.082$, approximately corresponding to a system gamma value of $\gamma = 2.2$ for fringe offset and contrast parameters $a = b$.

To gauge the magnitude of the phase measuring residual error, by setting $\frac{d\delta(x,y)}{d\omega(x,y)} = 0$, the maximum and minimum values of the 3 Step PMP phase residual, δ_{max} and δ_{min}, can be obtained. That is,

$$\delta_{max} = \arctan\left(\sqrt{\frac{p}{1-p}}\right) \tag{4.29}$$

and

$$\delta_{min} = -\arctan\left(\sqrt{\frac{p}{1-p}}\right) \tag{4.30}$$

and therefore, substituting Equations (4.29) and (4.30) into Equation (4.25), the maximum phase measuring error for the 3 Step PMP method can be given by

$$\varepsilon_{max} = 2\arctan\left(\sqrt{\frac{p}{1-p}}\right). \tag{4.31}$$

An interesting point to note is that the maximum phase measuring error is dependent only on the ratio of the second order harmonic to the fundamental.

4.3.2.2 4 Step

Similar to the 3 Step case, however, with substituting $N = 4$ into Equation (4.26) and simplifying, the estimation of the phase modulation term is given by

$$\hat{\omega}(x,y) = -\arctan\left(\frac{b\sin(\omega(x,y))}{b\cos(\omega(x,y))}\right). \tag{4.32}$$

Evidently, negating $\hat{\omega}(x,y)$ yields

$$\hat{\omega}(x,y) = \omega(x,y) \tag{4.33}$$

and

$$\delta(x,y) = 0, \tag{4.34}$$

and it becomes clear that the $N = 4$ PMP variation is immune to errors prominent with 2nd order harmonic distortion resulting from γ non-linearities.

4.3.3 90° 3 Step

The 90° 3 Step fringe processing algorithm requires the projection of 3 fringe images with the appropriate phase offsets $\zeta_n = -\frac{\pi}{2}, 0, \frac{\pi}{2}$ radians for $n = 0, 1, 2$ as outlined in Section 2.4.1.2. Substituting Equation (4.18) with the included phase offsets into Equation (2.21) and simplifying, reveals the phase term estimation for the 90° 3 Step algorithm as

$$\hat{\omega}(x,y) = \arctan\left(\frac{b\sin(\omega(x,y))}{b\cos(\omega(x,y)) + 2c\cos(2\omega(x,y))}\right) \tag{4.35}$$

Taking the tangent of both sides of this result and substituting into Equation (4.23) yields the resulting residual function for the 90° 3 Step method as

$$\begin{aligned}\delta(x,y) &= -\arctan\left(\frac{2c\sin(\omega(x,y))\cos(2\omega(x,y))}{b + 2c\cos(\omega(x,y))\cos(2\omega(x,y))}\right) \\ &= -\arctan\left(\frac{2\sqrt{p}\sin(\omega(x,y))\cos(2\omega(x,y))}{1 + 2\sqrt{p}\cos(\omega(x,y))\cos(2\omega(x,y))}\right)\end{aligned} \tag{4.36}$$

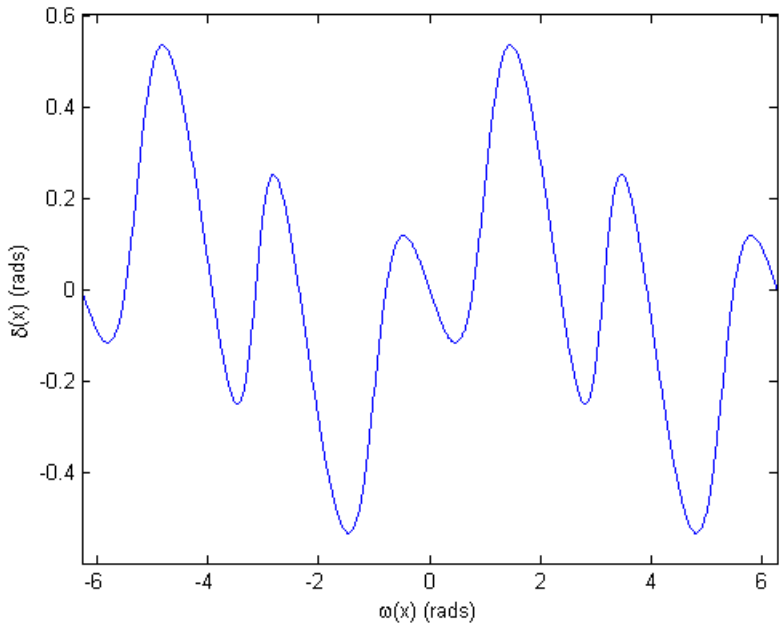

Figure 4.4: 90° 3 Step 2nd order harmonic phase measuring residual for constant phase modulation with $p = 0.082$ corresponding to $\gamma = 2.2$ for fringe offset and contrast parameters $a = b$

similar to the 3 Step PMP case the residual function is dependent on the phase modulation corresponding to the 3D distribution of the object's surface and also the ratio of the 2nd order harmonic component to the fundamental and therefore also presents an aperiodic nature. Figure 4.4 displays a plot of the 90° 3 Step phase measuring error associated with the 2nd order harmonic for a constant phase modulation with $p = 0.082$, approximately corresponding to a system gamma value of $\gamma = 2.2$ for fringe offset and contrast parameters $a = b$.

To gauge the magnitude of the 90° 3 Step residual phase measuring error we calculate via numerical analysis a curve fitting function to describe the curves δ_{max} and δ_{min} depicted in Figures 4.5 and 4.6. The two curve fits, fitted to the 3rd order were found to be

$$\delta_{max} = 254.1591p^3 - 82.3386p^2 + 10.7506p + 0.0745 \tag{4.37}$$

and

$$\delta_{min} = -254.1591p^3 + 82.3386p^2 - 10.7506p - 0.0745 \tag{4.38}$$

substituting Equations (4.37) and (4.38) into Equation (4.25), the maximum phase mea-

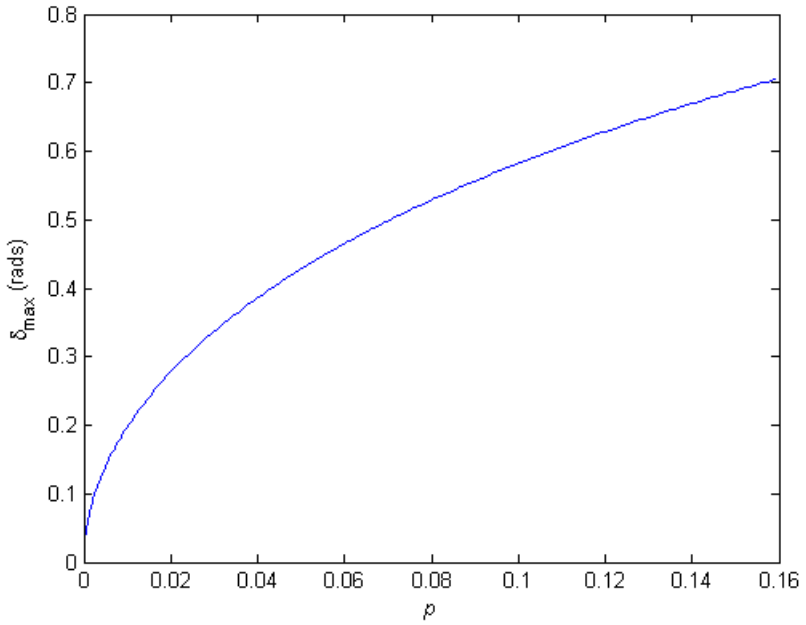

Figure 4.5: Maximum phase measuring error, δ_{max}, for the 90° 3 Step for various p corresponding to $1 < \gamma < 3$.

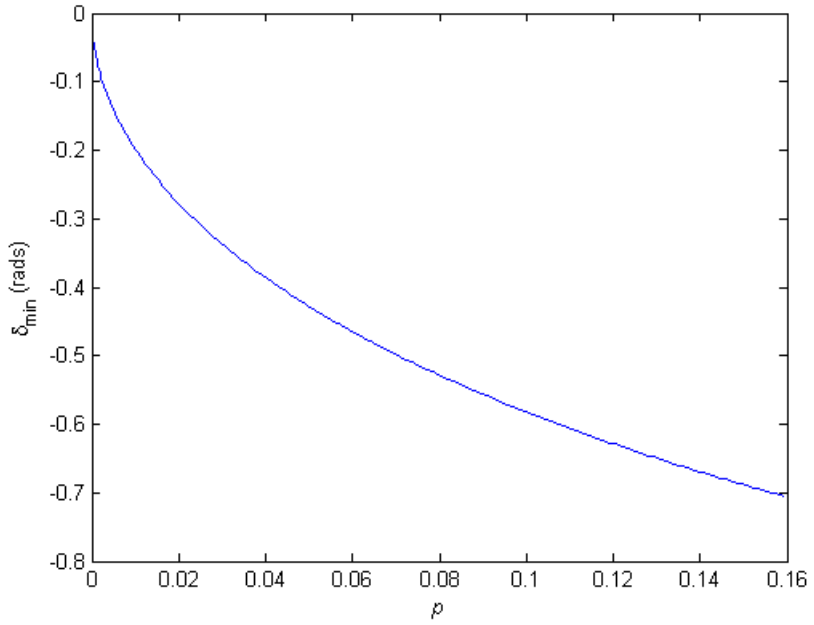

Figure 4.6: Minimum phase measuring error, δ_{min}, for the 90° 3 Step for various p corresponding to $1 < \gamma < 3$.

suring error for the 90° 3 Step method can be given by

$$\varepsilon_{max} = 2(254.1591p^3 - 82.3386p^2 + 10.7506p + 0.0745). \tag{4.39}$$

4.3.4 90° 3 Step with Phase Offset

Similar to the general 90° approach where each of the 3 fringe images are phase shifted by $\frac{\pi}{2}$, the 90° 3 Step with Phase Offset incorporates a further initial phase offset of $\frac{\pi}{4}$, purely for computational convenience. Therefore, substituting the appropriate phase offsets as indicated in Equation (2.23) into Equation (4.18) and subsequently Equation (2.24), the estimation of the phase modulation term $\omega(x, y)$ can be given by

$$\hat{\omega}(x, y) = \arctan\left(\frac{\frac{b}{\sqrt{2}}\sin(\omega(x, y)) - c\sin(2\omega(x, y))}{\frac{b}{\sqrt{2}}\cos(\omega(x, y)) - c\sin(2\omega(x, y))}\right) \tag{4.40}$$

Following this the phase measuring residual for the 90° 3 Step with Phase Offset technique can be found to be

$$\begin{aligned}\delta(x, y) &= \arctan\left(\frac{\sqrt{2}c\sin(2\omega(x, y))\Big(\sin(\omega(x, y)) - \cos(\omega(x, y))\Big)}{b - \sqrt{2}c\sin(2\omega(x, y))\Big(\sin(\omega(x, y)) + \cos(\omega(x, y))\Big)}\right) \\ &= \arctan\left(\frac{2\sqrt{p}\sin(2\omega(x, y))\sin(\omega(x, y) - \frac{\pi}{4})}{1 - 2\sqrt{p}\sin(2\omega(x, y))\sin(\omega(x, y) + \frac{\pi}{4})}\right)\end{aligned} \tag{4.41}$$

similar to the previously presented cases the residual function is dependent on the phase modulation corresponding to the 3D distribution of the object's surface and also the ratio of the 2nd order harmonic component to the fundamental and therefore also presents an aperiodic nature. Figure 4.7 displays a plot of the 90° 3 Step with Phase Offset phase measuring error associated with the 2nd order harmonic for a constant phase modulation with $p = 0.082$, approximately corresponding to a system gamma value of $\gamma = 2.2$ for fringe offset and contrast parameters $a = b$.

As can be seen the residual function for the offset approach is identical to the general 3 Step 90° variation, however, offset by exactly $\frac{\pi}{4}$ radians. Accordingly, the sensitivity of the 90° 3 Step with Phase Offset technique is identical to that of the typical 90° 3 Step method as represented in Equation (4.39).

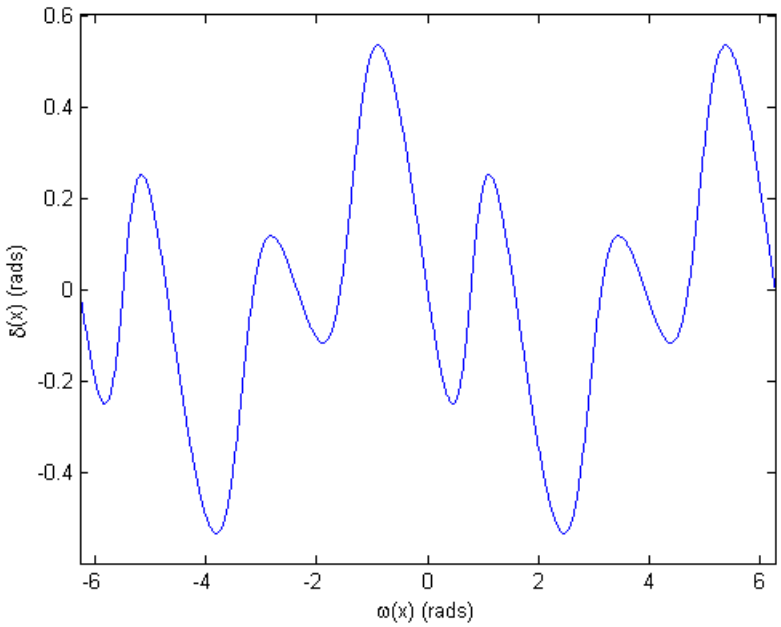

Figure 4.7: $90°$ 3 Step with Phase Offset 2nd order harmonic phase measuring residual for constant phase modulation with $p = 0.082$ corresponding to $\gamma = 2.2$ for fringe offset and contrast parameters $a = b$

4.3.5 2+1

Similar to the two previously presented 3 Step algorithms, the 2+1 algorithm is centered on the acquisition of three fringe images with a constant phase offset of $\frac{\pi}{2}$ radians between each. As indicated in Section 2.4.1.4 one fringe is acquired with the intention to remove the dc component from two orthogonally projected fringes. In the presence of gamma distortion the estimated dc term, $\hat{g}_{dc}(x, y)$, can be found by substituting Equation (4.18) with appropriate phase offsets into Equation (2.26)

$$\begin{aligned}
\hat{g}_{dc}(x,y) &= \frac{\hat{g}_0(x,y) + \hat{g}_2(x,y)}{2} \\
&= \frac{1}{2}\Big[a(x,y) + b(x,y)\cos(\omega(x,y)) + c(x,y)\cos(2\omega(x,y)) \\
&\quad + a(x,y) + b(x,y)\cos(\omega(x,y)+\pi) + c(x,y)\cos(2(\omega(x,y)+\pi))\Big] \\
&= \frac{1}{2}\Big[2a(x,y) + 2c(x,y)\cos(2\omega(x,y))\Big] \\
&= a(x,y) + c(x,y)\cos(2\omega(x,y)). \qquad (4.42)
\end{aligned}$$

Following the estimation of the dc term, the corresponding estimation of the phase modulation term can be found to be

$$\hat{\omega}(x,y) = \arctan\left(\frac{b\sin(\omega(x,y)) - 2c\cos(2\omega(x,y))}{b\cos(\omega(x,y))}\right) \tag{4.43}$$

and furthermore, taking the tangent of Equation (4.43) and substituting into Equation (4.23) the phase measuring error associated with the 2nd order harmonic for the 2+1 algorithm can be found, that is

$$\begin{aligned}\delta(x,y) &= -\arctan\left(\frac{2c\cos(\omega(x,y))\cos(2\omega(x,y))}{b-2c\sin(\omega(x,y))\cos(2\omega(x,y))}\right)\\ &= -\arctan\left(\frac{2\sqrt{p}\cos(\omega(x,y))\cos(2\omega(x,y))}{1-2\sqrt{p}\sin(\omega(x,y))\cos(2\omega(x,y))}\right)\end{aligned} \tag{4.44}$$

The residual phase measuring error for the 2+1 technique for a constant phase modulation is depicted in Figure (4.8). Interestingly, the residual is again identical to that of the two previously presented 90° 3 Step approaches, however, with a constant phase offset and therefore, the sensitivity of the 2+1 technique is also identical as indicated in Equation (4.39). By this result it can be concluded that the measuring error resulting from the 2nd order harmonic for stepping techniques is further dependent on the initial phase offset of fringe images and more importantly the sensitivity of the approach is dependent on the phase offset, ζ_n, between each of the acquired fringe images.

4.3.6 3+3

As concluded in Section 4.3.5 the initial phase offset has a significant influence on the resulting phase measuring residual. Averaging techniques such as the 3+3 or Double Three Step approaches utilise the phase offset principle to counter various forms of measurement error. The 3+3 approach was primarily designed to accommodate for phase shifting errors, based on the principle of phase offset as outlined in Section 2.4.1.5. Employing this variation the first estimation based on the first three fringe images denoted, $\hat{\omega_1}(x,y)$, is identical to that of the 90° 3 Step with Phase Offset as shown by shown Equation (4.40), therefore,

$$\hat{\omega_1}(x,y) = \arctan\left(\frac{\frac{b}{\sqrt{2}}\sin(\omega(x,y)) - c\sin(2\omega(x,y))}{\frac{b}{\sqrt{2}}\cos(\omega(x,y)) - c\sin(2\omega(x,y))}\right) \tag{4.45}$$

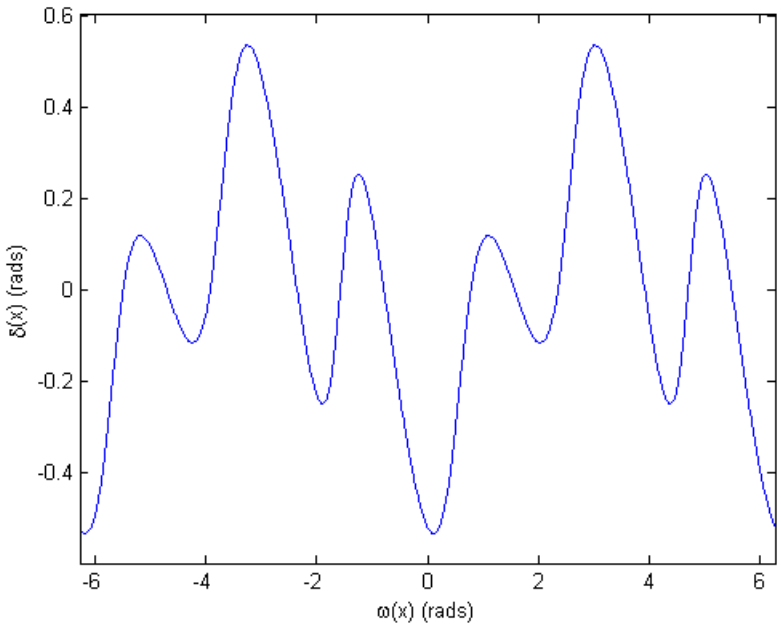

Figure 4.8: 2+1 2nd order harmonic phase measuring residual for constant phase modulation with $p = 0.082$ corresponding to $\gamma = 2.2$ for fringe offset and contrast parameters $a = b$

and accordingly the corresponding phase measuring residual, $\delta_1(x, y)$, is given by

$$\begin{aligned}\delta_1(x,y) &= \arctan\left(\frac{\sqrt{2}c\sin(2\omega(x,y))\Big(\sin(\omega(x,y))-\cos(\omega(x,y))\Big)}{b-\sqrt{2}c\sin(2\omega(x,y))\Big(\sin(\omega(x,y))+\cos(\omega(x,y))\Big)}\right)\\ &= \arctan\left(\frac{2\sqrt{p}\sin(2\omega(x,y))\sin(\omega(x,y)-\frac{\pi}{4})}{1-2\sqrt{p}\sin(2\omega(x,y))\sin(\omega(x,y)+\frac{\pi}{4})}\right)\end{aligned} \tag{4.46}$$

The following estimation denoted, $\hat{\omega_2}(x, y)$, based on the final three fringe images can therefore be given by

$$\hat{\omega_2}(x,y) = \arctan\left(\frac{\frac{b}{\sqrt{2}}\sin(\omega(x,y)) - c\sin(2\omega(x,y))}{\frac{b}{\sqrt{2}}\cos(\omega(x,y)) + c\sin(2\omega(x,y))}\right) \tag{4.47}$$

and accordingly the corresponding phase measuring residual, $\delta_2(x, y)$, is given by

$$\begin{aligned}\delta_2(x,y) &= \arctan\left(\frac{-\sqrt{2}c\sin(2\omega(x,y))\Big(\sin(\omega(x,y))+\cos(\omega(x,y))\Big)}{b-\sqrt{2}c\sin(2\omega(x,y))\Big(\sin(\omega(x,y))-\cos(\omega(x,y))\Big)}\right)\\ &= \arctan\left(\frac{-2\sqrt{p}\sin(2\omega(x,y))\sin(\omega(x,y)+\frac{\pi}{4})}{1-2\sqrt{p}\sin(2\omega(x,y))\sin(\omega(x,y)-\frac{\pi}{4})}\right)\end{aligned} \tag{4.48}$$

Following Equation (2.29) the phase measuring residual for the 3+3 method can be found by calculating

$$\begin{aligned}\delta(x,y) &= \frac{\delta_1(x,y)+\delta_2(x,y)}{2} \\ &= \frac{1}{2}.\arctan\Big(\tan(\delta_1(x,y)+\delta_2(x,y))\Big) \\ &= \frac{1}{2}.\arctan\left(\frac{\tan(\delta_1(x,y))+\tan(\delta_2(x,y))}{1-\tan(\delta_1(x,y))\tan(\delta_2(x,y))}\right)\end{aligned} \tag{4.49}$$

Therefore, taking the tangent of both sides of Equations (4.46) and (4.48) and substituting into Equation (4.49) the phase measuring residual error associated with the 2nd order harmonic for the 3+3 averaging technique can be found as

$$\delta(x,y) = \frac{1}{2}.\arctan\left(\frac{4p\sin^3(2\omega(x,y))}{1-2\sqrt{2p}\sin(2\omega(x,y))\sin(\omega(x,y))} \frac{-2\sqrt{2p}\sin(2\omega(x,y))\cos(\omega(x,y))}{-4p\sin^2(2\omega(x,y))\cos(2\omega(x,y))}\right) \tag{4.50}$$

Figure 4.9 depicts the residual phase measuring error for the 3+3 technique for a constant phase modulation with $p = 0.082$, approximately corresponding to a system gamma value of $\gamma = 2.2$ for fringe offset and contrast parameters $a = b$. Figure 4.10 depicts the sensitivity of the 3+3 algorithm in the presence of 2nd order harmonic distortion plotting ε_{max} as a function p. By numerical evaluation the fitting of this curve reveals the gamma distortion sensitivity of the 3+3 algorithm as

$$\varepsilon_{max} = 297.7522p^3 - 83.4221p^2 + 11.9055p + 0.0804. \tag{4.51}$$

4.3.7 Double Three Step

The averaging Double Three Step phase shifting technique is based on the traditional three step PMP, requiring the acquisition of two individual three step fringe sequences with the appropriate offsets as described in Section 2.4.1.6. Given the first fringe sequence is identical to that of the traditional 3 Step PMP approach, the initial estimation denoted, $\hat{\omega_1}(x,y)$, can be given by Equation (4.27), therefore

$$\hat{\omega_1}(x,y) = \arctan\left(\frac{b\sin(\omega(x,y)) - c\sin(2\omega(x,y))}{b\cos(\omega(x,y)) + c\cos(2\omega(x,y))}\right) \tag{4.52}$$

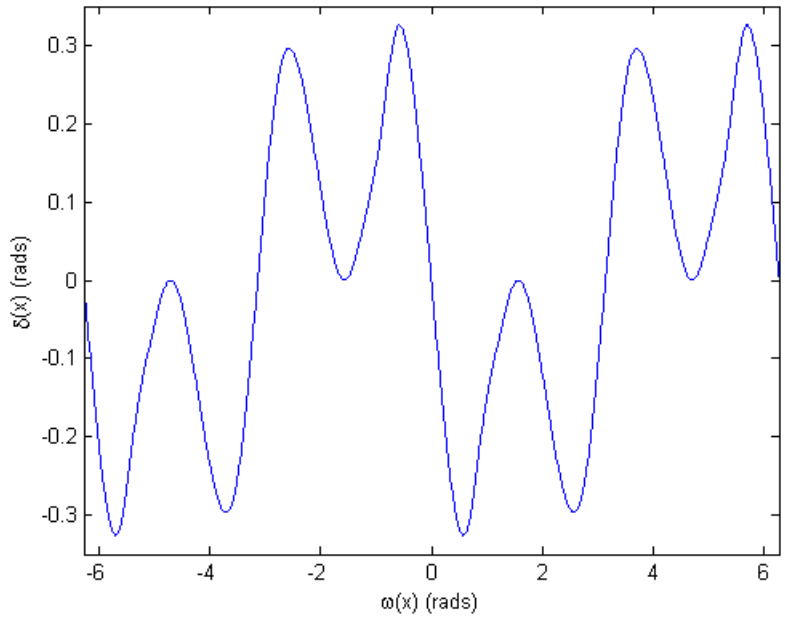

Figure 4.9: 3+3 2nd order harmonic phase measuring residual for constant phase modulation with $p = 0.082$ corresponding to $\gamma = 2.2$ for fringe offset and contrast parameters $a = b$

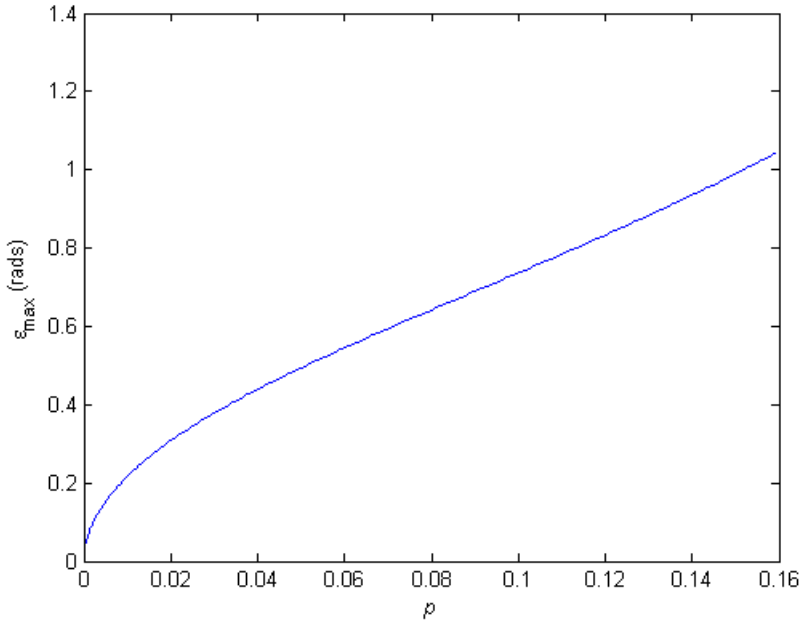

Figure 4.10: $\varepsilon_{max}(x, y)$ as a function of p for the 3+3 2nd order harmonic phase measuring residual

Accordingly the residual phase measuring error denoted, $\delta_1(x,y)$, based on the first estimation can be given by

$$\delta_1(x,y) = -\arctan\left(\frac{\sqrt{p}\sin(3\omega(x,y))}{1+\sqrt{p}\cos(3\omega(x,y))}\right) \tag{4.53}$$

Now for the second set of fringes offset by π radians relative to the initial set, the estimation can be given by

$$\hat{\omega_2}(x,y) = \arctan\left(\frac{b\sin(\omega(x,y)) + c\sin(2\omega(x,y))}{b\cos(\omega(x,y)) - c\cos(2\omega(x,y))}\right) \tag{4.54}$$

and accordingly the phase measuring residual denoted, $\delta_2(x,y)$ for the second estimation can be given by

$$\delta_2(x,y) = \arctan\left(\frac{\sqrt{p}\sin(3\omega(x,y))}{1-\sqrt{p}\cos(3\omega(x,y))}\right) \tag{4.55}$$

Similar to the 3+3 technique the phase measuring residual for the Double Three Step method can be found by calculating

$$\begin{aligned}\delta(x,y) &= \frac{\delta_1(x,y)+\delta_2(x,y)}{2} \\ &= \frac{1}{2}.\arctan\Big(\tan(\delta_1(x,y)+\delta_2(x,y))\Big) \\ &= \frac{1}{2}.\arctan\left(\frac{\tan(\delta_1(x,y))+\tan(\delta_2(x,y))}{1-\tan(\delta_1(x,y))\tan(\delta_2(x,y))}\right)\end{aligned} \tag{4.56}$$

Therefore, taking the tangent of both sides of Equations (4.53) and (4.55) and substituting into Equation (4.56) the phase measuring residual error associated with the 2nd order harmonic for the Double Three Step averaging technique can be found to be

$$\delta(x,y) = \frac{1}{2}.\arctan\left(\frac{p\sin(6\omega(x,y))}{1-p\cos(6\omega(x,y))}\right) \tag{4.57}$$

Figure 4.11 depicts the Double Three Step phase residual for a constant phase modulation with $p = 0.082$, approximately corresponding to a system gamma value of $\gamma = 2.2$ for fringe offset and contrast parameters $a = b$. Considering the shape of the Double Three Step residual relative to the single three step residual and also the form of Equations (4.57) and (4.28) the effect of the $6\omega(x,y)$ oscillation term can be clearly observed.

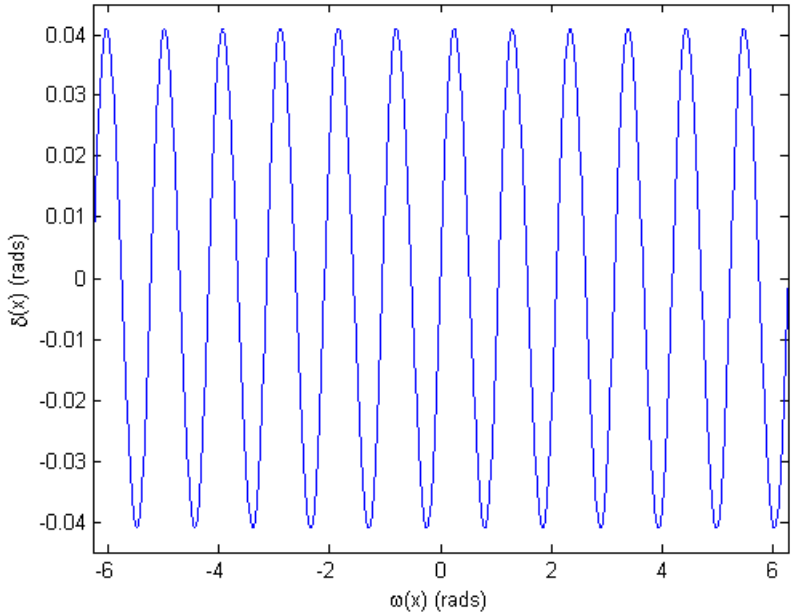

Figure 4.11: Double Three Step 2nd order harmonic phase measuring residual for constant phase modulation with $p = 0.082$ corresponding to $\gamma = 2.2$ for fringe offset and contrast parameters $a = b$

To gauge the magnitude of the phase measuring residual error, by setting $\frac{d\delta(x,y)}{d\omega(x,y)} = 0$, the maximum and minimum values of the Double Three Step phase residual, δ_{max} and δ_{min}, can be obtained. That is,

$$\delta_{max} = \frac{1}{2}.\arctan\left(\frac{p}{\sqrt{1-p^2}}\right) \tag{4.58}$$

and

$$\delta_{min} = -\frac{1}{2}.\arctan\left(\frac{p}{\sqrt{1-p^2}}\right) \tag{4.59}$$

and therefore, substituting Equations (4.58) and (4.59) into Equation (4.25), the maximum phase measuring error for the Double Three Step method can be given by

$$\varepsilon_{max} = \arctan\left(\frac{p}{\sqrt{1-p^2}}\right). \tag{4.60}$$

4.3.8 Fourier Transform Profilometry (FTP) [146]

Similar to the Phase Stepping approaches however with the ζ_n phase offset term set to zero, the harmonically distorted fringe rewritten in complex form is given by

$$\hat{g}(x,y) = a(x,y) + \frac{1}{2}b(x,y)\cdot e^{i\omega(x,y)} + \frac{1}{2}b(x,y)\cdot e^{-i\omega(x,y)} + \frac{1}{2}c(x,y)\cdot e^{2i\omega(x,y)} + \frac{1}{2}c(x,y)\cdot e^{-2i\omega(x,y)} \tag{4.61}$$

Therefore, after the appropriate filtering of each signal to remove the necessary direct component and negative frequency components the signal can be given as

$$\hat{\mathbf{g}}(x,y) = \frac{1}{2}b(x,y)\cdot e^{i\omega(x,y)} + \frac{1}{2}c(x,y)\cdot e^{2i\omega(x,y)} \tag{4.62}$$

Now substituting the harmonically distorted fringe signal into Equation (2.38), the estimation of the phase modulation term denoted, $\hat{\omega}(x,y)$ can be given by

$$\begin{aligned}
\hat{\omega}(x,y) &= Im\Big(\log(\frac{1}{2}b(x,y)\cdot e^{i(\omega(x,y))} + \frac{1}{2}c(x,y)\cdot e^{2i(\omega(x,y))})\Big) \\
&= Im\Big(\log(e^{i(\omega(x,y))} + \sqrt{p}\cdot e^{2i(\omega(x,y))})\Big) \\
&= Im\Big(i\cdot\omega(x,y) + \log(1+\sqrt{p}\cdot e^{i(\omega(x,y))})\Big) \\
&= \omega(x,y) + Im\Big(\log(1+\sqrt{p}\cdot e^{i(\omega(x,y))})\Big)
\end{aligned} \tag{4.63}$$

Substituting Equation (4.63) into Equation (4.22), the phase measuring residual, $\delta(x,y)$, corresponding to second order harmonic distortion for the FTP method can be given by

$$\begin{aligned}
\delta(x,y) &= \omega(x,y) + Im\Big(\log(1+\sqrt{p}\cdot e^{i(\omega(x,y))})\Big) - \omega(x,y) \\
&= Im\Big(\log(1+\sqrt{p}\cdot e^{i(\omega(x,y))})\Big)
\end{aligned} \tag{4.64}$$

Considering the operation of $Im(log(\cdot))$ is actually to get the phase angle of the complex number, Equation (4.64) can be rewritten as

$$\delta(x,y) = \arctan\left(\frac{\sqrt{p}\sin(\omega(x,y))}{1+\sqrt{p}\cos(\omega(x,y))}\right) \tag{4.65}$$

Interestingly, noting Equation (4.65) and the residual form for the 3 Step PMP technique (as shown by Equation (4.28)) the FTP residual is identical, however, oscillating only a third of the frequency of the 3 Step PMP residual case. The FTP phase residual is depicted in Figure 4.12 for a constant phase modulation with $p = 0.082$, approximately

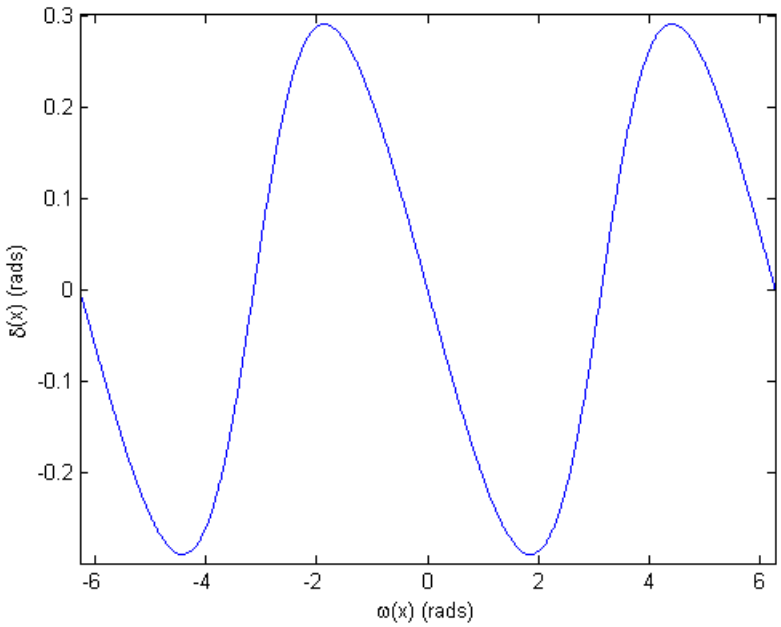

Figure 4.12: FTP 2nd order harmonic phase measuring residual for constant phase modulation with $p = 0.082$ corresponding to $\gamma = 2.2$ for fringe offset and contrast parameters $a = b$

corresponding to a system gamma value of $\gamma = 2.2$ for fringe offset and contrast parameters $a = b$.

Given the FTP residual is identical to the 3 Step PMP case (despite the frequency of oscillation), the sensitivity in terms of maximum and minimum phase residual is identical to the 3 Step PMP technique, therefore

$$\delta_{max} = \arctan\left(\sqrt{\frac{p}{1-p}}\right) \tag{4.66}$$

and

$$\delta_{min} = -\arctan\left(\sqrt{\frac{p}{1-p}}\right) \tag{4.67}$$

and accordingly

$$\varepsilon_{max} = 2\arctan\left(\sqrt{\frac{p}{1-p}}\right). \tag{4.68}$$

4.4 Display Gamma Measurement Error

4.4.1 Magnitude of Measurement Error

The derivations outlined in the previous section detail the sensitivity of each fringe processing algorithm by defining a maximum phase measuring error in radians. In order to calculate an actual error defining system accuracy, a final conversion step is required to convert the phase measurement error to a corresponding real world co-ordinate system. Assuming the projector / camera arrangement is situated far enough from the reference plane such that $l_0 \gg h(x,y)$, by substituting the maximum phase measurement error into Equation (2.69), an expression defining the maximum absolute system accuracy of the Fringe Projection measurement system in the presence of 2nd order harmonic fringe distortion can be derived, that is,

$$\begin{aligned} \epsilon &= \left| -\frac{l_0}{2\pi f_0 d_0} \right| \cdot \varepsilon_{max} \\ &= \frac{l_0}{2\pi f_0 d_0} \cdot \varepsilon_{max} \end{aligned} \tag{4.69}$$

4.4.2 Relating Gamma and System Accuracy

Since Gamma fringe distortion has been described as harmonic distortion, and more specifically as 2nd order harmonic distortion, the value of γ and system accuracy can be correlated. Utilising Equations (4.17) and (4.69) in accordance with the appropriate functions defining ε_{max} for each of the respective fringe processing techniques, γ and the system absolute maximum error can be linked for the case where fringe offset and contrast parameters $a = b$. For instance, assuming system parameters l_0, d_0 and f_0 are 5m, 2m and 10fringes/m respectively, we can plot a curve describing the maximum absolute measuring error versus the system γ value for each of the described fringe processing techniques, as depicted in Figure 4.13.

4.4.3 Frequency Dependence

Although the final accuracy is clearly dependent on spatial fringe frequency, f_0, (given Equation (4.69)), the frequency dependence of the Display Gamma phase residual error

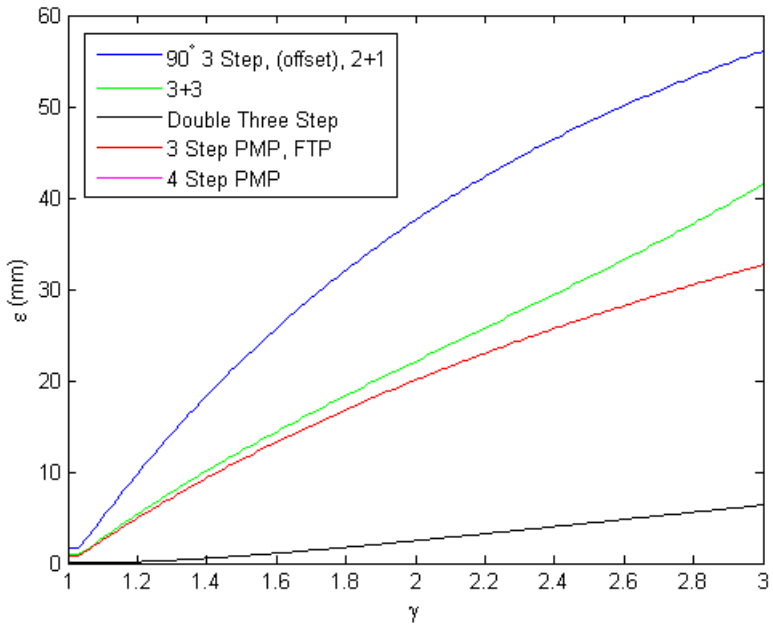

Figure 4.13: Maximum Absolute Measurement Error, ϵ Vs. γ for fringe parameters $a = b$

has yet to be discussed. One of the key conclusions Zhang and Yau [98] made in their investigation into the Display Gamma Fringe Projection phenomena was the frequency independence of the resulting residual phase measuring error (in this work denoted by $\delta(x, y)$). Zhang and Yau made this supposition based on empirical observation. This assumption makes it possible to normalise the spatial frequency and compose a single lookup table containing all possible combinations of $\delta(x, y)$ and $\omega(x, y)$, allowing for the effective elimination of the gamma residual error for any arbitrary spatial carrier frequency, f_0.

Through the work presented in this Chapter we have theoretically confirmed the frequency independence of the Display Gamma related residual phase measuring error. This frequency independence can be observed for each of the analytically derived phase measuring residuals presented in Section 4.3, where the residual measurement error was shown to be dependent only on harmonic ratio p and a phase component (for each of the presented fringe processing techniques).

Following these findings a distinct contradiction has been made in regard to the nature of the Display Gamma Fringe Projection issue. The preliminary experimental analysis presented in Chapter 3 indicated the Display Gamma associated errors had a distinct de-

pendence on fringe frequency, whereas, the current theoretical modeling of the problem indicates otherwise. The notion of this apparent contradiction can be attributed to the theoretical method by which the gamma distorted fringe has been modeled, with a more appropriate practical modeling and discussion about the implications for lookup table based gamma correction outlined in Chapter 5.

4.5 Simulation

In order to verify the validity of the analytical studies we simulated a range of digital fringe images with various values of gamma, projected onto a simulated surface and measure the corresponding system accuracy for the tested fringe processing techniques. The simulated fringe sets are given by

$$g_n(x,y) = [0.5 + 0.5\cos(\omega(x,y) + \zeta_n)]^\gamma$$
$$\text{for n=0,1,2,...,N-1,} \tag{4.70}$$

where the phase modulation term, $\omega(x,y)$, is given by

$$\omega(x,y) = 2\pi f_0 x + \varphi(x,y) \tag{4.71}$$

where $\varphi(x,y)$ represents the simulated phase distributions for either the reference or deformed projections i.e. $\phi(x,y)$ or $\phi_0(x,y)$ for the object and reference, respectively. It should be noted that the phase offset term, ζ_n, is set to zero for the FTP case where $N = 0$, and for all other stepping variations ζ_n is as defined in section 2.4.1.

4.5.1 Simulating an Appropriate Test Surface

In order to properly test the sensitivity of each fringe processing technique in the presence of γ distortion it is essential to appropriately simulate, $\omega(x,y)$, to reflect maximum phase measurement error conditions. Hence further examination of the nature of the phase residuals resulting from each of the phase measuring techniques is required.

Considering the phase residuals for each of the fringe processing approaches, it is evident that the residuals are largely dependent on p and also a phase component, $\omega(x,y)$. Now considering that a maximum phase measuring error will occur when minima and

maxima values of each the reference and deformed fringe residuals align, and also vice versa, the maximum phase measuring error can be given as

$$\begin{aligned} \varepsilon_{max} &= |\delta_{max} - \delta_{min}| \\ &= |\delta_{min} - \delta_{max}| \end{aligned} \tag{4.72}$$

where δ_{max} and δ_{min} represent the maximum and minimum values of the respect residual functions. Further observation of each of the depicted residual plots presented in section 4.3 reveals that either a maximum or minimum will always occur within a π radian modulation. Therefore, provided at least a minimum π radian modulation between $\phi_0(x, y)$ and $\phi(x, y)$ exists a maximum phase measurement error will be incurred.

To demonstrate this mathematically we consider the PMP / FTP residual for two chief reasons; Firstly, for mathematical convenience, (considering an analytical first order derivative can be easily obtained) and secondly since δ_{max} and δ_{min} are more significantly displaced relative to the other phase measuring residuals.

Now calculating $\dfrac{\partial \delta}{\partial \omega}$ it can be shown that the value of ω to maximise the phase residual can be given as

$$\omega_{max} = \arccos(-\sqrt{p}) \tag{4.73}$$

and thus a corresponding minimum is found at

$$\omega_{min} = 2\pi - \arccos(-\sqrt{p}) \tag{4.74}$$

Setting $\phi_0(x, y) = 0$ [4] the phase measuring error can be given by

$$\varepsilon = \delta(2\pi f_0 x) - \delta(2\pi f_0 x + \phi(x, y)) \tag{4.75}$$

and therefore to ensure ε_{max}, $\phi(x, y)$ must be chosen such that

$$|\phi(x, y)| \geq 2 \arccos(-\sqrt{p}) \tag{4.76}$$

or alternatively

$$|\phi(x, y)| \geq 2\pi - 2 \arccos(-\sqrt{p}) \tag{4.77}$$

Since the $\arccos$ function is bound to $[0, \pi]$ it is clear that either one of Equations (4.76) or (4.77) will be satisfied for the case when $|\phi(x, y)| \geq \pi$ for all p. It should be noted for

[4] It should be noted that since $\phi_0(x, y) = 0$ for the simulation, $\Delta\phi(x, y) = \phi(x, y)$

PMP the amount of phase required to maximise the measurement error is reduced by a factor of 3 relative to the FTP approach due to the 3ω term.

Hence to ensure the appropriate evaluation of the sensitivity of each fringe processing technique in the presence of γ distortion and furthermore, verify the analytical Display Gamma findings, the hemispherical convex phase distribution as seen in Figure 4.14 was simulated. The maximum phase displacement of the distribution is 4.154 radians corre-

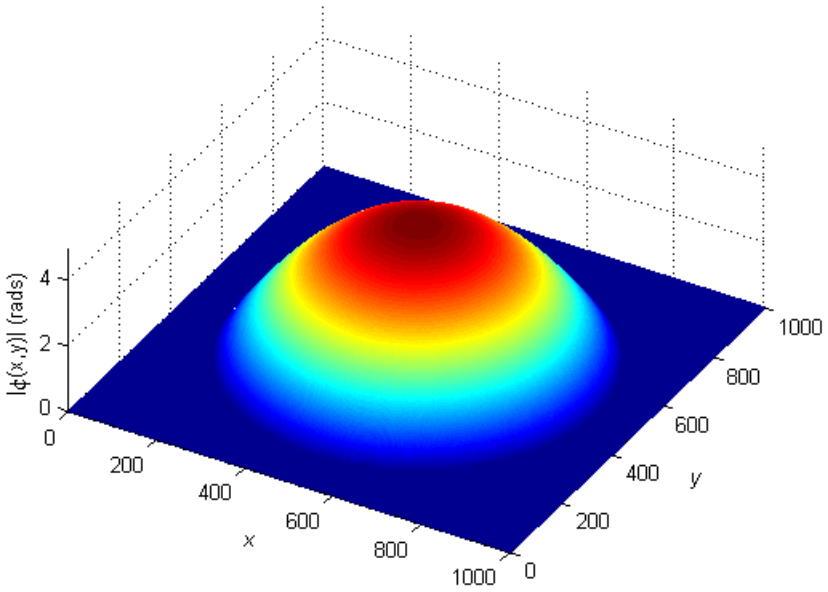

Figure 4.14: Simulated Phase Distribution $\phi(x, y)$

sponding to a maximum height of 160mm assuming system parameters l_0, d_0 and f_0 are 5m, 2m and 10fringes/m respectively [5]. Assuming a spatial resolution of 1pixel/mm and therefore corresponding spatial period of 100mm, the diameter of the surface is 800mm. The simulated fringe images are depicted in Figures 4.15 (a) and (b) while the fringe cross-sections shown in Figures 4.15 (c) and (d) clearly depict the non-sinusoidal attributes associated with the γ term.

[5] It should be noted that the selection of system parameters is arbitrary with parameter values selected to demonstrate example physical quantities.

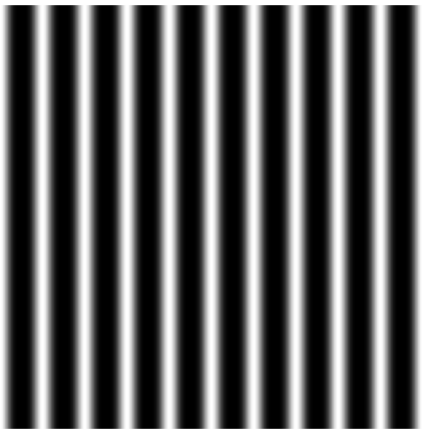

(a) Reference Fringe Image

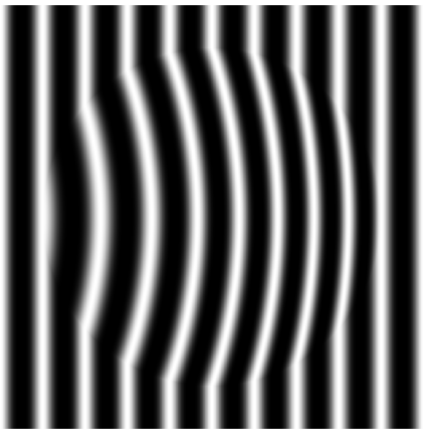

(b) Deformed Fringe Image

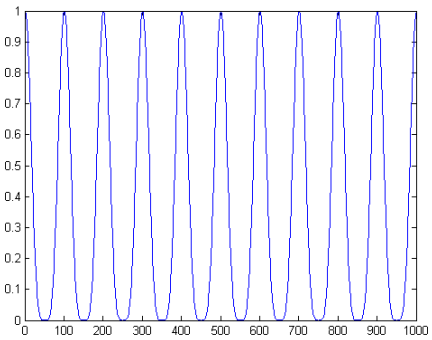

(c) Reference Fringe Cross-section

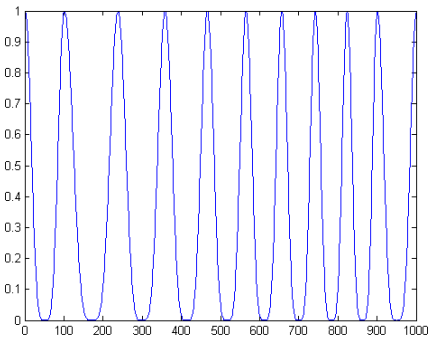

(d) Deformed Fringe Cross-section

Figure 4.15: Simulated Fringes, $\gamma = 2.2$

4.5.2 Traditional Phase Measuring Algorithm

4.5.2.1 3 Step

The 3 Step PMP simulation results are depicted in Figure 4.16. Figure (a) depicts both the analytical and simulation representations of the maximum absolute phase measuring error, ε_{max}, for the various typical values of γ. As can be seen the 2nd order analytical prediction of the 3 Step PMP γ sensitivity closely imitates that of the simulated case with little if any deviation even for higher values of γ where the higher order harmonic contribution is more significant. Figure 4.16 (b) and (c) display an example estimation of phase distribution $\Delta\phi(x, y)$ (Figure 4.14), and arbitrary cross-section, respectively, for a given γ value of 2.2. From these depictions the oscillatory nature of the residual

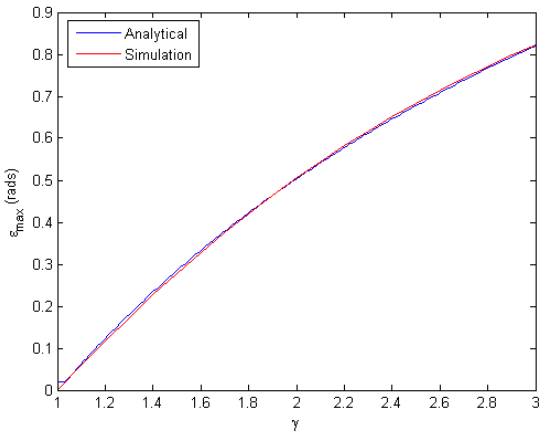

(a) Maximum Absolute Phase Measurement Error

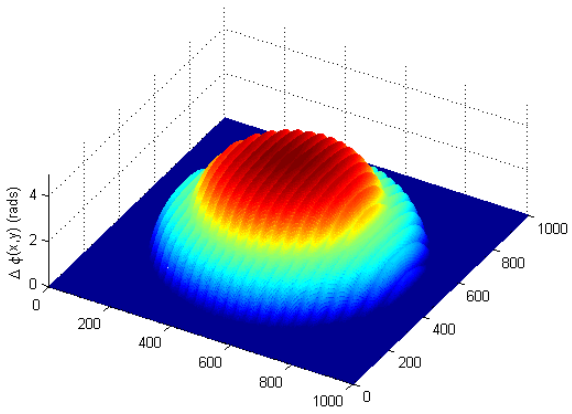

(b) $\Delta\phi(x, y)$ (rads), γ = 2.2

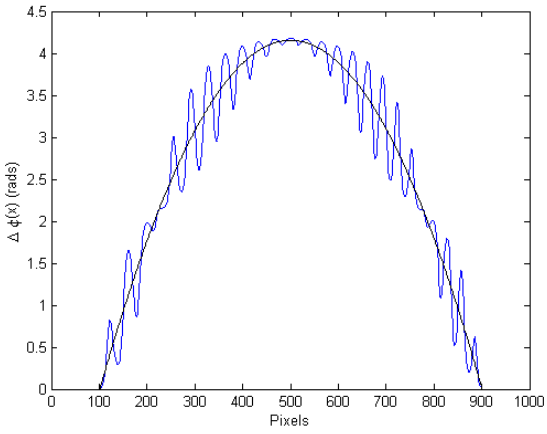

(c) Reconstruction Cross-section, γ = 2.2

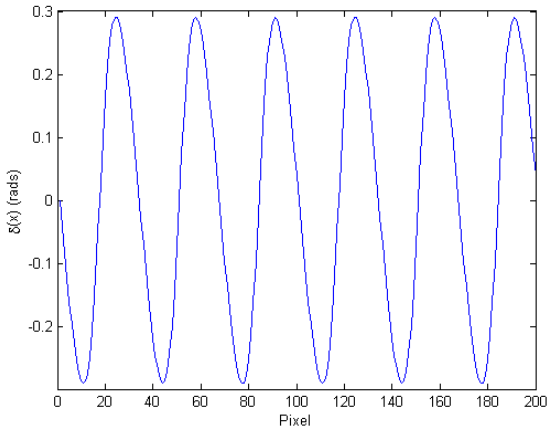

(d) Reference Phase Measuring Residual, γ = 2.2

Figure 4.16: 3 Step PMP Gamma distortion Simulation

similar to that previously demonstrated in Section 3.6.2.1 is clearly visible. The final plot (Figure 4.16 (d)) displays exactly two periods of the phase measuring residual as measured along the first 4π radians of the reference plane signal with the tilt term $2\pi f_0 x$ removed (for $\gamma = 2.2$). Visually comparing Figure 4.16 (d) with the analytical residual function estimation depicted in Figure 4.3, reveals the validity of the analytical findings. Considering the findings of this simulation we have verified Hu *et al.*'s [146] analytical study and thus described the relationship between projector gamma and reconstruction error for the 3 Step PMP approach.

4.5.2.2 4 Step

The 4 Step PMP simulation results are depicted in Figure 4.17. Figure 4.17 (a) depicts

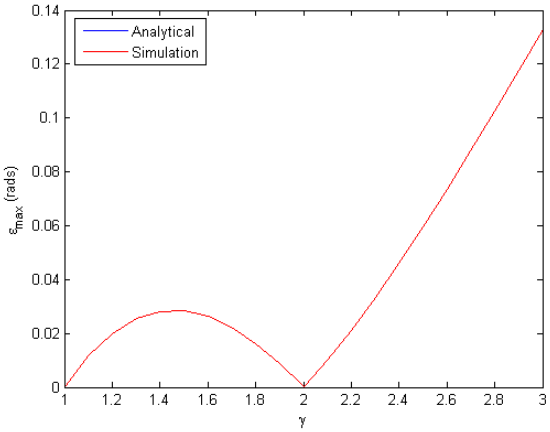

(a) Maximum Absolute Phase Measurement Error

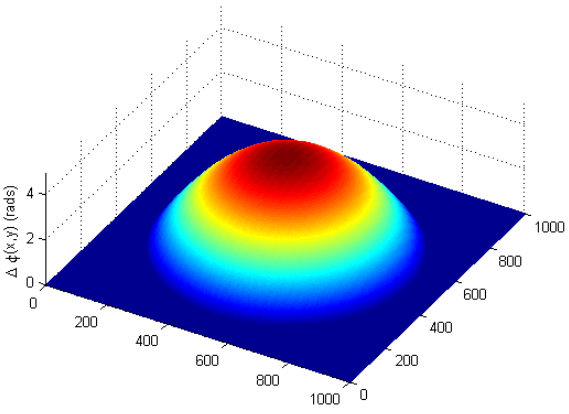

(b) $\Delta\phi(x, y)$ (rads), γ = 2.2

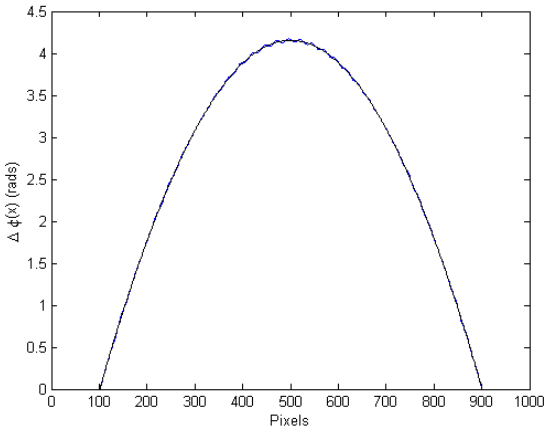

(c) Reconstruction Cross-section, γ = 2.2

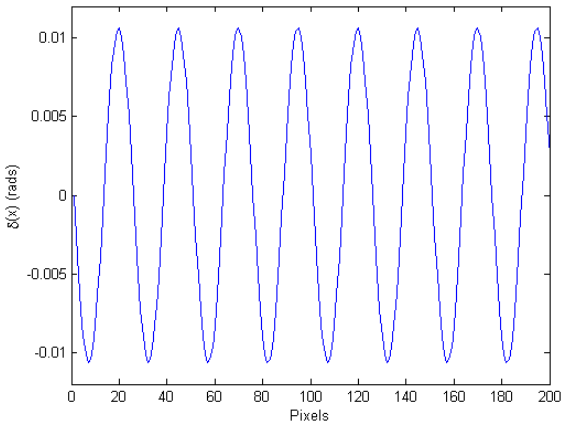

(d) Reference Phase Measuring Residual, γ = 2.2

Figure 4.17: 4 Step PMP Gamma distortion Simulation

both the analytical and simulation representations of the maximum absolute phase measuring error, ε_{max}, for the various typical values of γ. As concluded in Section 4.3.2.2 the 4 Step variation of the PMP algorithm is insensitive to 2nd order non-linearities and hence $\varepsilon_{max} = 0$ for all γ under these assumptions. Clearly, from the simulation results the 4 Step PMP algorithm is not completely insensitive to gamma non-linearities given the measurable phase estimation error. The phase measuring residual depicted in Figure 4.17 (d) is resultant of higher order harmonic terms (namely third order) considering as $\gamma \rightarrow \infty$, $\varepsilon_{max} \rightarrow \infty$. Nevertheless, the second order assumption still remains a valid approxi-

mation considering the magnitude of the maximum absolute phase measuring residual is just over 2% of a spatial period for the case when $\gamma = 3$. This is exemplified in Figure 4.17 (b) and (c) where the estimation of $\Delta\phi(x, y)$ closely represents the simulated phase distribution depicted in Figure 4.14.

The 4 Step PMP resilience to γ distortion under practical conditions is further justified considering phenomena such as noise will likely inhibit the accurate measurement of sub 2% of a wavelength (for an appropriately selected f_0). Another important practical justification is the further attenuation of higher order harmonics resultant of the optical transfer function of the projection optics. The effects of the optical transfer function of the projection optics on fringe harmonic structure will be considered in Chapter 5.

4.5.3 90° 3 Step

The 90° 3 Step simulation results are depicted in Figure 4.18. Figure 4.18 (a) depicts both the analytical and simulation representations of the maximum absolute phase measuring error, ε_{max}, for the various typical values of γ. As can be seen the 2nd order analytical prediction of the 90° 3 Step γ sensitivity closely imitates that of the simulated case with little if any deviation even for higher values of γ where the higher order harmonic contribution is more significant. Contrasting the phase estimations depicted in Figure 4.18 (b) and (c) for the 90° 3 Step case with the traditional 3 Step PMP case for $\gamma = 2.2$, the heighten sensitivity of the 90° 3 Step is clearly visually evident. Referring now to the plot depicted in Figure 4.18 (d) and that of the analytically predicted residual for $\gamma = 2.2$ shown in Figure 4.4, the similarities of the general shape and magnitude of the phase measuring residual associated with the 2nd order assumption can be clearly observed.

Therefore, given the findings of the 90° 3 Step simulation, the validity of the analytical findings has been verified, and moreover, the 2nd order γ sensitivity assumption for the 90° 3 Step technique.

4.5.4 90° 3 Step with Phase Offset

The 90° 3 Step with Phase Offset simulation results are depicted in Figure 4.19. Figure 4.19 (a) depicts both the analytical and simulation representations of the maximum abso-

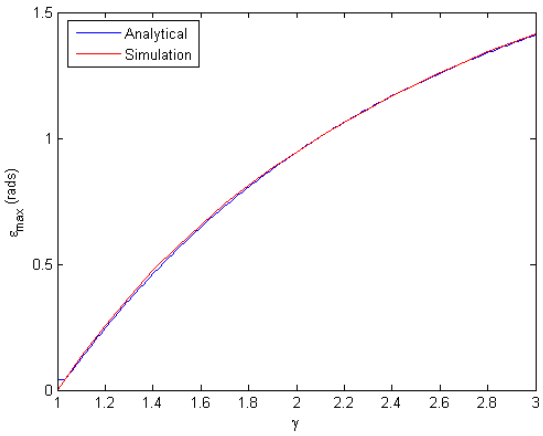

(a) Maximum Absolute Phase Measurement Error

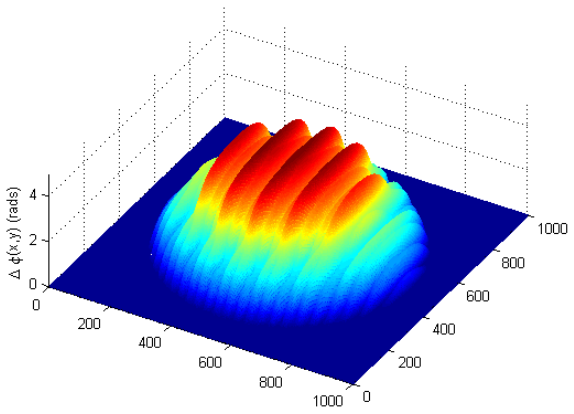

(b) $\Delta\phi(x, y)$ (rads), γ = 2.2

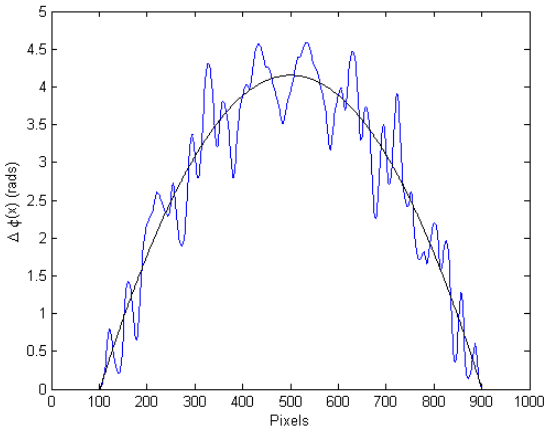

(c) Reconstruction Cross-section, γ = 2.2

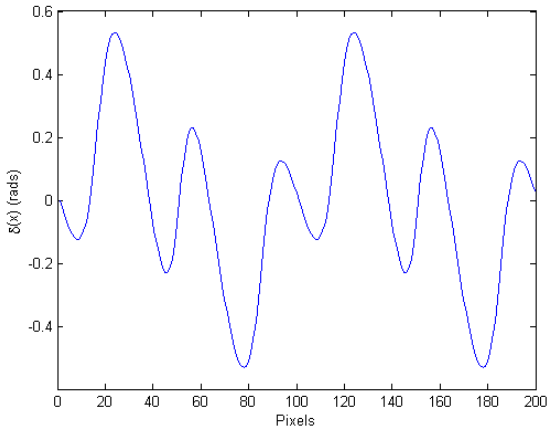

(d) Reference Phase Measuring Residual, γ = 2.2

Figure 4.18: 90° 3 Step Gamma distortion Simulation

lute phase measuring error, ε_{max}, for the various typical values of γ. As can be seen the 2nd order analytical prediction of the 90° 3 Step with Phase Offset γ sensitivity closely imitates that of the simulated case with little if any deviation even for higher values of γ where the higher order harmonic contribution is more significant. Considering Figure 4.19 (b), (c) and (d) relative to the standard 90° 3 Step case, the initial $\frac{\pi}{4}$ radian phase offset of the phase measuring residual is clearly evident, while the sensitivity is identical as anticipated. The phase residual as depicted in Figure 4.19 (d) also resembles the analytically estimated residual function as depicted in Figure 4.7.

Therefore, given the findings of the 90° 3 Step with Phase Offset simulation, the validity of the analytical findings has been verified, and moreover, the 2nd order γ sensitivity

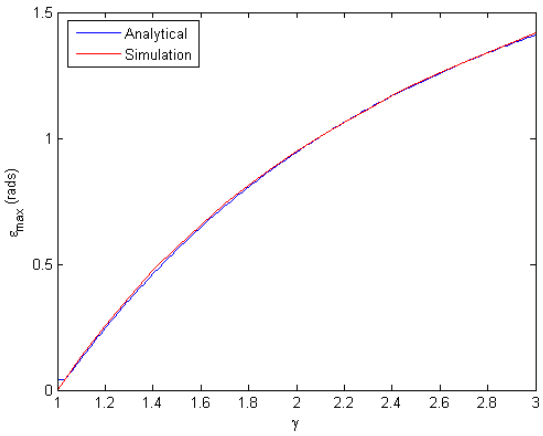

(a) Maximum Absolute Phase Measurement Error

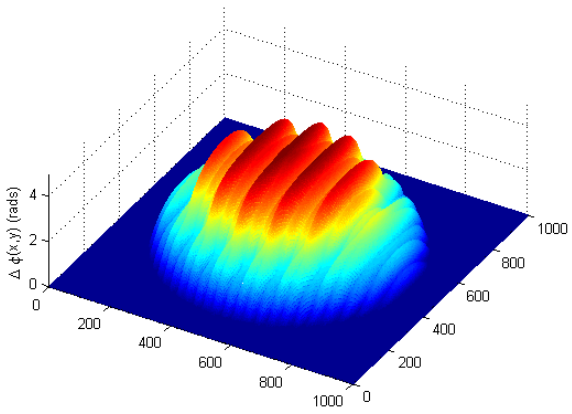

(b) $\Delta\phi(x, y)$ (rads), γ = 2.2

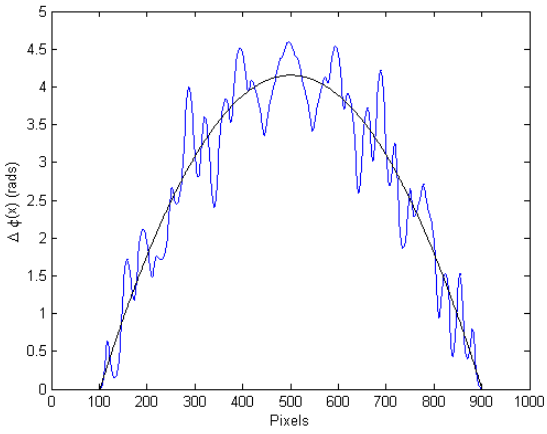

(c) Reconstruction Cross-section, γ = 2.2

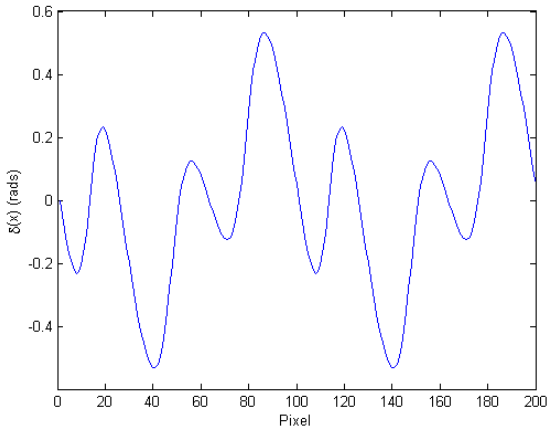

(d) Reference Phase Measuring Residual, γ = 2.2

Figure 4.19: 90° 3 Step with Phase Offset Gamma distortion Simulation

assumption for the 90° 3 Step with Phase Offset technique.

4.5.5 2+1

The 2+1 simulation results are depicted in Figure 4.20. Figure 4.20 (a) depicts both the analytical and simulation representations of the maximum absolute phase measuring error, ε_{max}, for the various typical values of γ. Similar to the two previously presented 90° variations, the 2nd order analytical prediction of the 2+1 γ sensitivity closely imitates that of the simulated case with little if any deviation over the entire range of typical γ values. Also similar to the two previously presented 90° variations the appropriate phase offset is observable in Figures 4.20 (b), (c) and (d), and furthermore, the phase residual as

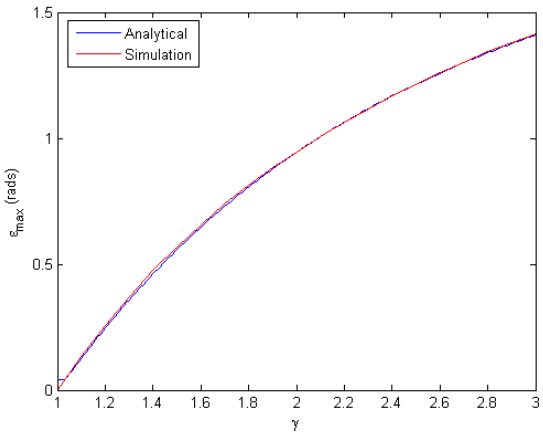

(a) Maximum Absolute Phase Measurement Error

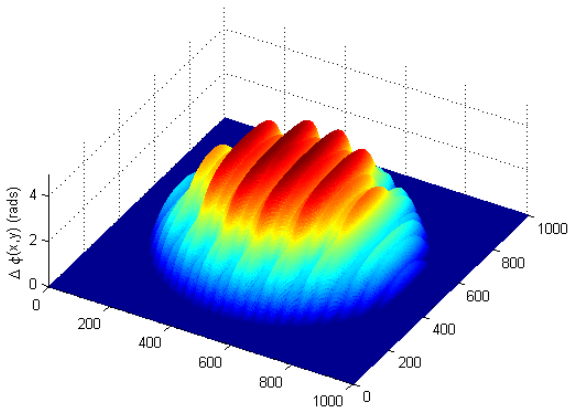

(b) $\Delta\phi(x, y)$ (rads), γ = 2.2

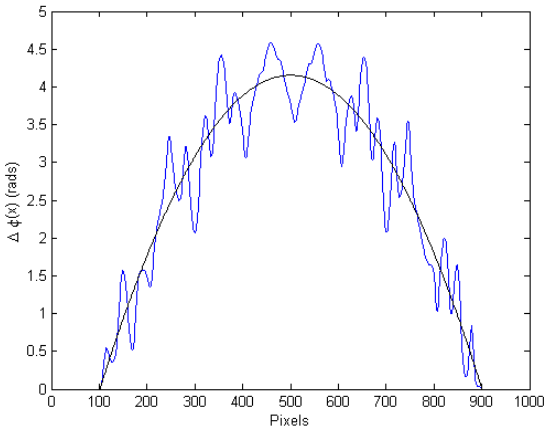

(c) Reconstruction Cross-section, γ = 2.2

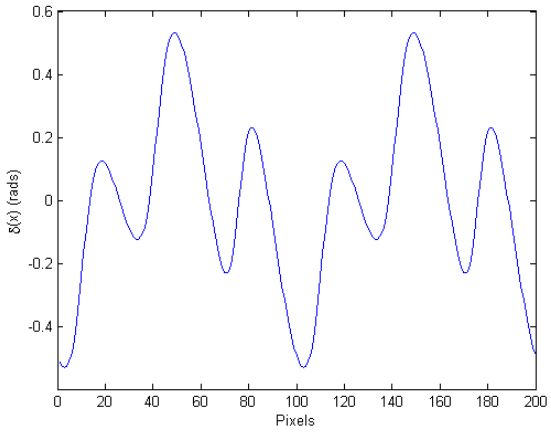

(d) Reference Phase Measuring Residual, γ = 2.2

Figure 4.20: 2+1 Gamma distortion Simulation

depicted in Figure 4.20 (d) also resembles the analytically estimated residual function as depicted in Figure 4.8. To more clearly demonstrate the significance of the initial fringe offset, the residual errors for each of the $90°$ techniques for $\gamma = 2.2$ is depicted in Figure 4.21. The plot clearly shows the respective phase offsets for each of the $90°$ variations and also the similar γ sensitivity. These results also further verify the previously demonstrated γ sensitivity dependence on phase stepping parameter ζ_n.

Therefore, given the findings of the 2+1 simulation, the validity of the analytical findings has been verified, and moreover, the 2nd order γ sensitivity assumption for the 2+1 technique.

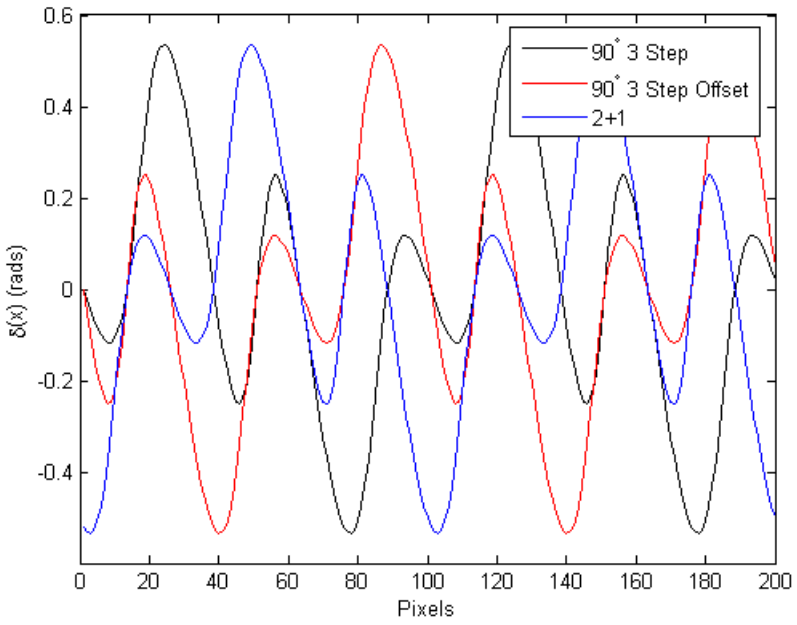

Figure 4.21: $90°$ Residual Functions

4.5.6 3+3

The 3+3 simulation results are depicted in Figure 4.22. Figure 4.22 (a) depicts both the analytical and simulation representations of the maximum absolute phase measuring error, ε_{max}, for the various typical values of γ. As can be seen in Figure 4.22 (a) in this case the analytical prediction based on the derivation outlined in Section 4.3.6 does not accurately represent the actual simulated scenario. This is somewhat demonstrated by contrasting Figure 4.22 (d) and the analytically derived residual shown in Figure 4.9 for the case where $\gamma = 2.2$, (although the result becomes more prominent as $\gamma \rightarrow 3$). The simulated residual function and the analytically derived function differ in magnitude and also in general appearance. Interestingly, for $\gamma > 2$ as the influence of higher order harmonic terms becomes more significant, the 2nd order prediction fails more significantly as shown in Figure 4.22 (a). Hence, the deviation can be assumed to be attributed to the contribution of higher order harmonic terms. To confirm this a secondary simulation demonstrating purely 2nd order harmonic distortion was conducted. The results of this simulation are depicted in Figure 4.23 (a). Given the secondary simulation results emulate the analytical findings quite well the assumption that higher order harmonics are contributing to the γ sensitivity of the 3+3 technique is confirmed. To further verify these findings Figure 4.23

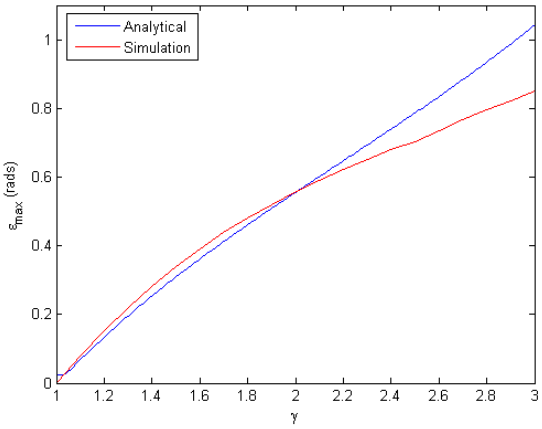

(a) Maximum Absolute Phase Measurement Error

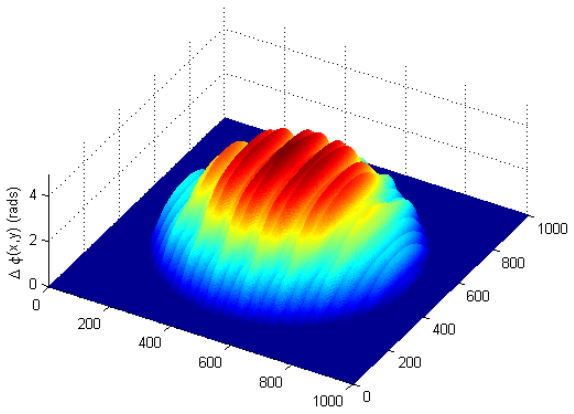

(b) $\Delta\phi(x, y)$ (rads), γ = 2.2

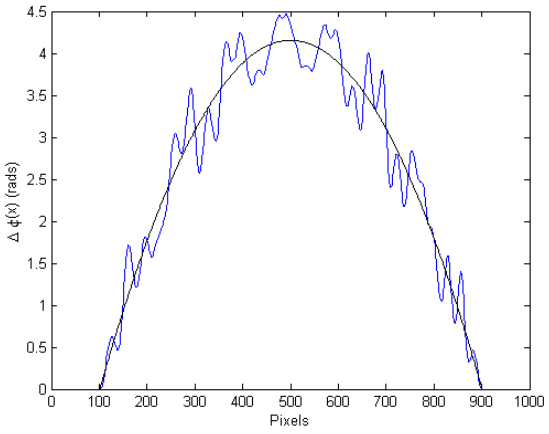

(c) Reconstruction Cross-section, γ = 2.2

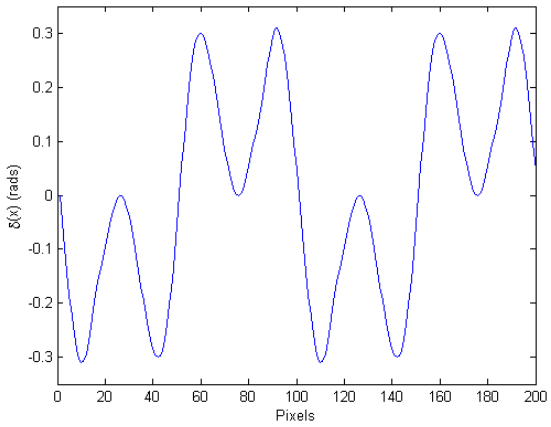

(d) Reference Phase Measuring Residual, γ = 2.2

Figure 4.22: 3+3 Gamma distortion Simulation

(b) depicts a plot of two cycles of both the analytically predicted and simulated $90°$ 3 Step residual function, for $\gamma = 3$. As can be seen although the maximum absolute phase measuring sensitivity is identical for both the simulated and analytical cases (as demonstrated for all $90°$ variations) the general appearance of the residual is influenced by higher order terms. Since the 3+3 estimation is obtained by averaging two $90°$ estimations, the deviations between the analytical and simulation residuals, (as depicted in Figure 4.23 (b)) are further compounded and are responsible for the poor analytical estimation of the 3+3 sensitivity as seen in Figure 4.22 (a).

Therefore, given the findings of 3+3 simulation it can be concluded that the 2nd order harmonic assumption is not an adequate assumption to gauge the sensitivity of the 3+3

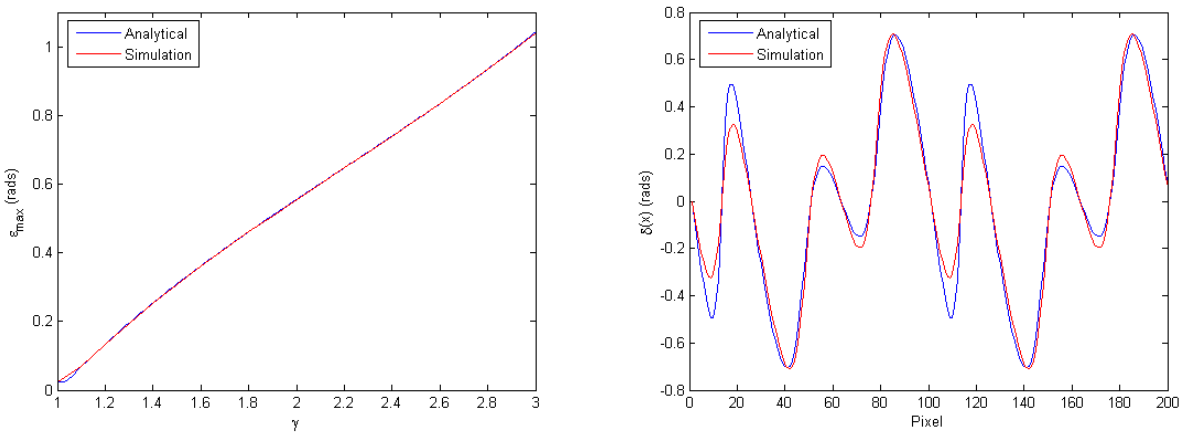

(a) Maximum Absolute Phase Measurement Error (b) Analytical and Simulated 90° Residual, γ = 3

Figure 4.23: 3+3 2nd order harmonic Simulation

technique in the presence of γ distortion.

4.5.7 Double Three Step

The Double Three Step simulation results are depicted in Figure 4.24. Figure 4.24 (a) depicts both the analytical and simulation representations of the maximum absolute phase measuring error, ε_{max}, for the various typical values of γ. As can be seen the 2nd order analytical prediction of the Double Three Step γ sensitivity closely imitates that of the simulated case with little if any deviation over the entire range of typical γ values. Figures 4.24 (b) and (c) display an example estimation of phase distribution $\Delta\phi(x, y)$, and arbitrary cross-section, respectively, for a given γ value of 2.2. Comparing the residual functions and phase estimations for both the Double Three Step and the traditional 4 Step PMP approach the shortcomings of the Double Three Step approach become evident. Although specifically designed to compensate for gamma distortion (and namely the 2nd order contribution [96]) the 4 Step PMP technique out performs the Double Three Step method, despite the requirement of two additional fringe images for both reference and object surfaces. It should be noted that such results are only prominent given the modeling of the camera / projector non-linear intensity response as gamma distortion as outlined in Section 4.2. If for instance a 3rd order contribution was present the Double Three Step approach may be more effective in elimination of the harmonic distortion given the tech-

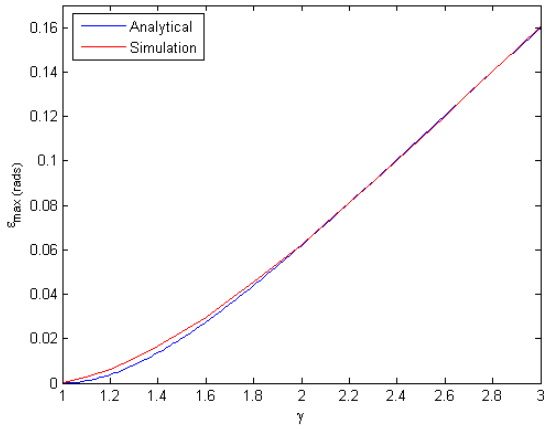

(a) Maximum Absolute Phase Measurement Error

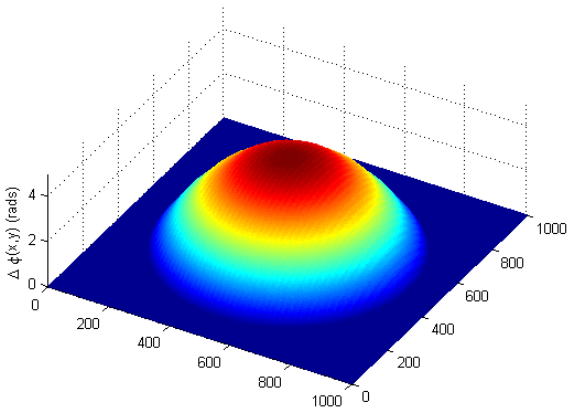

(b) $\Delta\phi(x, y)$ (rads), γ = 2.2

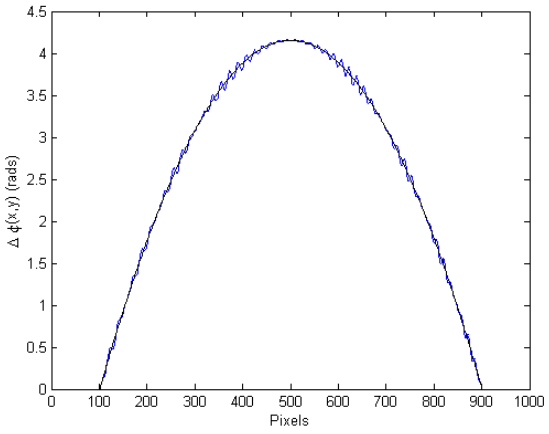

(c) Reconstruction Cross-section, γ = 2.2

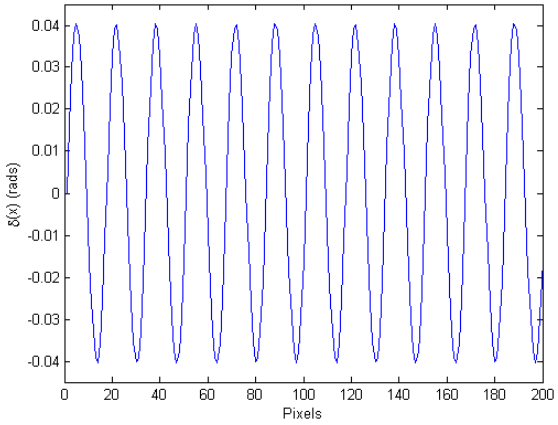

(d) Reference Phase Measuring Residual, γ = 2.2

Figure 4.24: Double Three Step Gamma distortion Simulation

nique is based on two 3rd order insensitive 3 Step estimations.

Therefore, given the findings of the Double Three Step simulation, the validity of the analytical findings has been verified, and moreover, the 2nd order γ sensitivity assumption for the Double Three Step technique.

4.5.8 Fourier Transform Profilometry (FTP)

The FTP simulation results are depicted in Figure 4.25. Figure 4.25 (a) depicts both the analytical and simulation representations of the maximum absolute phase measuring error, ε_{max}, for the various typical values of γ. Unlike the previous techniques where the influence of higher order harmonics can be somewhat eliminated through step selection

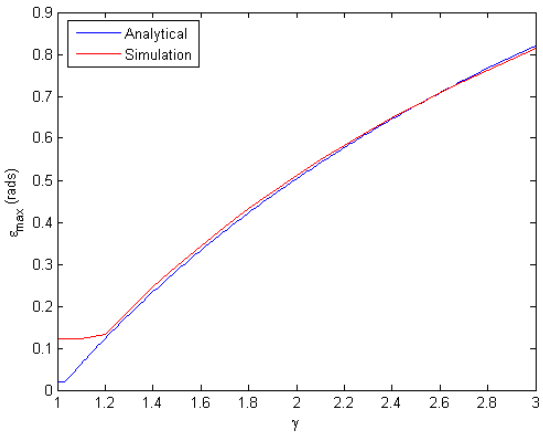

(a) Maximum Absolute Phase Measurement Error

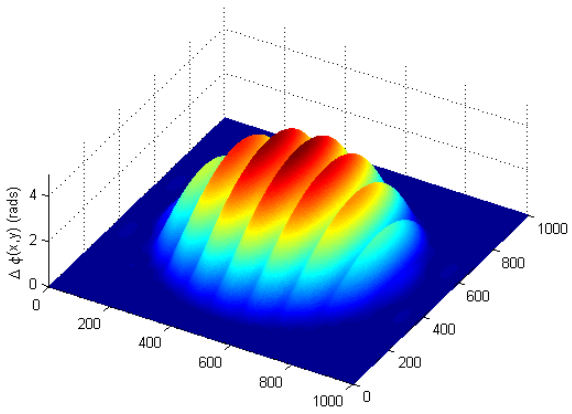

(b) $\Delta\phi(x, y)$ (rads), γ = 2.2

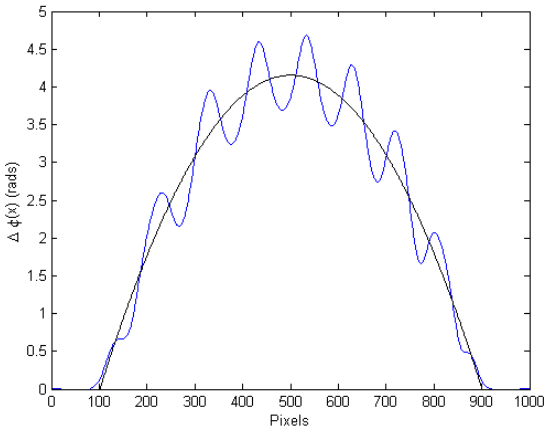

(c) Reconstruction Cross-section, γ = 2.2

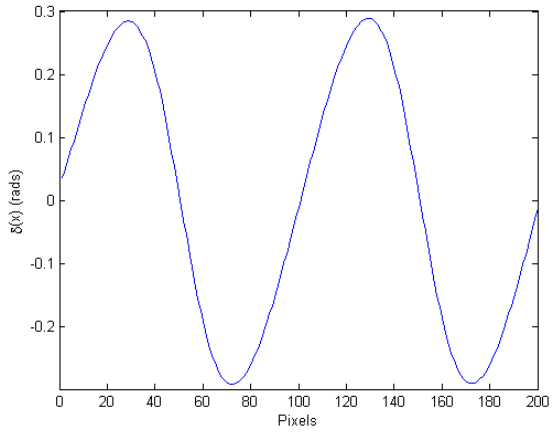

(d) Reference Phase Measuring Residual, γ = 2.2

Figure 4.25: Fourier Transform Profilometry Gamma distortion Simulation

as discussed in [146], the FTP technique relies on filtering approaches to attenuate higher order terms. In order to reveal the full influence of higher order γ related harmonics on the FTP technique we refrained from filtering in our FTP simulation [6]. And as can be seen even as $\gamma \rightarrow 3$ and the magnitude of the higher order harmonics increase, there is little if any deviation between the analytical and FTP simulated curves, with the only recognisable deviation occurring for the very low values of γ. This discrepancy is directly a result of the inherent accuracy limitations of the DFT operation involved in the FTP estimation.

[6] Apart from the necessary dc and negative frequency components

Subsequent to the sensitivity of the FTP approach is periodicity of the residual function depicted in Figure 4.25 (d). In contrast to the 3 Step PMP residual the period of oscillation is one third that of FTP approach as anticipated in the analytical derivations. Hence, it can be concluded that the 3 Step PMP and FTP approaches are equally sensitive in terms of absolute maximum phase measuring error, however, the PMP approach is exactly 3 times more sensitive in terms of how much phase modulation is required to incur a maximum phase measurement error.

Therefore, given the findings of the FTP simulation, we have verified Hu *et al.*'s [146] analytical study, and moreover, the 2nd order γ sensitivity assumption for the FTP technique.

4.5.9 Magnitude of Measurement Error

Taking into consideration the simulated system parameters, l_0, d_0 and f_0, the phase measurement error can be converted into mm's, and thereby, the sensitivity of each of the fringe processing techniques in the presence of gamma distortion can be compared in terms of an example physical quantity. The plot depicting this performance comparison is shown as Figure 4.26. As can be seen the traditional 4 Step PMP approach is least sensi-

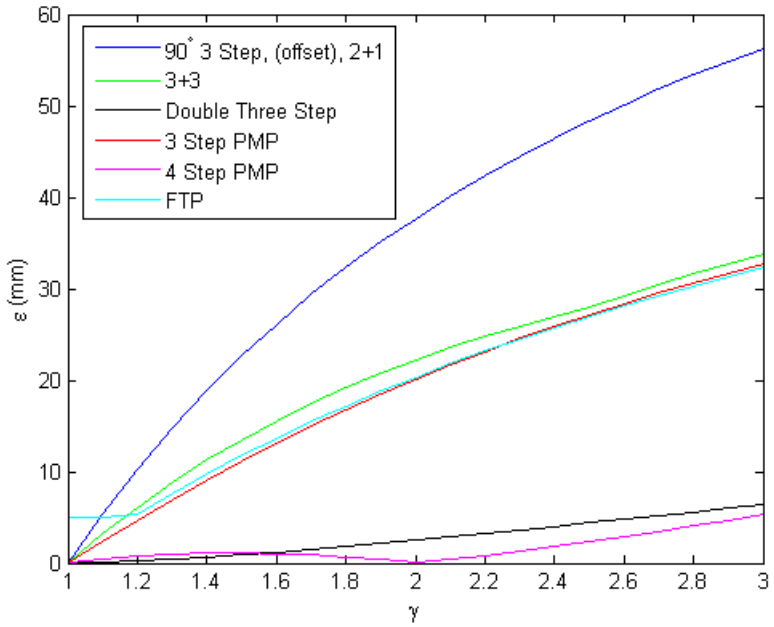

Figure 4.26: Various Fringe Processing technique and corresponding γ sensitivity, ϵ (mm)

tive to gamma non-linearities out performing the Double Three Step approach for almost all typical values of γ. The sensitivity of the PMP and FTP techniques are almost identical as anticipated, with the 3+3 technique demonstrating a slightly higher sensitivity to γ fringe non-linearities over the entire depicted range of γ. In fact, by this result, previous claims that the 3+3 technique was resilient in the presence of gamma fringe distortion [98] have been shown to be false. The 90° variations proved to be most sensitive to the γ fringe non-linearities, further confirming that the sensitivity of the stepping algorithms is highly dependent of the fringe phase offset term ζ_n as opposed to initial fringe offset. Finally, an important observation to note is the heightened γ sensitivity for minimum step techniques which are often associated with dynamic fringe profiling applications.

4.6 Experimentation Evaluation

To provide some insight into the practical significance of the Display Gamma study, experimental results were established in an effort to practically measure the influence the display phenomena has on the respective fringe processing algorithms. One of the significant problems associated with the true practical measurement of the influence of Display Gamma for fringe processing is the ability to accurately measure the amount of error by traditional experimentation. The accurate measurement of error is problematic in practical scenarios as the amount of actual phase modulation introduced into a fringe by the object's surface is an unknown variable. The approach utilised here addresses this concern by employing the phase emulation approach described in Section 3.6.1. By this method it is possible to artificially introduce a known modulation into experimentally captured fringe images in software, thereby, allowing for the appropriate practical evaluation of the Display Gamma phenomena for fringe processing.

To test each of the studied fringe processing techniques a number of reference fringe images with the appropriate phase offsets, ζ_n, were projected and acquired. The fringes were projected using a Hitachi CP-X260 3-LCD projector with a native XGA resolution (1024x768), while the fringe images were captured using a DuncanTech MS-3100 3-CCD camera with a resolution of 1392x1040. To convey as much relevance to the simulation results as possible, the spatial period of the projected fringe images was adjusted such

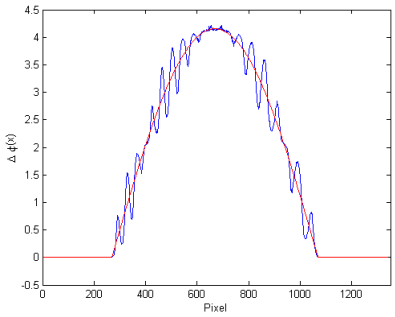

(a) 3 Step PMP

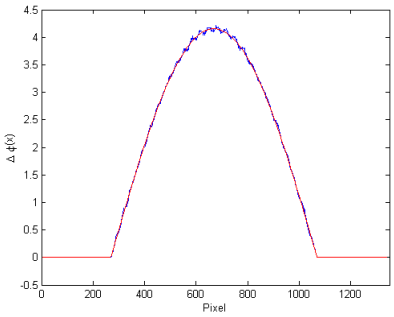

(b) 4 Step PMP

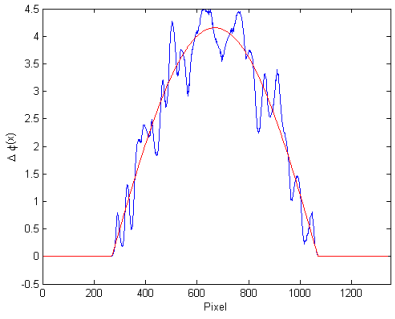

(c) 3 Step 90°

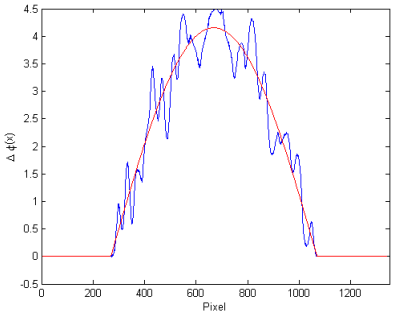

(d) 3 Step 90° with Offset

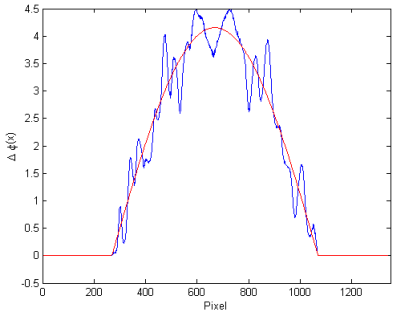

(e) 2+1

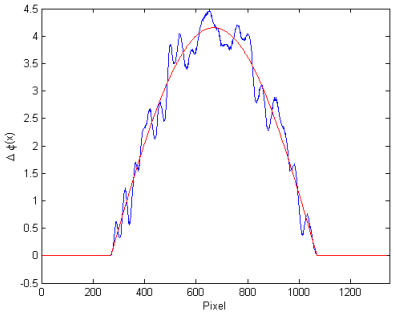

(f) 3+3

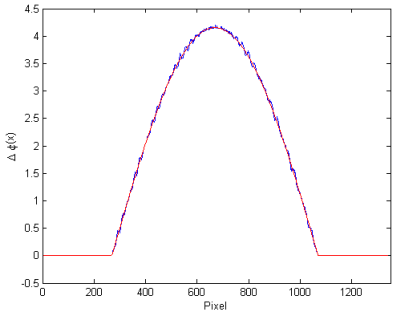

(g) Double Three Step

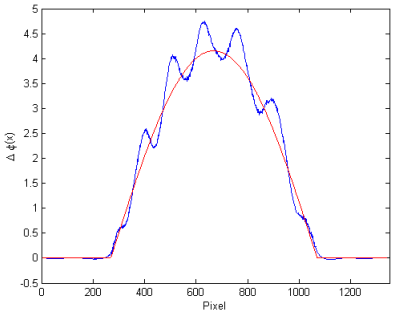

(h) FTP

Figure 4.27: Experimental Reconstructions

that approximately 10 fringes spanned the entire measurement volume. The continuity of results was further facilitated by introducing a similar dome shaped phase modulation with an identical peak value of 4.154rads. The results of the practical study for each of the 8 fringe processing algorithms is collectively demonstrated in Figure 4.27, with the measured maximum absolute phase measurement errors shown in Table 4.2. Also

Technique	Measured ε_{max} (rads)	Estimated ε_{max} (rads)
3 Step PMP	0.5815	0.5547
4 Step PMP	0.0875	0.0132
90° 3 Step	1.0185	1.0227
90° 3 Step with Offset	1.0205	1.0227
2+1	1.0563	1.0227
3+3	0.6014	0.5996
Double Three Step	0.1065	0.0742
FTP	0.7194	0.5547

Table 4.2: Measured Absolute Maximum Measurement Error (ε_{max}) and Estimated Absolute Maximum Measurement Error (ε_{max})

included in Table 4.2 is the estimated values of ε_{max}. The estimations are based on the analytical Display Gamma findings with $\gamma = 2.127$ (with the exception of the 4 Step PMP and 3+3 techniques in which the simulation results are provided). The γ value was determined by averaging the measured values of p for each of the fringe images and substituting into Equation (4.17).

As can be seen from the practical results, with the exception of the FTP approach, the relative gamma sensitivity of each of the various fringe processing algorithms reflects the estimated relative gamma sensitivities as demonstrated by the analytical and simulation findings. The FTP anomaly can be attributed to DFT leakage errors associated with the inadequate windowing of an integer number of fringes. This problem is inherent to the practical implementation of the FTP approach given an initial phase modulation is

unavoidable for triangulation projection systems. As anticipated, the 4 Step PMP and Double Three Step approaches provide a significantly more accurate estimation of the arbitrary phase modulation relative to the other techniques. It was however found that the camera / projector non-linearity utilised in this experimentation presented an elevated 3rd order component relative to the Display Gamma modeled response. This 3rd order contribution accounts for the discrepancy between the practically measured 4 Step PMP sensitivity, and the estimated sensitivity. Further, the 3rd order contribution also accounts for the marginally measurable 4 Step PMP gamma resilience relative to the Double Three Step technique. Nevertheless, all the remaining experimentally measured sensitivities closely reflect the analytical / simulation findings, with a maximum deviation of just 0.0336 radians. This deviation corresponds to approximately 0.5% of a wavelength, an error which is consistent with noise limitations inherent to the acquisition and processing of the experimental fringe images for the given practical arrangement.

4.7 Summary

The work embodied within this Chapter has thoroughly investigated the impact Display Gamma non-linear luminance effects have on the Fringe Projection techniques. Previously, misconstrued issues such as the spectral harmonic structure and magnitude of the harmonic distortion typical of a digitally projected fringe signal including the characteristics and magnitude of the resulting phase residual for a range of fringe processing algorithms have been clarified. The analytical findings including the digital fringe approximate analysis have been verified by simulation and, thereby, the 2nd order harmonic was identified as the single most significant contribution defining the magnitude of phase measuring error for the majority of tested fringe processing algorithms. It was however concluded that the 2nd order assumption does not hold for the 3+3 technique. The vulnerabilities of the purpose designed Double Three Step technique were also exposed, with the standard 4 Step PMP technique shown to be more resilient in the presence of γ distortion. A further important conclusion was the confirmation of a heighten γ sensitivity for minimum step techniques (including FTP). This is particularly important considering minimum step techniques are often associated with dynamic fringe profiling applications.

The practical significance of the Display Gamma study was verified with the practical findings demonstrating a consistency of results for experimentally captured fringe data.

Now that an analytical framework and moreover a verified study is in place to describe the nature and magnitude of γ related Fringe Projection errors, this model can be employed to study more practical Display Gamma related issues. The following chapter will now deal with some of the additional practical issues associated with Display Gamma and Fringe Projection 3D sensing.

Chapter 5

Additional Display Gamma Phenomena

5.1 Introduction

The objective of this chapter is to identify, examine and verify some of the key practical aspects associated with the Fringe Projection Display Gamma phenomena. In the past many of the supplementary practical Display Gamma Fringe Projection issues have gone either uninvestigated or misunderstood, primarily due to the lack of an adequate analytical framework to describe the influence of γ for projected fringes. Given the research provided in Chapter 4, the ability to effectively investigate some of the more practical Display Gamma phenomena is made possible. The issues of primary practical concern identified and examined in this chapter include:

- Fringe offset and contrast manipulation
- Temporal luminance (otherwise referred to as Temporal Display Gamma) and;
- The fringe image formation process.

Each of these phenomena are examined, identified and verified via analytical investigation, simulation and / or empirical analysis.

5.2 Fringe Offset and Contrast Parameter Manipulation

In the Display Gamma study presented in Chapter 4, it was assumed that fringe offset and contrast parameters, a and b, were equivalent. Naturally this is a specific case, and as

was shown the $a = b$ scenario is representative of a worst case scenario where harmonic distortion is maximised. The objective of this section is to investigate the influence of the fringe offset and contrast parameters on the harmonic structure of the digitally projected fringe and therefore system accuracy.

Referring to each of the Equations defining the absolute maximum phase measuring error, ε_{max}, for each of the fringe processing approaches (see Chapter 4), system accuracy is a monotonically increasing relation, increasing with p. Considering now that $\sum_{m=2}^{\infty} \frac{c_m}{c_1}$ (Equation (4.4)) has been shown to also be a monotonically increasing function for all γ (which is maximised when $\frac{b}{a}$ is maximised), it is therefore possible to reduce the influence of the γ of a projector through simple fringe parameter adjustment. In other words, it is possible to optimise the digitally projected fringe image and hence improve system accuracy by simple fringe parameter adjustment without having any prior system knowledge of γ. For instance, considering the well exploited 3 Step PMP technique for the following three scenarios

$$a = b$$

$$a = 0.6,\ b = 0.4$$

and

$$a = 0.8,\ b = 0.2,$$

where as per the previous simulation we assume that $l_0 = 5$m, $d_0 = 2$m and $f_0 = 10$ fringes/m, the corresponding improvement in maximum absolute system accuracy can be observed. Figure 5.1 displays ϵ for the $a = 0.6, b = 0.4$, $a = 0.8, b = 0.2$ and $a = b$ cases for the typical range of γ for visual comparison. The gamma sensitivity reduction for the $a = 0.6, b = 0.4$ case is clearly evident, and furthermore, for the $a = 0.8, b = 0.2$ case. To generalise the accuracy improvement Figure 5.2 displays the percentage improvement in absolute maximum error for the manipulation of fringe parameters, $a = 0.6, b = 0.4$ and $a = 0.8, b = 0.2$ with respect to the worst case scenario $a = b$.

Referring now to the input / output intensity curve for the cases where $\gamma = 1, 2, 3$, as seen in Figure 3.7 (page 74) the fringe parameter manipulation relation can be visualised graphically. Considering the case where fringe contrast b is small, the projected sinusoid will only be using a small range of intensity values and hence the relationship

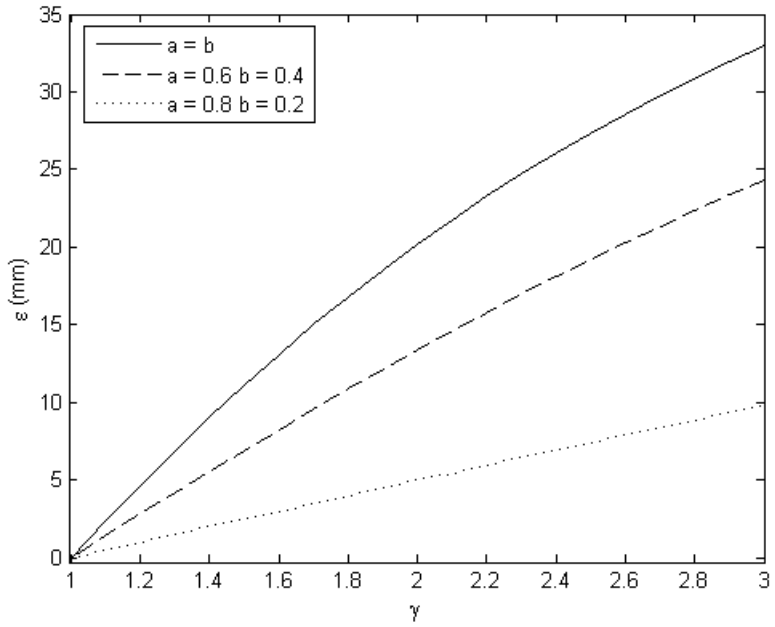

Figure 5.1: 3 Step PMP Maximum absolute error, $a = b$, $a = 0.6, b = 0.4$ and $a = 0.8, b = 0.2$

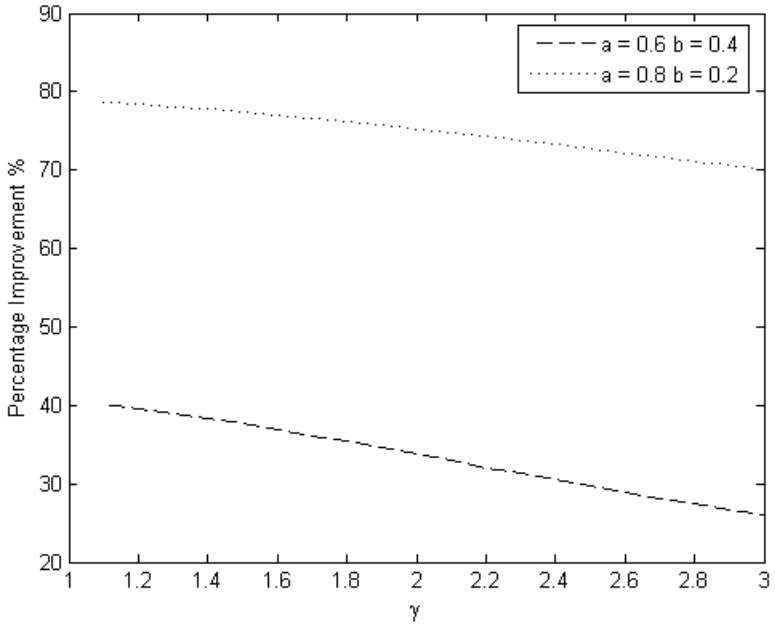

Figure 5.2: Percentage Improvement in system accuracy, for $a = 0.6, b = 0.4$ and $a = 0.8, b = 0.2$ relative to $a = b$ Vs. γ

between the neighbouring intensity values could be assumed linear. Altering a shifts the values the fringe contrast embraces and therefore increasing a shifts the fringe contrast towards the top right of the Figure 3.7, where the relation evidently presents a more linear characteristic.

Clearly, in the theoretical case significant improvements through simple manipulation of fringe contrast and offset are recognisable, however, in practice these manipulations are limited by contrast ratios of projected images and camera fidelity. Of particular concern is camera electronic noise. If we assume the noise power to be constant and denote the SNR when the entire contrast range is utilised as SNR_{MAX}, the SNR when partially utilising the contrast range is given as

$$\text{SNR} = \text{SNR}_{MAX} + 20\log(2b), \tag{5.1}$$

For the above example where $b = 0.4$, if we assume a SNR_{MAX} of 30dB the SNR becomes 25.56dB. Hence, the optimisation of system accuracy based on the adjustment of fringe parameters a and b is highly dependent on system projection and acquisition devices and / or further signal processing to improve SNR such as spatial filtering including median filtering or gaussian smoothing.

5.2.1 Empirical Verification

To verify the appropriate manipulation of fringe offset and contrast parameters to yield Fringe Projection optimisation, experimental results were established by profiling an actual surface. The spatial resolution of the captured fringe image was measured to be 0.194 mm/pixel, corresponding to a spatial period of 17.1mm or spatial frequency f_0 of 58.5 fringes/m. System parameters l_0 and d_0 were measured to be approximately 1.405m and 0.465m respectively. The profiled surface was a convex dome shape as depicted in Figure 5.3 (a). The maximum height of the hemispherical surface is 22.8mm with a diameter of 99mm with the thickness of the base material being approximately 16mm.

The 3 Step PMP reconstructions of the surface for the various fringe simulated fringe parameters are depicted in Figure 5.3. Figures 5.3 (b), (c) and (d) display the reconstructed surface for fringe parameters, $a = b$, $a = 0.6, b = 0.4$, and $a = 0.8, b = 0.2$, respectively. The suppression of the harmonic fringe components and corresponding fringe optimisa-

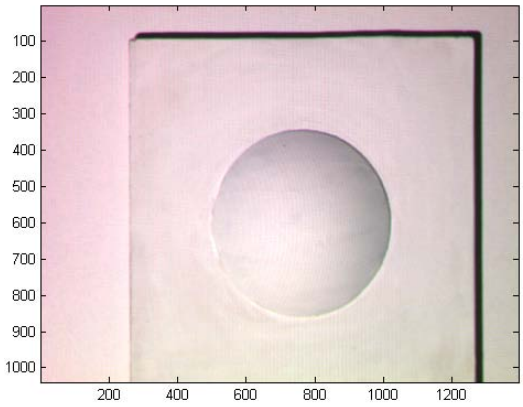

(a) Experimental Surface

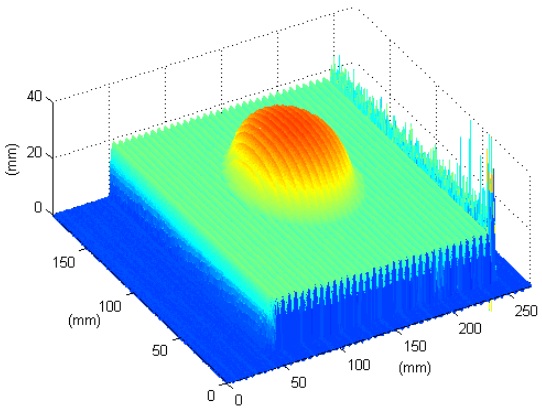

(b) Reconstruction of diffuse surface for fringe parameters, $a = b$.

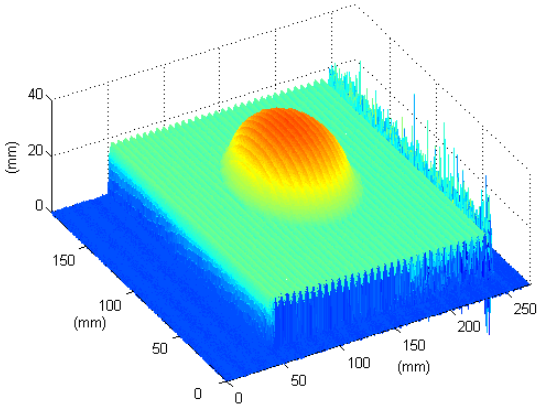

(c) Reconstruction of diffuse surface for fringe parameters, $a = 0.6, b = 0.4$.

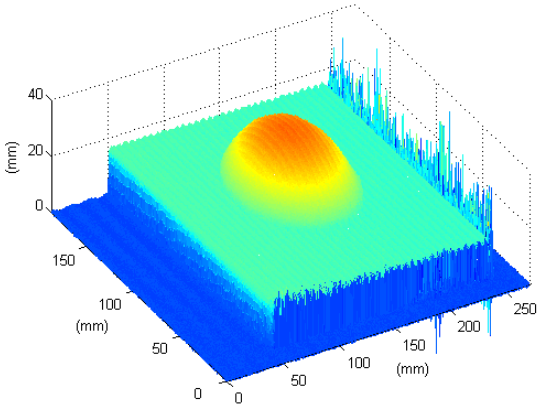

(d) Reconstruction of diffuse surface for fringe parameters, $a = 0.8, b = 0.2$.

Figure 5.3: Fringe parameter manipulation experimental results, 3-Step PMP reconstruction

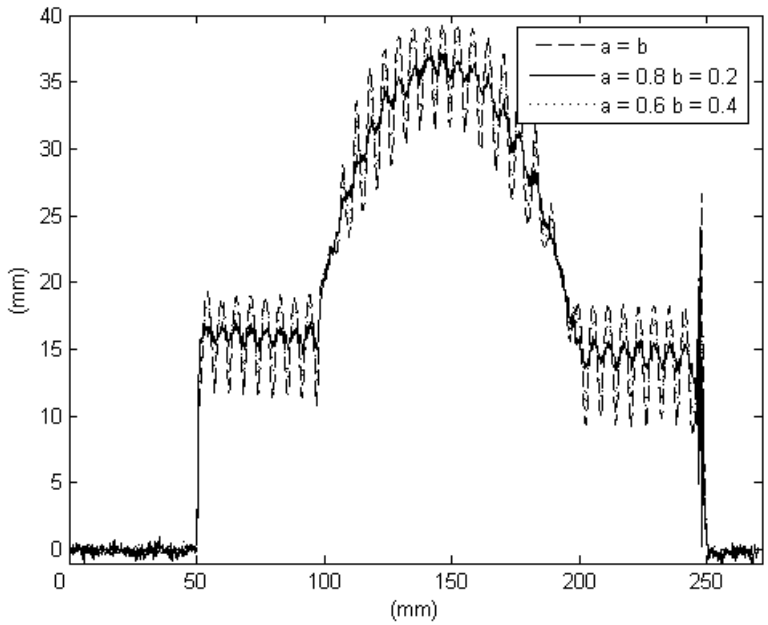

Figure 5.4: Cross-section of reconstructed diffuse surface for fringe parameters, $a = b$, $a = 0.6, b = 0.4$ and $a = 0.8, b = 0.2$

tion is clearly evident, with Figure 5.4 further emphasising the optimisation by depiction of an arbitrary cross-section of the reconstruction for each of the three cases. The depicted cross-section also clearly displays the decreased SNR for the $a = 0.8, b = 0.2$ case represented by the solid line relative to the $a = b$ case represented by the dashed line.

5.3 Temporal Gamma

Referring again to the Display Gamma derivations presented in the previous chapter, it was assumed that the γ of the projector / camera arrangement was a static phenomenon. Practically, gamma luminance presents temporal aspects, varying from fringe image to image and thereby resulting in further reconstruction error. The temporal instabilities of the projector / camera arrangement for DVP were first acknowledged by Rivera *et al.* [147] and later briefly discussed in Guo *et al.*'s [97] experimental analysis of gamma correction for DVP based fringe profilometers. Rivera *et al.* concluded that the temporal luminance effects were more prominent for large step numbers, however, this conclusion seems somewhat questionable, particularly, when taking the onset of single chip DLP

DVP technology into consideration. Single Chip DLP projectors temporally project images as a sequence of colour images with the human eye performing the integration of each primary component to form the appropriate colour. Therefore, considering that each primary channel typically has an individual gamma luminance attribute, temporal gamma becomes a identifiable concern. Furthermore, for minimum step based techniques including FTP, the temporal luminance effects become more influential in the estimation of phase component, $\omega(x, y)$, and have been practically observed for both LCD and DLP projection technologies.

Given the significant influence that temporal luminance poses for minimum step DFP approaches the implications regarding temporal gamma and its impact on system accuracy for the well known FTP fringe processing algorithm is investigated.

5.3.1 FTP Temporal γ / Harmonic Error Analysis

The residual phase error for the FTP approach presented in Section 4.3.8 assumed γ to be static. In practice it has been observed that the harmonic spectral distribution presents temporal aspects and hence further consideration of this analysis needs to be undertaken to measure the influence of this phenomenon.

Denoting γ and γ_0 as the gamma values for both the deformed and reference images respectively, the captured γ distorted fringe images can be defined as

$$\begin{aligned}\hat{g}(x, y) = a(x, y) + b(x, y)\cos[2\pi f_0 x + \phi(x, y)] \\ + c_m(x, y)\cos(m[2\pi f_0 x + \phi(x, y)])\end{aligned} \tag{5.2}$$

and

$$\begin{aligned}\hat{g}_0(x, y) = a(x, y) + b(x, y)\cos[2\pi f_0 x + \phi_0(x, y)] \\ + c_{0m}(x, y)\cos(m[2\pi f_0 x + \phi_0(x, y)])\end{aligned} \tag{5.3}$$

where $c_m(x, y)$ and $c_{0m}(x, y)$ are the functions representing the m-th order harmonic component for the deformed and reference fringe respectively.

Using the FTP method, an estimation of the actual phase map, $\Delta\phi(x, y)$, can be obtained by

$$\Delta\hat{\phi}(x, y) = Im(\log(\hat{g}(x, y)\hat{g_0}^*(x, y))) \tag{5.4}$$

Discarding the dc terms and substituting Equations (5.2) and (5.3) it can be seen that

$$\begin{aligned}
\Delta\hat{\phi} &= Im\Big(\log(b\cdot e^{i(2\pi f_0 x+\phi)}+c_m\cdot e^{i(2\pi f_0 x+\phi)m}) \\
&\quad +\log(b\cdot e^{-i(2\pi f_0 x+\phi_0)}+c_{0m}\cdot e^{-i(2\pi f_0 x+\phi_0)m})\Big) \\
&= Im\Big(\log(e^{i(2\pi f_0 x+\phi)}+\sqrt{p}\cdot e^{i(2\pi f_0 x+\phi)m}) \\
&\quad +\log(e^{-i(2\pi f_0 x+\phi_0)}+\sqrt{p_0}\cdot e^{-i(2\pi f_0 x+\phi_0)m})\Big) \\
&= Im\Big(i(2\pi f_0 x+\phi)+\log(1+\sqrt{p}\cdot e^{i(2\pi f_0 x+\phi)(m-1)}) \\
&\quad -i(2\pi f_0 x+\phi_0)+\log(1+\sqrt{p_0}\cdot e^{-i(2\pi f_0 x+\phi_0)(m-1)})\Big) \\
&= Im\Big(i(\phi-\phi_0)+\log(1+\sqrt{p}\cdot e^{i(2\pi f_0 x+\phi)(m-1)}) \\
&\quad +\log(1+\sqrt{p_0}\cdot e^{-i(2\pi f_0 x+\phi_0)(m-1)})\Big) \\
&= \Delta\phi+Im\Big(\log(1+\sqrt{p}\cdot e^{i(2\pi f_0 x+\phi)(m-1)}) \\
&\quad +\log(1+\sqrt{p_0}\cdot e^{-i(2\pi f_0 x+\phi_0)(m-1)})\Big)
\end{aligned} \tag{5.5}$$

where $p=\frac{c_m^2}{b^2}$ and $p_0=\frac{c_{0m}^2}{b^2}$ represent the power ratio of the m-th harmonic to the fundamental, for the deformed and reference fringe images.

Hence, the estimation error of the phase can be expressed as:

$$\begin{aligned}
\delta &= \Delta\hat{\phi}-\Delta\phi \\
&= \Delta\phi+Im\Big(\log(1+\sqrt{p}\cdot e^{i(2\pi f_0 x+\phi)(m-1)}) \\
&\quad +\log(1+\sqrt{p_0}\cdot e^{-i(2\pi f_0 x+\phi_0)(m-1)})\Big)-\Delta\phi \\
&= Im\Big(\log(1+\sqrt{p}\cdot e^{i(2\pi f_0 x+\phi)(m-1)}) \\
&\quad +\log(1+\sqrt{p_0}\cdot e^{-i(2\pi f_0 x+\phi_0)(m-1)})\Big)
\end{aligned} \tag{5.6}$$

Now defining $\Lambda(\cdot)$, as the function to extract the phase angle of the complex fringe term, it can be now shown that

$$\begin{aligned}
\Lambda(\omega,\rho) &= Im\Big(log(1+\sqrt{\rho}\cdot e^{i\omega(m-1)})\Big) \\
&= \arctan\left(\frac{\sqrt{\rho}\sin(\omega(m-1))}{1+\sqrt{\rho}\cos(\omega(m-1))}\right)
\end{aligned} \tag{5.7}$$

where $m=2$ for the second order contribution and ρ represents the respective fringe power ratios.

Now rewriting Equation (5.6), the phase measuring error can be given as

$$\begin{aligned}\delta &= \Lambda(2\pi f_0 x + \phi, p) + \Lambda(-(2\pi f_0 x + \phi_0, p_0)) \\ &= \Lambda(2\pi f_0 x + \phi, p) - \Lambda(2\pi f_0 x + \phi_0, p_0) \end{aligned} \tag{5.8}$$

Clearly the maximum measurement error can be defined as

$$\begin{aligned}\varepsilon_{max} &= \Lambda_{max}(2\pi f_0 x + \phi, p) - \Lambda_{min}(2\pi f_0 x + \phi_0, p_0) \\ &= \Lambda_{max}(\omega, p) - \Lambda_{min}(\omega, p_0) \end{aligned} \tag{5.9}$$

By now letting $\frac{\mathrm{d}\Lambda}{\mathrm{d}\omega} = 0$, the maximum and minimum values of Λ can be defined. That is

$$\Lambda_{max} = \arctan\left(\sqrt{\frac{p}{1-p}}\right) \tag{5.10}$$

and

$$\Lambda_{min} = -\arctan\left(\sqrt{\frac{p_0}{1-p_0}}\right) \tag{5.11}$$

Equation (5.9) can then be expressed as

$$\varepsilon_{max} = \arctan\left(\sqrt{\frac{p}{1-p}}\right) + \arctan\left(\sqrt{\frac{p_0}{1-p_0}}\right) \tag{5.12}$$

and hence substituting Equation (5.12) into Equation (2.69), the maximum absolute height measurement error ϵ is given as

$$\epsilon = \frac{l_0}{2\pi f_0 d_0} \cdot \left[\arctan\left(\sqrt{\frac{p}{1-p}}\right) + \arctan\left(\sqrt{\frac{p_0}{1-p_0}}\right)\right] \tag{5.13}$$

5.3.2 Gamma Compensated Analysis

Since an expression to describe the temporal measurement error is in place, the obvious question is what impact does the temporal variation of γ have on a γ compensated system. Naturally, this would be a factor dependent not only on the amount of temporal variation but also the way in which γ was compensated. For simplicity assuming that just one of the fringe images had been appropriately compensated the phase measuring error can be evaluated as

$$\delta = \Lambda(2\pi f_0 x + \phi, \rho) \tag{5.14}$$

and hence the maximum measurement error is

$$\epsilon = \frac{l_0}{2\pi f_0 d_0} \cdot \arctan\left(\sqrt{\frac{\rho}{1-\rho}}\right) \tag{5.15}$$

where ρ represents the temporal difference between the two γ compensated fringe images.

5.3.3 Simulation

In order to verify the validity of the analytical study a range of digitally projected fringe images with various values of γ and γ_0 were simulated and the corresponding system accuracy for the FTP reconstruction of a simulated surface measured. System parameters l_0, d_0 and f_0 were chosen to be 5m, 2m and 10 fringes/m respectively, corresponding to a spatial period of 100mm assuming an image spatial resolution of 1pixel/mm. The simulated fringe images are given as

$$g(x,y) = [0.5 + 0.5\cos(2\pi f_0 x + \phi(x,y))]^{\gamma}\,, \tag{5.16}$$

and

$$g_0(x,y) = [0.5 + 0.5\cos(2\pi f_0 x + \phi_0(x,y))]^{\gamma_0}\,, \tag{5.17}$$

where $\phi(x,y)$ corresponds to the hemispherical dome shape seen in Figure 5.7 (a) (and identical to the previous simulations). γ_0 was varied by +/- 5% of γ and based on the system parameters the expected maximum absolute error ϵ, was predicted according to the analytical study and the sensitivity resulting from the simulated gamma distorted fringes measured. Similar to the previous FTP simulation only the necessary dc and negative frequency components were removed to reveal the full influence of higher order harmonics. The results are displayed in Figure 5.5. The analytical error curves are represented with the solid line, with the simulation results indicated with the dotted lines.

As can be seen the analytical derivation accurately models the maximum absolute errors resulting from fringe temporal gamma distortion. In fact, it can be seen even as $\gamma \rightarrow 3$ and the magnitude of the higher order harmonics increase, there is little if any deviation between the analytical and FTP simulated curves. The only major discrepancy is seen for the very low values of gamma. This discrepancy is directly a result of the inherent accuracy limitations of the DFT operation involved in FTP reconstruction.

Based on these findings the analytical study describing the relationship between temporal projector gamma and reconstruction error for the FTP fringe processing approach has been verified. Furthermore, it can be concluded that for typical projector temporal γ fringe modeling, the 2nd order harmonic component is the single most significant contribution to phase measuring error for the FTP technique.

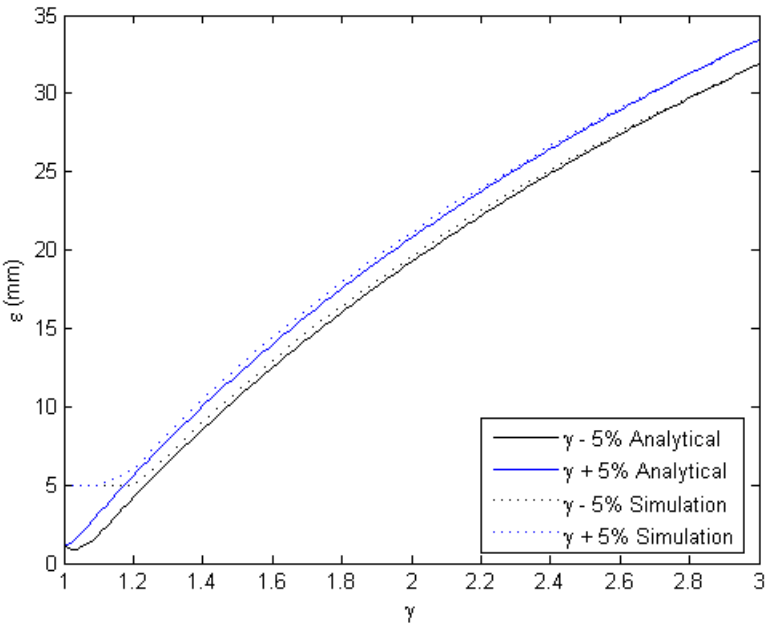

Figure 5.5: Maximum absolute profile measurement error: γ +/- 5%

5.3.4 Example FTP Reconstruction

To demonstrate the significance of this study, the temporal variance of γ for a typical DLP projector was measured as a practical example. Since DLP projectors temporally project RGB components, the temporal effects of γ are easily observed, as each colour channel typically yields an individual γ characteristic. An InFocus LP530 DLP projector was utilised to project a fringe image onto a reference plane from a distance of approximately 1500mm, while the projected fringe image was captured using a DuncanTech MS-3100 3-CCD camera. The integration time of the camera was adjusted to be approximately 20ms and a number of images of the projected fringe were obtained and the magnitude of p was measured. The variation in p is shown in Figure 5.6.

Based on the data obtained and displayed in Figure 5.6, using Equation (4.15) a maximum γ value of 2.47 and minimum of 2.13 was measured. Using these two values we simulated the reconstruction of the diffuse surface seen in Figure 5.7 (a) with system parameters l_0, d_0 and f_0 of 1500mm, 400mm and 10fringes/m respectively, where 1pixel = 1mm. The simulated projected fringes can be seen as Figures 5.7 (b) and (c) respectively, with the reconstructed surface shown as Figure 5.7 (d). As can be seen the harmonic distortion significantly reduces the accuracy of the FTP method. The mean measure-

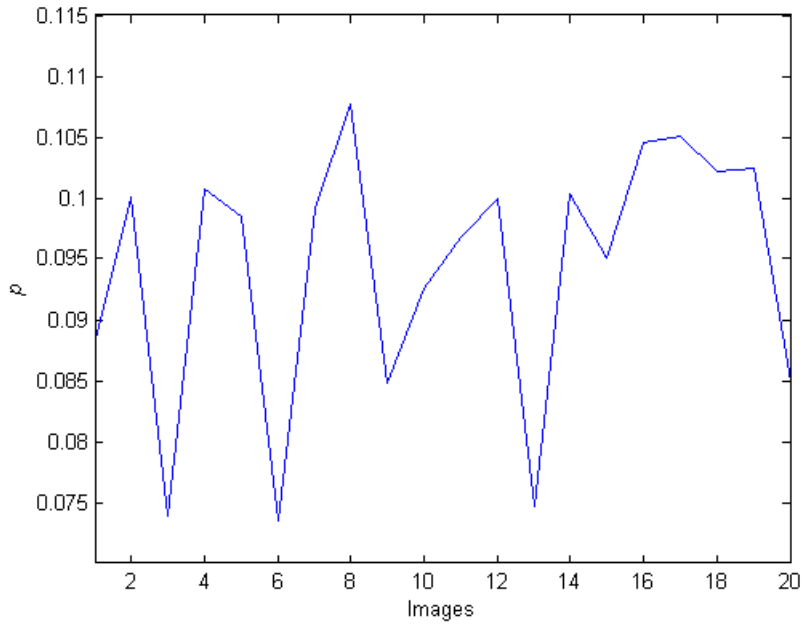

Figure 5.6: Temporal Variation in p

ment error and standard deviation was found to be 8.207mm and 5.191mm respectively. The rippled reconstruction clearly depicts the influence of harmonics, however, unlike the previously simulated FTP reconstruction seen in Figure 4.25 (b) the rippling effect is also prominent for the reference plane around the outer edges of the surface. The rippled reconstruction of the reference plane distinctly identifies the temporal variation of the fringe γ non-linear luminance.

5.3.5 Gauging the Magnitude of the Reference Ripple

Given the prominence of the rippling effect found on the reference plane, an expression defining the ripple and the magnitude of the ripple is investigated. Since the phase modulation term is identical for the reference plane surface the phase measuring residual can be given by

$$\delta_{ripple} = \Lambda(2\pi f_0 x + \phi_0, p) - \Lambda(2\pi f_0 x + \phi_0, p_0) \tag{5.18}$$

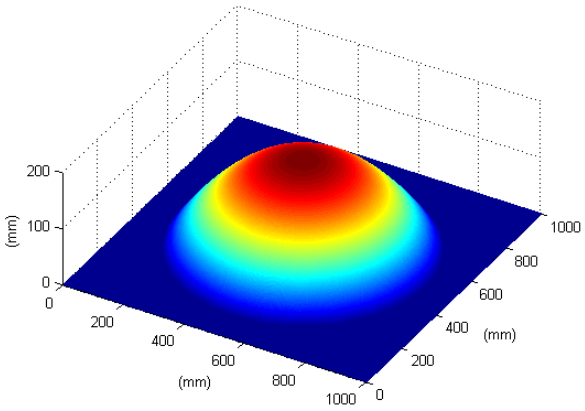

(a) Simulated Height Distribution

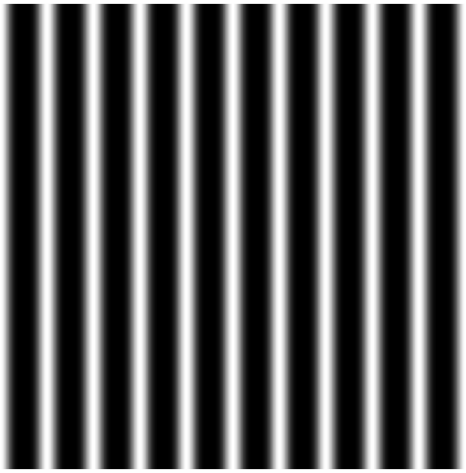

(b) Reference Fringe, $\gamma_0 = 2.47$

(c) Deformed Fringe, $\gamma = 2.13$

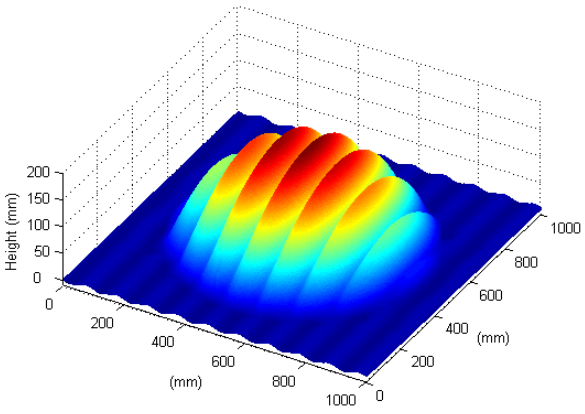

(d) FTP Reconstructed Surface

Figure 5.7: Simulated Reconstruction

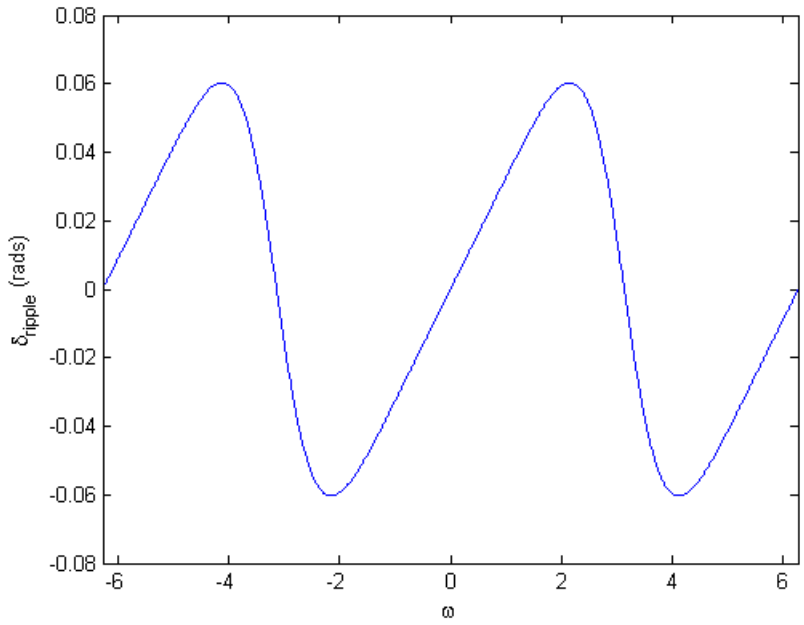

Figure 5.8: Temporal Reference Plane Residual Function, for $p_0 = 0.1084$ i.e $\gamma_0 = 2.47$ and $p = 0.0753$ i.e. $\gamma = 2.13$

Now substituting Equation (5.7) with the appropriate values for ρ, into Equation (5.18) and simplifying, the expression for the reference plane residual can be given by

$$\begin{aligned} \delta_{ripple} &= \arctan\left(\frac{\tan(\Lambda(2\pi f_0 x + \phi_0, p)) - \tan(\Lambda(2\pi f_0 x + \phi_0, p_0))}{1 + \tan(\Lambda(2\pi f_0 x + \phi_0, p)) \cdot \tan(\Lambda(2\pi f_0 x + \phi_0, p_0))}\right) \\ &= \arctan\left(\frac{(\sqrt{p} - \sqrt{p_0})\sin\omega}{1 + \sqrt{p.p_0} + (\sqrt{p} + \sqrt{p_0})\cos\omega}\right) \end{aligned} \tag{5.19}$$

A plot of the analytical reference residual function can be seen in Figure 5.8, for the example simulated parameters of $p_0 = 0.1084$ i.e $\gamma_0 = 2.47$ and $p = 0.0753$ i.e. $\gamma = 2.13$. Moreover, by setting $\frac{\mathrm{d}\delta_{ripple}}{\mathrm{d}\omega} = 0$, and solving for ω reveals that a maximum ripple value will occur when

$$\omega = \arccos\left(\frac{p_0 - p}{(1 + \sqrt{p_0 p})(\sqrt{p} - \sqrt{p_0})}\right) \tag{5.20}$$

Substituting Equation (5.20) into Equation (5.19) and simplifying, the magnitude of the reference ripple can be determined by calculating the maximum value, that is,

$$\delta_{ripple\,max} = \left(\frac{(\sqrt{p} - \sqrt{p_0})\sqrt{(1 + \sqrt{p_0 p})^2(\sqrt{p} - \sqrt{p_0})^2 - (p_0 - p)^2}}{(1 + \sqrt{p_o p})^2(\sqrt{p} - \sqrt{p_0}) + (\sqrt{p} + \sqrt{p_0})(p_0 - p)}\right) \tag{5.21}$$

This rippling effect was found to be commonplace in all experimental findings as will be demonstrated in the following empirical evaluation.

5.3.6 Empirical Example FTP Reconstruction

To clearly demonstrate the rippling effect associated with the temporal spectral characteristics of the projected fringe distributions, a simple surface was measured using the FTP method. The system parameters are identical to that of the previous fringe manipulation experimentation and the same surface was profiled. Fringe offset and contrast parame-

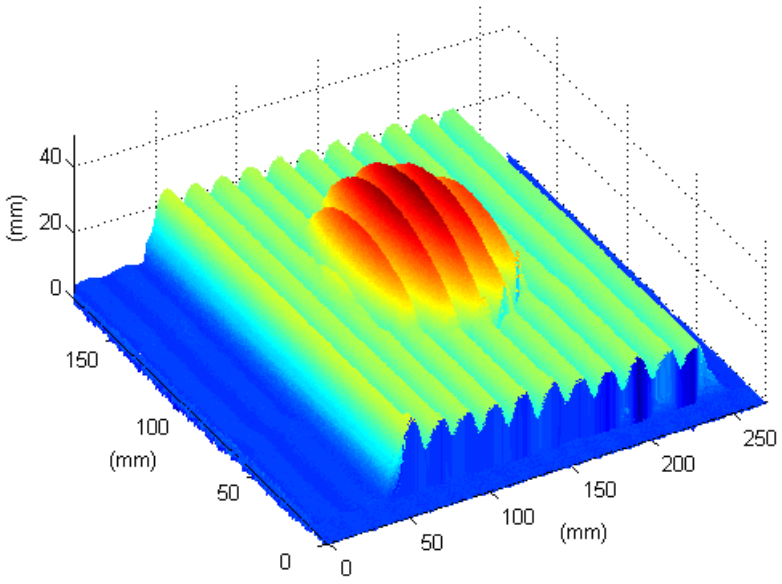

Figure 5.9: Empirical FTP reconstruction

ter were set such that $a = b$ for maximum harmonic distortion. The FTP reconstructed surface is shown as Figure 5.9. As can be seen the rippling effect is quite evident for the modulated parts of the image and also for the reference plane surface. This rippling effect in the reference plane reconstruction clearly demonstrates the temporal nature of the projected images.

5.4 Fringe Image Formation

The harmonic structure of the gamma distorted fringe has been extensively detailed in Section 4.2, however, the theoretical analysis does not consider rudimentary lens effects such as defocusing or radial lens aberration. Practically, the harmonic structure of the gamma distorted fringe is particularly sensitive to defocusing which is associated with the modulation transfer function of the projection optics. In fact, the defocusing of projection optics to optimise projected fringe images is by no means a new concept, Coggrave and Huntley [137] demonstrated a focused based optimisation of the "Screen Door Effect" for a 3D sensor based on digital projection. Also, Su *et al.* [148] showed that a defocused Ronchi grating could be utilised as a formidable sinusoidal substitute for the PMP algorithm. Despite the acceptance of defocusing for fringe optimisation, the effects of the projection imaging optics on the harmonic structure of a digitally projected fringe has yet to be examined. Furthermore, the significance of the practical fringe formation process becomes of particular importance when determining the frequency dependence of the resulting Display Gamma residual phase error. The previous two chapters have demonstrated an apparent contradiction in regard to the frequency dependence of the Display Gamma residual and therefore further verification of the issue is required.

This section is concerned with the formal modeling of the fringe image formation process from an optical perspective and further, the influence the projection optics has on the harmonic structure of a gamma distorted fringe. Subsequent to the derivation of the analytical focus model, the validity of the study is verified through the study of the minimum step requirements to eliminate gamma related errors for the well known PMP technique via both simulation and empirical analysis. Finally, the frequency dependence of the gamma residual phase error function is discussed.

5.4.1 Modeling the Optical Modulation Transfer Function

The derivations presented here follow that of Su *et al.* [148]. Assuming the typical digital video projector aperture is rectangular, the point spreading function otherwise referred to as the projection system impulse response can be given by

$$t(x) = rect\left(\frac{x}{a}\right) \tag{5.22}$$

where a is the width of the aperture. Therefore, the fringe image formed at the fictitious reference plane T (see Figure 2.4), can be given by

$$\hat{w}(x,y) = w(x,y) * rect\left(\frac{x}{a}\right) \tag{5.23}$$

To demonstrate the nature of the spatial frequency attenuation, the optical transfer function of the projection optics is derived by taking the Fourier Transform of the point spread function seen as Equation (5.22)

$$T(f) = \frac{\sin(\pi a f)}{\pi a f} \tag{5.24}$$

Now introducing a defocusing parameter, β,

$$\beta = a f_0 \tag{5.25}$$

and the frequency term $f = k f_0$, Equation (5.24) can be rewritten as

$$T(k f_0) = \frac{\sin(\pi \beta k)}{\pi \beta k} \tag{5.26}$$

As $\beta \rightarrow 1$ the integral of Equation (5.26) decreases and the first zero approaches the fundamental component i.e. $k = 1$ and the origin or dc component and therefore concentrates more energy in the central peak of the $sinc$ function. Clearly, by the nature of the image formation process, the projector lens will act as a low-pass filter attenuating higher order spatial frequencies, and thereby, optimising the projected gamma distorted fringe in terms of lessening higher order harmonic contributions. Therefore, rewriting Equation (5.23) the defocused gamma distorted fringe can be given by

$$\hat{w}(x,y) = c_0 + T(f_0).c_1 \cos(2\pi f_0 x) + \sum_{k=2}^{\infty} T(k f_0).c_k \cos(k[2\pi f_0 x]) \tag{5.27}$$

where the coefficients $T(k f_0)$ decay according to Equation (5.26) providing the desired low-pass filtering effect.

5.4.2 Elimination of γ Non-linear Luminance Effects for Stepping Techniques

Now that the gamma distorted fringe can be more accurately modeled, the practical magnitude of the residual phase measuring error for stepping algorithms in the presence of

gamma distortion can be more effectively established and, hence, the minimum requirements for the elimination of γ related errors can be determined. To demonstrate the minimum requirements for the practical elimination of γ related phase measuring errors for stepping techniques, the PMP algorithm was selected since it was shown in Section 4.3 to be the least sensitive to harmonic distortion. Also, as demonstrated in Section 4.3 the contribution of the 3rd order harmonic can be considered somewhat influential, particularly, for techniques such as the 4 Step PMP and the 3+3 approach. Therefore, to investigate this further, Equation (5.27) is considered up to the 3rd order harmonic and, hence, the distorted fringe can be given by

$$\begin{aligned} \hat{g}(x,y) &= \Big[a + b\cos(\omega(x,y)) + c\cos(2\omega(x,y)) + \\ &\quad d\cos(3\omega(x,y))\Big] \end{aligned} \tag{5.28}$$

where

$$b = T(f_0).c_1 \tag{5.29}$$

$$c = T(2f_0).c_2 \tag{5.30}$$

$$d = T(3f_0).c_3 \tag{5.31}$$

and where $\omega(x,y)$ denotes the appropriate phase modulation term, $2\pi f_0 x + \varphi(x,y)$.

Now, similar to the previous PMP harmonic derivations presented in Section 4.3.2, substituting Equation (5.28) into (2.18) an estimation of the fringe phase modulation in the presence of 2nd and also 3rd order harmonic distortion can be obtained for a given value of N. Firstly considering the $N = 3$ case, it can be shown that the resulting estimation of $\omega(x,y)$ can be given as

$$\hat{\omega}(x,y) = \arctan\left(\frac{b\sin(\omega) - c\sin(2\omega)}{b\cos(\omega) + c\cos(2\omega)}\right) \tag{5.32}$$

and the resulting phase residual error can be given by

$$\delta(x,y) = -\arctan\left(\frac{\frac{c}{b}\sin(3\omega)}{1 + \frac{c}{b}\cos(3\omega)}\right) \tag{5.33}$$

Now repeating the process for $N = 4$,

$$\hat{\omega}(x,y) = \arctan\left(\frac{b\sin(\omega) - d\sin(3\omega)}{b\cos(\omega) + d\cos(3\omega)}\right) \tag{5.34}$$

and the resulting phase residual error can be given by

$$\delta(x,y) = -\arctan\left(\frac{\frac{d}{b}\sin(4\omega)}{1+\frac{d}{b}\cos(4\omega)}\right) \tag{5.35}$$

As shown in Equations (5.32) and (5.34) the PMP algorithm for the $N = 3$ case is insensitive to the 3rd order contribution, and sensitive to the 2nd order harmonic, while the $N = 4$ case is insensitive to the 2nd order, but sensitive to the 3rd order harmonic. Therefore, given that $c \gg d$ due to the nature of the γ term in Equation (4.1), the $N = 4$ PMP case is certainly less sensitive to gamma distortion for DVP based sensing (as previously confirmed in Section 4.5.2.2).

Considering the practical situation where the overall γ of the projection system is often not exclusively a function inherent to the projector alone but also of the video card driving the projector, larger values of γ resulting in larger d are inevitable. Hence, a further attenuation of higher order terms is required to ensure the phase residual as specified by Equation (5.35) is eliminated.

5.4.3 Attenuating Higher Order Harmonics

Generally, when a signal presents unwanted high frequency content, the desired low frequency components of the signal can be retrieved by employing some form of analytical low-pass filtering. In this particular scenario the filtering can be undertaken by appropriately defocusing the projection optics to attenuate the unwanted higher order terms. According to Equation (5.26) the amount of attenuation can be determined by calculating

β	$T(f_0)$	$T(2f_0)$	$T(3f_0)$
0.1	0.9836	0.9355	0.8584
0.2	0.9355	0.7568	0.5046
0.3	0.8584	0.5046	0.1093
0.4	0.7568	0.2339	0.1559

Table 5.1: Various β and the corresponding gain coefficients $T(kf_0)$ for $k = 1, 2, 3$.

the $T(kf_0)$ coefficients. A range of the coefficients are shown in Table (5.1). The primary advantage of this very simple yet practical filtering approach is that it presents no further computational burden at the reconstruction stage. In order to verify the validity of the defocusing fringe optimisation approach and, therefore, confirm the theoretical modeling of the practical γ distorted fringe, simulation and empirical results were established.

5.4.4 Simulation

In order to verify the validity of the analytical fringe image formation process including the proposed fringe optimisation by defocus, we simulated a series of defocused γ dis-

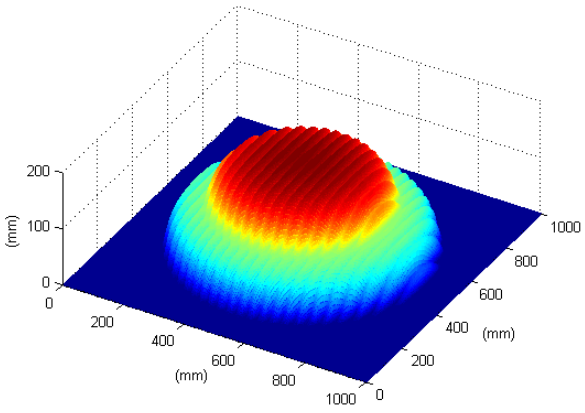

(a) 3 Step Focused

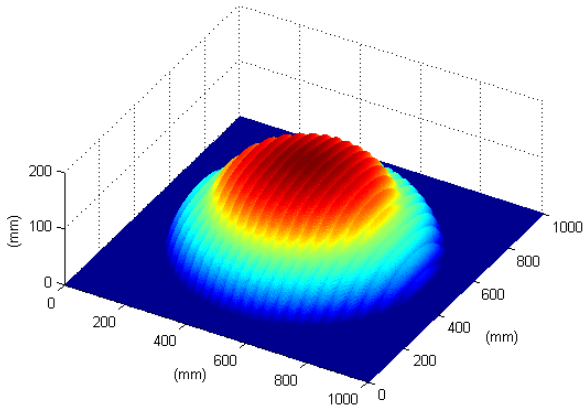

(b) 3 Step Defocused

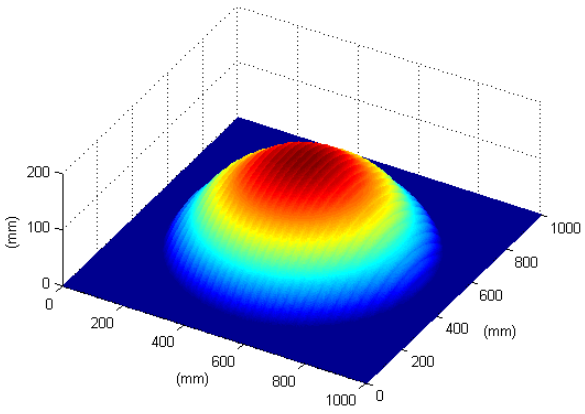

(c) 4 Step Focused

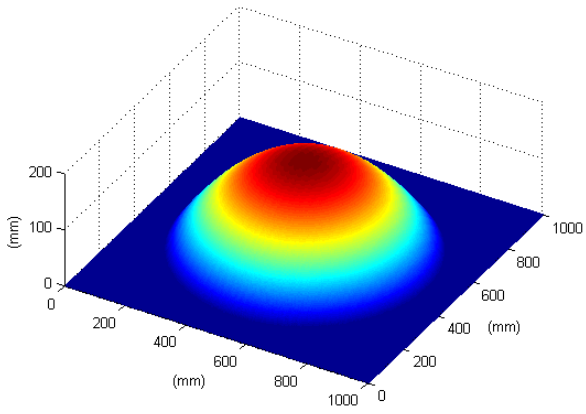

(d) 4 Step Defocused

Figure 5.10: Simulated Reconstructions

torted fringes projected onto a test surface and measure the surface using the 3 Step and

4 Step variations of the PMP algorithm. To demonstrate the effectiveness of the approach and emulate the maximum harmonic distortion conditions of a typical DVP system, the values of γ and fringe offset and contrast parameters were selected to be 3 and $a = b$, respectively. Further, to ensure the simulation provided as much insight in the practical application of defocusing, β was selected to be 0.3, since the attenuation in the fundamental component is minimal relative to the 2nd and 3rd order components given that SNR is an important consideration for practical situations.

System parameters l_0, d_0 and f_0 were chosen to be 5m and 2m and 10fringes/m respectively, corresponding to a spatial period of 100mm if we assume an image spatial resolution of 1pixel/mm. The test surface is a hemispherical convex shape with a diameter of 800mm and maximum height of 160mm corresponding to a maximum phase displacement 4.154 rads (as utilised in the previously described simulations). The reconstructed surfaces for the 3 and 4 Step PMP algorithms for both the focused and defocused cases are displayed in Figures 5.10 (a), (b), (c) and (d) respectively. Table 5.2 displays the Mean Error ($\bar{\epsilon}$), Standard Deviation ($\bar{\sigma}$) and Maximum Absolute Error (ϵ) in mm for both the PMP 3 and 4 Step algorithms for both the Focused and Defocused cases. Clearly, as

PMP ($N = 3$)	$\gamma = 3$		
	$\bar{\epsilon}\,(mm)$	$\bar{\sigma}\,(mm)$	$\epsilon\,(mm)$
Focused	6.6212	7.0163	32.4318
Defocused	3.8419	4.0781	18.7615
PMP ($N = 4$)	$\gamma = 3$		
	$\bar{\epsilon}\,(mm)$	$\bar{\sigma}\,(mm)$	$\epsilon\,(mm)$
Focused	1.0901	1.1572	5.1995
Defocused	0.1388	0.1474	0.6638

Table 5.2: Mean Error ($\bar{\epsilon}$), Standard Deviation ($\bar{\sigma}$) and Maximum Absolute Error (ϵ) in mm for the PMP 3 and 4 Step algorithms for both the Focused and Defocused cases with $\gamma = 3$

anticipated the 4 Step defocused case almost completely eliminates the systematic reconstruction errors associated with the γ term.

5.4.5 Empirical Verification

To verify the physical application of the PMP fringe optimisation approach, practical experimental results were established via the profiling of the previously presented convex dome shape seen in Figure 5.3(a). The projection system was composed of a Hitachi CP-

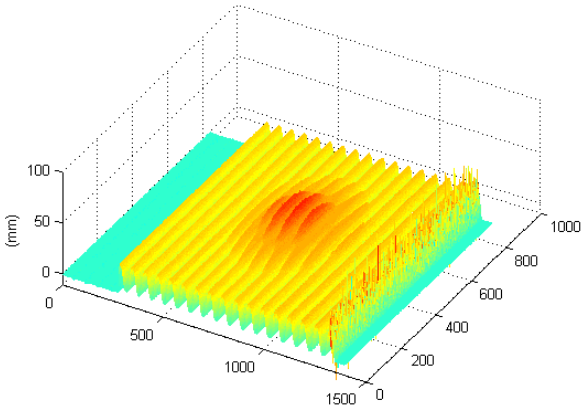

(a) 3 Step Focused

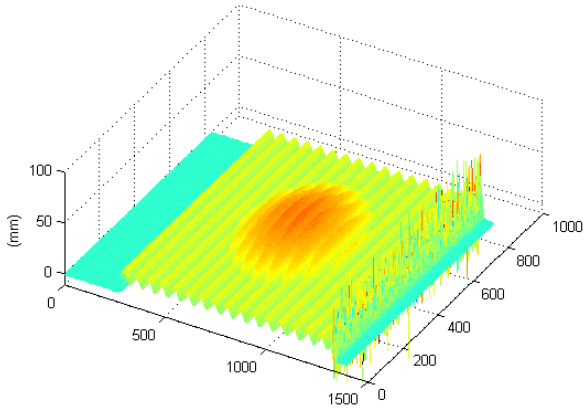

(b) 3 Step Defocused

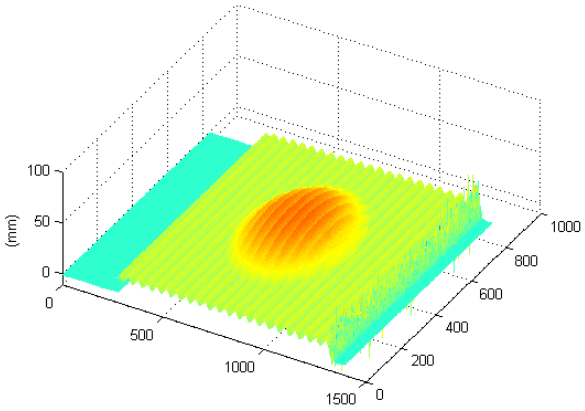

(c) 4 Step Focused

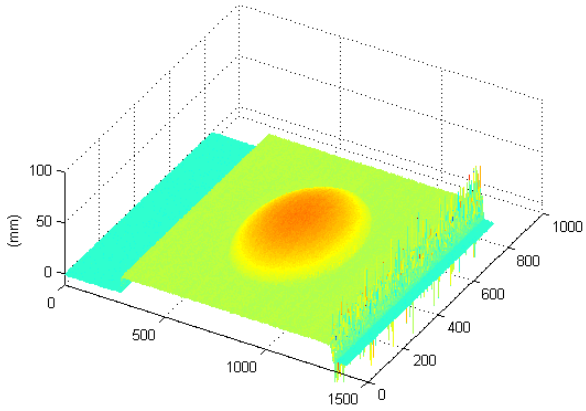

(d) 4 Step Defocused

Figure 5.11: Empirical Reconstructions

X260 LCD digital video projector interfaced to a dual head Matrox video card. Similar to the simulation, maximum harmonic distortion conditions were emulated by projecting a high contrast fringe with the γ value on the video card set to 3 in software. The fringes

were recorded using a MS3100 3-CCD camera with an effective resolution of 1039x1392. The surface was reconstructed using both the 3 and 4 Step variations of the PMP algorithm for both the focused and defocused scenarios. The 3D reconstructions are shown in Figures (5.11) (a)-(d) while Figures (5.12) (a) and (b) display an arbitrary cross-section of the 3 and 4 Step reconstructions for both the focused and defocused cases, respectively.

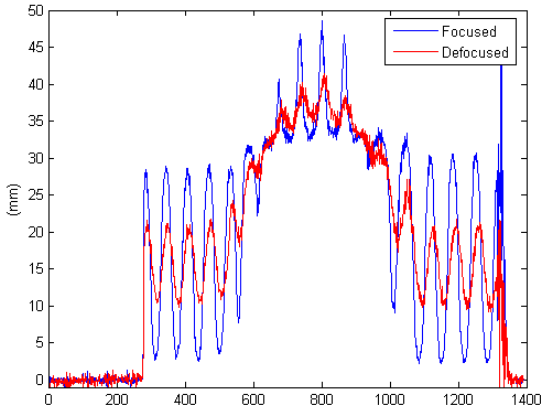

(a) 3 Step Focused

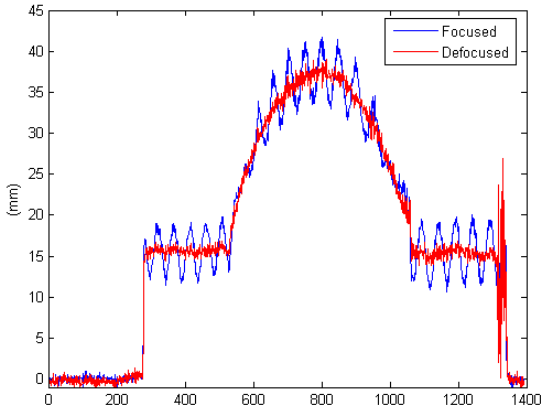

(b) 4 Step Defocused

Figure 5.12: Cross-sections of Empirical Reconstructions

An important aspect to note in each of the defocused cases is the reduced SNR. Given our experiment was adjusted to produce a large harmonic distortion, the amount of required attenuation by defocusing was also increased accordingly. Considering the typical practical situation where the harmonic distortion is likely to be less significant, the diminishing SNR due to significant defocusing is likely to be much less influential. Nevertheless, the verification of the fringe formation model and the practical low-pass effectiveness of defocusing the projection optical system to attenuate fringe γ distortion is clearly demonstrated.

5.4.6 Display Gamma Phase Residual Frequency Dependence

Referring to the Display Gamma residual phase error functions denoted $\delta(x, y)$ in Chapter 4, it is clearly evident that the residual error is dependent only on p and $\omega(x, y)$. Furthermore, since neither $\omega(x, y)$ or p have a dependence on fringe frequency f_0 it was theoretically shown that $\delta(x, y)$ was a frequency independent phenomena. However, given

the preliminary empirical findings in regard to this issue presented in Chapter 3, the theoretical frequency independence conclusion shown in Chapter 4 becomes questionable (as previously discussed in Section 4.4.3).

With the insight of a more formidable theoretical modeling of the fringe formation process, the true nature of the Display Gamma residual phase measuring error can be established and accordingly the true frequency dependence of the residual determined. Observing Equation (5.27) it is clear that the projection optics render the harmonic structure of the gamma distorted fringe frequency dependent for any given focus. Therefore, the harmonic ratio p is dependent on f_0 and accordingly so too $\delta(x, y)$, and the apparent frequency dependence contradiction is resolved.

Given that it has now been shown that the Display Gamma residual error is dependent on the fringe carrier frequency, the obvious question is what implications does this have for lookup table based gamma residual error elimination techniques, such as that proposed by Zhang and Yau [98]. Since frequency independence is one of the key assumptions made for lookup table methods (enabling a normalisation of the residual frequency), the frequency dependent nature of the residual error will inevitably result in error for f_0 scenarios other than the original case for which the lookup was composed. Obviously, the integrity of the frequency independence assumption is a practical factor dependent on the optical modulation transfer function of the projector (and the camera), and therefore the resulting errors are dependent on these practical phenomena also. However, to ensure the most appropriate functionality of such lookup table approaches it is ideal to compose an individual lookup table for each value of f_0 as opposed to the averaging approach demonstrated in [98].

5.5 Summary

This chapter addressed some of the more important practical Display Gamma Fringe Projection issues including, Fringe parameter manipulation, Temporal luminance instabilities, and the influence the projection optics has on the harmonic structure of a gamma distorted fringe. The importance of the fringe offset and contrast parameters was demonstrated and, moreover, the effective manipulation of fringe offset and contrast to min-

imise gamma associated reconstruction errors was undertaken. The temporal nature of the projector / camera luminance response was analytically evaluated for the temporally sensitive FTP approach. Although this derivation is primarily concerned with the FTP method, the results can be extended to gain an understanding of the temporal Display Gamma behaviour for stepping approaches. The important practical issue of focusing has also been dealt with, with the derivation of the optical modulation transfer function for the projection optics. The validity of this study has also been verified by defining the minimum stepping requirements to eliminate γ related phase estimation errors for stepping fringe processing techniques. The integrity of the Display Gamma residual error frequency independence assumption was shown to be invalid, therefore clarifying a supposed contradiction of results. Finally, the implications of frequency dependence was also discussed for lookup table based methods of eliminating γ related errors. Our investigation clearly shows that frequency independence cannot be assumed other than for specific cases considered in the lookup table.

Chapter 6

Digital Fringe Calibration using Neural Networks

6.1 Introduction

The preceding chapters have extensively identified and determined the characteristics and magnitude of Display Gamma related Fringe Projection issues, and thereby, the significant requirement for gamma correction for Fringe Projection 3D sensing techniques. The significance of the gamma correction process for dynamic fringe profiling applications has also been further exemplified in Chapter 4 where minimum step techniques (including FTP) were shown to demonstrate an increased sensitivity to γ associated errors relative to higher step techniques. In addition to the heightened γ sensitivity of minimum step fringe processing algorithms, dynamic fringe processing techniques are prone to a reduced SNR given that the surface of interest is not sampled as often relative to higher step techniques. Therefore, for dynamic Fringe Projection applications the adequate removal of additive noise is critical and supplementary the gamma correction process. Consequently, there is a need for robust and reliable techniques to address the accurate estimation of $\omega(x, y)$ in the presence of these fringe anomalies. One such approach is through fringe calibration. Fringe calibration refers to the enhancement of a fringe image using signal processing techniques prior to fringe processing. Traditionally, the enhancement of a fringe image will involve some form of digital filtering, with the filtering typically performed in the spatial frequency domain [149] or in the spatial domain [116, 150, 151] through convo-

lution, adaptive or non-linear processing. However, as previously highlighted with the onset of dynamic DVP based fringe profilometers, additional processing techniques are required to compensate for the non-linearities familiar with digitally projected images. A typical solution to counter digitally projected non-linearities involves photometric fringe calibration, whereby multiple intensity distributions varying over the full range of luminance values are recorded and a camera / projector illuminance curve is fitted [88, 139]. Although effective at alleviating gamma fringe non-linearities, photometric techniques require a substantial amount of additional data and are usually nonresilient to environmental change.

Another interesting digital fringe calibration technique was proposed by Guo *et al.* [97] whereby the iterative statistical analysis of digital fringe patterns was undertaken to remove gamma non-linearities inherent in digitally projected images. Such an approach is desirable as it requires no prior knowledge of the projected image and in contrast to polyspectral approaches [152] is less computationally stringent. This technique still nevertheless requires additional data for appropriate statistical analysis and therefore effective gamma correction.

Some other interesting approaches utilise Neural Networks to address nonlinearities associated in determining spatial phase displacements. These approaches involve directly obtaining a height distribution based on aberrated fringe data utilising appropriate photometric calibration and neural network training [153, 154, 155] or in indirect coordinate mapping methods [156, 157, 158, 159, 160]. Often these approaches can be laborious, time consuming and require a substantial amount of data with many of the proposed solutions specific to particular reconstruction techniques.

The potential usefulness of neural networks as a means for such direct and indirect profilometry applications has been clearly demonstrated, however, the application of neural networks to fringe enhancement has yet to be considered in literature. In this chapter a neural network based fringe calibration / enhancement technique is described, whereby, a digitally projected fringe pattern is input to a feed-forward backpropagation neural network trained using non-aberrated patterns. The generalisation properties of neural networks are exploited to interpolate modulated structured light patterns and consequentially are successfully capable of improving determination of spatial displacement $\overline{AC}$

and hence $h(x, y)$ (as seen in Figure 2.3). The proposed approach does not rely on prior calibration information and requires only a single cross-section from a single fringe image for calibration, thus, the technique is suitable for dynamic minimum shot techniques including robotic vision where rapid calibration is required. In contrast to filtering techniques the neural fringe calibration technique is significantly more computationally efficient and superior in suppressing fringe higher order harmonic anomalies. Finally, since the approach is aimed at calibrating a fringe image, its application and functionality is not limited to operation with specific reconstruction algorithms.

Further to describing the neural fringe calibration approach the remainder of this chapter is dedicated to the introduction of the concept of neural computing, the verification of the proposed approach via simulation and empirical analysis and also the comparative analysis of the proposed technique relative to existing approaches. Finally, the application of the neural fringe calibration approach in the multi-channel environment is considered.

6.2 Neural Computing

Artificial Neural Networks (ANN's) which are based on a paradigm of the biological neuron have been applied to solve many problems across a range of different disciplines due to their modelling, classification, generalisation and non-linear mapping abilities. Neural networks are taught from example through training processes where network outputs are repeatedly presented with the required responses to given input data and network parameters are adjusted as to minimise error between target and actual output vectors. If the training is successful the network will be able to interpolate an output from an input vector that is not a member of the training set.

The most rudimentary element of a neural network is the simple neuron. A simple neuron receives N weighted inputs, these weighted inputs are then summed together at the junction of the neuron and then past to an "activation" or "thresholding" function $f()$, as depicted in Figure 6.1. Hence the output of the neuron can be given mathematically as

$$Y = f\left(\sum_{i=1}^{N} w_i x_i\right), \tag{6.1}$$

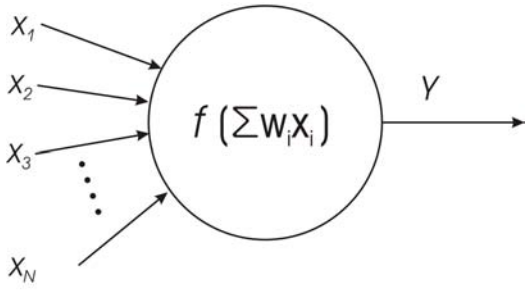

Figure 6.1: Simple Neuron

Typically, $f()$ is a sigmoidal function such as tansigmoidal or logsigmoidal and depending on the application of the neural network can also be hardlimiting e.g. classification. For a feedforward backpropagation network such as the networks utilised in this work it is desirable for network training purposes that the activation function is monotonic and continuously differentiable [161]. A neural network is comprised of a number of these simple neurons which are commonly arranged in a layered fashion with neurons of a common layer processing in a parallel manner. For the multilayer arrangement we can give the following mathematical generalisation for the output of the q_{th} neuron within the network at layer p as

$$Y_q^p = f^p\left(\sum_{i=1}^{N} w_{iq}^p Y_i^{p-1}\right), \tag{6.2}$$

where Y_i^{p-1} is the output from the i_{th} neuron of the $(p-1)_{th}$ layer with corresponding weight w_{iq}^p and $f^p()$ is the thresholding function associated with the p_{th} layer.

Multiple layer neural networks are quite powerful non-linear approximators. For instance, the feedforward backpropagation network topology which usually consists of three layers can be trained to approximate any function arbitrarily well. The first layer is referred to as the "input layer" with the chief purpose of distributing the values they receive to the next layer which is termed the "hidden layer". The final layer is the "output" layer, neurons in this layer utilise a pure linear activation function with the objective of scaling the range of outputs which is limited from the sigmoidal stages. The network is trained using a process whereby the error between target vectors and actual output is propagated back through the network from output layer to input layer adjusting network layer weights according to an error minimisation process. The learning algorithm for multilayer neural networks referred to as the "backpropagation rule" or the "generalised

delta rule" is extensively outlined in [161].

6.3 Proposed Neural Network Fringe Calibration

The proposed fringe calibration employs neural networks to reverse engineer the projection capture response exploiting the generalisation and nonlinear mapping abilities associated with neural networks. The technique endeavors to reproduce captured structured light patterns devoid of aberration from captured aberrated data via a multi-layer feedforward backpropagation neural network operating as a nonlinear signal map.

Considering the captured gamma distorted fringe projected onto the reference plane given by

$$\hat{g}_0(x,y) = [a(x,y) + b(x,y)\cos(2\pi f_0 x + \phi_0(x,y))]^{\gamma}, \tag{6.3}$$

an N x M fringe image, $\hat{I}$, can be defined as

$$\hat{I}(m,n) = \hat{g}_0(x,y) \tag{6.4}$$

where m and n represent the discrete sample co-ordinates of the continuous x and y co-ordinate sets for the distorted reference fringe distribution. Furthermore, a single training vector representing a non-aberrated fringe cross-section denoted $T(m)$, can be defined as

$$T(m) = a + b\cos(2\pi f_0 m + \phi_0(m)). \tag{6.5}$$

The training vector T represents the anticipated or desired fringe intensity distribution, such as the software input to a digital projection source with included phase modulation as described by Equation (2.10).

Considering now only a single cross section of $\hat{I}$, (i.e. $\hat{I}(m,a)$ for some arbitrary value $a \in n = 0,1,2,3...N$ where $m = 0,1,2,3....M$) a simple feedforward backpropagation neural network N_a, as seen in Figure 6.2, can be trained to map between $\hat{I}(m,a)$ and $I(m,a)$, the output of the neural network. Mathematically,

$$I(m,a) = f_2\left(\sum W_2 f_1(\hat{I}(m,a)W_1)\right) \quad \text{for } m = 0,1,2,3.....M, \tag{6.6}$$

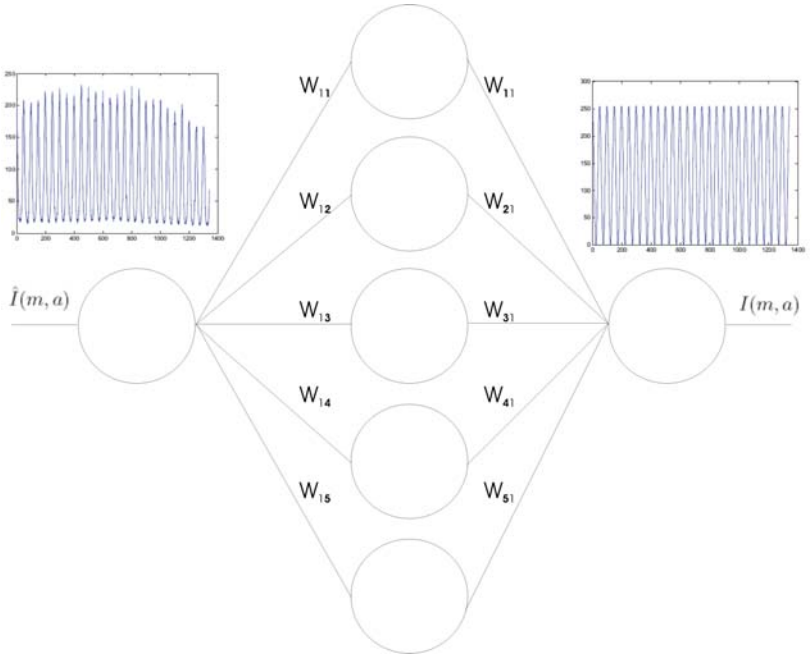

Figure 6.2: Proposed Multilayer Signal Mapping Calibration Neural Network for arbitrary $a \in n = 0, 1, 2, 3...N$

where

$$W_1 = \begin{bmatrix} w_{11} & w_{12} & w_{13} & w_{14} & w_{15} \end{bmatrix}^T.$$

and

$$W_2 = \begin{bmatrix} w_{11} & w_{21} & w_{31} & w_{41} & w_{51} \end{bmatrix}.$$

and $f_1()$ and $f_2()$ are the appropriate activation functions for the corresponding layers.

Extending the calibration to the entire image we have

$$I(m,n) = f_2\left(\sum W_2 f_1(\hat{I}(m,n)W_1)\right) \quad (6.7)$$
$$\text{for } m = 0, 1, 2, 3.....M,$$
$$\text{and } n = 0, 1, 2, 3.....N,$$

where $I(m,n)$ is the output of the neural network for the mth and nth sample of the reference image and W_1 and W_2 are the corresponding weight matrices.

Similarly, for a deformed fringe pattern given by

$$\hat{g}(x,y) = [a(x,y) + b(x,y)\cos(2\pi f_0 x + \phi_0(x,y) + \phi(x,y))]^{\gamma}, \quad (6.8)$$

an N x M fringe image denoted by, $\hat{D}$, can be defined and further by employing the trained neural network N_a, a calibrated image, D, can be obtained.

$$D(m,n) = f_2\left(\sum W_2 f_1(\hat{D}(m,n)W_1)\right) \quad \text{for } m = 0,1,2,3.....M, \quad \text{and } n = 0,1,2,3.....N, \tag{6.9}$$

An important issue to highlight for the proposed neural approach is the assumption that the system γ is a spatially uniform phenomena independent of variables x and y. This assumption makes it possible to train just a single neural network to calibrate the entire fringe image. In practice the Display Gamma non-linearities may not be explicitly spatially uniform and therefore dependent on both x and y. Hence to ensure a more reliable gamma correction process in the presence of spatially non-uniform Display Gamma an individual neural network N_n should be trained for each cross-section of $\hat{I}$.

Nevertheless, once all images have been calibrated (for both the reference and deformed cases) the estimation of phase component $\omega(x,y)$ can be more effectively undertaken by γ sensitive fringe processing algorithms such as 3 Step PMP or FTP.

6.3.1 Neural Network Design

Clearly, the design of any neural network is governed by the problem in which the network is attempting to solve. In this particular case the neural network is attempting to model the nonlinear intensity response otherwise referred to as Display Gamma. Therefore, the type of activation functions, the training of the network and moreover the dimension (in terms of number neurons in the hidden layer) are all directly dependent on the camera / projector nonlinear intensity response.

Based on the Display Gamma modeling presented in Chapter 4 it was empirically found that a network with 5 neurons in the hidden layer was ideal in terms of training convergence and furthermore, accurate approximation of the Display Gamma nonlinear intensity response. Clearly, from a practical perspective the optimum number of neurons in the hidden layer and training optimisation may vary from system to system as the camera / projector intensity response varies. Further details in regard to the ANN design and moreover the validation of the approach is subsequently outlined in Section 6.4.

6.3.2 Noise Removal

Whilst neural networks demonstrate strong non-linear mapping abilities, in the presence of random processes such as additive gaussian noise, the performance of neural networks for such purposes can be somewhat limited. Hence, an effective fringe noise removal process is necessary prior to the neural network phase to maximize the performance of the neural network calibration.

Traditionally, the removal of noise from a fringe image will involve some form of filtering. Typically, the filtering will be performed in either the spatial frequency domain [149] or in the spatial domain [116, 150, 151] through convolution based, adaptive or non-linear processing. Relative to spatial domain approaches spatial frequency techniques are often quite computationally demanding considering the requirement for a Fourier and Inverse Fourier Transformation of the signal of interest. The computational requirements for spatial frequency domain approaches often make real-time spatial frequency applications significantly more challenging and thereby spatial domain approaches are more appropriate under these conditions. Spatial domain techniques utilise neighbourhood spatial coherence and neighborhood pixel value homogeneity as a basis for calculating filtered pixel values [162].

Gaussian smoothing is a noise suppression technique where a "bell-shaped" gaussian kernel is utilised to act as a spatial lowpass filter with the intention to blur an image. A typical 1-D gaussian kernel is formed as:

$$G(x) = ke^{-\frac{x^2}{2\sigma^2}} \tag{6.10}$$

where,

$$k = \frac{1}{\sum_x e^{-\frac{x^2}{2\sigma^2}}}$$

In contrast to a mean or averaging filter with a rectangular kernel (which oscillates in the spatial frequency domain), the gaussian approach presents a similar gaussian form in the spatial frequency domain. The gaussian approach can therefore ensure an accurate attenuation of the appropriate frequency components provided the gaussian parameters are appropriately selected [163]. Since the phase modulation an object introduces into a

fringe pattern is considered to be slowly varying in contrast to the fringe carrier frequency and more importantly the signal noise, the blurring caused by the Gaussian smoothing process introduces minimal error provided the appropriate kernel parameters are selected.

It is important to note that in this case a filtering technique has been chosen based on the particular characteristics of the noise present in the fringe pattern. Obviously a gaussian smoothing technique will perform poorly in the presence of "salt and pepper" or impulsive noise, due to its point spreading nature. A more appropriate spatial filter for such an application would be the non-linear median filter [151, 163]

6.4 Simulation

In order to test the validity of the proposed calibration technique, simulation analysis involving the emulation of digitally projected fringe image was undertaken. The aberrated fringe was calibrated using the technique outlined in Section 6.3 and both the non-calibrated and calibrated fringe images processed using the well known 3-step PMP and FTP methods. The simulated reference fringe set can be expressed as

$$\hat{g}_{0n}(x,y) = [a + b\cos(2\pi f_0 x + \phi_0(x,y) + 2\pi n/N)]^{\gamma} + n_0(x,y), \tag{6.11}$$

$$\text{for } n = 0, 1, 2....N-1$$

where

$$a = \frac{127.5}{255},\ b = \frac{127.5}{255}$$

$$\gamma = 2.2,$$

where $N = 3$ for the 3-step algorithm and $N = 1$ for FTP, the noise vector $n_0(x,y)$ was added to yield an SNR of 25dB. Consequentially, the deformed phase modulated image is

$$\hat{g}_n(x,y) = [a + b\cos(2\pi f_0 x + \phi_0(x,y) + \phi(x,y) + 2\pi n/N)]^{\gamma} + n_0(x,y), \tag{6.12}$$

$$\text{for } n = 0, 1, 2....N-1$$

where $\phi(x, y)$ represents a hemispherical convex shape as seen in all other previous simulations. It is also important to note that noise vectors $n_0(x, y)$ are generated for each fringe image independently, as to properly emulate practical conditions.

The system parameters l_0, d_0 and f_0 were chosen to be 5m and 2m and 10 fringes/m respectively, corresponding to a spatial period of 100mm if we assume an image spatial resolution of 1 pixel/mm. The simulated captured intensity distributions $\hat{g}_0(x, y)$ and $\hat{g}(x, y)$ for $n = 0$ are shown as Figures 6.3 (b) and 6.3 (c) respectively with Figure 6.3(d) displaying an arbitrary cross section of the $\hat{g}_0(x, y)$.

The noise was removed from the simulated fringes using the gaussian smoothing technique described in Section 6.3.2, with filter kernel parameter σ and filter size of 10.5 and 35 samples respectively for the designated 25dB SNR. Given the gamma nonlinearity independence of the variable y, a single neural network as described in Section 6.3 was trained using a Levenberg-Marquardt numerical optimisation variation of the backpropagation algorithm [164] with target vector

$$R(x) = a + b\cos(2\pi f_0 x + \phi_0(x, y)), \tag{6.13}$$

It was found that a neural network with a single hidden layer of 5 neurons utilising a tansigmoidal activation function f and a pure linear output stage was ideal.

The filtered distorted fringe images $\hat{g}_{0n}(x, y)$ and $\hat{g}_n(x, y)$ were applied to the neural network to yield the calibrated $g_{0n}(x, y)$ and $g_n(x, y)$ images. A standard 3 step PMP and FTP technique was used to extract the phase distribution $\phi(x, y)$ for both calibrated and non-calibrated images $g_{0n}(x, y)$ and $g_n(x, y)$ and $\hat{g}_{0n}(x, y)$ and $\hat{g}_n(x, y)$ respectively (including the phase shifted calibrated and non-calibrated images required for the 3-step PMP algorithm). Table 6.1 displays the absolute mean profile reconstruction errors along with corresponding standard deviations for both the calibrated and non-calibrated situations for both the 3-step PMP and FTP techniques.

For the PMP case the mean measurement error has been improved from 5.4328mm to 0.5055mm improving the accuracy by more than 90%, while for the FTP case we observed an improvement from 6.2572mm to 0.9861mm, equating to an improvement of more than 84%. Figures 6.4 and 6.5 visually demonstrate the improvement for both the PMP and FTP cases. Figure 6.4 displays the complete reconstruction of the simulated hemispherical diffuse surface for calibrated and non-calibrated images, while Figure 6.5

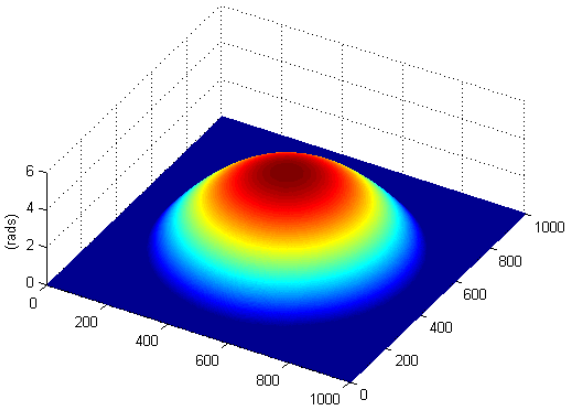

(a) Simulated Phase Distribution $|\phi(x, y)|$

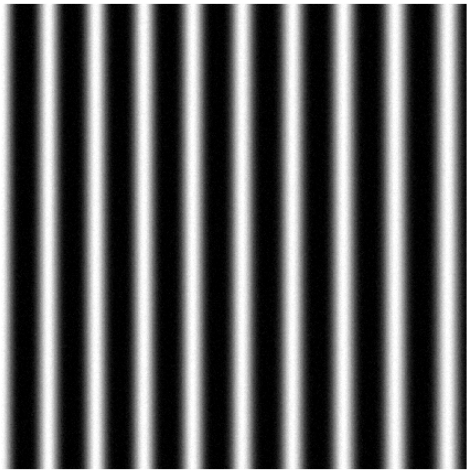

(b) $\hat{g}_{00}(x, y)$

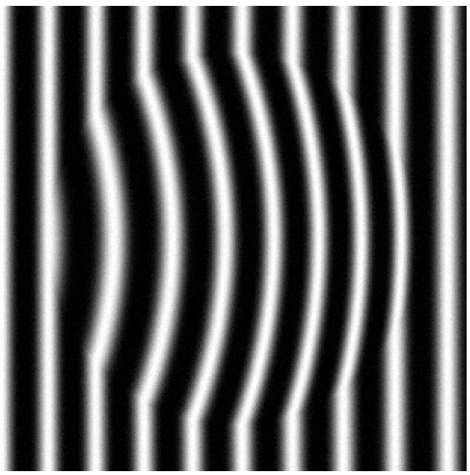

(c) $\hat{g}_0(x, y)$

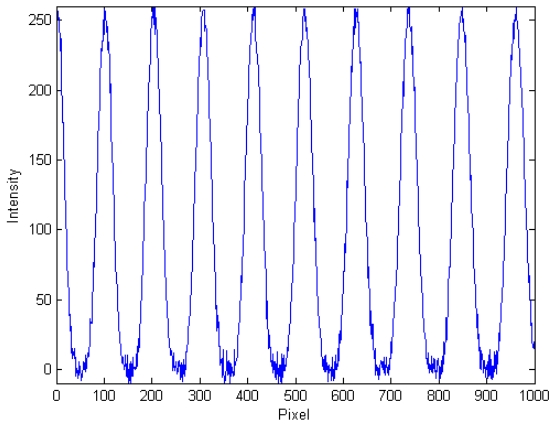

(d) Arbitrary Cross Section $\hat{g}_{00}(x, y)$

Figure 6.3: Simulated phase distribution, reference / deformed fringe and fringe cross-section

	PMP ($N = 3$)		FTP	
	$\bar{\epsilon}$ (mm)	$\bar{\sigma}$	$\bar{\epsilon}$ (mm))	$\bar{\sigma}$
Non-Calibrated	5.4328	4.9113	6.2572	4.7206
Calibrated	0.5055	0.4000	0.9861	0.7903

Table 6.1: Calibrated and Non-Calibrated Absolute Mean Profile Reconstruction Errors and Standard Deviations.

shows an arbitrary cross-section of the reconstructed surface for both PMP and FTP cases. Note that the actual height distribution is represented by the solid line, the calibrated result is shown by the dashed line and, the dotted curve represents the non-calibrated case for both Figures 6.5 (a) and (b). The errors introduced as a result of the fringe anomalies present in the simulated fringe pattern are clearly evident as shown by the dotted curves in Figure 6.5. Figure 6.5 also clearly reveals the successful calibration of the simulated fringe visually, with the calibrated reconstruction a much more accurate representation of the simulated diffuse surface.

6.5 Performance Comparison with existing approaches

6.5.1 Simple Filter Based Technique

Traditionally, filtering techniques are often utilised to attenuate unwanted spectral components present in noisy and distorted signals. These techniques are often very effective and could be successfully employed to enhance the quality of captured digital fringe images. However, filtering techniques are computationally demanding and introduce phase artifacts impacting the object height information modulated into the fringe image and therefore inevitably reduce reconstruction accuracy. In addition to these limitations filtering methods typically present transient periods where the filter buffer is not fully initialised, ultimately resulting in a reduction of the resolution of the final reconstructed 3D surface.

Insight into the limitations discussed above is highlighted by contrasting the neural approach and a simple low-pass filter. For this study it has been assumed that each calibration approach has been previously initialised prior to application i.e. initial neural

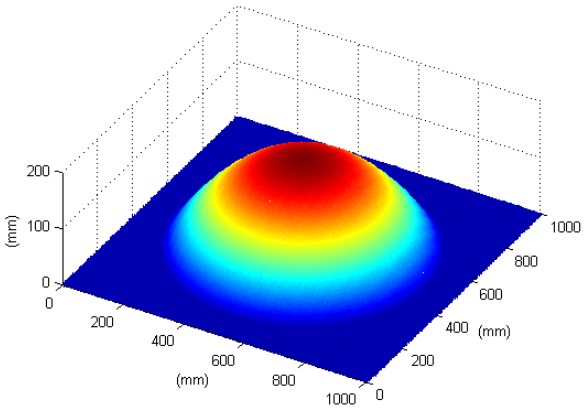

(a) 3-Step PMP Calibrated

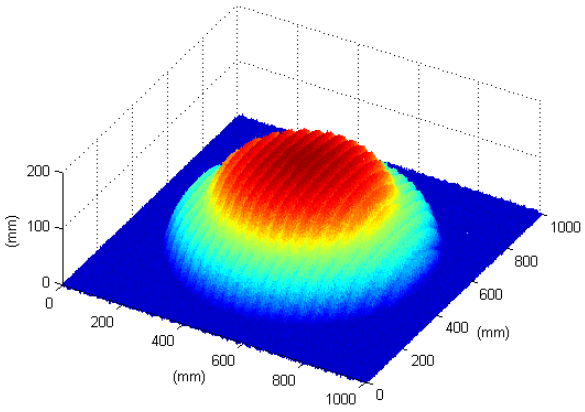

(b) 3-Step PMP Non-Calibrated

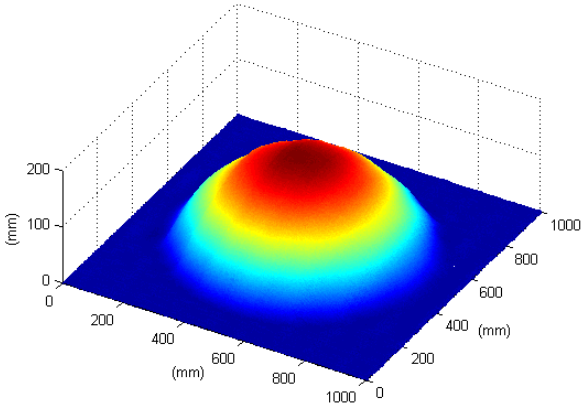

(c) FTP Calibrated

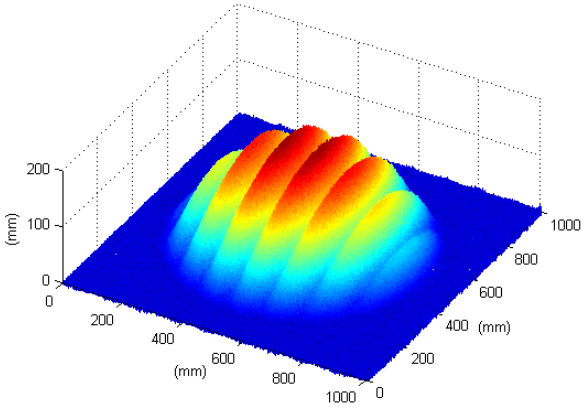

(d) FTP Non-Calibrated

Figure 6.4: Simulated reconstructed surfaces for 3-Step PMP and FTP with and without neural network calibration

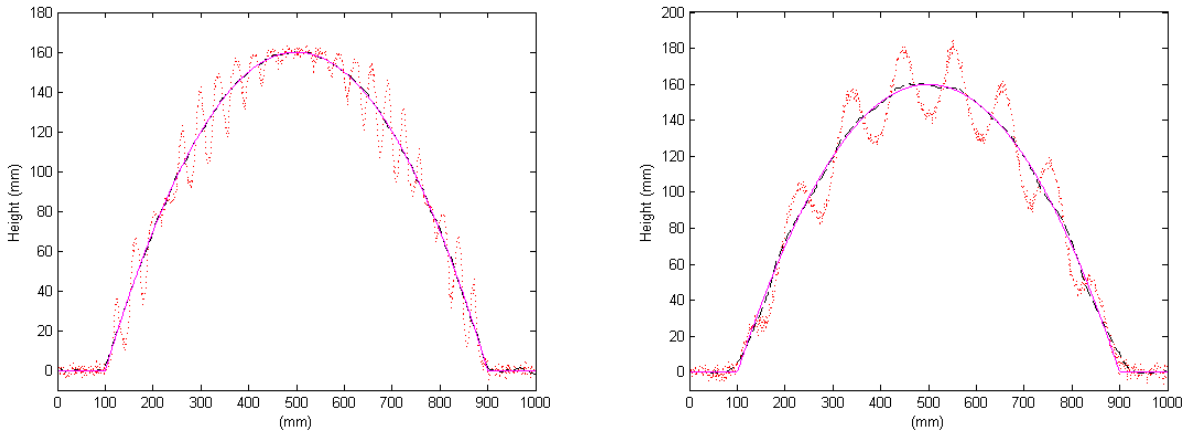

(a) 3-Step PMP (b) FTP

Figure 6.5: Cross section of reconstructed surface for simulated fringe images for both calibrated and non-calibrated scenarios

network training and filter coefficient selection has been undertaken for each of the respective approaches. Two low-pass filters are tested; one with 10 filter taps and a second with 100 filter taps. With the neural network approach utilising the same design topology as depicted in Figure 6.2 the 10 tap filter and the neural network approach can be considered approximately equivalent in terms of multiple/add complexity on a sample per sample basis. Symmetric Finite Impulse Response (FIR) filters were employed to yield an easily predicted constant phase response (translating to a simple delay in the spatial domain) in comparison to the non-linear phase response of Infinite Impulse Response (IIR) filters.

To contrast the ability of each technique to remove the nonlinearities from projected digital fringes, the performance of each approach is evaluated in ideal noiseless conditions. The noiseless distorted fringe images were filtered using the 10 tap and 100 tap low-pass filters and then utilised in the 3 Step PMP fringe processing algorithm to reconstruct the object simulated in the previous section. The distorted fringe set is identical to that specified in the previous simulation with $\gamma = 2.2$, however, with $n_0(x, y) = 0$. The results of this study can be seen in Table 6.2. As can be seen for a similar computation burden the 10 tap filter has marginally improved the reconstruction result. The 100 tap filter has significantly improved the result, however, it still struggles to compete with the neural approach which is more than 10 times more computationally efficient after network

Technique	$\bar{\epsilon}$ (mm)	$\bar{\sigma}$ (mm)
Non-Calibrated	4.5782	4.8747
Neural Network	0.0443	0.0471
10 Tap Low-pass Filter	4.4955	4.7847
100 Tap Low-pass Filter	0.5990	0.6231

Table 6.2: Absolute Mean Errors ($\bar{\epsilon}$) and Standard Deviations ($\bar{\sigma}$) for Neural and Filter Calibration

training.

Figure 6.6 displays an arbitrary cross-section of the reconstructed surfaces for the non-calibrated case, the neural approach, the 10 tap and 100 tap filters respectively. It is evident that the 10 tap low-pass filter has done little to alleviate the fringe anomalies in contrast to the 100 tap filter. An important aspect to note is the attenuation of the higher frequency content in the 100 tap reconstructed surface corresponding to high fringe modulation around the base of the surface. This result is commonplace when using FIR filtering techniques. The problem can be somewhat compensated for through more complex filter design, however, such an approach will typically incur further computation.

6.5.2 Double Three-Step

To further demonstrate the proficiency of the neural network fringe calibration technique, the approach is compared with the Double Three Step algorithm. The Double Three Step algorithm is a technique often quoted in literature as a viable solution for Display Gamma related fringe non-linearities. Again the distorted fringe set is identical to that specified in the previous simulation with $\gamma = 2.2$, however, with $n_0(x, y) = 0$. Figure 6.7 displays an arbitrary cross-section for both the neural calibration and also the Double Three Step technique respectively, while Table 6.3 displays the absolute mean error and standard deviation for each technique. Clearly, the neural approach is more effective in minimising the Display Gamma related errors and furthermore can do so, much more efficiently, with only half the data required relative to the Double Three Step approach. It is however

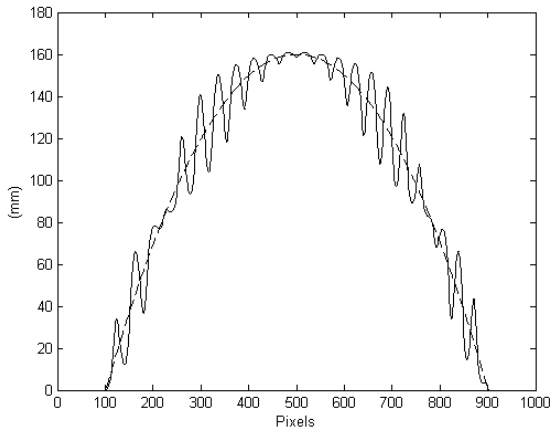

(a) Non-calibrated

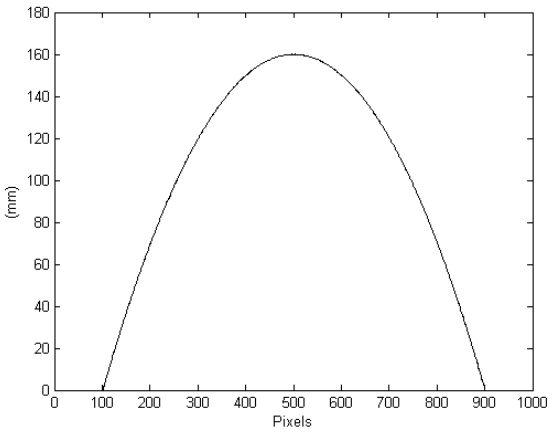

(b) Neural Calibration

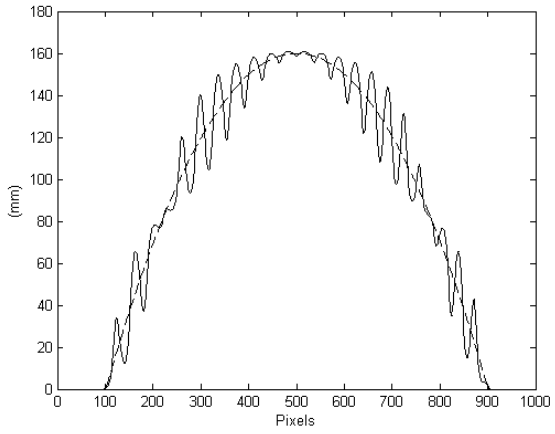

(c) 10 Tap Filter

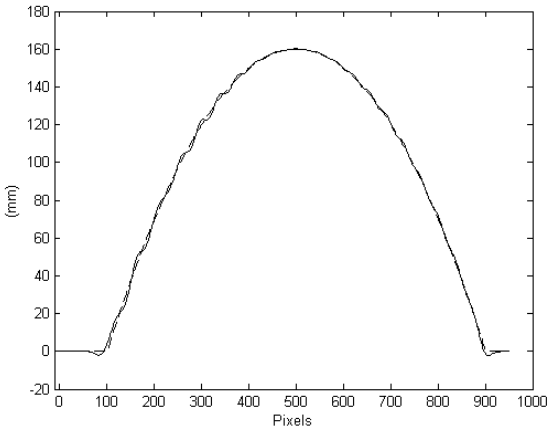

(d) 100 Tap Filter

Figure 6.6: Cross-sections of Reconstructed Surface for Non-calibrated, Neural Calibration and Filtering Calibration, 10 Tap and 100 Tap

important to note that this is a theoretical comparison of the two approaches, where the influence of additional practical phenomena such as temporal luminance artifacts and noise are not considered. Under these conditions the additional images associated with the Double Three Step method are likely to combat the additional fringe phenomena.

6.6 Experimental Verification

In order to verify the physical application of neural networks to signal calibration, practical experimental results were established by profiling a diffuse object. A set of sinusoidal

Technique	$\bar{\epsilon}$ (mm)	$\bar{\sigma}$ (mm)
Non-Calibrated	4.5782	4.8747
Neural Network	0.0443	0.0471
Double Three Step	0.6606	0.7179

Table 6.3: Absolute Mean Errors ($\bar{\epsilon}$) and Standard Deviations ($\bar{\sigma}$) for Neural and Double Three Step Technique

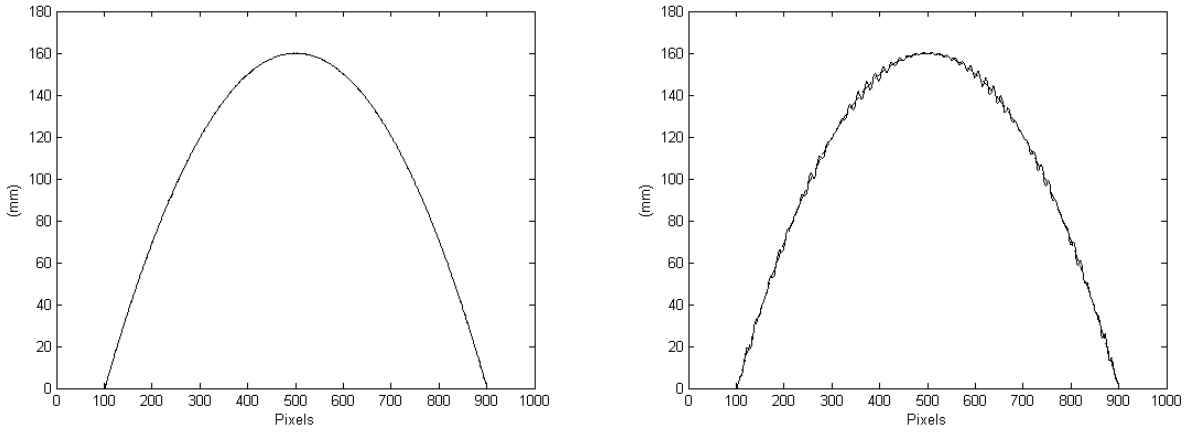

(a) Neural Calibration (b) Double Three Step

Figure 6.7: Cross section of reconstructed surface for neural calibration and Double Three Step scenario

fringe patterns were projected onto a diffuse surface using an InFocus LP530 digital video projector and captured using a MS3100 3-CCD camera. The resolution of the CCD camera is 1392 x 1039 pixels with a field of vision 260 x 194mm^2. This corresponds to a captured fringe pattern with a spatial resolution of 0.1868 mm/pixel, yielding a spatial period of 25.7mm equating to a spatial frequency f_0 of 38.9 fringes/m. It is important to again note that the selection of system parameters is arbitrary, however, to convey as much relevance to the simulation results as possible, the spatial period of the projected fringe images was adjusted such that approximately 10 fringes spanned the entire measurement volume.

System parameters l_0 and d_0 were measured to be 2m and 0.81m respectively. The profiled surface was a convex dome shape as seen in Figure 6.8 (a). The maximum height

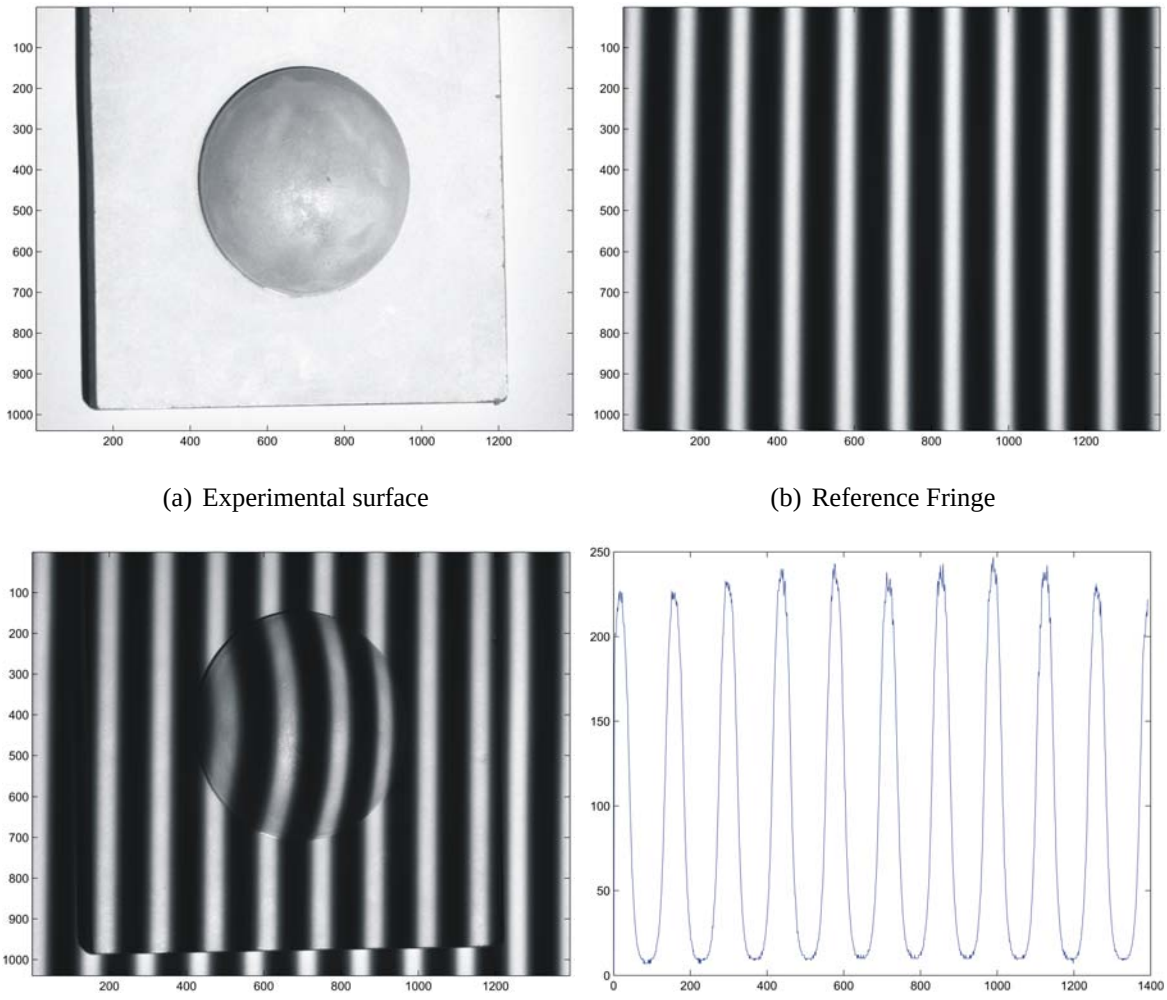

(a) Experimental surface

(b) Reference Fringe

(c) Deformed Fringe

(d) Fringe cross section

Figure 6.8: Experimental object and fringe patterns

of the hemispherical surface is 22.8mm with a diameter of 99mm with the thickness of the base material being 16mm. Figure 6.8 (d) displays a cross section of one of the projected fringe patterns where the nonlinear distortion is quite clearly observed. The distorted fringe images were calibrated using the neural network approach and both the 3 step PMP and FTP techniques were used to reconstruct the profile of the diffuse surface. Figure 6.9 displays the reconstructed surfaces for both calibrated and non-calibrated images for both the 3 step PMP and FTP techniques. An arbitrarily selected cross-section of the reconstructed surface is shown in Figures 6.10 (a) and (b) for both the PMP and FTP techniques respectively. The non-calibrated reconstruction is indicated with the dashed line with solid line indicating the calibrated reconstruction. It can be clearly seen that

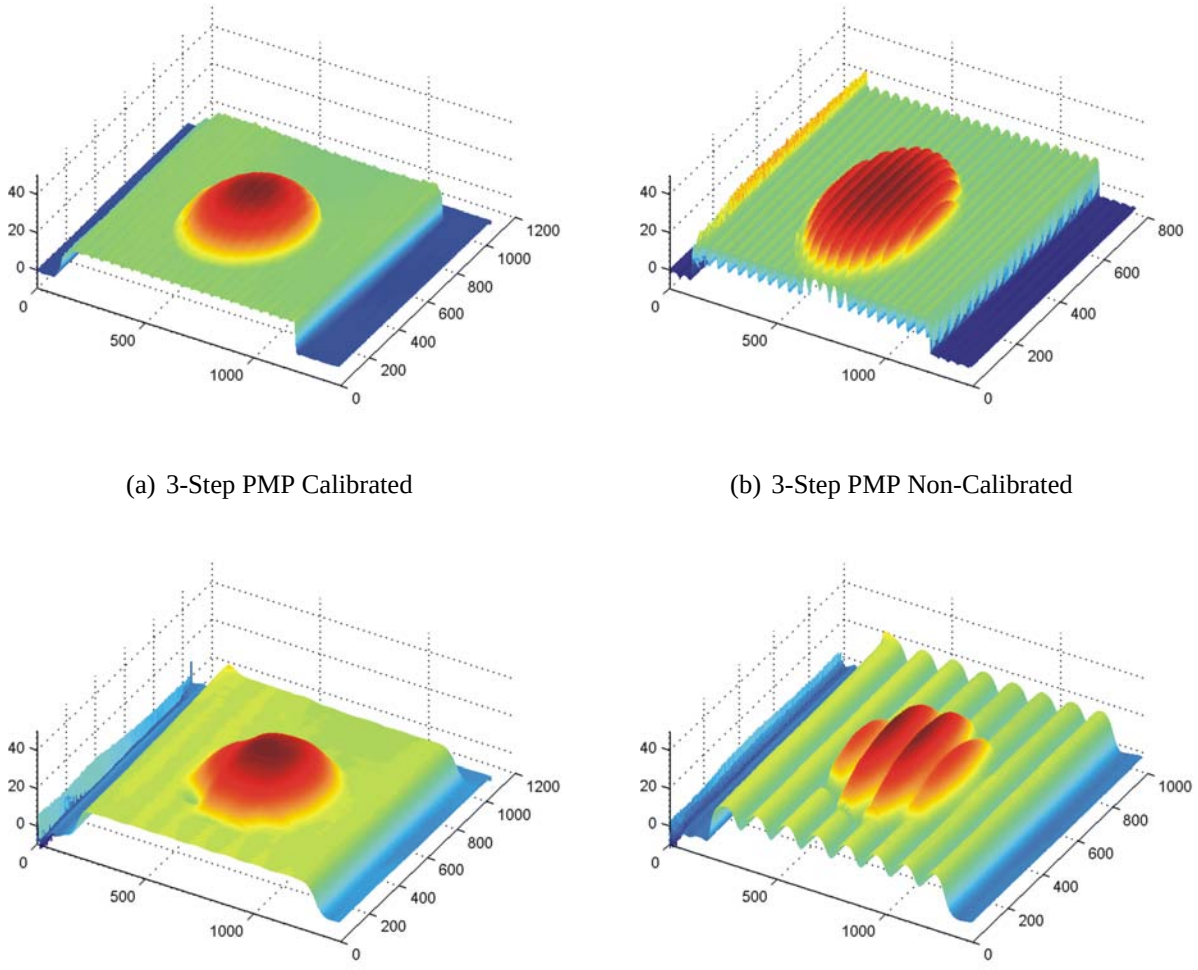

(a) 3-Step PMP Calibrated

(b) 3-Step PMP Non-Calibrated

(c) FTP Calibrated

(d) FTP Non-Calibrated

Figure 6.9: Experimental reconstructions for 3 Step PMP and FTP techniques with and without neural network calibration

the neural network calibration technique has been successful in reducing the non-linear distortions associated with the projection /capture system.

6.7 Multi-channel Digital Fringe Calibration using Neural Networks

As outlined in Section 3.5 digital multi-channel applications present significantly more complex fringe signals relative to the single channel scenario. Therefore, the requirement for effective yet robust fringe calibration is considered a mandatory process for princi-

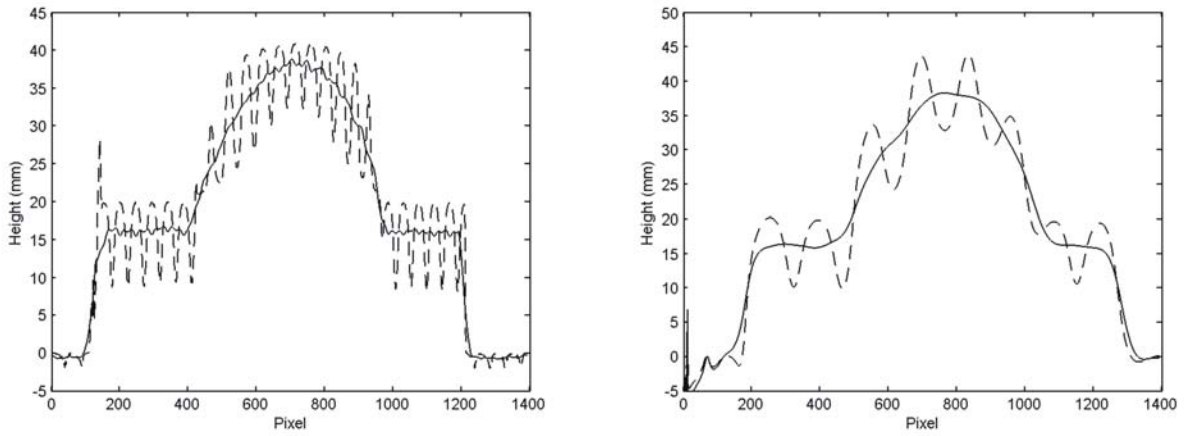

(a) 3-Step PMP (b) FTP

Figure 6.10: Cross section of Experimental reconstructions for both 3 Step PMP and FTP techniques

ple multi-channel approaches. In the past, solutions to counter such fringe anomalies typically involve photometric calibration. To alleviate the non-linear luminance effects, multiple intensity distributions varying over the full range of luminance values for each channel are recorded and a camera / projector luminance curve is fitted [88,90]. Similarly, to facilitate the adequate separation of a multi-channel fringe into its individual colour components, a number of colour images are projected / captured and a mixing matrix representing the portion of colour leakage to and from each channel is formed [88, 139]. Often such approaches can be laborious, time consuming, require a substantial amount of additional data and are typically nonresilient to environmental change.

Considering the notable success of the neural fringe calibration approach for the single channel scenario, one is motivated to extend the concept to the multi-channel case. Further given the significant increase in the amount of data typically required for photometric multi-channel calibration, the neural fringe calibration technique lends itself as an ideal solution for multi-channel fringe calibration since no additional data is required.

6.7.1 Principle Digital Multi-channel Fringe Profilometry

The ability to project and acquire colour fringe images has made possible the realtime application of popular non-single shot approaches such as PMP. Probably the most ex-

ploited multi-channel technique is the 3 Step PMP approach since all required data can be obtained in a single exposure. The principle digital multi-channel fringe can be given as

$$\begin{pmatrix} r(\hat{x}, y) \\ g(\hat{x}, y) \\ b(\hat{x}, y) \end{pmatrix} = \hat{K} \begin{pmatrix} [a + b\cos(\omega(x, y))]^{\gamma_R} \\ [a + b\cos(\omega(x, y) + 2\pi/3)]^{\gamma_G} \\ [a + b\cos(\omega(x, y) + 4\pi/3)]^{\gamma_B} \end{pmatrix} \tag{6.14}$$

where $r(\hat{x}, y)$, $g(\hat{x}, y)$ and $b(\hat{x}, y)$ represent the signals obtained at the respective colour CCD sensors of the acquisition device and, γ_R, γ_G and γ_B denote the non-linear luminance Display Gamma characteristics for the red, green and blue colour channels, respectively. The mixing matrix is given by

$$\hat{K} = \begin{pmatrix} 1 & k_{GR} & k_{BR} \\ k_{RG} & 1 & k_{BG} \\ k_{RB} & k_{GB} & 1 \end{pmatrix}$$

where k_{XY} represents the normalised proportion of colour coupling between the appropriate channels. Therefore substituting Equation (6.14) into Equation (2.18) with $N = 3$, an estimation of phase component $\omega(x, y)$ and hence $h(x, y)$ can be obtained in just a single image.

Examining Equation (6.14) reveals the considerable non-sinusoidal attributes associated with the multi-channel application and can therefore provide further insight into the various errors introduced into the measurement. The significance and nature of the Display Gamma related errors has already been extensively detailed previously, however, the measurement error associated with the coupling of colour channels has yet to be examined.

6.7.2 Error Analysis

This section investigates the influence the colour channel coupling effect has on the principle multi-channel phase measuring algorithm. Firstly, we assume similar linear channel luminance $\gamma_R = \gamma_G = \gamma_B = 1$. Clearly this is not true in practice, however, such assumptions help provide insight into the nature and also gauge the magnitude of resulting phase

measuring error. We can then denote the general amplitude, ψ_n and phase angle, ζ_n, of a crosstalk fringe as

$$\psi_n = \sqrt{3(k_{n1} - k_{n2})^2 + (2k_{n0} - k_{n1} - k_{n2})^2} \tag{6.15}$$

$$\zeta_n = \arctan\left(\frac{\sqrt{3}(k_{n1} - k_{n2})}{2k_{n0} - k_{n1} - k_{n2}}\right) \tag{6.16}$$

where k_{n0}, k_{n1} and k_{n2} for $0 \leq k_{n,012} < 1$ denote the normalised proportion of channels 1, 2 and 3, respectively, for the nth fringe image with corresponding 0, $2\pi/3$ and $4\pi/3$ phase shift. If we now assume the amplitude components of each fringe have been normalised i.e. $\psi_n = \psi_n = \psi_n = \psi$, we can see that a phase error for each fringe will be propagated through the phase measuring algorithm

$$\hat{\omega} = \arctan\left(\frac{\sqrt{3}\left(\cos(\omega + \zeta_1) - \cos(\omega + \zeta_2)\right)}{2\cos(\omega + \zeta_0) - \cos(\omega + \zeta_1) - \cos(\theta + \zeta_2)}\right) \tag{6.17}$$

where $\hat{\omega}$ represents the predicted value of ω, as evaluated in the presence of the colour coupling. Substituting Equation (6.16) into Equation (6.17) yields the phase prediction $\hat{\omega}$ as

$$\hat{\omega} = \arctan\left(\frac{\sqrt{3}(\alpha\cos\omega + \sqrt{3}\eta\sin\omega)}{\rho\cos\omega + \sqrt{3}\chi\sin\omega}\right) \tag{6.18}$$

where

$$\begin{aligned}
\alpha &= 2(k_{10} - k_{20}) - k_{12} + k_{21} \\
\eta &= k_{21} + k_{12} - 2 \\
\rho &= 6 - 2(k_{01} + k_{02} + k_{10} + k_{20}) + k_{12} + k_{21} \\
\chi &= 2(k_{02} - k_{01}) - k_{12} + k_{21}
\end{aligned}$$

Hence, it can be seen that the error introduced by the coupling of the colour channels is a function of the four crosstalk variables, α, η, ϵ and χ and also ω, and so we can conclude that the error will not only depend on the amount of crosstalk but also on the surface to be profiled.

6.7.3 Proposed Multi-channel Fringe Calibration Technique

Due to the nature of the multi-channel fringe anomalies we propose a two step calibration process; firstly the colour channel coupling is removed, followed by the intensity linearisation of each channel by the neural network approach.

6.7.3.1 Counter Coupling of Colour Channels

For most commercial digital video projectors, significant leakage from just one channel is typically observed, and therefore, only two coupling factors are considered influential [139]. If we now consider just two coupling factors and examine Equation (6.18) it can be revealed that colour channel selection would not lead to a significant improvement in the prediction of ω. Hence, in order to ensure the accurate prediction of ω, the accurate prediction of mixing matrix $\hat{K}$ and thus isolation of each fringe is essential. If $\hat{K}$ is known the coupling can be removed as follows

$$\begin{pmatrix} r(x,y) \\ g(x,y) \\ b(x,y) \end{pmatrix} = K. \begin{pmatrix} r(\hat{x},y) \\ g(\hat{x},y) \\ b(\hat{x},y) \end{pmatrix} \tag{6.19}$$

where

$$K = \begin{pmatrix} 1 & -k_{GR} & -k_{BR} \\ -k_{RG} & 1 & -k_{BG} \\ -k_{RB} & -k_{GB} & 1 \end{pmatrix}$$

Since K is a distinctive variable set for each projector camera arrangement it must be measured by photometric processes.

6.7.3.2 Multi-channel Display Gamma Non-linear Luminance

Subsequent to the counter coupling of colour channels the intensity of each channel is linearised and normalised via the neural network based approach as outlined in Section 6.3. The only differentiation between the single channel and multi-channel implementations is the training of three individual neural networks to compensate for the three individual Display Gamma non-linear luminance responses.

6.7.4 Simulation

To validate and also gauge the performance of the proposed calibration technique we simulate the reconstruction of a diffuse surface $h(x, y)$, illuminated by the multi-channel fringe described as follows

$$\begin{pmatrix} r(\hat{x}, y) \\ g(\hat{x}, y) \\ b(\hat{x}, y) \end{pmatrix} = K \begin{pmatrix} [a + b\cos(2\pi f_0 x)]^{\gamma_R} \\ [a + b\cos(2\pi f_0 x + 2\pi/3)]^{\gamma_G} \\ [a + b\cos(2\pi f_0 x + 4\pi/3)]^{\gamma_B} \end{pmatrix} \tag{6.20}$$

γ_r, γ_g and γ_b were chosen to be 2.2, 2.5, and 2.1 respectively with an appropriately simulated mixing matrix K. System parameters l_0, d_0 and f_0 were chosen to be 5m and 2m and 10 fringes/m respectively, corresponding to a spatial period of 100mm if we assume an image spatial resolution of 1 pixel/mm. Fringe parameters a and b were chosen to be equivalent to maximise the influence of the non-linear γ distortion. We reconstruct the non-calibrated and calibrated fringe images using the phase measuring algorithm. Table 6.4 displays the mean absolute measuring error $\bar{\epsilon}$ and standard deviation $\bar{\sigma}$ for both the calibrated and non-calibrated cases. A visual representation of the simulated fringe,

	PMP ($N = 3$)	
	$\bar{\epsilon}$ (mm)	$\bar{\sigma}$ (mm)
Non-Calibrated	5.443	5.4967
Calibrated	0.0403	0.0427

Table 6.4: Calibrated and Non-calibrated mean absolute reconstruction errors and standard deviations.

hemispherical test surface and calibrated and non-calibrated reconstructions can be seen in Figure 6.11. The improvement for the calibrated fringe in contrast to the non-calibrated is clearly evident visually.

6.7.5 Experimentation Verification

In order to verify the physical application of the multi-channel fringe calibration approach, practical experimental results were established through the profiling of a diffuse surface.

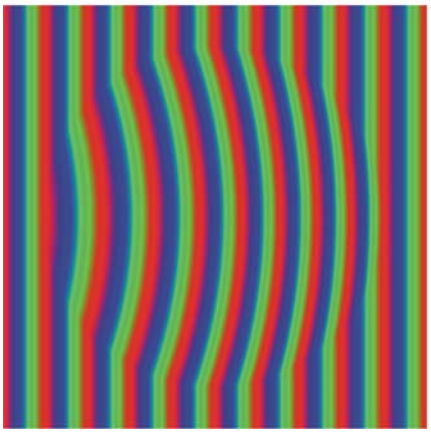

(a) Typical Multi-channel Fringe

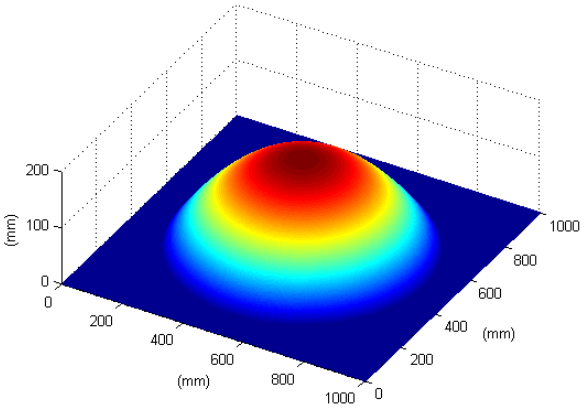

(b) Simulated 3D surface, $h(x, y)$

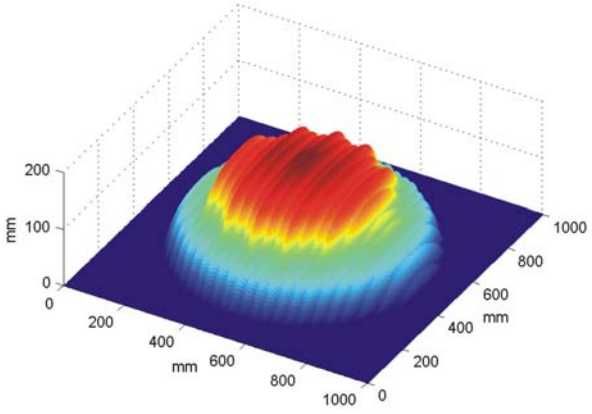

(c) Non-calibrated reconstruction

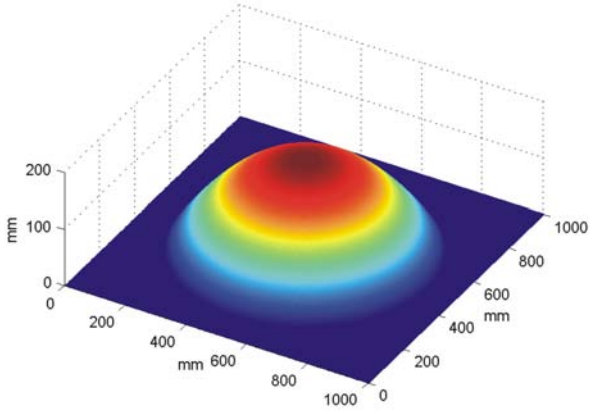

(d) Calibrated reconstruction

Figure 6.11: Simulated reconstructed surface with and without the proposed fringe calibration

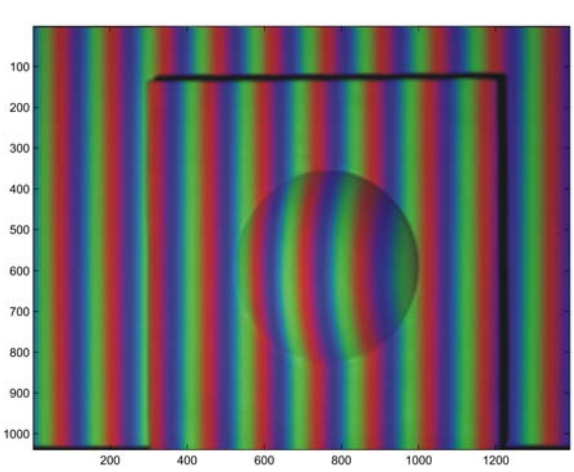

(a) Experimental surface

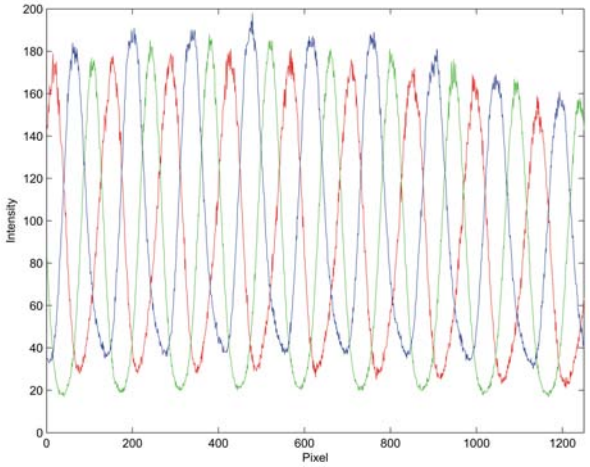

(b) Reference Fringe Cross-section

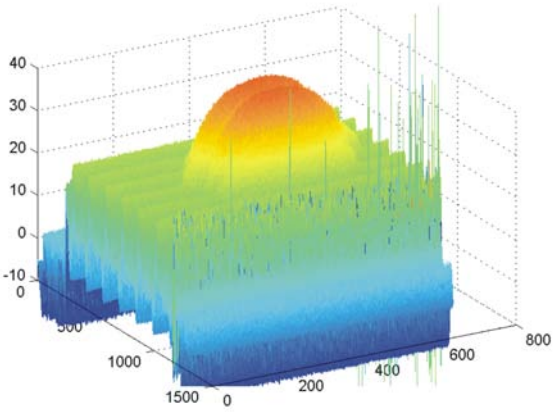

(c) Non-calibrated Reconstruction

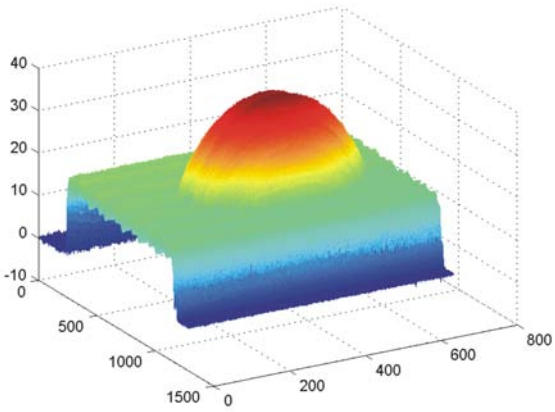

(d) Calibrated Reconstruction

Figure 6.12: Multi-channel Experimental Results

A multi-channel sinusoidal fringe pattern was projected using a Hitachi CP-X260 LCD digital video projector and captured using a DuncanTech MS3100 3-CCD camera. The spatial resolution of the captured fringe image was measured to be 0.215 mm/pixel, yielding a spatial period of 30.9mm equating to a spatial frequency f_0 of 32.4 fringes/m [1]. System parameters l_0 and d_0 were measured to be approximately 1.405m and 0.465m respectively. The profiled surface was a convex dome shape as seen in Figure 6.12 (a). The maximum height of the hemispherical surface is 22.8mm with a diameter of 99mm with the thickness of the base material being 16mm.

[1] Again f_0 was adjusted to provide as much correspondence to the simulated scenario

It was found that the only significant colour channel coupling was from the green to red and green to blue channels, all other terms in the mixing matrix were ignored. The photometric measurement of k_{rg} k_{bg} was undertaken via the projection of a pure green fringe and the red and blue components were measured. To ensure the integrity of the assumption of a static mixing matrix a high intensity fringe was projected, with $a = 150$ and $b = 100$. Despite our efforts to justify a uniform colour mixing, the colour mixing presented spatial attributes.

The projected fringe was filtered using the gaussian smoothing technique to maximise the performance of the neural approach. The three neural networks as described in Section 6.3 were used to counter the channel γ non-linearity sample by sample. The reconstructed surfaces for the non-calibrated and calibrated fringes is shown as Figures 6.12 (c) and (d) respectively. A cross-section of the reconstructed surface for both the calibrated and non-calibrated cases is shown in Figures 6.13 (a) and (b). The calibration technique has clearly been successful in minimising the associated fringe errors, however, a significant phase measuring error is still evident as indicated in Figure 6.13. Considering the notable success of the application of the neural network approach for single channel scenario the error can be attributed to the inadequate isolation of each colour channel, which then led to the poor training of the neural networks. It is believed that the static approximation of the mixing matrix given by Equation (6.19) is too strong an approximation of the actual mixing process [165, 166].

6.8 Summary

This chapter proposed, verified and demonstrated the application of neural networks for gamma correction of digitally projected fringe images. Unlike previously proposed gamma correction techniques, the neural fringe calibration technique requires no additional data acquisition with effective calibration requiring no more than a single cross-section of a reference fringe. Further, the neural approach was shown to significantly outperform simple filter based techniques of similar computational complexity. The neural calibration was also theoretically shown to be more effective and efficient in minimising Display Gamma related measurement errors relative to the apparent Display Gamma

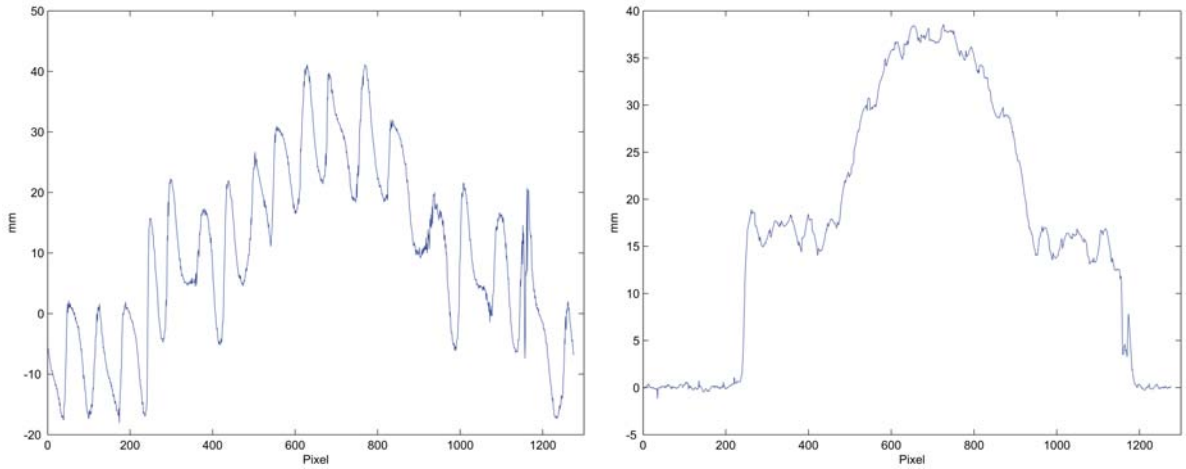

(a) Non-calibrated Reconstruction (b) Calibrated Reconstruction

Figure 6.13: Cross-section of reconstructed diffuse surface seen in Figure 6.12(a)

insensitive Double Three Step approach.

Given the reduced data requirements for the neural approach its application for multi-channel fringe calibration was also considered. The neural approach was shown to be somewhat effective for this purpose, however, the empirical isolation of each colour channel significantly impeded the effectiveness of the calibration approach in the multi-channel scenario.

Chapter 7

Conclusions and Suggestions for Further Research

7.1 Conclusions

The collective research initiative of the work presented in this thesis has been divided between two principle objectives. The first objective of this thesis has been to effectively identify, describe and study the limitations associated with the application of DVP for Fringe Projection 3D sensing techniques, while the second objective of the work has been concerned with improving the effectiveness of the deployment of DVP for Fringe Projection 3D sensors. The first objective has been facilitated through extensive analytical, computer and practical analysis of the application of DVP for Fringe Projection 3D sensing (Chapters 3, 4 and 5), while the second objective has been facilitated through the proposal and verification of novel digital fringe calibration procedures (Chapters 5 and 6).

Initially, as demonstrated in Chapter 3, the concept of DVP for Fringe Projection 3D sensing was introduced and the key shortcomings of the digitally projected fringe image established. With the insight of the key projection limitations a novel phase emulation approach was proposed and employed to assess the integrity of the application of DVP for Fringe Projection. More specifically, the phase emulation approach was utilised to establish insight into the veracity of the two chief DVP technologies (LCD and DLP) as a reliable fringe projection source, for both single and multi-channel scenarios. It was found

that the deployment of DLP technology for Fringe Projection ideally requires the synchronisation of projection and acquisition devices to ensure the appropriate attenuation of temporal fringe artifacts for both the single and multi-channel scenarios. Furthermore, by this empirical analysis the most significant and prominent DVP Fringe Projection shortcoming was revealed to be the camera / projector non-linear intensity response. This result was found to be equally significant and commonplace for both LCD and DLP projection technologies.

Following the findings presented in Chapter 3, the camera / projector non-linear intensity phenomena was examined more closely. Chapter 4 described the camera / projector non-linear intensity response as being characterised by the projector Display Gamma luminance response. The harmonic structure and magnitude of a typical digitally projected fringe was analytically studied and an approximate analysis framework was formed. Given the analytical framework, the influence of γ for a range of fringe processing algorithms was analytically established by defining a set of functions describing both the residual phase error and associated sensitivity of the phase measuring process in the presence of Display Gamma. The validity of the analytical findings was later established by computational evaluation and, furthermore, by practical experimentation via the phase emulation approach. The results of this study revealed the true Display Gamma sensitivity for a range of well exploited fringe processing algorithms, clarifying the previously misconstrued issue [96]. The vulnerabilities of the purpose designed Double Three Step technique were also exposed, with the standard 4 Step PMP technique shown to be more resilient in the presence of γ distortion. A further important conclusion revealed by this investigation was the confirmation of a heighten γ sensitivity for minimum step techniques (including FTP). This result is particularly important as it signifies the considerable role gamma correction has in the effective application of DVP for dynamic fringe profiling implementations.

Although many aspects of the Display Gamma investigations demonstrated in Chapters 3 and 4 complement their respective findings, a distinct contradiction in regard to the frequency dependence of the resulting Display Gamma residual phase error had been revealed. The practical Display Gamma findings presented in Chapter 3 demonstrated a frequency dependence, while Chapter 4 demonstrated a theoretical frequency indepen-

dence. The conspicuous nature of the contradiction fueled the need to further facilitate a more thorough investigation into the practical nature of the Display Gamma phenomena and moreover the practical gamma distorted fringe. Consequentially, Chapter 5 was concerned with investigating the additional practical phenomena associated with a projected gamma distorted fringe. More specifically, Chapter 5 examined the manipulation of fringe offset and contrast parameters, the temporal fringe artifacts associated with Display Gamma and the effects of the projection optics on the formation of digitally projected fringe images.

The harmonic dependence of a gamma distorted fringe on the fringe offset and contrast parameters was demonstrated and, moreover, the effective manipulation of fringe offset and contrast to minimise gamma associated reconstruction errors was experimentally verified. Further, the important practical correlation between fringe contrast and SNR was demonstrated. Although it was shown that the effective manipulation of fringe parameters could yield digital fringe optimisation, the practical limitations of a diminished SNR resulting from finite projection / acquisition device fidelity was shown to ultimately inhibit the approach.

The important issue of temporal non-linear luminance was investigated by studying the effects of temporal Display Gamma for the well exploited minimum shot FTP fringe processing algorithm. The analytical findings of this investigation were verified by simulation analysis and further a practical example of the temporal variation of the luminance was demonstrated. The practical temporal variation was then utilised in a computer simulated reconstruction to demonstrate the influence of temporal Display Gamma. The results of this analysis revealed a ripple function present on the reference plane object. The rippling of the reference plane was further identified as a key indication of the presence of temporal fringe artifacts. Although this derivation was primarily concerned with the FTP method, the results can be extended to gain an understanding of the temporal Display Gamma behaviour for stepping approaches and, furthermore, to provide insight into the influence of temporal Display Gamma for gamma corrected systems.

The final investigation presented in Chapter 5 was concerned with examining the digital fringe image formation process. This entailed the derivation of the optical modulation transfer function for the projection optics of the typical DVP source. The validity of

this study and hence the effectiveness of digital fringe optimisation by projector defocusing was verified by defining the minimum stepping requirements to eliminate gamma related phase estimation errors for stepping fringe processing techniques. These findings were demonstrated through both simulation and empirical analysis. It was shown that the Display Gamma residual error commonplace with typical values of γ can be effectively eliminated by employing the 4 Step PMP variation with a simple defocusing optimisation. In other words, it was shown that by marginally increasing the data requirements, the need for Display Gamma compensation techniques can be omitted with no additional computational overhead. This result is particularly interesting when considering the amount of research effort aimed at gamma correction and / or the alleviation of Display Gamma related errors for highly gamma sensitive minimum shot techniques. The importance of this finding for dynamic applications is further highlighted when considering the rapidly evolving high speed digital acquisition and display technologies.

A further important issue resolved in Chapter 5 was the question of the frequency dependence of the Display Gamma residual phase measuring error. With the insight of a more formidable theoretical modeling of the practical nature of the gamma distorted fringe, it was shown that the Display Gamma residual error was in fact a frequency dependent phenomena. The implications of this for lookup table based gamma compensation approaches which assume frequency independence was also discussed. Our investigation clearly showed that frequency independence cannot be assumed other than for specific cases considered in the lookup table.

Finally, Chapter 6 proposed, verified and demonstrated the application of neural networks for gamma correction of digitally projected fringe images. Unlike previously proposed gamma correction techniques, the neural fringe calibration technique requires no additional data acquisition with effective calibration requiring no more than a single cross-section of a reference fringe. Further, the neural approach was shown to significantly outperform simple filter based techniques of similar computational complexity.

Given the reduced data requirements for the neural approach its application for multi-channel fringe calibration was also considered. The neural approach was shown to be somewhat effective for this purpose, however, the experimental isolation of each colour channel significantly impeded the effectiveness of the calibration approach in the multi-

channel scenario.

7.2 Suggestions for Further Research

While this thesis has concentrated specifically on improving the deployment of DVP for 3D sensing using Fringe Projection techniques, a number of issues beyond the scope of this thesis require further attention to facilitate effective Fringe Projection 3D data acquisition.

Perhaps the most rudimentary yet challenging issue inhibiting the full scale deployment of Fringe Projection 3D sensing for a diverse range of applications is the infamous phase unwrapping dilemma. For many of the simulated and actual object shapes demonstrated in this thesis (given their simplistic geometries) very simple phase unwrapping procedures suffice for the appropriate estimation of the true phase map. In the practical environment beyond the laboratory robust and noise resilient phase unwrapping procedures are paramount for the accurate estimation of discontinuous and complex surfaces. A foreseeable area of research to aid in the phase unwrapping process for Fringe Projection is the projection of coded sinusoidal fringe images. Combining the coded light approach with Fringe Projection would ensure reliable scene correspondence, while the sinusoidal fringe would ascertain the required spatial sensitivity of the measurement. In fact, it is very likely that 3D sensing apparatus of the future will combine the technology of multiple sensing techniques, to provide an interpolated result for optimal measurements under various application specific conditions. An interesting development would likely see the combination and further exploitation of generic signal techniques such as that proposed by Hu *et al.* [146] with Fringe Projection techniques.

Another important issue to highlight for future work would be the consideration of temporal ambient lighting conditions for fringe processing. This is particularly interesting considering the significant influence temporal fringe variations present for fringe processing, as demonstrated in Chapter 5. Ambient lighting conditions outside the laboratory scenario would certainly pose as an unpredictable and temporal phenomena and reliable techniques to address this concern must be considered in future work.

Future endeavors related more specifically to some of the concepts and research pre-

sented in this thesis would see a number of aspects of the research extended to further facilitate the effective application of DVP for Fringe Projection 3D sensing. In particular, the following issues require further research attention;

- The temporal gamma compensation of digitally projected fringe signals.
- The implications of the assumption of Display Gamma phase residual frequency dependence for lookup table based gamma compensation and;
- The effective elimination of the coupling of colour channels phenomena.

An important issue to acknowledge in regard to the neural network based digital fringe calibration presented in Chapter 6 is that although the approach can efficiently and effectively calibrate digitally projected fringe images, the solution still fails to address the temporal aspects associated with Display Gamma. In fact, all current gamma compensation approaches operate under the assumption that γ is a static phenomena with any temporal variation of γ resulting in further phase estimation error. This therefore, signifies the distinct requirement to further facilitate firstly, an adequate investigation into the true temporal nature of the digitally projected fringe (for both LCD and DLP projection technology) and, secondly, the development of temporal gamma compensation techniques.

As demonstrated in Chapter 5 the Display Gamma residual phase error function was shown to be a frequency dependent phenomena. This finding challenges the frequency normalisation of phase lookup table based solutions such as that presented by Zhang and Yau [98]. Considering the possible future exploitation of the novel approach, it is essential to evaluate the shortcomings of the assumption of Display Gamma phase residual frequency independence. Chapter 5 discusses the implications of such assumptions, however, a thorough mathematical investigation followed up with empirical analysis of the issue is required for clarification.

Finally, as demonstrated in Chapter 6, the application of colour for Fringe Projection 3D sensing is a difficult task. The most significant outstanding issue that needs to be addressed before colour can be effectively employed for Fringe Projection is the adequate isolation of each colour channel by removal of the inherent cross-talk that naturally

arises in practice. Current solutions proposed on this issue are based on the rudimentary principles of colour theory (as demonstrated in Chapter 3) and the assumption that the mixing is static and linear [88, 95, 139]. However, through this work the mixing was shown to present spatial attributes and depending on the projection technology temporal attributes also. Therefore, this issue requires further attention in the future if colour is to be effectively utilised in Fringe Projection sensing arrangements. Supplementary to this shortcoming, a further concern for multi-channel implementations is the influence of the spectral content of the surface being profiled. This issue has seen current multi-channel applications effectively limited to the profiling of neutral or uniformly coloured surfaces.

Appendix A

Finite Projection Empirical Verification

In order to demonstrate the validity of the finite projection analytical derivation (as shown in Chapter 3), practical experimental results were established to measure the size of projected pixels. The experiment utilised an optical arrangement similar to that as seen in Figure 2.3 to project a Ronchi grating onto a flat surface that served as a reference plane. The plane corresponded to an object with a uniform height distribution and gradient of 0. Each fringe of the software generated bitmap grating was exactly 10 projected pixels in width with the intensity varying from white (255,255,255) to black (0,0,0). The Ronchi distribution was projected using an InFocus LP530 DLP projector with an effective resolution of 1024 by 768 pixels. A DLP projector was selected due to its superior fill factor, following the fill factor assumption made in the finite projection derivation. The grating pattern was captured using a DuncanTech MS3100 3-CCD camera with an effective resolution of 1392 by 1039 pixels. To accurately measure the fringe pattern the capture device was fitted with a zoom lens and placed onto a sliding apparatus enabling precision capture of the entire projected image. From the captured intensity distribution projected pixel size was calculated based on fringe widths. To improve the edge detection process and reduce the influence of temporal intensity variations resulting from the temporal nature of the DLP projection source, multiple fringe shots were averaged. Furthermore, the temporal artifacts were further minimised by increasing the integration time of each of the three CCD sensors in the camera. The index of the ith fringe local maximum and minimum denoted, i_{MAX} and i_{MIN} respectively, were determine by performing a 40 point running average on the captured Ronchi grating, $\Psi(x)$, to accommodate for spatial variations in

intensity resulting from non-uniformities in both the projection source and also the projection surface. To further accommodate for this phenomenon the gains of the each of the 3 CCD channels were adjusted such that the mean value of fringe data was approximately 128. The intensity value of the ith fringe edges $E(i_1)$ and $E(i_2)$ were then determined by

$$E(i_1) = \left[\frac{\Psi(i_{MAX}) - \Psi(i_{MIN})}{2}\right] + \Psi(i_{MIN}) \quad \text{(A.0.1)}$$

$$E(i_2) = \left[\frac{\Psi([i+1]_{MAX}) - \Psi(i_{MIN})}{2}\right] + \Psi(i_{MIN}) \quad \text{(A.0.2)}$$

The original fringe data, $\Psi(x)$, was then linearly interpolated and the fringe data searched to find the appropriate fringe edges based on the intensity values, $E(i_1)$ and $E(i_2)$ in terms of number of camera pixels. The fringe width was then determined using calibration factor $k_x = 6.47 \times 10^{-5}$ m/pixel to convert the fringe width from pixels to meters.

System parameters β, α and l_0 were measured as 1.708 rads, 0.00533 rads and 1.896 m respectively to be within 0.08% accuracy. Using these parameters the predicted values for pixel size as determined by means of the analytical model could be ascertained. Figure A.1 displays both the experimental and simulated results for fringe size in the x direction, with the experimental data represented with corresponding error bars and the simulated data as produced using the model represented by the solid red line. Close examination of Figure A.1 indicates that from approximately fringe 20 onwards the distribution of the experimental results closely imitates that of the analytical data, however, the model does not accurately describe the experimental data for earlier fringes. This error can be attributed to the characteristics of the projector optics. Considering, that the fundamental assumption made in deriving the model is that the angle subtended by any one pixel is identical, the supposition that this assumption holds true for the outer edges of the projected image (where lens abberation is greatest i.e. fringes 1 through to 20) is inaccurate and hence the model performs poorly under such conditions. Also taking into account the fact that digital video projectors are designed to project onto flat surfaces from an approximately orthogonal angle relative to the intended image plane, the projector lens may be designed to accommodate for more evenly distribution pixel sizes on the edges of the picture, hence further contributing to aberration effects. Ignoring the data affected by the projector lens abberation experimental results were found to be within experimental error with an abso-

lute average error of 3.313 x 10^{-5} m when taking into consideration the calibration factor k_x, with the peak relative error measured being 0.818% with an average relative error of 0.281%.

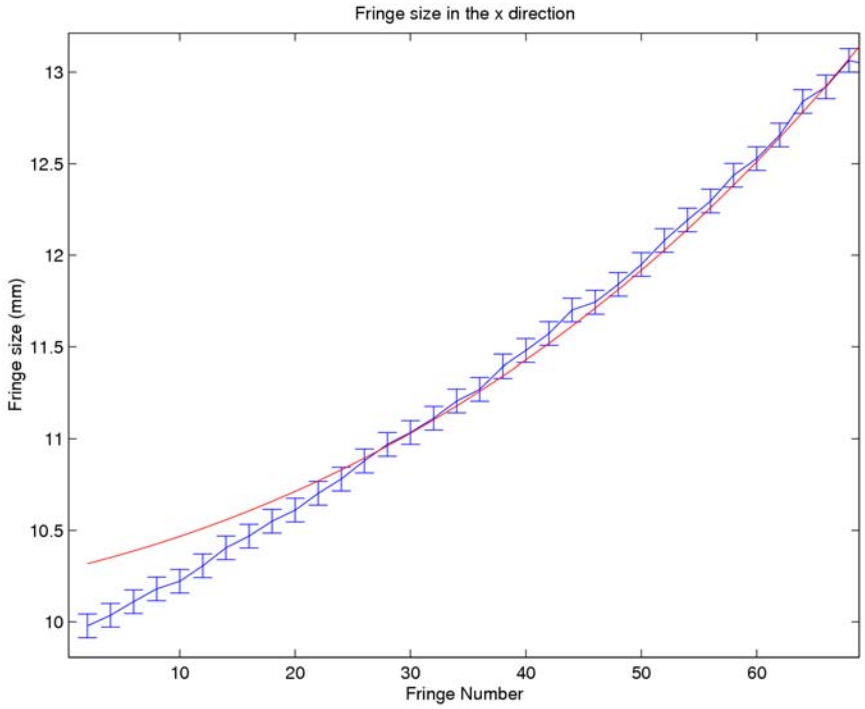

Figure A.1: Finite Projection Experimental Verification

Apart from the obvious camera quantisation errors, other error sources stem predominantly from the following; measurement of system parameters β, α and l_0 and focusing of the projector. The former directly impacts the resulting model data and hence accurate measurement of these parameters is essential for accurately predicting projected pixel size. The measurement errors in system parameters for this experimentation proved negligible in contrast to the camera quantisation errors. The latter introduces a small degree of subjectivity into the results as the projector was focused visually and considering that the projection surface was not orthogonal to the projector optical axis the projector had to be refocused for different portions of the image. As a consequence of refocusing the projector, the system parameters α and β were slightly altered, according to the change of magnification of the projection optics. For the experimental data shown in Figure 2.3 the image had three distinct focal adjustments made. However, the measurable change in system parameters and their impact on the resulting model data in contrast with the error

introduced as a result of the finite spatial size of a camera pixel, this variation was also considered negligible.

Following the empirical study of the proposed analytical findings it was therefore concluded that the finite projection model could serve as suitable tool for the prediction of the theoretical spatial accuracy of a structured light profilometer based on DVP, with it's application somewhat limited as a result of the projection optics.

Appendix B

Physical Fringe Projection Arrangement

The physical Fringe Projection 3D sensing arrangement utilised for much of the work presented in this dissertation is depicted in the schematic diagram shown as Figure B.1. As can be seen a Personal Computer (PC) is interfaced to both the projection and capture

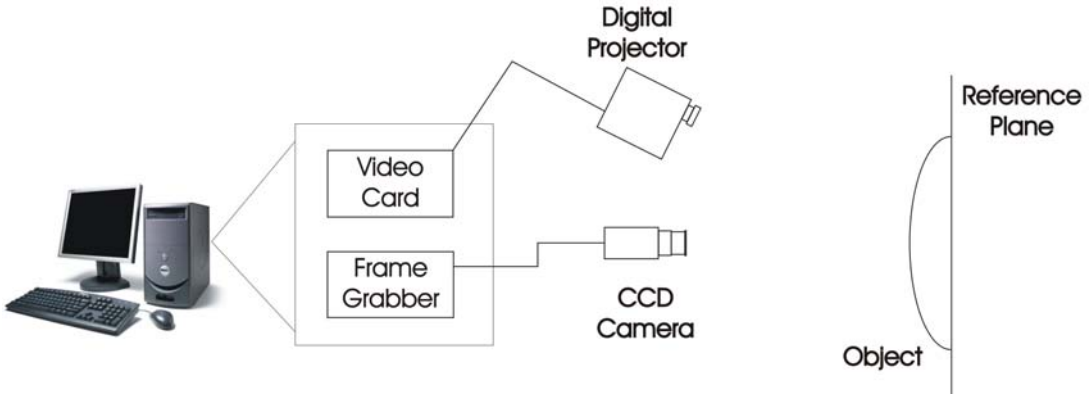

Figure B.1: Physical Fringe Projection Arrangement

devices via a video and frame-grabber card respectively. The PC simultaneously controls the projection and acquisition devices in software and further coordinates the processing of acquired data. The physical arrangement and sensing system can be broadly characterised into three individual sub-systems; Projection; Acquisition and Software. Each of the various components will now be further detailed.

B.1 Projection

The projection sub-system is essentially an extension of the PC display system. A digital video projector is connected to the computer via a Matrox multiple head video card and configured as an independent display device using standard operating system display settings. A Matrox Parhelia PH-A128B video card provides both DVI and standard RGB computer jacks for the projection device. The Matrox card is accompanied with a ”Coloreal Visual” software module to facilitate the appropriate configuration of each of the display outputs individually. The software allows the precise calibration of each display output in terms of individual colour channel Display Gamma, Brightness and Contrast to yield a desired display output response.

Primarily, two projection devices were utilised for the various empirical procedures demonstrated throughout the dissertation; An InFocus LP530 Single Chip DLP projector and a Hitachi CP-X260 3-LCD projector. The more significant specifications for the two projectors are displayed in Table B.1.

Specification	Hitachi CP-X260	InFocus LP530
Technology	1.6 cm Poly-Si 3-LCD	Single DLP 0.7” +/- 12° DDR
Native Resolution	1024x768	1024x768
Contrast Ratio	500:1	400:1
Brightness (ANSI Lumens)	2500	2000

Table B.1: Projector Specifications

B.2 Acquisition

The acquisition component of the 3D sensor was specifically selected to accommodate for both the single and multi-channel environments. A high resolution multi-spectral Duncan-Tech MS3100 3-CCD camera interfaced to the PC via a National Instruments IMAQ-1428 frame grabber card forms the basis of the acquisition sub-system. The camera utilises a dichroic prism and three individual imaging channels each with an independent resolution

of 1392x1040 pixels at an 8 or 10 bit precision to allow for simultaneous high precision image acquisition through a common aperture. The camera / frame grabber combination can support a 7.5 frame per second digital video stream corresponding to a maximum data transfer rate of 14.318 MHz. The hardware / software integration is facilitated though the NI-IMAQ driver library, which provides a range of functionality to acquire images from the camera.

The camera is configured via the RS-232 port of the PC. A specialised DTControl software developed by DuncanTech facilitates the control and configuration of the camera (although user defined software can also be employed). The DTControl software allows the individual control of various aspects of the acquisition device including:

- Individual channel gain
- Individual channel integration time and overall integration time
- Quantisation Precision (8 or 10 bit) and;
- Triggering mode

Supplementary to providing the various methods to configure the camera other auxiliary functionality to display and record images and image data are also made available by the software.

The camera was fitted with a Nikon NIKKOR 28-70mm zoom lens with a manual aperture ring and FSTOP rating of 1:3.5-4.5D. The variable focal length provides the sensing system with a diverse measurement volume.

B.3 Software Interface

The software interface responsible for the integration of hardware components is of Graphical User Interface design and is written in Visual C++ 2005. The software interface serves to control two distinct roles; Projection Control and Camera Control.

The projection functionality allows the individual colour channel manipulation of fringe

- Contrast

- Offset
- Phase and;
- Frequency

Once the user has entered the desired fringe parameters, the image can be drawn on the projector display. An image displaying the current fringe image on the projection display is also provided as reference for the user as seen in Figure B.2. In its current state the functionality to project sinusoidal fringes is in place, however, the application of other signal types will be considered in future versions of the software.

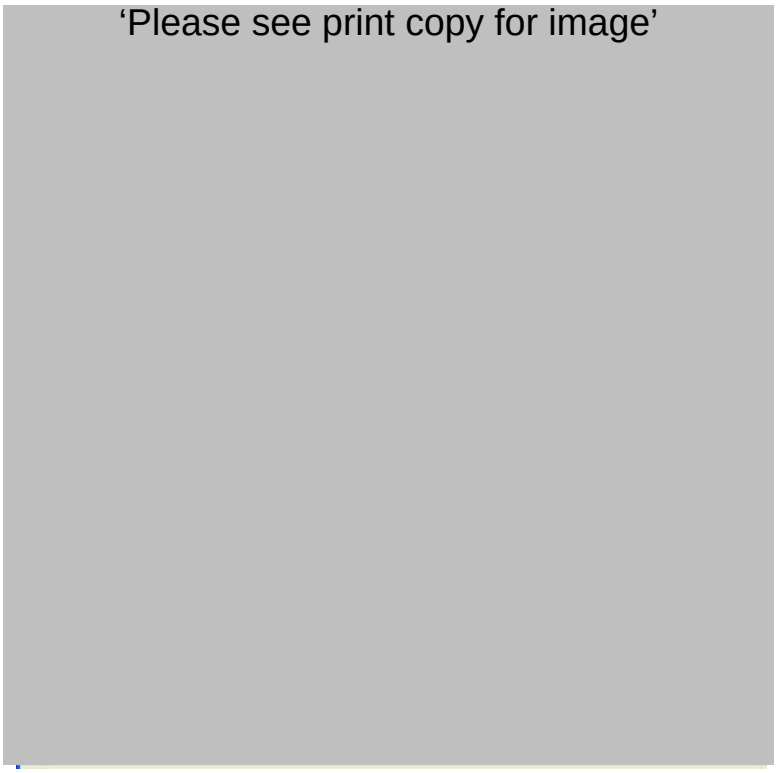

Figure B.2: Software Interface Screen Shot

The camera control structure provides rudimentary control over the acquisition and recording of images, with the DTControl software required for more complex configuration and control of the camera. A display image depicting the most current acquired image from the camera is also provided for user reference as seen in Figure B.2.

While the software interface can be employed to effectively produce and acquire the required fringe signals and data for 3D sensing, the processing of the acquired data is

performed by a 3rd party software package, namely, MATLAB. The full co-ordination and integration of acquisition and processing will be undertaken in a future version of the software.

References

[1] F. Chen, G. M. Brown and M. Song, "Overview of three-dimensional shape measurement using optical methods," *Optical Engineering*, vol. 39, no. 1, pp. 10–22, January 2000.

[2] R. A. Jarvis, "A perspective on range finding techniques for computer vision," *IEEE Transactions on Pattern Analysis and Machine Intelligence*, vol. PAMI-5, no. 2, pp. 122–139, March 1983.

[3] *Manual of Photogrammetry*, 4th ed. American Society of Photogrammetry, 1980.

[4] U. R. Dhond and J. K. Aggarwal, "Structure from stereo - a review," *IEEE Transactions on Systems, Man, and Cybernetics*, vol. 19, no. 6, November/December 1989.

[5] M. Z. Brown, D. Burschka and G. D. Hager, "Advances in computational stereo," *IEEE Transactions on Pattern Analysis and Machine Intelligence*, vol. 25, no. 8, pp. 993–1008, August 2003.

[6] P. Aschwanden and W. Guggenbuhl, *Robust Computer Vision*. Wickmann, 1993, ch. Experimental Results from a Comparative Study on Correlation-Type Registration Algorithms, pp. 268–289.

[7] D. N. Bhat and S. K. Nayar, "Ordinal measures for image correspondence," *IEEE Transactions on Pattern Analysis and Machine Intelligence*, vol. 20, pp. 415–423, 1998.

[8] O. Faugeras, B. Hotz, H. Matthieu, T. Vieville, Z. Zhang, P. Fua, E. Theron, L. Moll, G. Berry, J Vuillemin, P. Bertin and C. Proy, "Real time correlation-based

stereo: Algorithm, implementations and applications," INRIA Technical Report 2013, Tech. Rep., 1993.

[9] R. Zabih and J. Woodfill, "Non-parametric local transforms for computing visual correspondence," in *Proc. Third European Conf. Computer Vision*, 1994, pp. 150–158.

[10] T. Kanade and M. Okutomi, "A stereo matching algorithm with an adaptive window: Theory and experiment," *IEEE Transactions on Pattern Analysis and Machine Intelligence*, vol. 16, pp. 920–932, September 1994.

[11] B. D. Lucas and T. Kanade, "An iterative image registration technique with an application to stereo vision," in *Proc. Int'll Joint Conf. Artificial Intelligence*, 1981, pp. 674–679.

[12] J. Weng, N. Ahuja and T. S. Huang, "Matching two perspective views," *IEEE Transactions on Pattern Analysis and Machine Intelligence*, vol. 14, pp. 806–825, August 1992.

[13] V. S. Kluth, G. W. Kunkel and U. A. Rauhala, "Global least squares matching," in *Proc. Int'l Geoscience and Remote Sensing Symp*, 1992, pp. 1615–1618.

[14] W. Hoff, N. Ahuja, "Surfaces from stereo: Integrating feature matching, disparity estimation, and contour detection," *IEEE Transactions on Pattern Analysis and Machine Intelligence*, vol. 11, pp. 121–136, February 1989.

[15] V. Venkateswar and R. Chellappa, "Heirarchical stereo and motion correspondence using feature groupings," *Int'l J. Computer Vision*, vol. 15, pp. 245–269, 1995.

[16] C. Schmid and A. Zisserman, "The geometry and matching of curves in multiple views," in *Proc. European Conf. Computer Vision*, 1998, pp. 104–118.

[17] S. Birchfield and C. Tomasi, "Depth discontinuties by pixel-to-pixel stereo," in *Proc. IEEE Int'l Conf. Computer Vision*, 1998, pp. 1073–1080.

[18] C. Tomasi and R. Manduchi, "Stereo matching as a nearest-neighbor problem," *IEEE Transactions on Pattern Analysis and Machine Intelligence*, vol. 20, pp. 333–340, 1998.

[19] V. Kolmogorov and R. Zabih, "Computing visual correspondence with occlusions using graph cuts," in *Proc. Int'l Conf. Computer Vision*, 2001.

[20] K. Kanatani and T. Chou, "Shape from texture: General principle," *Artificial Intelligence*, vol. 38, pp. 1–48, 1989.

[21] R. Zhang, P. Tsai, J. E. Cryer and M. Shah, "Shape from shading: A survey," *IEEE Transactions on Pattern Analysis and Machine Intelligence*, vol. 21, no. 8, pp. 690–706, August 1999.

[22] J. E. Cryer, P. Tsai and M. Shah, "Integration of shape from x modules: Combining stereo and shading," in *IEEE Computer Society Conference on Computer Vision and Pattern Recognition*, 1993, pp. 720 – 721.

[23] H. Lange, "Advances in the cooperation of shape from shading and stereo vision," in *IEEE Conference on 3-D Digital Imaging and Modeling*, 1999, pp. 46 – 58.

[24] E. Prados, O. Faugeras, "Shape from shading: a well-posed problem?" in *IEEE Computer Society Conference on Computer Vision and Pattern Recognition*, 2005, pp. 870 – 877.

[25] A. Tankus, N. Sochen and Y. Yeshurun, "A new perspective [on] shape-from-shading," in *IEEE International Conference on*, October 2003, pp. 862 – 869.

[26] Ahmed, Abdelrehim H.; Farag, Aly A., "Shape from shading under various imaging conditions," in *IEEE Conference on Computer Vision and Pattern Recognition (CVPR '07)*, June 2007, pp. 1–8.

[27] S. K. Nayar and Y. Nakagawa, "Shape from focus," *IEEE Transactions on Pattern Analysis and Machine Intelligence*, vol. 16, no. 8, pp. 824–831, August 1994.

[28] M. Subbarao, T. Choi, "Accurate recovery of three-dimensional shape from image focus," *IEEE Transactions on Pattern Analysis and Machine Intelligence*, vol. 17, no. 3, pp. 266–274, March 1995.

[29] E. Krotkov, "Focusing," *International Journal of Computer Vision*, vol. 1, pp. 223–237, 1987.

[30] K. S. Pradeep, and A. N. Rajagopalan, "Improving shape from focus using defocus cue," *IEEE Transactions on Image Processing*, vol. 16, no. 7, pp. 1920–1925, July 2007.

[31] M. B. Ahmad and T. Choi, "Shape from focus using optimization technique," in *ICASSP 2006*, 2006, pp. 493–496.

[32] I. Moring and H. Ailisto, "Active 3-d vision system for automatic model-based shape inspection," *Optics and Lasers in Engineering*, vol. 10, pp. 149–160, 1989.

[33] J. S. Massa, G. S. Buller, A. C. Walker, S. Cova, M. Umasuthan and A. M. Wallace, "Time-of-flight optical ranging system based on time correlated single-photon counting," *Applied Optics*, vol. 37, no. 31, pp. 7298–7304, November 1998.

[34] D. Malacara, Ed., *Optical Shop Testing*, 2nd ed. John Wiley & Sons, 1992.

[35] C. Polhemus, "Two-wavelength interferometry," *Applied Optics*, vol. 12, no. 9, p. 20712074, September 1973.

[36] Y. Cheng and J. C. Wyant, "Multiple-wavelength phase-shifting interferometry," *Applied Optics*, vol. 24, no. 6, pp. 804–807, March 1985.

[37] ——, "Two-wavelength phase shifting interferometry," *Applied Optics*, vol. 23, no. 24, pp. 4539–4543, December 1984.

[38] K. Hanies and B. P. Hildebrand, "Contour generation by wavefront reconstruction," *Physics Letters*, vol. 19, no. 1, pp. 10–11, September 1965.

[39] Y. Y. Hung, J. L. Turner, M. Tafralian, J. D. Hovanesian and C. E. Taylor, "Optical method for measuring contour slopes of an object," *Applied Optics*, vol. 17, no. 1, pp. 128–131, January 1978.

[40] H. El-Ghandoor, "Tomographic investigation of the refractive index profiling using speckle photography technique," *Optics Communications*, vol. 133, pp. 33–38, January 1997.

[41] R. Rodriguez-Vera, D. Kerr and F. Mendoza-Santoyo, "Electronic speckle contouring," *Journal of the Optical Society of America A*, vol. 9, no. 11, pp. 2000–2008, November 1992.

[42] T. Maack, G. Notni and W. Schreiber, "Three-coordinate measurement of an object surface with a combined two-wavelength and two-source phase-shifting speckle interferometer," *Optics Communications*, vol. 115, pp. 576–584, April 1995.

[43] R. S. Sirohi and F. S. Chau, *Optical Methods of Measurement Wholefield Techniques*, ser. Optical Engineering. Marcel Dekker, 1999, ch. 6, pp. 127–182.

[44] J. H. Bruning, *Optical Shop Testing*. Wiley, 1978, ch. Fringe Scanning Interferometers.

[45] K. Creath, *Progress in Optics*. Elsevier, 1988, vol. 26, ch. Phase-Measurement Interferometry Techniques, pp. 357–373.

[46] ——, "Step height measurement using two-wavelength phase-shifting interferometry," *Applied Optics*, vol. 26, pp. 2810–2816, July 1987.

[47] S. Kuwamura and I. Yamaguchi, "Wavelength scanning profilometry for real-time surface shape measurement," *Applied Optics*, vol. 36, pp. 4473–4482, July 1997.

[48] P. J. Caber, "Interferometric profiler for rough surfaces," *Applied Optics*, vol. 32, no. 19, pp. 3438–3441, July 1993.

[49] A. F. Fercher, H. Z. Hu, and U. Vry, "Rough surface interferometry with two-wavelength heterodyne speckle interferometer," *Applied Optics*, vol. 24, no. 14, pp. 2181–2188, July 1985.

[50] K. J. Gasvik, *Optical Metrology*, 3rd ed. John Wiley & Sons, 2002, ch. Moiré Methods. Triangulation, pp. 173–174.

[51] D. M. Meadows, W. O. Johnson and J. B. Allen, "Generation of surface contours by moiré patterns," *Applied Optics*, vol. 9, no. 4, pp. 942–947, April 1970.

[52] H. Takasaki, "Moiré topography," *Applied Optics*, vol. 9, no. 6, pp. 1467–1472, June 1970.

[53] T. Yoshizawa, "The recent trend of moiré metrology," *Journal of Robotics and Mechatronics*, vol. 3, no. 3, pp. 157–162, May 1991.

[54] T. Yoshizawa and T. Tomisawa, "Shadow moiré topography by means of the phase-shift method," *Optical Engineering*, vol. 32, no. 7, pp. 1668–1674, July 1993.

[55] Y. Choi and S. Kim, "Phase-shifting grating projection moiré topography," *Optical Engineering*, vol. 37, no. 3, pp. 1005–1010, March 1998.

[56] A. Asundi, "Computer aided moiré methods," *Optics and Lasers in Engineering*, vol. 18, pp. 213–238, March 1993.

[57] K. Harding, "High speed moiré contouring methods analysis," in *SPIE Condference on Three-Dimensional Imaging, Optical Metrology, and Inspection IV*, vol. 3520. Boston, Massachusetts: SPIE, November 1998, pp. 27–35.

[58] J. Batlle, E. Mouaddib and J. Salvi, "Recent progress in coded structured light as a technique to solve the correspondence problem: A survey," *Pattern Recognition*, vol. 31, no. 7, pp. 963–982, 1998.

[59] Z. Ji and M. C. Leu, "Design of optical triangulation devices," *Optics and Laser Technology*, vol. 21, no. 5, pp. 335–338, 1989.

[60] A. Asundi and Z. Wensen, "Unified calibration technique and its applications in optical triangular profilometry," *Applied Optics*, vol. 38, no. 16, pp. 3556–3561, June 1999.

[61] C. P. Keferstein and M. Marxer, "Testing bench for laser triangulation sensors," *Sensor Review*, vol. 18, no. 3, pp. 183–187, 1998.

[62] X. Cheng, X Su and L. Guo , "Automated measurement method for 360-degree profilometry of 3-d diffuse objects," *Applied Optics*, vol. 30, no. 10, pp. 1274–1278, April 1991.

[63] A. Asundi and W. Zhou, "Mapping algorithm for 360-deg profilometry with time delayed integration imaging," *Optical Engineering*, vol. 38, no. 2, pp. 339–344, February 1999.

[64] J. Salvi, J. Pages and J. Batlle, "Pattern codification strategies in structured light systems," *Pattern Recognition*, vol. 37, pp. 827–849, 2004.

[65] J. L. Posdamer and M. D. Altschuler, "Surface measurement by space-encoded projected beam systems,," *Computer Graphics and Image Processing*, vol. 18, no. 1, pp. 1–17, 1982.

[66] S. Inokuchi, K. Sato and F. Matsuda, "Range imaging system for 3-d object recognition," in *Proceedings of the International Conference on Pattern Recognition*, 1984, pp. 806–808.

[67] G. Sansoni, S. Corini, S. Lazzari, R. Rodella and F. Docchio, "Three-dimensional imaging based on gray-code light projection: characterization of the measuring algorithm and development of a measuring system for industrial applications," *Applied Optics*, vol. 36, no. 19, pp. 4463–4472, July 1997.

[68] E. Horn and N. Kiryati, "Towards optimal structured light patterns," *Image and Vision Computing*, vol. 17, pp. 87–97, 1999.

[69] D. Caspi, N.Kiryati and J. Shamir, "Range imaging with adaptive color structured light," *IEEE Transactions on Pattern Analysis and Machine Intelligence*, vol. 20, no. 5, pp. 470–480, May 1998.

[70] G. Sansoni, M, Carocci and R. Rodella, "Three-dimensional vision based on a combination of gray-code and phase-shift light projection: analysis and compensation of the systematic errors," *Applied Optics*, vol. 38, no. 31, pp. 6565–6573, November 1999.

[71] W. Krattenhaler, K.J. Mayer and H. Duwe, "3d-surface measurement with coded light approach," in *Fourth International Workshop for Digital Image Processing and Computer Graphics*. Proceedings of Osterreichische Arbeitsgem, 1993, pp. 103–114.

[72] T. G. Stahs and F. M. Wahl, "Fast and robust range data acquisition in a low-cost environment," in *Close-Range Photogrammetry Meets Machine Vision*, E. P. Baltsavias and A. Gruen, Ed. SPIE, 1990, pp. 496–503.

[73] K. L. Boyer and A. C. Kak, "Color-encoded structured light for rapid active ranging," *IEEE Transactions on Pattern Analysis and Machine Intelligence*, vol. 9, no. 1, pp. 14–28, January 1987.

[74] W. Liu, Z. Wang, G. Mu and Z. Fang, "Color-coded projection grating method for shape measurement with a single exposure," *Applied Optics,* vol. 39, no. 20, pp. 3504–3508, July 2000.

[75] C. Lu and L. Xiang, "Optimal intensity-modulation projection technique for three-dimensional shape measurement," *Applied Optics*, vol. 42, no. 23, pp. 4649–4657, August 2003.

[76] H. Hugli and G. Maitre, "Generation and use of color pseudo random sequences for coding structured light in active ranging," in *Industrial Inspection*, 1989, pp. 75–82.

[77] Y. C. Hsieh, "A note on the structured light patterns for three-dimensional imaging systems," *Pattern Recognition*, pp. 315–318, 1998, lett. 19.

[78] Y. Hsieh, "Decoding structured light patterns for three-dimensional imaging systems," *Pattern Recognition*, vol. 34, pp. 343–349, 2001.

[79] L. Zhang, B. Curless and S. M. Seitz, "Rapid shape acquisition using color structured light and multi-pass dynamic programming," in *International Symposiumon 3D Data Processing Visualization and Transmission, Padova, Italy*. IEEE Computer Society, 2002, pp. 1–13.

[80] P. Griffin, L. Narasimhan and S. Yee, "Generation of uniquely encoded light patterns for range data acquisition," *Pattern Recognition*, vol. 25, no. 6, pp. 609–616, 1992.

[81] B. Carrihill and R. Hummel, "Experiments with the intensity ratio depth sensor," *Computer Vision, Graphics, and Image Processing*, vol. 32, pp. 337–358, 1985.

[82] C. Wust and D. W. Capson, "Surface profile measurement using color fringe projection," *Machine Vision and Applications*, vol. 4, pp. 193–203, 1991.

[83] V. Srinivasan, H. C. Liu and M. Halioua, "Automated phase-measuring profilometry of 3-d diffuse objects," *Applied Optics*, vol. 23, no. 18, pp. 3105–3107, September 1984.

[84] M. Takeda and K Mutoh, "Fourier transform profilometry for the automatic measurement of 3-d object shapes," *Applied Optics*, vol. 22, no. 24, pp. 3977–3982, December 1983.

[85] X. Su and L. Su, "New 3d profilometry based on modulation measurement," in *Automated Optical Inspection for Industry: Theory, Technology, and Applications II*, vol. 35558. SPIE - The Internation Society for Optical Engineering, September 1998, pp. 1–7.

[86] S. Toyooka and Y. Iwaasa, "Automatic profilometry of 3-d diffuse objects by spatial phase detection," *Applied Optics*, vol. 25, no. 10, pp. 1630–1633, May 1986.

[87] R. Rodriguez-Vera and M. Servin, "Phase locked loop profilometry," *Optics and Laser Technology*, vol. 26, no. 6, pp. 393–398, 1994.

[88] P. S. Huang, Q. Hu, F. Jin, F. Chiang, "Color-encoded digital fringe projection technique for high speed three-dimensional surface contouring," *Optical Engineering*, vol. 38, pp. 1065–1071, 1999.

[89] P. S. Huang, C. Zhang, F. Chiang, "High-speed 3-d shape measurement based on digital fringe projection," *Optical Engineering*, vol. 42, no. 1, pp. 163–168, January 2003.

[90] S. Zhang, P. Huang, "High-resolution, real-time 3d shape acquisition," in *Conference on Computer Vision and Pattern Recognition Workshop on Realtime 3D Sensors and their uses (CVPRN' 04)*, vol. 3. Washington D.C USA: IEEE, June - July 2004, pp. 28–37.

[91] P. S. Huang and S. Zhang, "Fast three-step phase-shifting algorithm," *Applied Optics*, vol. 45, no. 21, pp. 5086–5091, July 2006.

[92] S. Zhang and S. Yau, "High-resolution, real-time 3d absolute coordinate measurement based on a phase-shifting method," *Optics Express*, vol. 14, no. 7, pp. 2644–2649, April 2006.

[93] S. Zhang, D. Royer and S. Yau, "Gpu-assisted high-resolution, real-time 3-d shape measurement," *Optics Express*, vol. 14, no. 20, pp. 9120–9129, October 2006.

[94] L. Chen, C Huang, "Miniaturized 3d surface profilometer using digital fringe projection," *Measurement Science and Technology*, vol. 16, pp. 1061 – 1068, March 2005.

[95] O. A. Skydan, M. J. Lalor, D. R. Burton, "Technique for phase measurement and surface reconstruction by use of colored structured light," *Applied Optics*, vol. 41, no. 29, pp. 6104–6117, October 2002.

[96] P. S. Huang, Q. J. Hu and F. Chiang, "Double three-step phase-shifting algorithm," *Applied Optics*, vol. 41, no. 22, pp. 4503–4509, August 2002.

[97] H. Guo, H. He, M. Chen, "Gamma correction for digital fringe projection profilometry," *Applied Optics*, vol. 43, no. 14, pp. 2906 – 2914, May 2004.

[98] S. Zhang and S. Yau, "Generic nonsinusoidal phase error correction for three-dimensional shape measurement using a digital video projector," *Applied Optics*, vol. 46, no. 1, pp. 36–43, January 2007.

[99] J. C. Wyant, "Phase shifting interferometry," http://www.optics.arizona.edu/jcwyant/Optics513/optics513.htm, 1998.

[100] K. Creath, *Progress in Optics XXVI*. Elsevier Science Publishers, 1988, ch. Phase-Measurement Interferometry Techniques, pp. 349–393.

[101] J. C. Wyant and C. L. Koliopoulos, "An optical profilometer for surface characterzation of magnetic media," *ASLE Transactions*, vol. 27, no. 2, pp. 101–113, April 1983.

[102] B. Bhushan, J. C. Wyant and C. L. Koliopoulos, "Measurement of surface topography of magnetic tapes by mirau interferometry," *Applied Optics*, vol. 24, no. 10, pp. 1489–1497, May 1985.

[103] P. L. Wizinowich, "Phase shifting interferometry in the presence of vibration: a new algorithm and system," *Applied Optics*, vol. 29, no. 22, pp. 3271–3279, August 1990.

[104] J. Schwider, R. Burow, K.-E. Elssner, J. Grzanna, R. Spolaczyk and K. Merkel, "Digital wave-front measuring interferometry: some systematic error sources," *Applied Optics*, vol. 22, no. 21, pp. 3421–3432, November 1983.

[105] M. Takeda, H. Ina and S. Kobayashi, "Fourier-transform method of fringe-pattern analysis fro computer-based topography and interferometry," *J. Optical Society of America*, vol. 72, no. 1, pp. 156–160, January 1.

[106] J. Li, X. Su and L. Guo, "Improved fourier transform profilometry for the automatic measurement of three-dimensional object shapes," *Optical Engineering*, vol. 29, no. 12, pp. 1439–1444, December 1990.

[107] J. Yi and S. Huang, "Modified fourier transform profilometry for the measurement of 3-d steep shapes," *Optics and Lasers in Engineering*, vol. 27, pp. 493–505, 1997.

[108] J. Lin and X. Su, "Two-dimensional fourier transform profilometry for the automatic measurement of three-dimensional object shapes," *Optical Engineering*, vol. 35, no. 11, pp. 3297–3302, November 1995.

[109] M. Takeda, Q. Gu, M. Kinoshita, H. Takai and Y. Takahashi, "Frequency-multiplex fourier-transform profilometry: a single-shot three-dimensional shape measure-

ment of objects with large height discontinuities and/or surface isolations," *Applied Optics*, vol. 36, no. 22, pp. 5347–5354, August 1997.

[110] X. Su, Jian Li and L. Guo, "An improved fourier transform profilometry," in *Optical Testing and Metrology II*, vol. 954, 1988, pp. 241–244.

[111] Y. Hu, J. Xi, J. Chicharo and Z. Yang, "Improved three-step phase shifting profilometry using digital fringe pattern projection," in *Proceedings of the International Conference on Computer Graphics, Imaging and Visualisation (CGIV'06)*. IEEE Computer Society, 2006.

[112] M. Takeda and M. Kitoh, "Spatiotemporal frequency multiplex heterodyne interferometry," *J. Opt. Soc. Am. A*, vol. 9, no. 9, pp. 1607–1614, September 1992.

[113] V. I. Gushov and Y. N. Solodkin, "Automatic processing of fringe patterns in integer interferometers," *Optics and Lasers in Engineering*, vol. 14, pp. 311–324, 1991.

[114] Y. Ichioka and M. Inuiya, "Direct phase detecting system," *Applied Optics*, vol. 11, no. 7, pp. 1507–1514, July 1972.

[115] S. Tang and Y. Y, Hung, "Fast profilometer for the automatic measurement of 3-d object shapes," *Applied Optics*, vol. 29, no. 20, pp. 3012–3018, July 1990.

[116] J. Villa, M. Servin and L. Castillo, "Profilometry for the measurement of 3-d object shapes based on regularized filters," *Optics Communications*, vol. 161, pp. 13–18, March 1999.

[117] K. Itoh, "Analysis of the phase unwrapping algorithm," *Applied Optics*, vol. 21, no. 14, pp. 2470–2470, July 1982.

[118] D. C. Ghiglia and M. D. Pritt, *Two-Dimensional Phase Unwrapping, Theory, Algorithms, and Software*. John Wiley & Sons, 1998.

[119] R. M. Goldstein, H. A. Zebker and C. L. Werner, "Satellite radar interferometry: Synthetic aperture radar observations," *Radio Science*, vol. 23, pp. 713–720, 1988.

[120] J. M. Huntley, "Noise-immune phase unwrapping algorithm," *Applied Optics*, vol. 28, no. 15, pp. 3268–3270, August 1989.

[121] X. Su, and W. Chen, "Reliability-guided phase unwrapping alogorithm: a review," *Optics and Lasers in Engineering*, vol. 42, pp. 245–261, 2004.

[122] D. C. Ghiglia, G. A. Mastin and L. A. Romero, "Cellular-automata method for phase unwrapping," *J. Opt. Soc. Am*, vol. 4A, pp. 267–280, 1987.

[123] J. J. Gierloff, "Phase unwrapping by regions." SPIE, 1987, pp. 2–9.

[124] J. M. Huntley and H. Saldner, "Temporal phase-unwrapping algorithm for automated interferogram analysis," *Applied Optics*, vol. 32, no. 17, pp. 3047–3052, June 1993.

[125] S. Zhang, "High-resolution, real-time 3-d shape measurement," Ph.D. dissertation, Stony Brooke University, May 2005.

[126] K. G. Harding and S. L. Cartwright, "Phase grating use in moire interferometry," *Applied Optics*, vol. 23, no. 10, pp. 1517–1520, May 1984.

[127] E. B. Li, X. Peng, J. Xi, J. F. Chicharo, J. Q. Yao and D. W. Zhang, "Multi-frequency and multiple phase-shift sinusoidal fringe projection for 3d profilometry," *Optics Express*, vol. 13, no. 5, pp. 1561–1569, March 2005.

[128] G. Sansoni, L. Biancardi, U. Minoni, F. Docchio, "A novel, adaptive system for 3-d optical profilometry using a liquid crystal light projector," *IEEE Transactions on Instrumentation and Measurement*, vol. 43, no. 4, pp. 558 – 566, August 1994.

[129] W. Su, H. Liu, K. Reichard, S. Yin, F T. S. Yu, "Fabrication of digital sinusoidal gratings and precisely controlled diffusive flats and their application to highly accurate projected fringe profilometry," *Optical Engineering*, vol. 42, pp. 1730–1740, June 2003.

[130] H. O. Saldner, J. M. Huntley, "Profilometry using temporal phase unwrapping and a spatial light modulator-based fringe projector," *Optical Engineering*, vol. 36, no. 2, pp. 610 – 615, February 1997.

[131] S. M. Kelly, M. ONeill, *Liquid Crystals for Electro-optic applications*. Academic Press, 2000.

[132] M. G. Robinson, J. Chen, G. D. Sharp, *Polarization Engineering for LCD Projection*. John Wiley and Sons, July 2005.

[133] L. A. Yoder, "An introduction to the digital light processing (dlp) technology," *White Paper*, vol. www.dlp.com, Texas Instruments.

[134] L. J. Hornbeck, "Digital light processing for high-brightness, high resolution applications," vol. 3013. SPIE, 1997, pp. 27–40.

[135] "www.dlp.com, texas instruments."

[136] J. M. Huntley, H. O. Saldner, "Error-reduction methods for shape measurement by temporal phase unwrapping," *Journal of the Optics Society America*, vol. 14, no. 12, pp. 3188–3196, December 1997.

[137] C. R. Coggrave, J. M. Huntley, "Optimization of a shape measurement system based on spatial light modulators," *Optical Engineering*, vol. 39, no. 1, pp. 91 – 98, January 2000.

[138] C. A. Poynton, "Gamma and it disguises: The nonlinear mappings of intensity in perception, crts, film and video," *SMPTE Journal*, pp. 1099–1108, 1993.

[139] L. Kinell, "Multichannel method for absolute shape measurement using projected fringes," *Optics and Lasers in Engineering*, vol. 41, pp. 57–71, 2004.

[140] M. C. Stone, "Representing colors as three numbers," *Tutorial IEEE Computer Graphics and Applications*, pp. 78–85, July / August 2005.

[141] Geospatial Systems Incorporated, "Spectral and polarization configuration guide for ms series 3-ccd cameras."

[142] Y. Hu, J. Xi, E. Li, J. Chicharo, Z. Yang and Y. Yu, "A calibration approach for decoupling colour cross-talk using nonlinear blind signal separation network," in *COMMAD Conference*. IEEE, 2004.

[143] D. Malacara, Ed., *Optical Shop Testing*, 3rd ed. Wiley & Sons, 2007.

[144] k. Kinnstaetter, A. W. Lohmann, J. Schwider and N. Streibl, "Accuracy of phase shifting interferometry," *Applied Optics*, vol. 27, no. 24, pp. 5082–5089, December 1988.

[145] K. Hibino, B. F. Oreb, D. I. Farrant and K. G. Larkin, "Phase shifting for non-sinusoidal waveforms with phase-shift errors," *Journal of the Optical Society of America*, vol. 12, no. 4, pp. 761–768, April 1995.

[146] Y. Hu, J. Xi, E. Li, J. Chicharo, Z. Yang, "Three-dimensional profilometry based on shift estimation of projected fringe patterns," *Applied Optics*, vol. 45, no. 4, pp. 678 – 687, Feburary 2006.

[147] M. Rivera, J. L. Marroquin, S. Botello and M. Servin, "Robust spatiotemporal quadrature filter for mulitphase stepping," *Applied Optics*, vol. 39, no. 2, pp. 284–292, January 2000.

[148] X. Su, W. Zhou, G. Bally and D. Vukicevic, "Automated phase-measuring profilometry using defocused projection of a ronchi grating," *Optics Communications*, vol. 94, pp. 561–573, 1992.

[149] J. Xu, Y. Wang, S. Si, C. Gao, D. Yun, "Research on application of special filter in projecting grating profilometry," *Optical Technology and Image Processing for Fluids and Solids Diagnostics SPIE*, vol. 5058, pp. 532–536, 2003.

[150] H. Zhi, R. B. Johansson, "Adaptive filter for enhancement of fringe patterns," *Optics and Lasers in Engineering*, vol. 15, pp. 241–251, 1991.

[151] S. Ryoo, T. Choi, "3-d profilometry by analysis of noisy white-light interferograms," *In three-dimensional and Multidimensional Microscopy: Image Acquisition Processing VII SPIE*, vol. 3919, pp. 152–160, 2000.

[152] H. Farid, "Blind inverse gamma correction," *IEEE Transactions on Image Procecssing*, vol. 10, pp. 1428–1433, 2001.

[153] F. J. Cuevas, M. Servin, O. N. Stavroudis, R. Rodriguez-Vera, "Multi-layer neural network applied to phase and depth recovery from fringe patterns," *Optics Communications*, vol. 181, pp. 239–259, July 2000.

[154] H. Mills, D. R. Burton, M. J. Lalor, "Applying backpropagation neural networks to fringe analysis," *Optics and Lasers in Engineering*, vol. 23, pp. 331–41, 1995.

[155] D. Ganotra, J. Joseph, K. Singh, "Profilometry for the measurement of three-dimensional object shape using radial basis function, and multi-layer perceptron neural networks," *Optics Communications*, vol. 209, pp. 291–301, August 2002.

[156] ——, "Second-and first-order phase locked loops in fringe profilometry and application of neural networks for phase-to-depth conversion," *Optics Communications*, vol. 217, pp. 85–96, 2003.

[157] ——, "Object reconstruction in multilayer neural network based profilometry using grating structure comprising two regions with different spatial periods," *Optics and Lasers in Engineering*, vol. 42, pp. 179–192, 2004.

[158] G. Zhang, Z. Wei, "A novel calibration approach to structured light 3d vision inspection," *Optics and Laser Technology*, vol. 34, pp. 373–380, 2002.

[159] F. J. Cuevas, M. Servin, R. Rodriguez-Vera, "Depth object recovery using radial basis functions," *Optics Communications*, vol. 163, pp. 270–277, May 1999.

[160] M. Chang W. Tai, "360-deg profile noncontact measurement using a neural network," *Optical Engineering*, vol. 34, no. 12, pp. 3572–3576, December 1995.

[161] R. Beale, T. Jackson, *Neural Computing an introduction*. Adam Hilger, 1990.

[162] R. M. Haralick, L. G. Shapiro, *Computer and Robot Vision*. Addison-Wesley, 1992, vol. 1.

[163] E. R. Davies, *Machine Vision: Theory Algorithms Practicalities*, 3rd ed. Elsevier, 2005.

[164] G. Horvath, *Neural Networks for Instrumentation, Measurement and Related Industrial Applications*. IOS Press Ohmsha, 2003.

[165] G. Marcu, “Gray tracking correction for tft-lcds,” in *Color Imaging IX: Processing, Hardcopy, and Applications*, R. Eschbach, G. Marcu, Ed. SPIE-IS&T Electronic Imaging, 2004, pp. 277–285.

[166] G. Marcu, W. Chen, K. Chen, P. Graffagnino and O. Andrade, “Color characterization issues for tft-lcd displays,” in *Color Imaging: Device-Independent Color, Color Hardcopy, and Applications VII*, R. Eschbach and G. Marcu, Ed. SPIE, Jan 2002, pp. 187–198.